



Swansea University
Prifysgol Abertawe

COLLEGE OF ENGINEERING
SWANSEA UNIVERSITY
SWANSEA

LUXEMBOURG
INSTITUTE OF SCIENCE
AND TECHNOLOGY



LUXEMBOURG INSTITUTE OF
SCIENCE AND TECHNOLOGY
LUXEMBOURG

Multiscale Modelling of Anisotropic Composite Media for EMC Applications

SUBMITTED TO SWANSEA UNIVERSITY IN FULFILLMENT OF THE REQUIREMENTS FOR
THE DEGREE OF DOCTOR OF PHILOSOPHY

ALEX GANSEN

SWANSEA UNIVERSITY 2017

IN COLLABORATION WITH THE
TRANSPARENT ELECTRONICS AND OPTICAL TUNEABLE NANOCOMPOSITES GROUP
MATERIAL RESEARCH AND TECHNOLOGY DEPARTMENT
LUXEMBOURG INSTITUTE OF SCIENCE AND TECHNOLOGY

Abstract

The aim of this research project is the modelling of complex anisotropic composites and metamaterials with sub-wavelength inclusions at low frequencies. Metamaterials are artificial materials with properties which do not exist in nature. These properties are achieved by merging resonating metallic inclusion in a dielectric matrix. Depending on the shape of the inclusions, they may change the polarisation of the incoming light or completely stop the transmission for a given frequency. Such materials are very challenging to model due to their frequency dependence, anisotropy and coupling between the electric and magnetic fields. A metamaterial may consists of hundreds or thousands of inclusions that interact with each other. To reduce the computational costs, a multi-scale approach is developed that allows the computation of effective medium parameters from a unit cell of a metamaterial. Finally an experimental setup was build to compare the theoretical predictions with the experiment. For most of the simulations I rely on a Finite Difference Time based Method, a generalised version of the Yee algorithm. The classical Yee algorithm is a second order time domain algorithm and often the method of choice for industrial simulations because of its simplicity and low computational costs. Furthermore the boundary conditions are naturally treated in the algorithm when the physical boundary conforms to the orthogonal mesh, which is not the case for curved boundaries introducing simulation errors. To circumvent this problem we generalised the Yee algorithm to unstructured meshes using a Delaunay mesh and its orthogonal Voronoi dual graph. I demonstrate how this method can be used to model isotropic, anisotropic, dispersive and even more complicated materials. As we demonstrate throughout this thesis this method may significantly reduce the computational costs and it still allows to model numerically challenging materials like bi-anisotropic metamaterials.

Declaration and Statements

Declaration

This work has not been accepted in substance degree and is not concurrently submitted in candidature for any degree.

Signed(Candidate)

Date.....

Statement 1

This thesis is the result of my own investigations, except where otherwise stated. Other sources are acknowledged by footnotes giving explicit references. A bibliography is appended.

Signed(Candidate)

Date.....

Statement2

I hereby give consent for my thesis, if accepted, to be available for photocopying and for inter-library loan, and for the title and summary to be made available to outside organisations.

Signed(Candidate)

Date.....

Contents

1. Introduction	1
1.1. Motivation	1
1.2. Aims and Objectives	4
1.3. Outline	5
I. Numerical Modelling of Maxwell Equations	9
2. Maxwell and Constitutive Material Equations	11
2.1. Maxwell equations	12
2.1.1. Interpretation of Maxwell equations	13
2.2. Electromagnetic boundary conditions at material interfaces	14
2.3. TE and TM modes	15
2.4. Constitutive equations	16
2.4.1. Electric and magnetic conductivities	17
2.4.2. Lorentz material	17
2.4.3. Debye material	18
2.4.4. Drude material	19
2.4.5. Causality condition	20
2.5. Anisotropic material	20
2.6. Metamaterial modelling	21
2.6.1. Group and phase velocity of double negative metamaterials	22
2.6.2. Negative index of refraction	24
2.6.3. Absorption and evanescent waves	26
2.7. Electrical wire grid resonators	27
2.8. Magnetic resonator	29
2.9. Effective LHM medium	31
2.10. Chiral and pseudo-chiral materials	31
2.11. Classification of metamaterials	34
3. Numerical Solution of Maxwell Equations	37
3.1. Review of numerical techniques for the solution of Maxwell's equations	37
3.2. Pure scattered field formulation	42
3.3. Classical 3D Yee algorithm	43
3.4. Modelling of isotropic dielectrics using the co-volume method	46
3.4.1. Problem formulation	46
3.4.2. Discrete equations	47

3.5.	Mesh generation	49
3.5.1.	Boundary conditions	53
3.6.	Modelling of anisotropic dielectrics	57
3.6.1.	Problem formulation	58
3.6.2.	Discrete equations	58
3.6.3.	Material interface boundary conditions	60
3.6.4.	Obtaining approximated field vectors from edge projections	60
3.6.5.	Local orthogonal unit vectors	62
3.6.5.1.	Coordinate transformation	63
3.6.6.	Time updating scheme	64
3.7.	Modelling of isotropic chiral material	65
3.7.1.	Problem formulation	66
3.7.2.	Discrete equations and Z-Transform	68
3.7.3.	Boundary conditions	71
3.7.4.	Updating scheme	72
3.8.	Modelling of bi-anisotropic materials	73
3.8.1.	Problem formulation	73
3.8.2.	Update equations	81
3.8.3.	Updating scheme	82
4.	Code Validation and Numerical Examples	85
4.1.	Radar cross section and transmission	85
4.1.1.	Radar cross section	85
4.1.2.	Transmission	86
4.2.	Isotropic lossy material	86
4.2.1.	Comparison between standard FDTD and co-volume method	86
4.2.2.	Convergence of the leapfrog scheme	89
4.2.3.	Scattering by a spherical object	90
4.2.3.1.	Scattering by a coated spherical object	93
4.2.3.2.	Transmission of a narrow band pulse	96
4.3.	Numerical Validation for anisotropic lossy objects	99
4.3.1.	Scattering on sphere	99
4.3.1.1.	Magnetically uniaxial non-lossy anisotropic sphere	99
4.3.1.2.	Electrically uniaxial non-lossy anisotropic sphere	100
4.3.2.	Electrically lossy anisotropic sphere	101
4.3.3.	Magnetically lossy anisotropic sphere	102
4.3.4.	Computational cost of the anisotropic model	103
4.3.5.	Transmission of a narrow band pulse	105
4.4.	Numerical validation for isotropic chiral material	109
4.4.1.	Rotation of the plane of polarisation	109
4.4.2.	Reflection and transmission on a chiral slab	110
4.4.3.	Numerical stability without damping	113
4.4.4.	Numerical stability with damping	115

4.5.	Numerical validation for bi-anisotropic media	116
4.5.1.	Radar cross section on anisotropic dispersive sphere	116
4.5.1.1.	Isotropic permittivity	117
4.5.1.2.	Anisotropic permittivity	117
4.5.1.3.	Isotropic permeability	118
4.5.1.4.	Anisotropic permeability	119
4.5.1.5.	isotropic chiral vs bi-anisotropic	120
II.	Multiscale Approach for Metamaterial Modelling	123
5.	Micro to Macro Approach	125
5.1.	Analytical microscale homogenisation techniques	126
5.2.	Numerical microscale techniques	127
5.2.1.	Indirect microscale parameter retrieval	129
5.2.2.	Direct mean field technique	131
6.	Experimental Characterisation of Material Properties	135
6.1.	Introduction	135
6.2.	Review of experimental procedures for the characterisation of material properties	135
6.3.	Free space measurement setup	138
6.4.	Scattering parameters	139
6.5.	Time Gating	141
6.6.	Review of calibration techniques of the free space setup	146
6.7.	Practical considerations	150
6.8.	Dielectric properties from S-parameters	151
6.9.	Retrieval of constitutive parameters from a bi-anisotropic metamaterial	155
6.10.	Metamaterial with metallic omega inclusions	158
7.	Experimentally Measured Material Parameters	161
7.1.	Experimental validation for an isotropic dielectric	161
7.1.1.	Discussion of the retrieved material parameters of simple dielectrics	164
7.2.	Experimental results for a bi-anisotropic material	165
7.2.1.	Discussion of the experimental results	174
8.	Results of the Multiscale Approach	177
8.1.	Microscale simulation of the bi-anisotropic media	177
8.1.1.	Method 1 “Indirect retrieval method”	177
8.1.2.	Method 2 “Direct retrieval method”	181
8.2.	Macroscale Simulation	183
9.	Conclusion and Future Work	187
9.1.	Isotropic lossy materials	187
9.2.	Anisotropic lossy materials	187

Contents

9.3. Isotropic chiral materials	188
9.4. Bi-anisotropic materials	188
9.5. Multiscale Approach	188
9.6. Experimental setup	189
A. The Z-Transform	203
A.1. Derivation of the z-Transform from the Laplace transform	203
A.2. Dispersive chiral FDTD Formulation using the Z Transform	204
A.2.1. Definition and Properties of the Z-Transform	205
A.2.2. Examples	206
A.3. Z-Transform of material parameters using an analytical method	208
A.4. Z-Transform using padé approximants	210
A.4.1. Obtaining Padé coefficients	211
B. Finite Differences	215
C. Phase unwrapping	217

Acknowledgments

During my PhD I participated in several courses and summer schools. During a project management course I participated in, in my second year the presenter asked how we would rate our supervisors on a scale from one to ten, because we are actually one of their projects. The overall rating was devastating. Many students gave a rating of three or even one out of ten. I just thought, what the hell, I would easily give them a twelve or more. That moment I realised how lucky I actually was. During my stay in Swansea I felt perfectly supervised all the time. Although I went to the office of my supervisors several times a week, without appointment, they always had time to help me. When I was in Luxembourg we stayed in touch via Skype and e-mail. Therefore the first big thank goes to my supervisors professor Oubay Hassan and professor Kenneth Morgan. Not to forget my co-supervisor Dr Salim Belouettar, head of Modelling and Simulation unit (at the research center Henri Tudor). I will especially keep in mind the time we spent together at conferences. I also would like to thank all the PhD students from the College of Engineering in Swansea who took care of me and integrated me into their group during my stay. Especially I would like to thank Luke Rees and Sean Walton for this. Nevertheless, most of the time I stayed in Luxembourg at the Luxembourg Institute of Science and Technology (LIST). Actually when I started in 2012, I got employed in the research center Henri Tudor which in 2015 merged with the research center Gabriel Lippman to form LIST. Until 2015, I was part of the Modelling and Simulation Unit (MODSI) and I really had a great time when we participated in summer schools, conferences or even during lunch. It was a pleasure for me to work in this group and I would like to thank all the PhD students, interns and senior researchers with whom I spent these years and especially Sandra Porn and Qian Shao with whom I had the pleasure to share the office. After the merging in 2015 we moved in another building and the MODSI group got split up. From that moment on I was part of the Material Research and Technology (MRT) department and member of the transparent electronics and optical tuneable nanocomposites group. I now shared an office with ten other PhDs. An unique feature of Luxembourg is probably the melting pot of different cultures you can find in a very restricted area. In my office, from ten persons, we had people from Belgium, Russia, Venezuela, Portugal, France, India, Italy and Luxembourg. The atmosphere was great under the PhDs and in this case I cannot thank one single person because everybody contributed to this. Therefore a big thanks to all of them. I would also like to acknowledge the patience and motivation of André Stemper from the university of Luxembourg who was essential to the succes of the experimental part of my thesis. With him I had many discussions about the components of the free wave setup and he furthermore designed the whole support for the antennas. Although both of us never worked with a free space setup, his knowledge in electrical engineering definitely

Contents

was a key component to the success of the experiment. Due to the collaboration between LIST and Swansea university I had several supervisors. One of them needs an extra heartfelt, my main supervisor Mohamed El Hachemi. I still remember when I had my interview with him in November 2012 and when accepted me a few weeks later for this project. It was also challenging for me because I was not familiar with the numerical method we were going to use, my programming skills where rather basic and I only had one semester course in electromagnetics. But Mohamed supported me with everything I needed to learn the required basics. He seems to have an unlimited patience when I asked stupid questions and his door was always open for me, although I entered several times, asking if he has two minutes for me, often ending in a several hour long discussion. I think he finally starts getting a bit suspicious when I ask if he as a few minutes to help me. During this project he also gave me a lot of autonomy and allowed me to follow my instinct when it came down to solve a problem. Nevertheless he always had an eye on my work and brought me back on the right track when I started getting lost. To summarise, except some delays due to equipment that has not arrived on time this was at least in my opinion a very interesting and satisfying thesis, with respect to the supervisors, topic and results. I would also like to thank my two examiners David Rowse and Dr Ruben Sevilla for the challenging viva I had. I am very grateful for their fair comments and helpful advices. To finish, I would also like to thank all the other people I forgot to mention who contributed to the success of this project with their support, time or whatever.

List of Figures

1.1.	(a) <i>Amplid builds lightest Snowboard in the world using composite materials.</i> ; (b) <i>Airbus A350XWB.</i>	2
1.2.	(a) <i>Split ring resonator unit cell.</i> ; (b) <i>Metamaterial consisting of a periodic array of wires and split ring resonators.</i> [117]	2
2.1.	(a) <i>Ampere's law</i> ; (b) <i>Faraday's law</i>	13
2.2.	; (c) <i>Gauss' law for a positive charge density</i> ; (b) <i>Gauss' law for magnetic field</i>	14
2.3.	<i>Boundary condition for electric field vector with $\epsilon_1 < \epsilon_2$</i>	15
2.4.	<i>TE and TM mode of an electric field.</i>	16
2.5.	<i>Lorentz permittivity</i>	18
2.6.	<i>Debye permittivity</i>	19
2.7.	<i>Drude permittivity</i>	20
2.8.	(a) <i>Left Hand Material (LHM)</i> ; (b) <i>Right Hand Material (RHM)</i>	23
2.9.	<i>Phase- and group velocity of a plane wave and a wave packet in a LHM and RHM</i> (a) <i>plane wave</i> ; (b) <i>wave packet</i>	23
2.10.	(a) <i>p-polarised wave</i> ; (b) <i>s-polarised wave</i>	24
2.11.	<i>Snell's law</i>	25
2.12.	<i>Reflection and ransmission properties for different material parameters</i>	27
2.13.	<i>Drude permittivity, with $Re(\epsilon) = \epsilon'$ and $Im(\epsilon) = \epsilon''$</i>	28
2.14.	(a) <i>cut wire grid resonator</i> ; (b) <i>comparison between "wire" and "cut wire" transmission and permittivity</i>	29
2.15.	<i>magnetic moment generated by incident wave.</i>	30
2.16.	<i>Rectangular SRR, circular SRR, nested SRR (Double split ring resonators (DSRR)), SRR back-to-back configuration.</i> [99]	30
2.17.	(a) <i>Metamaterial developed by Smith et al.</i> [119] ; (b) <i>Metamaterial suited for smaller wavelengths build using print circuit board technology</i>	31
2.18.	(a) <i>hand and chiral molecules</i> ; (b) <i>left- (on the left) and right-handed (on the right) helices</i>	32
2.19.	<i>Effect of Pasteur parameter</i> (a) <i>Optical rotatory dispersion (ORD).</i> ; (b) <i>Circular dichroism (CD)</i>	33
2.20.	<i>Standard unit cell of Ω-Medium.</i> [10]	34
3.1.	(a) <i>3D Yee cell for a rectangular grid.</i> . ; (b) <i>slices of the Yee cell at positions i and $i - \frac{1}{2}$.</i> [118]	44
3.2.	(a) <i>Delaunay Edge and Voronoi face.</i> ; (b) <i>Voronoi Edge and Delaunay face.</i>	49

List of Figures

3.3.	(a) Delaunay and Voronoi mesh in 2D. ; (b) Cut through hybrid mesh used to model sphere object. The displayed mesh consists of tetrahedra inside the sphere (white) and it's vicinity with few layers (blue). One layer of pyramids (yellow) links the tetrahedra to the hexahedra (red).	50
3.4.	An illustration, in 2D, of the merging process for cells sharing the same circumcentre.	51
3.5.	shifting the circumcenter from the outside to the inside of a triangle . . .	52
3.6.	Simulation of scattering by a 3D dielectric sphere in free space.	54
3.7.	Averaging of material properties at interfaces for : (a) Delaunay edges in free space in blue, within the dielectric in green, at interface in red. ; (b) Voronoi edges crossing triangles at the interface in black.	55
3.8.	Averaging of material properties at interfaces for (a) Delaunay edge (magenta) surrounded by four Voronoi edges (dark red). ; (b) two sub-volumes (blue, yellow) of equal volume inside a given cell.	56
3.9.	Results of a comparison of the use of different averaging methods across dielectric interface : (a) RCS calculations. ; (b) Relative L^2 Errors of each method.	57
3.10.	Interpolation of the field vector at node n_1 : (a) Tetrahedra in the Delaunay mesh containing the point n_1 . ; (b) edges in the 3 Delaunay mesh containing the point n_1	61
3.11.	Generating the orthonormal local coordinate system. (a) Consider Delaunay edge \mathbf{e}_1 from a given tetrahedron ; (b) Create two linear independent vectors \mathbf{e}'_2 and \mathbf{e}'_3 ; (c) Orthogonalisation of the vectors \mathbf{e}'_2 and \mathbf{e}'_3 with respect to \mathbf{e}_1 using the Gram Schmidt orthogonalisation procedure. . . .	63
3.12.	Associating electric field to Voronoi edges: (a) Reconstruct the electric field vector from its projections on the Delaunay edges and link this vector to the corresponding cell center. ; (b) average electric field vectors from cell centers linked to the same Voronoi edge \mathbf{v} and project them to the corresponding edge.	71
3.13.	Representation of a voronoi Edge and the corresponding cells.	72
3.14.	Comparison of permeability model suggested by Nayyeri and the Lorentz model (a) $\xi_\mu = 0.1$; (b) $\xi_\mu = 0.5$	79
3.15.	Replacing the constant term μ_s by μ_∞ by maintaining a high damping of $\xi_\mu = 0.5$	79
4.1.	Structured sphere's surface meshes (a) $\lambda/15$ spacing ; (b) $\lambda/60$ spacing . .	87
4.2.	Scattering of a plane wave by a PEC sphere of electrical length 2λ comparing the co-volume and standard FDTD method: (a) co-polarised RCS distribution; (b) cross-polarised RCS distribution	87
4.3.	Scattering of a plane wave by a dielectric sphere of electrical length 2λ comparing the co-volume and standard FDTD method, for the case $\varepsilon = 2$, $\mu = 1$, $\sigma = \sigma_m = 0$: (a) co-polarised RCS distribution; (b) cross-polarised RCS distribution	88

4.4.	<i>Order of convergence of the scheme using the L^2 error for varying number of cells per wavelength (a) co polarised (b) cross polarised</i>	89
4.5.	<i>(a) View of a cut through the discretised dielectric sphere. (b) Detail of a cut through the mesh showing the different cell types.</i>	90
4.6.	<i>Scattering of a plane wave by a dielectric sphere of electrical length 2λ with $\epsilon_r = 2$, $\mu_r = 1$ and $\sigma = \sigma_m = 0 S/m$; (a) co-polarised RCS distribution; (b) cross-polarised RCS distribution</i>	91
4.7.	<i>Scattering of a plane wave by a dielectric lossy sphere of electrical length 2λ with $\epsilon_r = 2$, $\mu_r = 1$ and $\sigma = 0.7 S/m$, $\sigma_m = 0 S/m$: (a) co-polarised RCS distribution; (b) cross-polarised RCS distribution</i>	92
4.8.	<i>Scattering of a plane wave by a PEC sphere of electrical length 2λ with $\epsilon_r = 1, \mu_r = 1, \sigma = \sigma_m = 10^6 S/m$; (a) co-polarised RCS distribution; (b) cross-polarised RCS distribution.</i>	92
4.9.	<i>Scattering of a plane wave by sphere covered with a resistive sheet of conductivity $\sigma = \sigma_m = 10^6 S/m$: (a) co-polarised RCS distribution; (b) cross-polarised RCS distribution</i>	93
4.10.	<i>Cut through a coated sphere (a) View of the mesh used to represent a coated dielectric sphere, with the blue cells representing the coating and the red cells the dielectric.; (b) Graphical representation of the scattered field for the coated dielectric sphere</i>	94
4.11.	<i>Scattering of a plane wave by a coated PEC sphere of electrical length 2λ: (a) co-polarised RCS distribution; (b) cross-polarised RCS distribution</i>	95
4.12.	<i>Scattering of a plane wave by a PEC sphere coated with a conducting dielectric of total electrical length 2λ: (a) co-polarised RCS distribution; (b) cross-polarised RCS distribution</i>	95
4.13.	<i>Scattering of a plane wave by a coated dielectric sphere of electrical length 2λ: (a) co-polarised RCS distribution; (b) cross-polarised RCS distribution</i>	96
4.14.	<i>(a) View of the coarse mesh used for the radome example, with the yellow cells representing the dielectric and the white and blue cells representing free space.; (b) Graphical representation of the scattered field induced by an EM pulse (c) mesh with 40 degrees of freedom per wavelength</i>	97
4.15.	<i>Transmission of a Narrowband pulse centered at 1.2 GHz, through a dielectric radome with 40 degrees of freedom per wavelength</i>	98
4.16.	<i>Scattering by a dielectric anisotropic sphere: (a) cut through the mesh used to represent the sphere; (b) contours of E_y on a cut through the computational domain.</i>	99
4.17.	<i>Scattering of a plane wave by a dielectric sphere of electrical length 2λ with anisotropic permeability: (a) co-polarised RCS distribution; (b) cross-polarised RCS distribution.</i>	100
4.18.	<i>Scattering of a plane wave by a dielectric sphere of electrical length 2λ with anisotropic permittivity: (a) co-polarised RCS distribution ; (b) cross-polarised RCS distribution.</i>	101

List of Figures

4.19. Scattering of a plane wave by a dielectric sphere of electrical length 2λ with anisotropic permittivity and electrical conductivity: (a) co-polarised RCS distribution; (b) cross-polarised RCS distribution.	102
4.20. Scattering of a plane wave by a dielectric sphere of electrical length 2λ with anisotropic permeability and magnetic conductivity: (a) co-polarised RCS distribution; (b) cross-polarised RCS distribution.	103
4.21. Scattering of a plane wave by a fully anisotropic dielectric sphere of electrical length 2λ : (a) contours of H_z shown on a cross-section through the mesh; (b) contours of E_y shown on a cross section through the mesh.	104
4.22. Radome (yellow) in free space (white, blue)	105
4.23. Composite material: (a) material frame (b) Distance between cell centers and material frame located at surface	106
4.24. Radome of composite material: (a) Construction of orthonormal material frame (b) Distance between cell centers and material frame located at surface	107
4.25. Transmission of 1.2 GHz pulse through a radome made out of a composite dielectric	108
4.26. Chiral slab (yellow) in free space (blue)	109
4.27. Rotation of the plane of polarisation for 6 different chiralities over time. The black line corresponds to the analytical value.	110
4.28. Analytical vs Numerical Transmission coefficients (a) T_{co} ; (b) T_{cr}	112
4.29. Analytical vs Numerical Reflection coefficients R_{co}	113
4.30. Relative Error of the numerically computed rotation of the plane of polarisation with increasing chirality compared to analytical values for two meshes (a) mesh with $\Delta z = 0.003$ (b) mesh with $\Delta z = 0.0025 m$	114
4.31. Effect on mesh refinement and time steps on the results (a) same chirality, different meshes (b) same mesh, different time step	114
4.32. relative error of computed angle over 20 cycles	115
4.33. Real and imaginary part of the chirality for varying damping factors (a) Real part of the chirality ; (b) imaginary part of the chirality	116
4.34. Scattering of a plane wave by a dielectric sphere of electrical length 2λ with anisotropic dispersive permittivity: (a) co-polarised RCS distribution; (b) cross-polarised RCS distribution.	117
4.35. Scattering of a plane wave by a dielectric sphere of electrical length 2λ with anisotropic dispersive permittivity: (a) co-polarised RCS distribution; (b) cross-polarised RCS distribution.	118
4.36. Scattering of a plane wave by a dielectric sphere of electrical length 2λ with anisotropic dispersive permittivity: (a) co-polarised RCS distribution; (b) cross-polarised RCS distribution.	119
4.37. Scattering of a plane wave by a dielectric sphere of electrical length 2λ with anisotropic dispersive permittivity: (a) co-polarised RCS distribution; (b) cross-polarised RCS distribution.	120
4.38. Analytical isotropic chiral vs Numerical bi-anisotropic transmission coefficients (a) T_{co} ; (b) T_{cr}	121

4.39. Analytical isotropic chiral vs Numerical bi-anisotropic reflection coefficients R_{co}	121
5.1. Schematic representation of the multiscale approach	126
5.2. Effective medium from a two phase composite	127
5.3. Unit cell surrounded by free space and PML along the optical axis	129
5.4. Phase of S_{11} and S_{21} corrected by $\Phi_{add} = k_0(c_0/l_{fs})$ for transmitting and receiving ports located at the interface between the dielectric and free space (a) $ S_{11} $; (b) $ S_{21} $	130
5.5. Material parameters of FR4 after phase correction (a) relative permittivity ; (b) relative permeability	131
6.1. Illustration of circular waveguide setup.	136
6.2. (a) Experimental setup ; (b) Different field regions	137
6.3.	139
6.4. 2 port system.	140
6.5. frequency response of a coax device under test.	141
6.6. Time domain response and identification of the different reflection peaks, due to non-continuities, with the corresponding parts of a coaxial line.	142
6.7. Time Domain response of a coax adapter and antenna	142
6.8. Frequency domain response of the effect of a metal plate located at two different positions.	143
6.9. Time domain response of the effect of a metal plate located at two different positions.	144
6.10. Time Gating using a band pass or notch.	145
6.11. Frequency domain representation of band pass filtered signal of a coax adapter and horn antenna.	145
6.12. Comparison between an ungated and a gated signal in the frequency domain.	146
6.13.	147
6.14. TRL calibration.	148
6.15. GRL calibration.	149
6.16. Applying time gates of different widths (blue) on a given response in time domain (a) Large gate. ; (b) Narrow gate.	151
6.17. asymmetric time gating (blue) with respect to the peak.	151
6.18. S-parameters of a planar dielectric sample in free space.	152
6.19. (a) wavevector \mathbf{k} parallel to \mathbf{x} ; (b) wavevector \mathbf{k} anti-parallel to \mathbf{x}	156
6.20. (a) size of single Omega particle. ; (b) Periodicity of array of Omega cells.	158
6.21. Periodic arrangement of omega structures on FR4 substrate	159
7.1. Material parameters for a 2.94 mm PMMA sample from NRW algorithm (a) relative permittivity ; (b) relative permeability	162
7.2. Material parameters for a 10 mm PMMA sample NRW algorithm (a) relative permittivity ; (b) relative permeability	162

List of Figures

7.3.	<i>Comparison of experimental and analytical S_{11} for (a) 2.94 mm thick PMMA sample ; (b) 10 mm thick PMMA sample</i>	163
7.4.	<i>Material parameters for a 3 mm polystyrene sample NRW algorithm (a) complex permittivity ; (b) complex permeability</i>	163
7.5.	ϵ_{\perp} for (a) 2.94mm PMMA slab using low loss formula ; (b) 3mm polystyrene slab	164
7.6.	<i>Electric field oriented parallel to the arms and magnetic field perpendicular to the loop. A strong coupling is expected for this configuration</i>	165
7.7.	S_{11} and S_{22} parameters of the bi-anisotropic material for 0 dBm (a) magnitude ; (b) phase	166
7.8.	S_{12} and S_{21} parameters of the bi-anisotropic material for 0 dBm (a) magnitude ; (b) phase	166
7.9.	S_{11} and S_{22} parameters of the bi-anisotropic material for 3 dBm (a) magnitude ; (b) phase	167
7.10.	S_{12} and S_{21} parameters of the bi-anisotropic material for 3 dBm (a) magnitude ; (b) phase	167
7.11.	(a) relative permittivity ; (b) relative permeability	168
7.12.	chirality	168
7.13.	<i>Magnetic field parallel to the arms and electric field perpendicular to the loop. Only a very weak coupling is expected</i>	170
7.14.	S_{11} and S_{22} parameters of the bi-anisotropic material for 3 dBm (a) magnitude ; (b) phase	170
7.15.	S_{12} and S_{21} parameters of the bi-anisotropic material for 3 dBm (a) magnitude ; (b) phase	171
7.16.	(a) relative permittivity ; (b) relative permeability	171
7.17.	chirality	172
7.18.	<i>Magnetic field parallel to the arms and electric field perpendicular to the loop. Only a very weak coupling is expected</i>	172
7.19.	S_{11} and S_{22} parameters of the bi-anisotropic material for 3 dBm (a) magnitude ; (b) phase	173
7.20.	S_{12} and S_{21} parameters of the bi-anisotropic material for 3 dBm (a) magnitude ; (b) phase	173
7.21.	(a) relative permittivity ; (b) relative permeability	174
7.22.	chirality	174
8.1.	(a) Mesh of omega including the free space region and the PML ; (b) Intensity of the electric field at (9.4 GHz)	177
8.2.	(a) relative permittivity ; (b) relative permeability	178
8.3.	chirality	178
8.4.	(a) relative permittivity ; (b) relative permeability	179
8.5.	chirality	179
8.6.	(a) relative permittivity ; (b) relative permeability	180
8.7.	chirality	180

8.8. (a) <i>Unit cell with omega inclusion ; (b) Intensity of the electric field at the resonance frequency</i>	181
8.9. <i>Orientation of omega</i>	182
8.10. (a) $\epsilon_{r,xx}, \epsilon_{r,yy}, \epsilon_{r,zz}$; (b) $\mu_{r,xx}, \mu_{r,yy}, \mu_{r,zz}$	182
8.11. <i>Experimental vs numerical transmission from direct multiscale approach</i>	184
C.1.	218
C.2. <i>Effect of wrapped vs unwrapped phase on the permittivity retrieval.</i>	219
C.3. <i>Effect of different starting frequencies on the phase</i>	220
C.4. <i>Effect of different starting frequencies on the permittivity</i>	220

List of Tables

2.1. <i>Classification of reciprocal bi-anisotropic media</i>	35
3.1. <i>Analytical Z-Transform. ρ, β are constants</i>	75
4.1. Relative L2-Error with respect to different meshes computed in linear scale of (a) PEC sphere ; (b) Dielectric sphere	89
A.1. Transforming among the time, Frequency and Z Domain, ($\alpha, \beta \in \mathbb{R}$ are constants)	204

Variables

A refers to an arbitrary vector. May be a field vector for example, it is only used to illustrate the notation.

ε : electric permittivity

ε_0 : permittivity of free space

μ : magnetic permeability

μ_0 : permeability of free space

σ_m : magnetic conductivity

σ : electric conductivity

$\bar{\epsilon}$: 3×3 matrix

A: bold letters are vectors

H: magnetic field vector

B: magnetic flux density vector

E: electric field vector

D: displacement field vector or electric flux density vector

J_f: total current density

J_e: electric current

J_m: magnetic current

J: current density from other sources than conductivity

$d\mathbf{A}$: infinitesimal surface element

$d\mathbf{l}$: infinitesimal line element

$d\mathbf{V}$: infinitesimal volume element

∂A : closed curve bonding a surface **A**

A_{tot}: total field vector **A**

A_{scat}: scattered field vector **A**

A_{inc}: incident field vector **A**

Aⁿ: field vector at time step n

$A_i = \langle \mathbf{A}, \mathbf{i} \rangle$: projection (dot product) of vector **A** to vector **i**

t : time

Δt : time step

r: position vector

A_n: normal component of a vector **A**

A_t: tangential component of a vector **A**

A_s: s-polarised vector

A_p: p-polarised vector

k: wavevector

k : wavenumber

k_0 : wavenumber in free space

N_e : number of electric dipoles

P: polarisation vector

l_{av} : average distance between two electric charges

χ_e : electric susceptibility

χ_m : magnetic susceptibility

M: magnetic polarisation vector
m: magnetic moment
i: imaginary unit $i^2 = -1$
I: electric current
 $a' = Re(a)$: real part of complex number *a*
 $a'' = Im(a)$: imaginary part of complex number *a*
 ω : angular frequency
W: energy density
c: speed of light in medium
 c_0 : speed of light in free space
 η : impedance in dielectric
 η_0 : impedance in free space
S: poynting vector
 $\hat{\mathbf{a}}$: unit vector of vector **a**
 λ : wavelength
 ∞ : parameter at high frequency limit
s: parameter at low frequency limit
 $\omega_0, \omega_\varepsilon, \omega_\mu, \omega_\kappa$: different resonance frequencies
 ω_p : plasma frequency
R: resistance
L, L₀: inductance
C, C₀: capacitance
 κ : chirality, pasteur parameter
 χ : tellegen parameter
S: scattering parameters
 Γ : interface reflection coefficient
T: phase shift function
 $z_{in} = \eta/\eta_0$: normalised characteristic impedance
 γ_0 : propagation constant of free space
 γ : propagation constant inside a dielectric
 $\varepsilon_{r\parallel}$: electric permittivity from parallel polarisation
 $\varepsilon_{r\perp}$: electric permittivity from perpendicular polarisation
 θ : angle
 Φ : phase
tanδ: loss tangent
n: refractive index
d: thickness of a sample

Abbreviations

FRP : Fiber Reinforced Polymer
CFRP : Carbon Fiber Reinforced Plastic
CEM : Computational Electromagnetics
RCS : Radar Cross Section
EMC : Electromagnetic Compatibility
PED : Personal Electronic Devices
RTCA : Radio Technical Commission for Aeronautics
RF : Radio Frequency
VOR : Very High-Frequency Omnidirectional Range
ILS : Instrument Landing System
GPS : Global Positioning System
EMI : Electromagnetic Interference
TE : Transverse Electric
TM : Transverse Magnetic
PEC : Perfect Electric Conductor
RHM : Right Handed Material
LHM : Left Handed Material
DNG : Double Negative
DPS : Double Positive
SNG : Single Negative
ENG : Epsilon Negative
MNG : Mu Negative
SRR : Split Ring Resonator
DSRR : Double Split Ring Resonator
PCB : Printed Circuit Board
VNA : Vector Network Analyzer
DUT : Device Under Test
FR4 : Fire Retardant 4
FDTD : Finite Difference Time Domain
FEM : Finite Element Method
FVTD : Finite Volume Time Domain
FD : Frequency Domain
TD : Time Domain
DG : Discontinuous Galerkin
MoM : Method of Moments
PML : Perfectly Matched Layer
ABC : Absorbing Boundary Conditions
PBC : Periodic Boundary Conditions

1. Introduction

1.1. Motivation

During the last decades so called composites started to play a significant role in our everyday life, by replacing metals and metallic alloys in items we use on a daily basis. As the name says a composite is a combination of different materials. The idea is to combine two or more materials, the combination of which are stronger than the individual materials by themselves. This allows, for example, the construction of composites that are far stronger than steel or aluminum and at the same time being lighter and more flexible than their “normal” counterparts. Typically the name composite refers to Fiber Reinforced Polymer (FRP) composites. In the past they were named reinforced plastics. The development of composites started with the discovery and development of plastics (vinyl, polystyrene) at the beginning of the twentieth century. Later, the defense industry significantly pushed the research in composites until in the 1940s the first FRP was developed. These were a class called glass fiber reinforced composites uniting high mechanical strength and light-weight in comparison to metals. Also in the following decades military were pushing the development of composites particularly for aerospace and naval applications due to their inherent resistance to weather and corrosive defects. Simultaneously, the emergence of new polymers helped to further refine and adapt the properties of composites [3]. Nowadays composites are part of our everyday life. They are used in snowboards (Figure 1.1a), golf clubs, cars and increasingly in civil aircraft. According to Airbus, 50 percent of the A350 XWB (Figure 1.1b) is constructed of composites (mostly Carbon Fiber Reinforced Plastic (CFRP)). Although it is harder to manufacture an aircraft mainly based upon composites, it offers several advantages. First of all, they are lighter and more resilient than metals, reducing the fuel consumption. Furthermore the service intervals can be increased from 6 to 12 years, less fatigue related inspections are required and the number of corrosion-related maintenance checks are decreased, reducing significantly maintenance costs for the customers [2]. Besides composites, a new class, so called metamaterials has recently attracted the interest of researchers due to the numerous possible applications such as antenna radomes [130, 131], waveguides [145, 22, 23], polarisation transformers [105], cloaking materials [58, 6, 114] and many more. Metamaterials can be generally defined as a class of artificial media, possessing extraordinary properties that cannot be found in nature [61]. In this work I restrict my attention to the electromagnetic properties of these materials therefore I use the more specific definition: “A metamaterial is an artificial material in which the electromagnetic properties, as represented by the permittivity and permeability, can be controlled. It is made up of periodic arrays of unit cells, metallic resonant elements. Both the size of the element and the unit cell are small relative to the wavelength”. Such

1. Introduction



Figure 1.1.: (a) *Amplid builds lightest Snowboard in the world using composite materials.* ; (b) *Airbus A350XWB.*

electromagnetic metamaterials have first been theoretically predicted by H.Lamb [63] in 1904 and later by the Russian physicist Georgievich Veselago in 1968 when he was thinking about the effects on the reflection and refraction of electromagnetic waves in materials with simultaneously negative permittivity and permeability [135]. In 1999 Sir John Pendry [101] suggests a method of creating a lens based upon a metamaterial with a theoretically perfect focus. In 2000 David R.Smith was able to build the first metamaterial with a negative permittivity and permeability, leading to a negative index of refraction, in the microwave range [119]. In Figure 1.2 such a metamaterial used by R.A. Shelby [117] with a simultaneous negative permittivity and permeability is represented. The simulation of electromagnetic phenomena in such complex (anisotropic, frequency

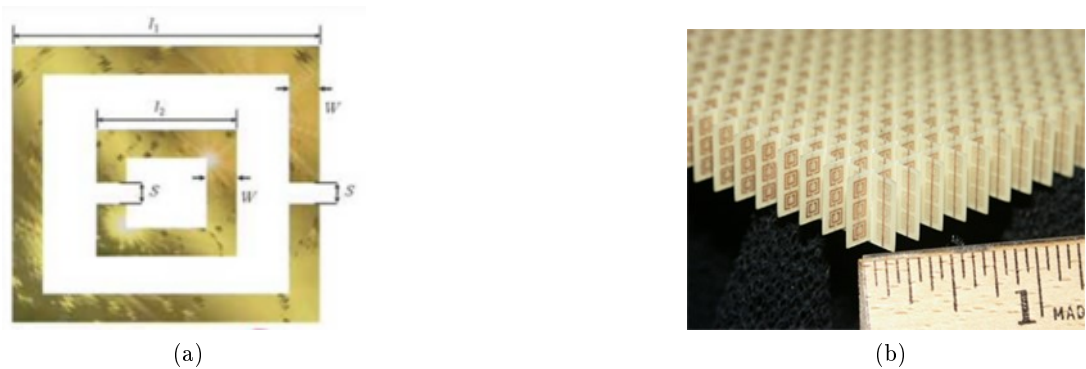


Figure 1.2.: (a) *Split ring resonator unit cell.* ; (b) *Metamaterial consisting of a periodic array of wires and split ring resonators.* [117]

dependent) materials becomes increasingly important due to rising manufacturing costs. Imagine a plane manufacturer that would always have to build an entire plane to test for the effect of lightning strike until they found the best suited material and shape. To prevent such time consuming and expensive tests during the development of a prototype, numerical simulations replace the experiments during the development process. The development of faster and cheaper computers lead to an extensive use of simulation

methods in Computational ElectroMagnetics (CEM) to replace usually unfeasible or very costly real world measurements. For example a wafer fabrication of different electrical components may take 6 months and cost a couple of millions of dollars. Or the development of a stealth aircraft like the Lockheed F117 Nighthawk or the B2 Spirit. In 1998 an F117 cost 80 Million US Dollars. This plane was designed to allow the supercomputers at that time to calculate the Radar Cross Section (RCS) (parameter characterising the scattering properties of an object) in a reasonable amount of time. So, again the military pushed the development of numerical methods since the 80's during the cold war to improve the design of radar systems, aircraft and ships. After the end of the cold war the rapidly developing market in mobile telephony and personal communication systems, and the proliferation of electronic systems in motor vehicles, continued to drive the technology forward [35]. The complexity of electronic system is increasing rapidly and so is their sensitivity to electromagnetic disturbances. Often it is crucial to prevent these disturbances of different electromagnetic components. These problems are classified as ElectroMagnetic Compatibility (EMC), which is the ability of an electronic system to (1) function properly in its intended electromagnetic environment and (2) not be a source of pollution to that electromagnetic environment [136]. A simple example of ElectroMagnetic Interference (EMI) is the characteristic noise we hear when a mobile phone is close to a radio when a call or SMS is incoming. Another example concerns businessman or other frequent flyer. Probably a lot of people are wondering why it is forbidden to use the cell phone or Laptop during take off and landing of an airplane. The reason is again EMC issues. Personal Electronic Devices (PEDs) like smart phones, laptops... may interfere with the electronics of an airplane. Studies from the Radio Technical Commission for Aeronautics (RTCA) which have been conducted in the 1960's, 80's and 90's found that while the risk of interference with on board electronic equipment due to PEDs is extremely low, it is highest during take-off and landing. Finally it depends upon the sensitivity of the on board electronic to a given frequency. The navigational receivers located in or close to the cockpit are most likely to be disturbed by radio frequency (RF), emitted by PEDs. Airplanes nowadays are equipped with at least two Very high-frequency Omnidirectional Range (VORs) receivers, two Instrument Landing Systems (ILS), two Global Positioning (GPS) receivers. PEDs may interfere with any of those receivers but the area of concern is their effect on the GPS system. In a NASA report from 2004 GPS receivers lost satellite lock in several general aviation aircraft during their approach to landing due to interferences with a cell phone [31]. Other NASA reports stating that pilots suspect problems during flight due to PEDs. But until now not a single plane crash has been proven to be caused by a PED on board a plane. Whereas the risk of a plane crash induced by a smartphone is quite small, the effect of a lightning strike however is much more dangerous. Statistically every plane is struck once a year by a lightning strike, inducing very high surface currents which may damage the electronic systems in an aircraft. Simulations of these effects of EMI and protecting the system against it (EMC) is a crucial part, underlying very high requirements, in the development of an electronic device [43]. With the development of aircraft mainly based upon composites, EMC is even more crucial than before because composites generally have a lower conductivity than metal increasing the damages of a lightning. Therefore

1. Introduction

these composites have to be coated with a high conductive paint or metallic wires have to be added to the composite to increase the conductivity. From the simulation point of view composites and metamaterials cannot be modelled in the same way as simple dielectric materials like glass for example because of the microstructure (Figure 1.2). The orientation of the fiber makes the composite anisotropic, meaning the index of refraction depends on the orientation of the fibers. The same is true for the metamaterial where the index of refraction depends upon the orientation of the unit cells. At microscale the material looks completely different than at macroscale, but it is the microstructure that gives the material its special properties. During the simulation of a macroscale object, like an aircraft, the microstructure of the composite has to be taken into account. For example carbon-fiber-reinforced carbon, a composite commonly used in aerospace engineering due to its high mechanical strength and temperature resistance, is made by very thin carbon fibers with a diameter between $5 - 10 \mu m$ embedded in a carbon matrix. The airbus A350 XWB however has a length of $67 m$ and a wingspan of $64 m$. This makes a difference of about 7 orders of magnitude between the micro and macroscale. These materials can be considered as a 3 dimensional array of unit cells. In the most general case, the material parameters of a composite, namely the permittivity and permeability, are frequency dependent second order tensors due to the anisotropy of the material. In the case of a metamaterial an additional material parameter tensor may be required to take the coupling of the electric and magnetic field into account induced by the unit cells. Direct simulation of every single unit cell is impossible. To overcome the problem a multiscale approach can be used. The idea of multiscaling is to consider the problem at two different length scales. First I retrieve the properties of a unit cell (microscale) using a homogenisation procedure. These parameters are then used to simulate an effective medium at macroscale with the same electromagnetic properties as an array of unit cells. Semi analytical homogenisation techniques, referred to as “Effective medium approximations” or “mean field theories” based upon very simple mixing formulas as suggested by Maxwell Garnett [50], Bruggemann [21], Luebbers [85] and Bergman [17] only depending upon a single parameter, the volume fraction V_f may give satisfying results for composites but completely fail for metamaterials. These methods cannot be applied to metamaterials because the shape of the unit cell may lead to resonance phenomena which usually do not appear in composites.

1.2. Aims and Objectives

The aim of this work is the simulation of electromagnetic effects on composite and metamaterials. These materials can be considered as a 3 dimensional array of unit cells. The standard homogenisation methods working reasonably well for composites cannot be applied to metamaterials because the shape of the unit cell may lead to resonance phenomena which usually do not appear in composites. Therefore I suggest a numerical multiscale procedure which I adapted from a mechanical engineering method as suggested by El Hachemi et al. [60]. This new method allows me to retrieve all the material parameters from a single unit cell, even for metamaterials. Tretyakov [128] suggested some

models, mostly variations of the Lorentz model, to describe the effective material parameters of metamaterials. I use these models to fit the data I obtained from the simulation of a unit cell. The final step consists in the transition from a unit cell to the complete material using the fitted data. Therefore I use a Finite Difference Time Domain (FDTD) approach. In contrast to the standard method as suggested by Yee [146], relying on a structured mesh, I further improved a FDTD method based on an unstructured mesh [144]. This modified version is referred to as “UM-FDTD” throughout the thesis where “UM” stands for unstructured mesh. This method was initially limited to perfect electric conductors (PECs). The different objectives of the thesis to model metamaterials are listed below.

- Modification of UM-FDTD to model isotropic dielectric conductive (lossy) materials [48].
- Further generalisation to anisotropic lossy materials, allowing the simulation of composites [49].
- Extension of UM-FDTD to dispersive materials using the Z-transform method [103, 123].
- Development of a numerical simulation technique to model bi-isotropic or in a specific case isotropic chiral materials characterised by a coupling between the electric and magnetic fields.
- Development of a numerical simulation technique to model bi-anisotropic materials. In this case, additionally to the coupling of the electric and magnetic field the metamaterial is anisotropic.
- Development of a numerical multiscale procedure to retrieve the material parameters from a single unit cell.
- Design of a free space setup [108, 94] that allows me to measure the reflection and transmission of a material.
- Computation of electromagnetic material parameters [96, 77, 28] from measurements and comparison with numerical results.

1.3. Outline

This thesis is divided in two parts. The first part deals with the theory, the different algorithms I developed and their numerical validation. The second part is dedicated to the experimental setup and the multiscale approach.

Part 1 Numerical Modelling of Maxwell Equations

Chapter 2, Maxwell and Constitutive Material Equations

This chapter introduces Maxwells equations and the corresponding boundary conditions. My aim is the simulation of electromagnetic in dielectric materials. A typical dielectric is characterised by the electric permittivity, magnetic permeability and electric and magnetic conductivities. These quantities are introduced and their physical origins are explained. Depending on the simulation the dielectric material parameters can be simple scalars, matrices or even complex functions in the case of frequency dependent materials. Finally I introduce metamaterials, artificial materials with properties which do not exist in nature and explain their extraordinary physical properties. To finish, I describe how such materials can be constructed and discuss possible applications.

Chapter 3, Numerical Solution of Maxwells Equations

Chapter 3 is devoted to the numerical simulation of Maxwells equations and is mainly based upon the published results [48, 49]. First I introduce the scattered field formulation which I employ throughout this chapter to solve Maxwells equations. Next I do a small recall of the standard Yee algorithm on structured meshes. Before I derive the Yee algorithm for unstructured meshes (UM-FDTD), I give a brief introduction to the mesh generation and necessary requirements for a high-quality mesh [144]. UM-FDTD is generalised to isotropic, anisotropic and frequency dependent materials. To model isotropic metamaterials, the chirality, describing the coupling between the electric and magnetic fields needs to be taken into account. For this case, I adapted the method suggested by [103] to the unstructured mesh. I finish this chapter with a method that allows me to model bi-anisotropic materials using unstructured meshes. In this case the three material parameters, namely the permittivity, permeability and chirality are frequency dependent second order tensors. This last part combines everything I derived so far and follows the ideas of Nayyeri [95].

Chapter 4 Code Validation and Numerical Examples

The results and benchmark tests validating my algorithms from chapter 4 are presented. For the different cases I numerically compute the RCS of a sphere or the transmission through a dielectric slab. Analytical solutions are available for this problems and allow me to compare the accuracy of my numerical solutions with the analytical ones. Furthermore I compare the efficiency of the co-volume method with the standard Yee algorithm.

Part 2, Multiscale Approach for Metamaterial Modelling

Chapter 5, Micro to Macro Approach

A metamaterial may consist of hundreds of unit cells which makes it nearly impossible to model the material by considering every single cell. Therefore I suggest a multiscale

technique to predict the behaviour of the whole material by restricting the simulation to a single unit cell.

Chapter 6, Experimental Characterisation of Material Properties

To compare my numerical results with experimental data I built a free space measurement setup which allows us to retrieve the dielectric material parameters from experimental measurements. The advantages and disadvantages of different experimental setups and the retrieval algorithms for isotropic and bi-anisotropic materials are explained. By comparing my experimental results for different test materials with data found in literature I validate my setup.

Chapter 7, Experimentally Measured Material Parameters

To compare the predictive capabilities of my multiscale approach I build a metamaterial based upon the same unit cell as I used for the numerical simulation. From a transmission/reflection measurement I am able to compute the material parameters which are later compared with the results from the multiscale approach.

Chapter 8, Results of the Multiscale Approach

In this chapter the results of the two multiscale approaches are presented. I demonstrate that the commonly used “indirect” multiscale approach based on the numerical computation of the scattering parameters reaches its limits for the simulations of metamaterials. I also present an alternative, “direct” multiscale approach, that I developed, which does not rely on the scattering parameters but which is based on a field averaging technique. This method leads to results that are more coherent with experimental measurements.

Chapter 9, Conclusion and Future Work

All the results of the preceding chapters are summarised and some possible perspectives and further applications are outlined. I discuss the advantages and drawbacks of UM-FDTD with respect to the standard Yee algorithm by analysing the isotropic, anisotropic and chiral cases. Furthermore I comment my multiscale technique and the corresponding results. I finish with a discussion about the free wave setup I used and how to further improve the measurements in the future.

Part I.

Numerical Modelling of Maxwell Equations

2. Maxwell and Constitutive Material Equations

In this chapter I introduce the basic concepts needed for the theoretical description of dielectric, lossy, frequency dependent and anisotropic materials. I start with the definition and illustration of the four Maxwell equations which are later numerically solved. As soon as interfaces of different media like dielectrics or metals are considered, we have to be aware of the boundary conditions and assure that they are also fulfilled in our numerical scheme. A revision of the boundary conditions and its effects on the electric and magnetic fields is given. Next I introduce the definition of TE “transverse electric” and TM “transverse magnetic” modes because this definition is commonly used in literature. The first solver, generalising the Yee algorithm to unstructured meshes [144] was limited to perfect electric conducting materials in free space. I extended it to dielectric materials [48]. Therefore in my opinion a small repetition of the physical origin of the materials parameters like electric permittivity ε , the magnetic permeability μ and the conductivity σ is helpful for a good understanding of the different concepts. Many isotropic materials may be described in a good approximation by frequency independent (non-dispersive) material parameters. For other materials, especially metamaterials, the frequency dependence of the material parameters has to be taken into account. I make a brief summary of the different models, namely, the Drude, Lorentz or Debye model before I introduce the concept of metamaterials and investigate the uncommon physical properties they have. First I demonstrate how metamaterials influence the phase and group velocity before I examine the effect of a negative index of refraction on the electric and magnetic field vectors at an interface. These effects which cannot be observed in materials found in nature are due to the microstructure, an arrangement of unit cells. These cells typically are a combination of two different structures. One structure influences the electric permittivity and the other one the magnetic permeability. I explain how a wire grid allows me to tune the electric permittivity depending on the frequency and how magnetic resonators allow the control over the magnetic permeability. Adding both structures together and arranging all the resulting unit cells periodically leads to a metamaterial. Different kind of metamaterials need to be distinguished. A very common one is based upon a magnetic resonator and wire combined in a single unit cell which may lead to a negative index of refraction. Chiral metamaterials on the other hand are based on chiral unit cells and show other interesting phenomena. As an example, left or right handed (chiral) steel springs dispersed homogeneously in a matrix may lead to a coupling of the electric and magnetic field in the constitutive equations changing the polarisation of the incident field. This and other effects will be discussed in the corresponding subchapter. Finally I finish this chapter with so called pseudo-chiral materials. Pseudo-chiral

2. Maxwell and Constitutive Material Equations

means that the unit cell by itself is not chiral, nevertheless due to its special shape and spatial orientation, it leads to the same electromagnetic phenomena than materials with chiral unit cells.

2.1. Maxwell equations

The Maxwell equations, a set of four coupled equations describe the interactions of electric and magnetic fields with matter[118, 57]. They form the foundation of classical optics, electrodynamics and circuit theory.

Maxwell Equations in Differential form

$$\nabla \times \mathbf{H} = \mathbf{J}_f + \frac{\partial \mathbf{D}}{\partial t} \quad (2.1)$$

$$\nabla \times \mathbf{E} = -\frac{\partial \mathbf{B}}{\partial t} - \mathbf{J}_m \quad (2.2)$$

$$\nabla \cdot \mathbf{B} = 0 \quad (2.3)$$

$$\nabla \cdot \mathbf{D} = \rho \quad (2.4)$$

Maxwell Equations in Integral Form

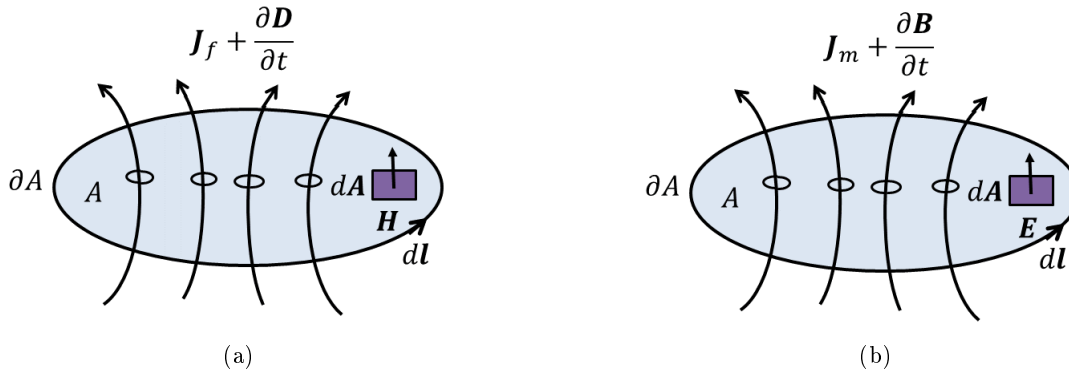
$$\int_{\partial A} \mathbf{H} \cdot d\mathbf{l} = \int_A \left(\mathbf{J}_f + \frac{\partial \mathbf{D}}{\partial t} \right) \cdot d\mathbf{A} \quad (2.5)$$

$$\int_{\partial A} \mathbf{E} \cdot d\mathbf{l} = -\int_A \left(\mathbf{J}_m + \frac{\partial \mathbf{B}}{\partial t} \right) \cdot d\mathbf{A} \quad (2.6)$$

$$\int_{\partial V} \mathbf{D} \cdot d\mathbf{A} = \int_V \rho dV = Q \quad (2.7)$$

$$\int_{\partial V} \mathbf{B} \cdot d\mathbf{A} = 0 \quad (2.8)$$

Where \mathbf{E} is the electric and \mathbf{H} the magnetic field respectively and \mathbf{B} and \mathbf{D} represent the magnetic and electric flux densities. $\mathbf{J}_f(\mathbf{r}, t) = \mathbf{J}_e + \mathbf{J}$ is the total current density where \mathbf{J}_e is the electric current density and \mathbf{J} the current density arising from sources other than conductivity. $\mathbf{J}_m = \sigma_m \mathbf{H}$ with σ_m the magnetic conductivity, no real physical quantity but usually used for artificial absorption at simulation space boundaries. ρ corresponds to the charge density and Q to the total charge. In the integral formulation $d\mathbf{l}$ is an infinitesimal line segment, $d\mathbf{A}$ is an infinitesimal surface element, dV refers to a volume element, ∂A is the contour enclosing the surface A and ∂V is the surface enclosing the volume V . The different fields and currents are position and time dependent vectors. For simplicity we omit writing explicitly the time and spatial dependence e.g $\mathbf{E} = \mathbf{E}(\mathbf{r}, t)$. If we allow materials with isotropic, non-dispersive (ε and μ are independent of the frequency of the incoming wave) electric losses attenuating \mathbf{E} fields via conversion to heat energy, the electric current density becomes $\mathbf{J}_e = \sigma \mathbf{E}$, where σ is the conductivity.

Figure 2.1.: (a) *Ampere's law* ; (b) *Faraday's law*

For the simplest case, a linear, isotropic and non-dispersive material we have the following constitutive relations

$$\mathbf{D} = \varepsilon \mathbf{E} \quad (2.9)$$

$$\mathbf{B} = \mu \mathbf{H} \quad (2.10)$$

Relating the flux densities to the fields, with μ the magnetic permeability and ε the electric permittivity where $\varepsilon = \varepsilon_r \varepsilon_0$ and $\mu = \mu_r \mu_0$. $\varepsilon_0 = 8.854187817 \cdot 10^{-12} \text{ As/Vm}$ is the electric permittivity of free space and $\mu_0 = 4\pi \cdot 10^{-7} \text{ N/A}^2$ the magnetic permeability of free space. ε_r and μ_r are the relative electric permittivity and relative magnetic permeability. They characterise a dielectric material and are explained in all detail in section 2.4.

2.1.1. Interpretation of Maxwell equations

Ampere's and Faraday's laws

To graphically illustrate Maxwell's equations we restrict ourselves to the integral formulation. Equation (2.5) is referred to as Ampere's law and states that a time varying electric flux density $\partial \mathbf{D} / \partial t$ and an electric current density \mathbf{J}_f create an eddy magnetic field as illustrated in Figure 2.1a. Equation (2.6) represents Faraday's law and states that a time varying magnetic flux density $\partial \mathbf{B} / \partial t$ creates an eddy magnetic field as illustrated in Figure 2.1b.

Gauss' law for magnets and electric charges

Equation (2.7) is the Gauss' law for the electric field. It mathematically expresses the experimental fact that electric charges attract or repel each other. A surface ∂V encloses the Volume V which contains a volume charge quantity ρ . If equation (2.7) is positive the electric field lines point away from the charges (positive charges), this corresponds

2. Maxwell and Constitutive Material Equations

to a source. If on the other hand equation (2.7) is negative the electric field lines point towards the charges (negative charges), this corresponds to a sink. In the differential

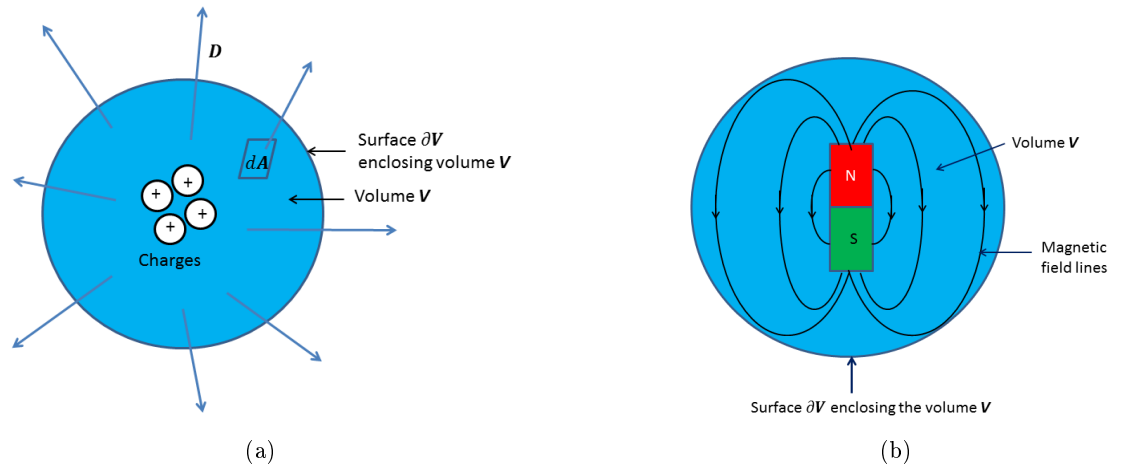


Figure 2.2.: (a) Gauss' law for a positive charge density ; (b) Gauss' law for magnetic field

formulation a source corresponds to a positive divergence of the field vector and a sink to a negative divergence of the field vector. Similarly equation (2.8) is called Gauss' law for the magnetic field. In contrast to the Gauss' law for electric fields it states that no magnetic charges (monopoles) exist. Therefore the field lines always close on in contrast to the electric Gauss' law. Figures 2.2a and 2.2b illustrate the difference between the electric and magnetic case.

2.2. Electromagnetic boundary conditions at material interfaces

Boundary conditions describe the behaviour of the field at interfaces. Typical interface that occur may be air-metal or dielectric-metal or other combinations. A metal, also referred to as perfect electric conductor (PEC) has a very high conductivity σ of several million S/m , therefore for metals commonly $\sigma = \infty$ is used. This is typically not the case for dielectrics which called finite conductivity media with $\sigma \neq \infty$. The boundary conditions for two finite conductivity media $\sigma_1, \sigma_2 \neq \infty$ defined by $\epsilon_1, \epsilon_2, \mu_1, \mu_2$ are

$$\hat{\mathbf{n}} \times (\mathbf{E}_2 - \mathbf{E}_1) = \mathbf{0} \quad (2.11)$$

$$\hat{\mathbf{n}} \times (\mathbf{H}_2 - \mathbf{H}_1) = \mathbf{0} \quad (2.12)$$

$$\hat{\mathbf{n}} \cdot (\mathbf{D}_2 - \mathbf{D}_1) = 0 \quad (2.13)$$

$$\hat{\mathbf{n}} \cdot (\mathbf{B}_2 - \mathbf{B}_1) = 0 \quad (2.14)$$

They may also be displayed in a slightly different form

$$E_{2t} = E_{1t} \quad (2.15)$$

$$H_{2t} = H_{1t} \quad (2.16)$$

$$E_{2n}\epsilon_2 = E_{1n}\epsilon_1 \quad (2.17)$$

$$H_{2n}\mu_2 = H_{1n}\mu_1 \quad (2.18)$$

where “*t*” refers to “tangential” and “*n*” to “normal”. For further information please refer to [12]. The boundary conditions for the electric field are graphically represented in Figure 2.3

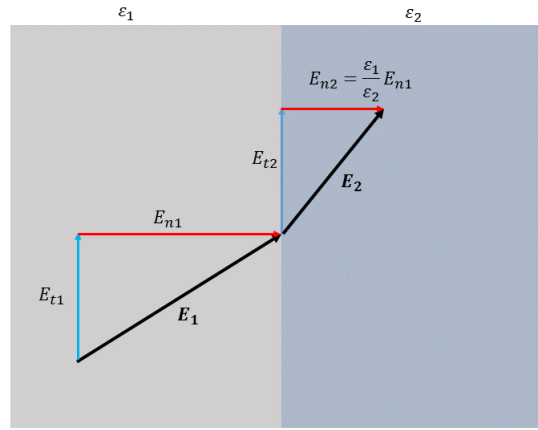


Figure 2.3.: Boundary condition for electric field vector with $\epsilon_1 < \epsilon_2$

2.3. TE and TM modes

Because the boundary conditions differ for the normal and tangential components it is often useful to split the incoming wave in two parts by defining a plane spanned by the incident and reflected wavevector \mathbf{k}_i and \mathbf{k}_r . The incoming electric field vector is now separated in a part perpendicular to the plane of incidence, the s-polarised wave (TE mode) and another part parallel to the plane of incidence, the p-polarised Wave (TM mode). S-polarised comes from the German word “senkrecht” which means “perpendicular” and p-polarised from the German word “parallel”. $\mathbf{E} = \mathbf{E}_p + \mathbf{E}_s$ is graphically represented in Figure 2.4. For the TE mode only the electrical field component is perpendicular to the direction of propagation, whereas the magnetic field component is parallel with respect to the wavevector. Similarly for the TM mode, the magnetic field components are perpendicular with respect to the direction of propagation. Only the electric field components is parallel to the wavevector. Or in a less scientific way: TE means, the electric field does not exist in the direction of propagation and TM means, magnetic field does not exist along the direction of propagation.

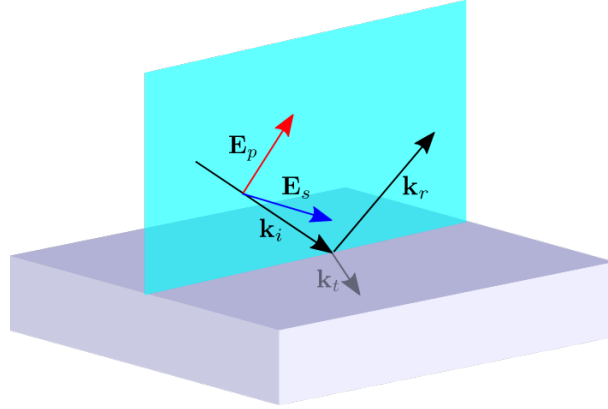


Figure 2.4.: *TE and TM mode of an electric field.*

2.4. Constitutive equations

This subchapter explains the origin of the electric permittivity and magnetic permeability in dielectrics and is based upon the book *Advanced Engineering Electromagnetics* [12]. In a dielectric the charges in atoms and molecules, which are held in place by atomic and molecular forces, are not free to travel. If an external electric field is applied, the centroid of these bound positive and negative charges is slightly shifted in position relative to each other, creating an electric dipole moment. For a polar material, even if no electric field is applied, local dipole moments $d\mathbf{p}_i$ exist between the charges. But the electric polarisation vector is still zero because due to the random orientation of the dipole moments, the local polarisation vectors cancel each other. Application of an electric field leads to an alignment of all the charges along the field lines. However, all the charges in between the top and bottom surface of the dielectric cancel each other. Only the charges $+q_{sp}$ and $-q_{sp}$ at the surfaces remain. These charges create the polarisation density vector \mathbf{P} . The polarisation does not change the value of the applied electric field \mathbf{E} but the value of the electric flux density \mathbf{D} inside the material. In free space $\mathbf{D}_{freeSpace} = \varepsilon_0\mathbf{E}$ in a dielectric with the same applied electric field $\mathbf{D}_{Dielectric} = \varepsilon_0\varepsilon_r\mathbf{E} = \varepsilon\mathbf{E}$ or $\mathbf{D}_{Dielectric} = \varepsilon_0\mathbf{E} + \mathbf{P}$. Assuming a linear proportionality between \mathbf{P} and \mathbf{E} leads to the definition $\mathbf{P} = \varepsilon_0\chi_e\mathbf{E}$ where χ_e is the electric susceptibility (dimensionless quantity). Resulting in

$$\mathbf{D}_{Dielectric} = \varepsilon_0\mathbf{E} + \mathbf{P} = \varepsilon_0\mathbf{E} + \varepsilon_0\chi_e\mathbf{E} = \varepsilon_0(1 + \chi_e)\mathbf{E} = \varepsilon_0\varepsilon_r\mathbf{E} \quad (2.19)$$

For magnetic dipoles in a dielectric under the influence of a magnetic field a similar relation for the magnetic polarisation vector $\mathbf{M} = \mu_0\chi_m\mathbf{H}$ (for linear dependency between magnetisation and magnetic field) where χ_m is the magnetic susceptibility is obtained. In general the susceptibilities are tensors and the relation between polarisation and the corresponding fields are linear if the applied fields are not too strong. To summarise, the permittivity (permeability) is a measure of how much a medium changes to absorb electric (magnetic) energy when subjected to an electric (magnetic) field.

2.4.1. Electric and magnetic conductivities

The conductivity is linked to the amount of free charges inside a material and therefore how easily a current can flow through it. In dielectrics most of the charges are bound to the atoms and cannot move freely around. In metals on the other hand, all the electrons in the outer shell (with energy near Fermi level) are free to move. Therefore conductivities in metals are much higher than in dielectrics. The permittivity and permeability can be expressed as a complex number $\varepsilon = \varepsilon' + i\varepsilon'' = \varepsilon' + i\sigma/\omega$, $\mu = \mu' + i\mu'' = \mu' + i\sigma/\omega$, where ε' , μ' and ε'' , μ'' refer to the real and imaginary parts of the permittivity and permeability respectively and ω to the angular frequency. As can be seen, the conductivity is linked to the imaginary part of ε or μ , representing a power loss. Materials with σ , $\sigma_m \approx 0$ are called lossless materials (air or vacuum). Lossy materials are characterised by σ , $\sigma_m > 0$ (for example, sea water, carbon and germanium). Metals on the other hand are characterised by a very high conductivity σ , $\sigma_m \approx \infty$ (for example silver, copper, iron). The conductivity may vary over a huge range from $\sim 10^{-24} S/m$ (lossless) for Teflon to $6.3 \times 10^7 S/m$ for Silver (metals generally have a very high conductivity). The resistivity is the inverse of the conductivity $\varrho = 1/\sigma$. Ohm's law links the electric Field \mathbf{E} to the electric current density \mathbf{J} via the electric conductivity.

$$\mathbf{J} = \sigma \mathbf{E} = \frac{1}{\varrho} \mathbf{E} \quad (2.20)$$

Inside a conductor, after a very short time no electric field exists anymore. To explain this, imagine bringing a positive charge close to a conductor. For a very short moment an electric field will form due to the charge separation. This field will displace the electrons that are free to move until the electric field is cancelled. Therefore metals are also referred to as perfect electric conductors (PEC). For a lossy (conducting) dielectric, conductivity corresponds to a power loss because some of the energy is converted to heat [13]. The constitutive equations for isotropic linear materials are typically written as in the equations 2.10 and 2.9. The material parameters may be simple scalars as used in frequency independent cases or frequency dependent functions $\varepsilon(\mathbf{r}, \omega)$, $\mu(\mathbf{r}, \omega)$. For anisotropic cases they even become matrices $\bar{\bar{\varepsilon}}$, $\bar{\bar{\mu}}$.

2.4.2. Lorentz material

The Lorentz type of dispersion is based upon the assumption that, in contrast to a metal, the electrons are strongly bounded to the atom. An external field will displace the electrons from their initial position, but due to attraction between the electrons and the atoms they cannot move freely through the material but start oscillating around their equilibrium position (see Figure 2.5). The permittivity and permeability linked to this model are

$$\frac{\varepsilon(\omega)}{\varepsilon_0} = \varepsilon_\infty + \frac{(\varepsilon_s - \varepsilon_\infty)\omega_0^2}{\omega_0^2 - \omega^2 + i2\omega_0\xi_0\omega} \quad (2.21)$$

$$\frac{\mu(\omega)}{\mu_0} = \mu_\infty + \frac{(\mu_s - \mu_\infty)\omega_0^2}{\omega_0^2 - \omega^2 + i2\omega_0\xi_0\omega} \quad (2.22)$$

2. Maxwell and Constitutive Material Equations

where ε_s , $\varepsilon_\infty(\mu_s, \mu_\infty)$ is the permittivity (permeability) at the lower and upper end of the frequency band, ω_0 is the resonance frequency, ω the angular frequency, ξ_0 the damping and I the imaginary unit. For a given set of parameters $\varepsilon_\infty = 2$, $\varepsilon_s = 5$, $\omega_e = 2\pi \times 5 \text{ GHz}$, $\xi_0 = 0.5$ the Lorentz permittivity is represented in Figure 2.5.

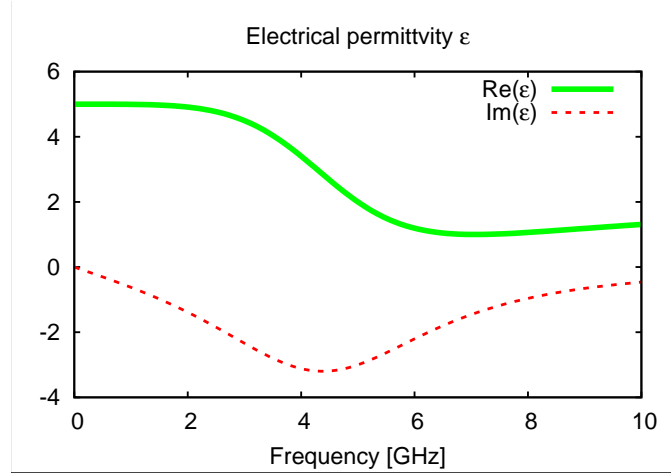


Figure 2.5.: Lorentz permittivity

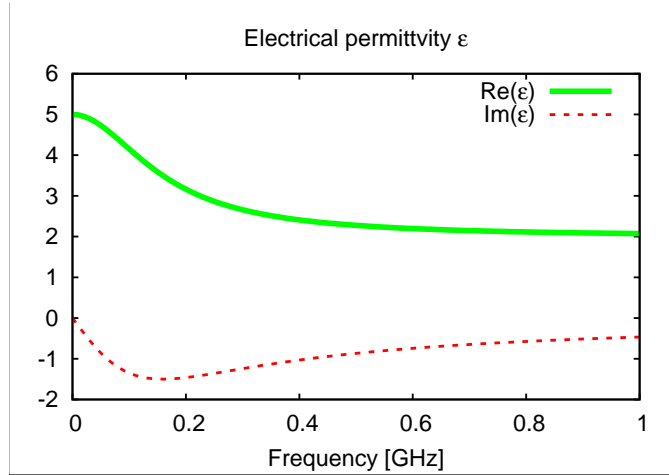
The function used for the material parameters depends upon the type of material needs to be modelled. There are typically three different types of materials. Lorentz, Debye or Drude materials, depending if one is interested in modelling solid dielectrics, liquids or metals, whereas Lorentz and Drude models offer the best theoretical description of metamaterials [153]. The derivation of $\varepsilon(\omega)$, $\mu(\omega)$ (the spatial dependence has been omitted for simplicity) for a given type of material can be found in every standard textbook [13].

2.4.3. Debye material

Liquids, exhibiting orientational polarisation are often modelled as Debye materials, because the molecules re-orient themselves under the influence of an electric field. This re-orientation is not instantaneous due to the inertia of the polarisation. If the frequency passes a given threshold, the molecules cannot follow the variations of the field, leading to a relaxation of the permittivity. This is taken into account by the Debye relaxation time τ leading to a permittivity

$$\frac{\varepsilon(\omega)}{\varepsilon_0} = \varepsilon_\infty + \frac{\varepsilon_s - \varepsilon_\infty}{1 + i\omega\tau} \quad (2.23)$$

For a given set of parameters $\varepsilon_\infty = 2$, $\varepsilon_s = 5$, $\tau = 1$ the Debye permittivity is represented in Figure 2.6.

Figure 2.6.: *Debye permittivity*

2.4.4. Drude material

In a perfect electric conductor the electrons are assumed free to move without interactions and therefore they are accelerated perfectly in phase with the incident field. In a realistic metal (non-perfect conductor) internal electrons are accelerated, but their motion is damped by collisions with the atoms or molecules, leading to the dispersion

$$\frac{\varepsilon(\omega)}{\varepsilon_0} = \varepsilon_\infty + \frac{\omega_p^2}{i\omega\Gamma - \omega^2} \quad (2.24)$$

where $\omega_p^2 = ne^2/\varepsilon_0m$ is the plasma frequency, with n the density of electrons, e and m the charge and mass of an electron respectively and Γ the collision frequency (probability that a collision occurs). For a given set of parameters $\varepsilon_\infty = 2$, $\omega_p = 2\pi \times 5 \text{ GHz}$, $\Gamma = 0.5$ the Drude permittivity is represented in Figure 2.7.

2. Maxwell and Constitutive Material Equations

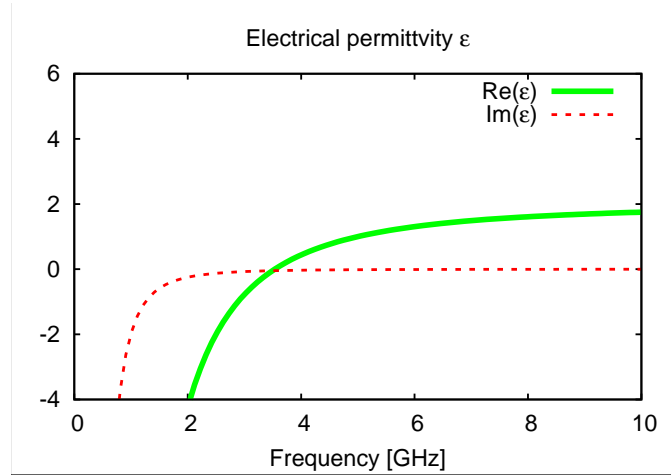


Figure 2.7.: *Drude permittivity*

2.4.5. Causality condition

In dispersive media, the material parameters are not simple scalars anymore. They become frequency dependent functions $\varepsilon, \mu \rightarrow \varepsilon(\omega), \mu(\omega)$. Modelling of frequency dependence is crucial for the simulation of metamaterials because frequency-independent negative material parameters are not realizable [61]. To verify this we consider the relation between the energy density W , and the electric \mathbf{E} and magnetic \mathbf{H} fields respectively

$$W = \frac{1}{2} \left(\varepsilon |\mathbf{E}|^2 + \mu |\mathbf{H}|^2 \right) \quad (2.25)$$

If the permittivity and permeability are frequency-independent and negative, this would lead to a negative energy violating the causality principle. For frequency-dependent material parameters equation (2.25) has to be rewritten to

$$W = \frac{1}{2} \left(\frac{\partial [\varepsilon(\omega)\omega]}{\partial \omega} |\mathbf{E}|^2 + \frac{\partial [\mu(\omega)\omega]}{\partial \omega} |\mathbf{H}|^2 \right) \quad (2.26)$$

and the material parameters have to fulfill the condition

$$\frac{\partial [\varepsilon(\omega)\omega]}{\partial \omega} > 0 \quad , \quad \frac{\partial [\mu(\omega)\omega]}{\partial \omega} > 0 \quad (2.27)$$

which is fulfilled by the Lorentz and Drude model.

2.5. Anisotropic material

In anisotropic materials, the electromagnetic material parameters, such as permittivity, permeability and conductivity, may vary in the different crystal directions, so that they must be treated as tensors. It is assumed that already 1000 years ago, before the invention of magnetic compasses, Vikings used crystals, a naturally occurring anisotropic

material, in Norse sagas referred to as sunstones to navigate on open water on cloudy days. In accordance to researchers these sunstones could have been calcite crystals where anisotropy leads to the phenomenon of birefringence (crystalline materials with different indices of refraction with different crystallographic directions). Their sunstone came within 1% of the true location of the sun [109]. Nowadays anisotropic materials offer many new and interesting perspectives in engineering. A thin anisotropic coating may, for example, significantly change the radar cross section of an aircraft. Composites, anisotropic materials with applications initially limited to stealth bombers, satellites and space shuttles become part of our everyday life. Due to their advantages with respect to mechanical strength and weight compared to metals they are now used in civil aircrafts, trains, automobiles, trucks, sports equipment and so on. Especially in plane and cars electromagnetic compatibility is an issue which can be dealt with using numerical simulations. Other applications are the design of patch antennas where anisotropy can be used as a design parameter [82]. Analytical solutions to wave propagation problems in electromagnetics are mainly restricted to problems involving simple geometrical shapes and diagonal, uniaxial or biaxial, tensors [39, 113]. In anisotropic materials, like crystals or composites, the material parameters $(\varepsilon, \mu, \sigma, \sigma_m)$ are a function of the vector direction of the wave electric and magnetic fields. In 3D they are represented as 3×3 matrices.

$$\bar{\bar{a}} = \begin{pmatrix} a_{xx} & a_{xy} & a_{xz} \\ a_{yx} & a_{yy} & a_{yz} \\ a_{zx} & a_{zy} & a_{zz} \end{pmatrix}, a = \varepsilon, \mu, \sigma, \sigma_m$$

The constitutive equations become

$$\mathbf{D} = \bar{\bar{\varepsilon}}\mathbf{E} \quad (2.28)$$

$$\mathbf{B} = \bar{\bar{\mu}}\mathbf{H} \quad (2.29)$$

This means that the electric and magnetic fields are generally not parallel anymore to the electric, magnetic fluxes. The only exception would be if $a_{ij} = a$ for $i = j$ and $a_{ij} = 0$ for $i \neq j$. More intuitively this means the index of refraction depends on the direction of the field vectors. The components a_{ij} may also be frequency dependent functions $a_{ij} \rightarrow a_{ij}(\omega)$ following a Drude, Lorentz or Debye model. This becomes important for metamaterials which are introduced in the next section.

2.6. Metamaterial modelling

The term metamaterial first appeared in the year 2000 in the paper [119] but until now there is no consensus about the definition of a metamaterial. I only concentrate on materials with exceptional electromagnetic properties where the unit cell is small relative to the wavelength [121]. It is however important to mention that metamaterials can also be designed for acoustic [33], structural [151] or thermodynamic applications [89].

2.6.1. Group and phase velocity of double negative metamaterials

The underlying principle of metamaterials has been discovered by the Russian physicist Victor Georgievich Veselago. He was the first (known) person noticing that Maxwell's equations do not exclude the existence of materials with negative permeability and permittivity. In his paper published in 1968 [135] Veselago thinks about the effects on the reflection and refraction of electromagnetic waves in a material with negative permittivity and permeability. For him, there are three possible results

1. Properties of a substance are not affected by a simultaneous change the signs of ε and μ .
2. Simultaneously negative values of ε and μ conflict with some fundamental laws of nature and therefore no such substance can exist.
3. Simultaneously negative values of ε and μ are possible, but the electrodynamics of such materials differs from electrodynamics for the case of positive ε and μ [134].

Veselago comes to the conclusion that only the third case is correct. What effect does a negative permeability and permittivity has on the propagation of a wave in a medium? First a small reminder on physical relations:

- $v_p = \omega/k$ phase velocity (magnitude)
- $v_G = \partial\omega/\partial k$ group velocity (magnitude)
- $n = \sqrt{\varepsilon_r\mu_r}$ index of refraction
- $c = 1/\sqrt{\mu\varepsilon} = 1/\sqrt{\mu_0\mu_r\varepsilon_0\varepsilon_r} = c_0/\sqrt{\varepsilon_r\mu_r} = c_0/n$ speed of light in a medium
- $\eta = \sqrt{\mu/\varepsilon} = \eta_0 n/\varepsilon_r$ impedance

Introducing a plane wave ansatz in equations (2.2) and (2.1) leads to

$$\mathbf{k} \times \mathbf{E} = \omega\mathbf{B} = \omega\mu\mathbf{H} \quad (2.30)$$

and

$$-\mathbf{k} \times \mathbf{H} = \omega\mathbf{D} = \omega\varepsilon\mathbf{E} \quad (2.31)$$

These two equations give us information about the relative position of the vectors to each other. \mathbf{E} , \mathbf{H} , \mathbf{k} are perpendicular to each other. But their orientation depends upon the sign of ε and μ . If $\varepsilon > 0$ and $\mu > 0$ the field vectors form a right handed system with \mathbf{B} parallel to \mathbf{H} and \mathbf{D} parallel to \mathbf{E} and the material is called right handed material (RHM). If $\varepsilon < 0$ and $\mu < 0$ the field vectors form a left handed material (LHM) and \mathbf{B} anti parallel to \mathbf{H} and \mathbf{D} anti parallel to \mathbf{E} . Materials with $\varepsilon < 0$ and $\mu < 0$ respective $\varepsilon > 0$ and $\mu > 0$ may also be referred to as “double negative” (DNG) or double positive (DPS).

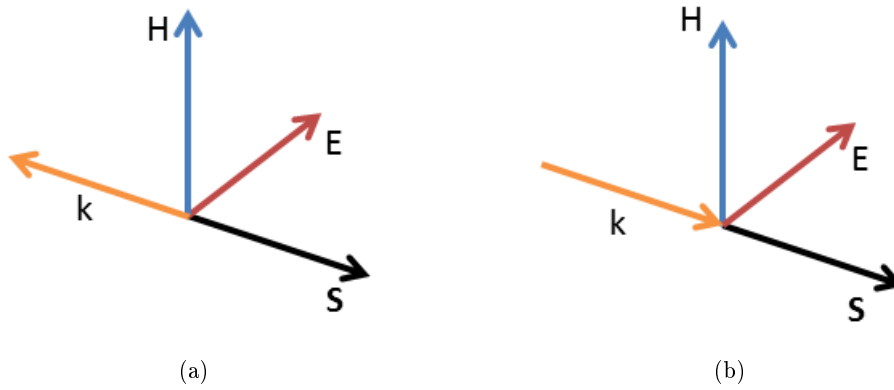


Figure 2.8.: (a) Left Hand Material (LHM) ; (b) Right Hand Material (RHM)

Materials with one negative parameter are named “single negative” (SNG) and can even further be specified as “epsilon-negative” (ENG) or “mu-negative” (MNG). For a DPS (or RHM) and DNG (or LHM) the Poynting vector defined as $\mathbf{S} = (\mathbf{E} \times \mathbf{H}) = 1/(\epsilon\mu)(\mathbf{D} \times \mathbf{B})$, representing the energy flux, always points in the same direction. Waves with a wave vector pointing in the opposite direction with respect to the Poynting vector are referred to as backward waves. Figure 2.8 illustrates the difference between a RHM and LHM. To clarify the consequences of this new concept let’s introduce the phase and group velocity. The phase velocity $\mathbf{v}_p = (\omega/k) \hat{\mathbf{k}}$, with the unity wave vector $\hat{\mathbf{k}}$, points in the same direction as the wavevector.

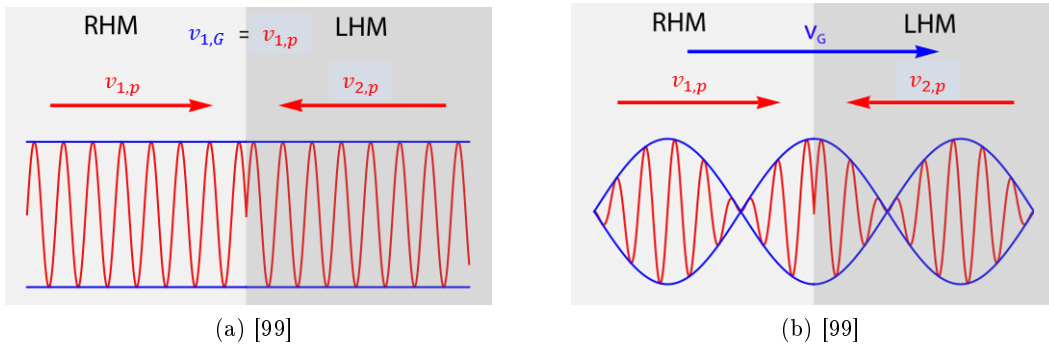


Figure 2.9.: Phase- and group velocity of a plane wave and a wave packet in a LHM and RHM (a) plane wave; (b) wave packet

Therefore the group velocity is parallel to the wavevector and it is negative for a LHM and positive for a RHM. The group velocity $\mathbf{v}_g = (\partial\omega/\partial k) \hat{\mathbf{k}} = \partial/\partial k \left(k/\sqrt{\epsilon\mu} \hat{\mathbf{k}} \right) = 1/\sqrt{\epsilon\mu} \hat{\mathbf{k}}$ on the other hand is independent of the direction of \mathbf{k} . The group velocity is parallel to the Poynting vector and pointing in the same direction. A wave with a positive Poynting vector and anti-parallel wavevector as in a LHM corresponds to a wave where the phase and group velocities go in opposite directions as illustrated in Figure 2.9

2. Maxwell and Constitutive Material Equations

2.6.2. Negative index of refraction

Using the boundary conditions and the definition of the TE, TM modes (section 2.3) I am now able to derive a continuity condition for the wavevector. For a TM mode, H_z is equal to zero for a wave propagating in z direction, leading to $H_t = H_y$, $H_n = H_x + H_y = 0$, where “t” refers to tangential and “n” to normal. For simplicity I define the interface at $z = 0$. The magnetic field inside the material is referred to as \mathbf{H}_2 and elsewhere as $\mathbf{H} = \mathbf{H}_1$. H_y is assumed to be a plane wave. H_y is the sum of the incident and the reflected wave whereas $H_{2,y}$ only contains the transmitted wave propagating along the z direction

$$H_y = Ae^{-i(k_z z + k_x x)} + Be^{i(k_z z - k_x x)} \quad (2.32)$$

$$H_{2,y} = Ce^{-i(k_{2,z} z + k_{2,x} x)} \quad (2.33)$$

where A, B, C are the amplitudes. Using the boundary conditions (equation (2.16)) and the fact that the boundary is located at $z = 0$

$$H_t = H_{2,t} \quad (2.34)$$

$$(A + B)e^{-ik_x x} = Ce^{-k_{2,x} x} \quad (2.35)$$

This condition can only be fulfilled if $k_x = k_{2,x}$ and $A + B = C$. The similar reasoning follows for a TE mode with a tangential E-field. If the second medium is a LHM, the wavevector inside this material \mathbf{k}_2 is anti parallel to the wavevector in the RHM \mathbf{k} (see section 2.6.1). But the condition $k_x = k_{2,x}$ is still valid, so $k_{2,z}$ has to be negative leading to a wave (\mathbf{k}_3) which is refracted above the perpendicular as illustrated in Figure 2.10. This is called a negative refraction. To derive Snell’s Law, the condition $k_x = k_{2,x}$ with

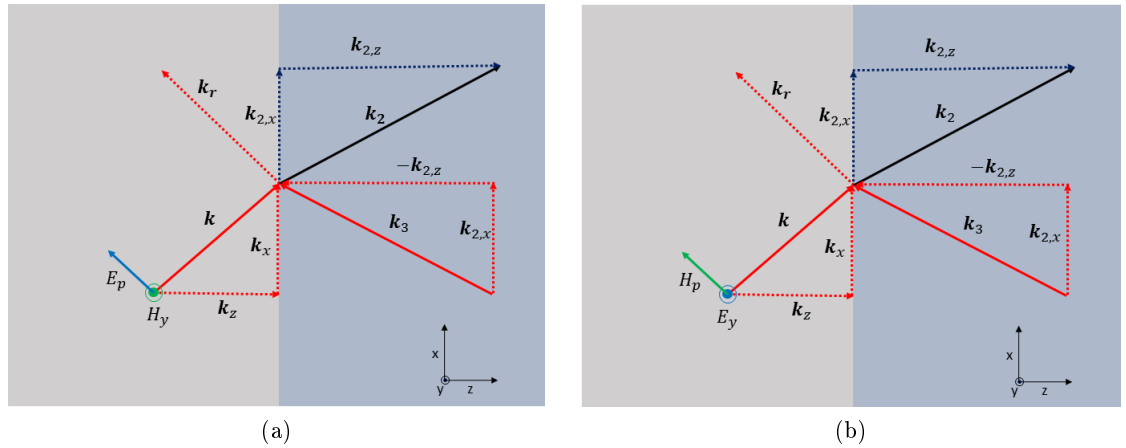


Figure 2.10.: (a) *p*-polarised wave ; (b) *s*-polarised wave

$k_x = k \sin(\theta)$ and $k_{2,x} = k_2 \sin(\theta_2)$ needs to be fulfilled. With the dispersion relation $\omega = k/\sqrt{\epsilon\mu}$ this leads to

$$\sqrt{\varepsilon\mu} \sin(\theta) = \sqrt{\varepsilon_2\mu_2} \sin(\theta_2) \quad (2.36)$$

$$\Leftrightarrow n \sin(\theta) = n_2 \sin(\theta_2) \quad (2.37)$$

For a negative refraction θ' becomes negative. Next I use $\sin(-\theta_2) = -\sin(\theta_2)$ and introduce it in equation (2.37). Rearranging it leads to

$$n_2 = n \frac{\sin(\theta)}{-\sin(\theta_2)} \quad (2.38)$$

but in this case equation (2.37) would be violated because $n \sin(\theta) = -n_2 \sin(\theta')$ therefore n_2 has to be negative. Corresponding to a negative index of refraction in a LHM. This is illustrated in Figure 2.11.

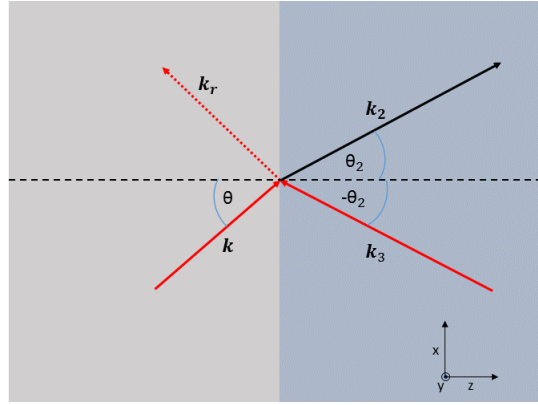


Figure 2.11.: *Snell's law*

Let us now further investigate the index of refraction, which is defined as $n = \sqrt{\varepsilon\mu}$. According to this definition the material parameters ε , μ have to be complex for a LHM, otherwise a negative index of refraction is not possible. The real part of n , $Re(n) = n'$ corresponds to the classical index of refraction and the imaginary part $Im(n) = n''$ corresponds to the absorption .

$$n^2 = \varepsilon\mu \quad (2.39)$$

$$\Leftrightarrow (n' + in'')^2 = (\varepsilon' + i\varepsilon'')(\mu' + i\mu'') \quad (2.40)$$

$$\Leftrightarrow n'^2 - n''^2 + i2n'n'' = \varepsilon'\mu' - \varepsilon''\mu'' + i(\varepsilon'\mu'' + i\varepsilon''\mu') \quad (2.41)$$

Everything I derived until now remains true for the real parts of the considered quantities $\varepsilon' < 0$, $\mu' < 0$, $n' < 0$. Therefore, by only considering the imaginary part of equation (2.41) I get

$$n' = \frac{\varepsilon'\mu'' + \varepsilon''\mu'}{2n''} < 0 \quad (2.42)$$

The absorption n'' is always > 0 . Therefore the remaining condition is

$$\varepsilon'\mu'' + \varepsilon''\mu' < 0 \quad (2.43)$$

2. Maxwell and Constitutive Material Equations

2.6.3. Absorption and evanescent waves

To prove that n_i is linked to the absorption of a wave let's consider a plane wave propagation in x direction inside a medium with index of refraction n .

$$E(t, x) = E_0 e^{-i(kx - \omega t)} \quad (2.44)$$

using the dispersion relation

$$k = \frac{n\omega}{c_0} = (n' + in'') \frac{\omega}{c_0} \quad (2.45)$$

and introducing it in equation (2.44) leads to

$$E(t, x) = E_0 e^{-i\left(\frac{\omega}{c_0} n' x - \omega t\right)} e^{-\frac{\omega}{c_0} n'' x} \quad (2.46)$$

where n'' leads to an exponential damping of the incident wave. In the next step I link the imaginary part of the index of refraction using Lambert Beer Law which is only defined for intensities

$$I(x) = I_0 e^{-\alpha x} \quad (2.47)$$

with x the thickness of the sample, α the absorption coefficient and I_0 the initial intensity. The intensity of the electric field is proportional to the square of the field

$$I(x) \propto |E|^2 = E_0^2 e^{-i2\left(\frac{\omega}{c_0} n' x - \omega t\right)} e^{-2\frac{\omega}{c_0} n'' x} = I_0 e^{-2\frac{\omega}{c_0} n'' x} \quad (2.48)$$

where $E_0^2 e^{-i2\left(\frac{\omega}{c_0} n' x - \omega t\right)}$ got absorbed in I_0 . Comparing the coefficients from equations (2.47) and (2.48) leads to

$$\alpha = \frac{2\omega n''}{\varepsilon_0} \quad (2.49)$$

Until now I investigated how the wave propagates in RHM ($\varepsilon, \mu > 0$) and LHM ($\varepsilon, \mu < 0$). But, what happens if $\varepsilon < 0, \mu > 0$ or $\varepsilon > 0, \mu < 0$. Using the dispersion relation, leads to

$$k = \omega c = \omega n = \omega \sqrt{\varepsilon_0 \mu_0} \sqrt{\varepsilon \mu} \quad (2.50)$$

where μ, ε refers to the relative material parameters in this case. If $\varepsilon < 0, \mu > 0$ or $\varepsilon > 0, \mu < 0$, k has to be a complex number $k = k' + ik''$, so k'' is again linked to the imaginary index of refraction n'' . For a plane wave, propagating in positive x direction the electric field is

$$E(t, x) = E_0 e^{-i(kx - \omega t)} = E_0 e^{-i(k'x - \omega t)} e^{k''x} \quad (2.51)$$

Where the term $\exp(k''x)$ leads to an exponential damping in x direction. Therefore the penetration depth is very limited. Such a wave is referred to as evanescent. A summary of the reflection/transmission properties for different material parameters is summarised in Figure 2.12

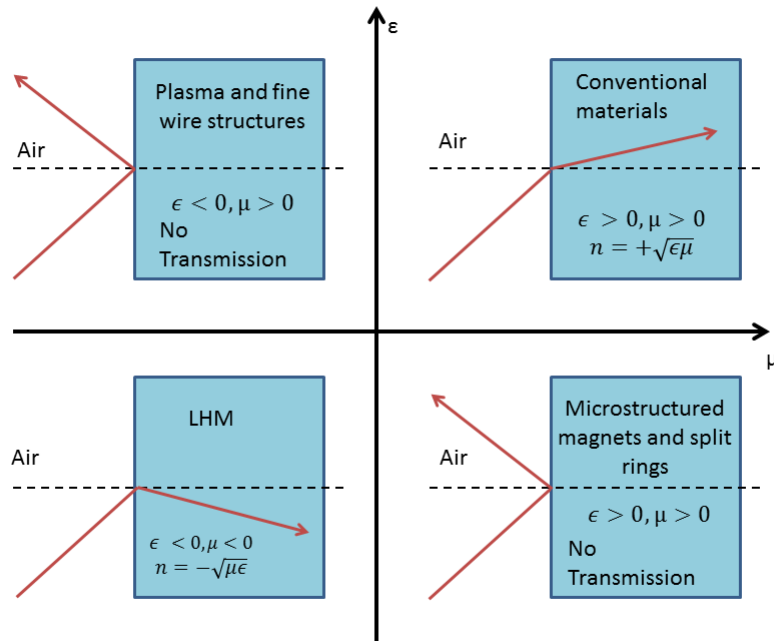


Figure 2.12.: Reflection and transmission properties for different material parameters

2.7. Electrical wire grid resonators

Until now no DNG materials has been discovered in nature. But in 1999 Sir John Pendry [101] got the idea to build a LHM by assembling two different structures. One leading to a $\mu < 0$ and another leading to a $\epsilon < 0$ by using split ring resonators and wires. The basic idea is to choose inclusions on a mesoscopic scale (smaller than the wavelength but larger than atoms) with respect to the wavelength, because they will behave like a homogeneous material. The size of such inclusions should be at least $\lambda/6$.

wire grid resonator

According to the Lorentz model $\epsilon(\omega) < 0$ close to the resonance frequency. Unfortunately no naturally occurring dielectric material is known with this property. But many metals have this property $\epsilon(\omega) < 0$. In contrast to dielectrics where electrons are bound to the atoms, metals are described using a Drude model because the conducting electrons are free to move. There exists no restorable force and the electrons oscillate with the electric field. In Figure 2.13 a negative permittivity occurs for angular frequencies smaller than ω_p . Due to the absorption only a small band may be used for creating a negative index of refraction which can be controlled by tuning the the plasma frequency by changing the density of charges.

2. Maxwell and Constitutive Material Equations

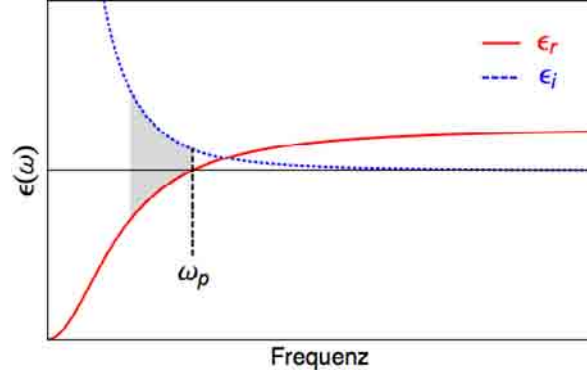


Figure 2.13.: Drude permittivity, with $Re(\varepsilon) = \varepsilon'$ and $Im(\varepsilon) = \varepsilon''$

Unfortunately it is not simply possible to generate a plasma and control the position of all the charges. Therefore Sir John Pendry had the idea to assemble long metallic wires which appear to an incoming wave as effective electron plasma (because the charges are free to move along the wire) if the wavelength is long enough. The electric field is polarised along the wires. This allows the design of negative permittivity materials in the frequency range below $2GHz$. But the exponentially increasing absorption limits the use of such a material. To improve the efficiency the “cut wire grid” method is developed.

Cut wire grid resonator

To increase the bandwidth the resonant behaviour of short wires can be used. For this case the Drude model is not suited because due to the short wires the ideal plasma assumption doesn't hold anymore. For short wires the electrons will accumulate at the boundaries generating an opposing field leading to a resetting force proportional to the deflection. This force depends on the length of the wire. By considering this effect, the permittivity becomes a mixture between a Lorentz and a Drude model leading to

$$\varepsilon(\omega) = 1 - \frac{\omega_p^2 - \omega_\varepsilon^2}{\omega^2 - \omega_\varepsilon^2 + i\xi_\varepsilon\omega} \quad (2.52)$$

with

$$\omega_p = \frac{2\pi c_0^2}{a^2 \ln(a/r)} \quad \omega_0 = \frac{\pi c_0}{l} \quad (2.53)$$

where a is the lattice parameter, r the radius and l the length and ω_0 the fundamental mode. Details about the derivation of this function can be found in [100] and [45].

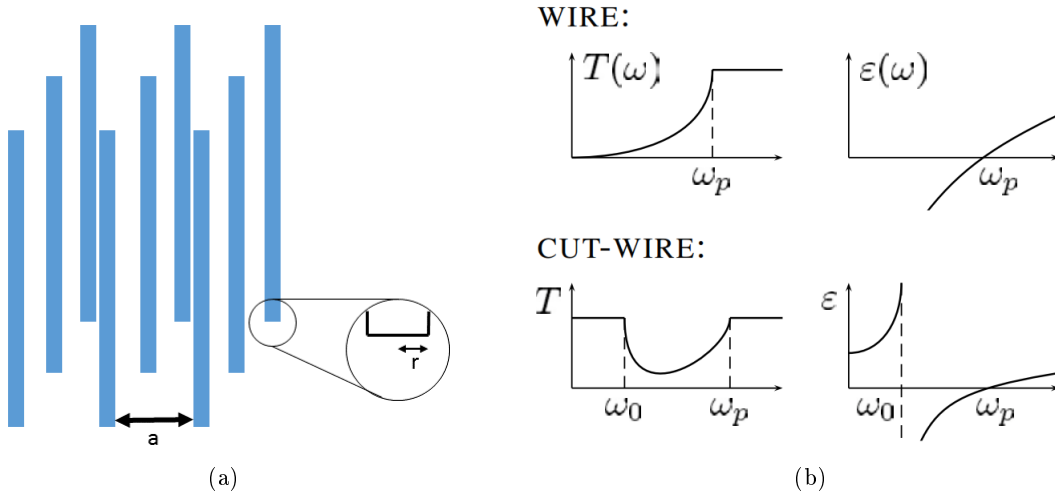


Figure 2.14.: (a) cut wire grid resonator ; (b) comparison between “wire” and “cut wire” transmission and permittivity

The wire has an inductive behaviour and the edges are the capacity. The “cut wire grid” is represented in Figure 2.14a. In Figure 2.14b the transmission and permittivity of a “wire” and “cut wire” are compared. As can be seen the transmission for a “wire grid” decreases exponentially to zero. Due to the resonance in the “cut wire grid” the frequency band from ω_0 to ω_p is much wider. Such “cut wire” materials are not only interesting for DNG materials but are already used to improve standard horn antennas [79].

2.8. Magnetic resonator

On a microscopic scale magnetism is the result of unpaired electron spins. Probably the simplest way to generate a magnetic moment on a macroscale is to bend a metallic wire to a circle and apply a current to it. A magnetic moment perpendicular to the plane of the wire is generated according to

$$\mathbf{m} = \frac{1}{2} \int_V (\mathbf{r} \times \mathbf{J}) dV \quad (2.54)$$

with \mathbf{J} the current density and \mathbf{r} the radius. As depicted in Figure 2.15 incoming plane wave with a time varying magnetic field perpendicular to the plane of the conducting ring will induce an electric field along its contour leading to an electric current \mathbf{I} . According to Amperes law this time varying current will induce an magnetic field leading to an magnetic moment \mathbf{m} . Unfortunately this magnetic moment is too weak. Even for a closed packed configuration of conducting rings only $\mu < 1$ is realisable, but not $\mu < 0$. As for the electric case, the magnetic moment may be increase by making use of a resonance, leading to the design of the so called split-ring resonator.

2. Maxwell and Constitutive Material Equations

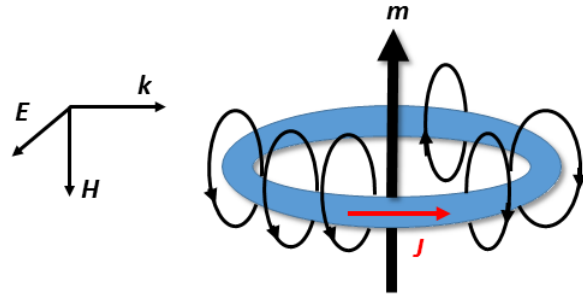


Figure 2.15.: *magnetic moment generated by incident wave.*

In contrast to the conducting ring the split ring is not completely closed leading to a capacitance C at both ends of the wire connected in series to the inductance L of the ring. Strictly speaking the split ring resonators do not have to be rings. They may appear in different configurations as depicted in Figure 2.16.



Figure 2.16.: *Rectangular SRR, circular SRR, nested SRR (Double split ring resonators (DSRR)), SRR back-to-back configuration.* [99]

For a known L, C and resistance R , the differential equation describing a RLC-circuit is

$$L \frac{d^2 I(t)}{dt^2} + R \frac{dI(t)}{dt} + \frac{1}{C} I(t) = 0 \quad (2.55)$$

$$\Leftrightarrow \frac{d^2 I(t)}{dt^2} + \alpha \frac{dI(t)}{dt} + \omega_0^2 I(t) = 0 \quad (2.56)$$

where the damping is $\alpha = R/L$ and the resonance frequency $\omega_0 = 1/\sqrt{LC}$. L, C mainly depends upon the geometry. DSRRs (Figure 2.16) show a sharper resonance and are a popular choice for metamaterials with $\mu < 0$. They lead to an effective permeability of [74]

$$\mu^{eff}(\omega) = 1 - \frac{\omega_m^2 - \omega_0^2}{\omega^2 - \omega_0^2 + i\alpha\omega} \quad (2.57)$$

where ω_m is the “magnetic plasma frequency” equivalent to the plasma frequency, for a closed packed arrangement a strong magnetic response leads to $\mu < 0$.

2.9. Effective LHM medium

To finally build a negative index of refraction metamaterial typically alternating layers of electric and magnetic resonators are used. The first metamaterial developed by Smith [119] is represented in Figure 2.17a. The wires and DSRRs are clearly distinguishable. Later, printed circuit board (PCB) technology is used to reduce the dimensions of the metamaterial making it useful for smaller wavelengths. On PCBs the DSRRs are printed on one side and the wires on the other side of the board as depicted in Figure 2.17b. These are only examples of 2D metamaterials.

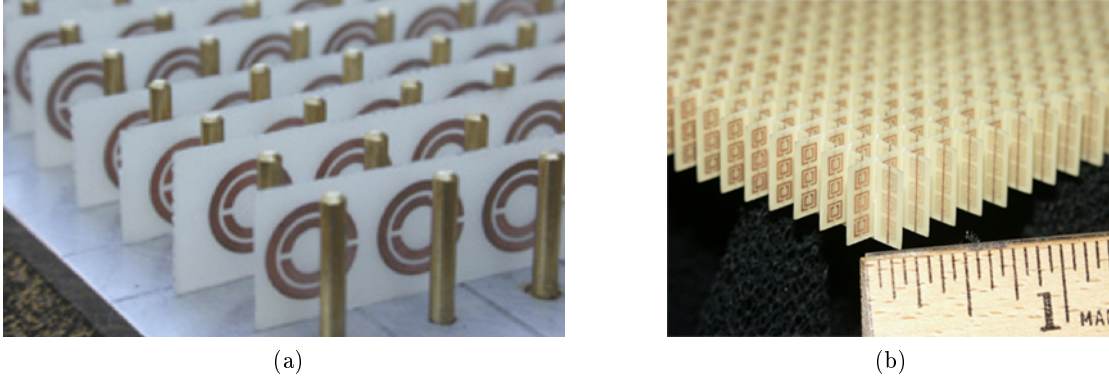


Figure 2.17.: (a) Metamaterial developed by Smith et al. [119] ; (b) Metamaterial suited for smaller wavelengths build using print circuit board technology

2.10. Chiral and pseudo-chiral materials

A Chiral material is a metamaterial but it is not part of the double negative materials because the permittivity and permeability may remain positive. The negative index of refraction may be obtained using an additional material parameters referred to as chirality. Chirality is derived from the Greek word for “hand”, therefore it is also referred to as handedness. An object is chiral if it is distinguishable from its mirror image and consequently if it cannot be superimposed with it by translation and rotation. This is for example the case for the left and right hand. In chemistry, chiral molecules are referred to as enantiomers (Figure 2.18a). If a chiral object is left handed, its enantiomorph is right-handed (see Figure 2.18b). On the other hand, an achiral object like a sphere cannot be distinguished from its mirror image. The interaction of an electromagnetic wave with a collection of randomly oriented chiral objects (small helices for example) leads to the phenomenon of optical activity causing a rotation of the plane of polarisation to the right or to the left depending on the chirality of the object [67]. In 1811 Arago [7] first discovered optical activity in quartz crystals and 1815 Biot [18] discovered this phenomenon in other media such as oil of turpentine. 1848 Louis Pasteur [83] identified the chirality of the molecules as cause of the optical activity. Finally, in 1920 and 1922, Lindman [73, 81] set up a model based upon microwaves instead of light by replacing chiral molecules by

2. Maxwell and Constitutive Material Equations

wire spiral entities (macroscopic molecules). Which has been experimentally validated by Pickering [104]. Lindman and Pickering showed that a collection of randomly oriented left-handed helices turns the plane of polarisation of the incident wave one way whereas the right-handed helices turns it the other way [94].

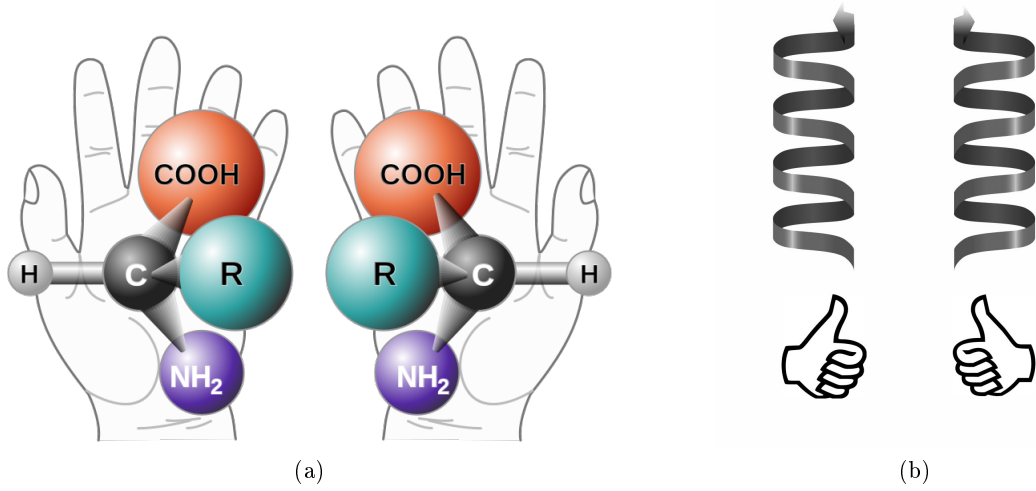


Figure 2.18.: (a) hand and chiral molecules ; (b) left- (on the left) and right-handed (on the right) helices

Chiral materials are a special case of bi-isotropic materials. Due to the discovery of new properties and fabrication techniques they become increasingly popular. Especially because they offer a negative index of refraction without requiring a negative permittivity or chirality. In the mathematical description bi-isotropy is taken into account in the constitutive equations

$$\mathbf{D}(\omega) = \varepsilon(\omega)\mathbf{E} + \xi(\omega)\mathbf{H} \quad (2.58)$$

$$\mathbf{B}(\omega) = \mu(\omega)\mathbf{H} + \zeta(\omega)\mathbf{E} \quad (2.59)$$

ξ, ζ are the cross coupling parameters defined as

$$\zeta(\omega) = \frac{\chi(\omega) + i\kappa(\omega)}{c} \quad (2.60)$$

$$\xi(\omega) = \frac{\chi(\omega) - i\kappa(\omega)}{c} \quad (2.61)$$

where c is the speed of light, χ the Tellegen parameter and κ the chirality, sometimes also referred to as Pasteur parameter. In this thesis I will only focus on chiral materials therefore we neglect the Tellegen parameter especially because it's existence is still controversial. Hence our constitutive equation simplifies to

$$\mathbf{D}(\omega) = \varepsilon(\omega)\mathbf{E} - \frac{i\kappa(\omega)}{c}\mathbf{H} \quad (2.62)$$

$$\mathbf{B}(\omega) = \mu(\omega)\mathbf{H} + \frac{i\kappa(\omega)}{c}\mathbf{E} \quad (2.63)$$

As can be seen the chirality leads to a coupling between the electric and magnetic fields. The Pasteur parameter leads to two interesting effects

- Optical rotatory dispersion (ORD): continuous rotation of the plane of polarisation of a linearly polarised incident wave inside the chiral material
- Circular dichroism (CD): change of the polarisation from linear to elliptical due to different absorption coefficients of a right and left circularly polarised wave

These phenomenon are illustrated in Figure 2.19.

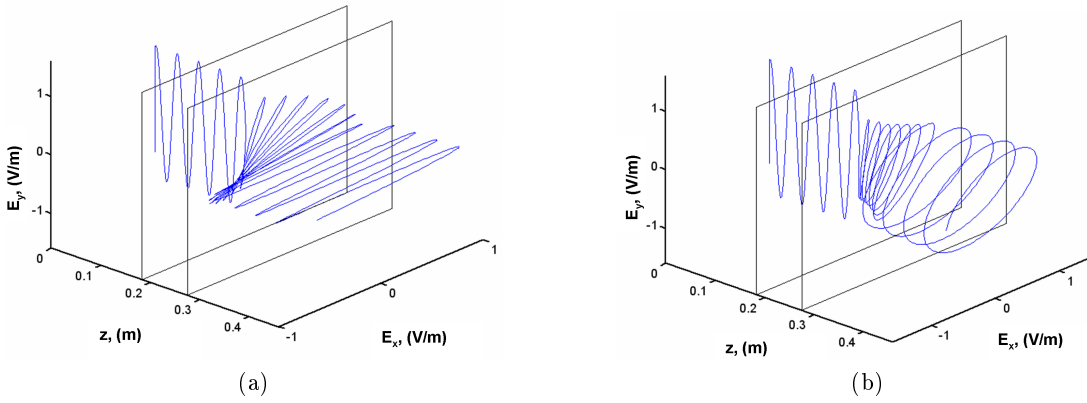


Figure 2.19.: *Effect of Pasteur parameter (a) Optical rotatory dispersion (ORD). ; (b) Circular dichroism (CD)*

A pseudo-chiral material is used in bi-anisotropic metamaterials and may show a similar optical activity with the phenomena of CD and ORD without being chiral [110]. The unit cells of a pseudo-chiral material are by itself not chiral but they nevertheless lead to a coupling between the electric and magnetic field, described by the chirality (Pasteur) parameter if they are arranged in a specific way. This coupling does not exist in a LHM where the magnetic resonators (SRR) are spatially separated from the electric resonators (wires). An omega particle for example (Figure 2.20) is a combination of the SRR and wire. Therefore the coupling of the electric and magnetic field arises, mathematically taken into account by the chirality parameter in the constitutive equations.

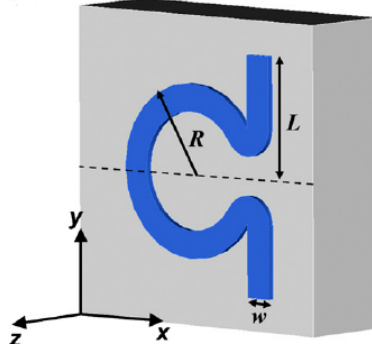


Figure 2.20.: Standard unit cell of Ω -Medium. [10]

2.11. Classification of metamaterials

In 1998 Tretyakov et al. [129] suggested a method to classify different kind of metamaterials. They define the constitutive equations as in the isotropic case but the material parameters are complex tensors instead of scalars.

$$\mathbf{D} = \bar{\bar{\epsilon}}\mathbf{E} + \bar{\bar{\xi}}\mathbf{H} \quad (2.64)$$

$$\mathbf{B} = \bar{\bar{\mu}}\mathbf{H} + \bar{\bar{\zeta}}\mathbf{E} \quad (2.65)$$

$$\bar{\bar{\xi}} = \frac{1}{c}(\bar{\bar{\chi}}^T - i\bar{\bar{\kappa}}^T) \quad (2.66)$$

$$\bar{\bar{\zeta}} = \frac{1}{c}(\bar{\bar{\chi}} + i\bar{\bar{\kappa}}) \quad (2.67)$$

$\bar{\bar{\chi}}$ is the Tellegen or non-reciprocal parameter which I do not consider in the following classification because I am only interested in reciprocal bi-anisotropic media. In this case $\bar{\bar{\epsilon}}$ and $\bar{\bar{\mu}}$ are symmetric tensors and $\bar{\bar{\xi}} = -\bar{\bar{\zeta}}^T = -i\bar{\bar{\kappa}}^T$ where $\bar{\bar{\kappa}}$ is the chiral tensor responsible for the magnetoelectric coupling. Rewriting $\bar{\bar{\kappa}}$ as

$$\bar{\bar{\kappa}} = \frac{1}{3}Tr(\bar{\bar{\kappa}})\bar{\bar{I}} + \bar{\bar{M}} \quad (2.68)$$

where $Tr()$ is the trace of a matrix. In the original publication the term $1/3$ in front of the trace is not used but in our opinion it should be added. $\bar{\bar{I}}$ is the unity matrix and the trace of $\bar{\bar{M}}$ equals zero. It is furthermore possible to decompose every square matrix in a symmetric and antisymmetric matrix.

$$\bar{\bar{M}} = \bar{\bar{N}} + \bar{\bar{J}} \quad (2.69)$$

Where $\bar{\bar{N}} = (\bar{\bar{M}} + \bar{\bar{M}}^T)/2$ is symmetric and $\bar{\bar{J}} = (\bar{\bar{M}} - \bar{\bar{M}}^T)/2$ is antisymmetric. As a reminder a matrix $\bar{\bar{A}}$ is symmetric if $A_{ij} = A_{ji}$ and antisymmetric if $A_{ij} = -A_{ji}$. In

our case $Tr(\bar{M}) = 0$, therefore $Tr(\bar{N}) = 0$. Therefore there must be at least two set of virtual inclusions with opposite handedness. In these media effects known from isotropic chiral media like optical rotatory dispersion and circular dichroism may occur. Interestingly the microstructure of these materials doesn't has to be chiral to lead to the same effects as observed in isotropic chiral media. Therefore they are called pseudo-chiral.

$$\bar{\kappa} = \frac{1}{3}Tr(\bar{\kappa})\bar{I} + \bar{N} + \bar{J} \quad (2.70)$$

Equation (2.70) allows us to classify several metamaterials (Table 2.1)

Coupling Parameters	Class
$Tr(\bar{\kappa}) \neq 0, \bar{N} = 0, \bar{J} = 0$	Isotropic chiral medium
$Tr(\bar{\kappa}) \neq 0, \bar{N} \neq 0, \bar{J} = 0$	Anisotropic chiral medium
$Tr(\bar{\kappa}) = 0, \bar{N} \neq 0, \bar{J} = 0$	Pseudo-chiral
$Tr(\bar{\kappa}) = 0, \bar{N} = 0, \bar{J} \neq 0$	Omega medium
$Tr(\bar{\kappa}) \neq 0, \bar{N} = 0, \bar{J} \neq 0$	Chiral omega medium
$Tr(\bar{\kappa}) = 0, \bar{N} \neq 0, \bar{J} \neq 0$	Pseudo-chiral omega medium
$Tr(\bar{\kappa}) \neq 0, \bar{N} \neq 0, \bar{J} \neq 0$	General reciprocal bi-anisotropic medium

Table 2.1.: Classification of reciprocal bi-anisotropic media

3. Numerical Solution of Maxwell Equations

In computational electromagnetics (CEM) there exist various methods for solving Maxwell's equations. They all have their advantages and disadvantages and depending on the case one method may be better suited than another.

3.1. Review of numerical techniques for the solution of Maxwells equations

Time Domain vs Frequency Domain

CEM programs can be separated in two main groups. Time domain (TD) and frequency domain methods. Time domain methods are interesting if a broadband analysis is required. An example would be the transmission and reflection coefficients (expressed in the frequency domain) of an electromagnetic pulse (time domain) interacting with a dielectric material. Therefore a pulse is defined in the time domain and after it interacted with the dielectric when the Fourier transform is applied to convert the response from the time to frequency domain. The result is a very broadband response in the frequency domain by running the algorithm only once in time domain. If on the other hand we are only interested in a time-harmonic steady state solution at a single frequency the frequency domain method is much more efficient because no time stepping is required and the solution is obtained through a matrix inversion process. Another big advantage of a frequency domain method is the simplicity to implement frequency dependent (dispersive) material parameters (ϵ , μ , σ), because the scalar values can be used directly. In the time domain this is more cumbersome because the constitutive equation, which is a multiplication in the frequency domain, becomes a convolution in the time domain. To obtain a broadband response a frequency domain method can also be used by running multiple simulations, one at each frequency. Although it is more complicated to deal with frequency dependent material parameters in a TD method, the broadband response obtained in the frequency domain after a single run in the time domain outweighs the disadvantages. Therefore I restrict my attention only to TD methods. The advantages and disadvantages of the most common methods are presented in the following paragraphs.

Method of Moments (MoM) or Boundary Element Method (BEM)

The Method of Moments (MoM), or Boundary Element Method (BEM) solves linear partial differential equations formulated as integral equations. Applications range from

3. Numerical Solution of Maxwell Equations

electromagnetics over acoustics to fracture mechanics. The numerical implementations of the method go back to the 60s but it became popular in the late 1970s. The main difference between the MoM and the presented finite element and finite difference methods (FDM) is that the MoM is a boundary method whereas the others are domain methods. In a BEM method for a 3D case, the discretisation is only applied to the boundary surface, whereas in domain methods, the whole space needs to be discretised. This reduced dimension leads to lower computational requirements due to the smaller systems. This method is especially suited for problems with a small surface to volume ratio and excel in modelling open radiation problems, particularly when the geometry includes large metallic surface or resonant length wires. The ray tracing techniques is part of the BEM methods and results from the high frequency approximation of Maxwell's equations. As a geometrical method ray tracing adds no penalty on the runtime if the frequency is increased. This becomes useful when other methods become computationally to expensive because of the vanishing wavelengths. If the size of the obstacle is much bigger than the incoming wavelength this method is typically applied. Common applications of ray tracing are the propagation of radio signals through the ionosphere, ocean acoustics or the design of lenses and optical systems. I am however interested in objects with a size in the order of magnitude of the exciting wavelength, making this method not suitable for my applications. Generally BEM methods result in fully populated matrices, leading to a grow of the storage requirements and the computational time proportional to the square of the problem size. For Finite Element Methods the storage requirements however only grow linearly with the problem size [29]. BEM methods are best suited for problems in linear homogeneous media where Green's functions can be calculated, which is a non-negligible restriction for this method especially for my applications. Therefore I concentrate on volume discretisation methods.

Finite Difference Time Domain Method

The publication from 1928 from Courant, Friedrichs and Lewy can be considered as starting point of the Finite Difference Method [32]. They investigated the solution of problems by means of finite different methods. They even defined a finite difference approximation for the wave equation and the derived the CFL stability condition necessary for the convergence of the solution. This condition is a key parameter in the FDTD formulation because it links the time step to the spatial step of the mesh. In 1930 Gerschgorin [53] derived the error bounds for the difference approximation of elliptic problems. Twenty years later after the Second World War, the improvement of computers lead to practical applications pushing the development of the Finite Difference Time Domain Method. During the 1950s and 1960s key protagonists in the further development and generalisation of the method where O'Brian, Hyman, Kaplan [98], John [68] and many others. Probably the most common FDTD method in electromagnetics is the Yee algorithm [146] named after his inventor Kane S. Yee. A two-point centered difference form is used to obtain second-order accuracy. In its standard form a structured staggered spatial mesh is used. The staggered mesh allows the interleaved placement of the electric and magnetic field components. The main advantages of this methods are [118, 126]:

3.1. Review of numerical techniques for the solution of Maxwell's equations

- Simple discretisation procedure allowing to model a 3D problem in less than 100 lines of code
- Easy to understand due to simple discretisation
- No inherent limit to the size of a simulation due to explicit nature. No linear algebra or matrix inversions are required
- Gauss laws are inherently fulfilled
- Scheme preserves the energy and amplitude of the wave
- As a time domain method one single run of the simulation allows the whole representation of the frequency domain by using the Fourier transform.
- Accurate and robust method
- Method can easily be parallelised on CPU's and GPU's

The main drawbacks are:

- A stability condition links the time step to the spatial size of the smallest mesh elements. This makes it problematic for the method to deal with large scale applications.
- As a low order method the accuracy of the results may suffer from numerical dispersion.

Finite Volume Time Domain (FVTD)

Initially finite-volume techniques were used to solve the governing equations in fluid dynamics. Beginning of the 90's Madsen [88], and Shankar [116] adapted this method for the solution of Maxwell's equations. Similar to the Yee algorithm, Madsen suggested an interleaving of the fields. In this case the method may be referred to as a hybrid FDTD-FVTD method. The electric and magnetic field components are stored on the edges of the primal and dual cell respectively. Yee and Chen [147, 148] also suggested their own FVTD method. In contrast to Madsen they store the fields on the vertices of the cells, simplifying the derivation of the update equations. In FVTD the integral form of Maxwell's equations is used to conserve the field quantities. Whereas in the standard FDTD formulation the electric and magnetic field vectors are stored on the nodes of grid cells, in FVTD the fields are defined in small volumes in space. The main advantage of the FVTD method compared to the standard FDTD method is the generalisation to unstructured meshes, allowing the conformal approximation of curved surfaces. Furthermore the method can be used on non-uniform meshes. For linear, non-dispersive materials the spatial discretisation has to be smaller than $\lambda_{Diel}/10$, where λ_{Diel} is the wavelength inside the dielectric. Materials with a large electric permittivity can be discretised with smaller cells compared to low electric permittivity materials. The unstructured mesh allows a smooth transition between high and low permittivity

3. Numerical Solution of Maxwell Equations

materials. This significantly reduces the number of cells in the overall mesh. Overall the FVTD method combines an explicit time domain method with an unstructured mesh. The drawbacks of the methods are the required dual grid, which may be challenging to generate and the larger stencils, required for higher accuracy, destroying the locality of the scheme. Furthermore this method is not divergence free.

Finite Element Method (FEM)

The finite element method has originally been developed in the 1940's for structural mechanic applications [152]. The popularity for electromagnetic application rise end of the 1960s. Nevertheless FDTD was the most popular method until the 1990s due to its simplicity and efficiency with respect to computational resources. By further developing the Finite Element method in Time Domain (FETD) and by using improved algorithms higher accuracy and efficiency could be achieved. In contrast to the standard FDTD method, FETD can be used on unstructured meshes. FETD on the other hand can deal with higher-order polynomial basis functions. There is also a conceptual difference between the finite difference and finite element methods. FD methods approximate the operators (derivatives) $\partial u/\partial t \approx (u(t_{i+1}) - u(t_i))/\Delta t$ whereas FE methods approximate the solution of the differential equation $u(t) \approx \sum_i^N u_i \phi_i(t)$, where $\phi_i(t)$ is a local basis of expansion function defined over a local finite element, and then adapt the solution to minimise the difference between the numerical and exact solution. A big drawback of the FE method is that a large albeit often sparse matrix has to be solved in implicit schemes, to enforce continuity at element boundaries, leading to a serious overhead often limiting the applications of the method. In a second order central finite difference method the scheme is explicit. Restricting the method to low orders allows an iterative scheme through mass lumping for example. However, in this case it is not divergence free and it introduces dissipation [44].

Discontinuous Galerkin Finite Element Method (DG-FEM)

The Discontinuous Galerkin Method (DGM) has first been used by Reed and Hill [142] to solve the neutron transport equation. Over the decades the method has been further refined and has been successfully applied in electrodynamics, fluid mechanics and plasma physics. In the last decade a lot of research has been done in the development of high-order discontinuous galerkin methods for electromagnetic simulations in time domain [62, 30, 84, 70, 27]. DGM combines the advantages of the FEM and FVTD method, leading to a scheme that is local, explicit in time and able to deal with higher order of accuracy. In contrast to the standard FDTD, DGM works on unstructured meshes and no staggered grids are required. Furthermore, the block-diagonal structure of the matrix induces a trivial parallization of this scheme. Another major advantage is the facility to use non-uniform-uniform degrees of approximations. As with all the FE methods the problem lies in the complexity of the algorithms compared to FDTD methods, but it would in my opinion be the best choice out of the FE methods.

UM-FDTD (Co-Volume Method)

Although FE methods can employ polynomials of higher orders and are not restricted to a structured mesh, the algorithms themselves are much more complicated to implement and computationally expensive compared to FDTD schemes. A possible solution would be the use of hybrid solution techniques. In this case an unstructured finite element or finite volume method is combined with a structured FDTD method [59, 36]. This allows one to model the scatterer accurately with tetrahedra for example whereas the rest of the domain is filled with hexahedra, significantly reducing the computational costs. However special care has to be taken at the transition between the higher order FE and FD regions because non-physical diffraction effects may occur due to linear approximation of curved boundaries [115]. Although the hybrid method is more efficient than the standard FEM it complicates the algorithm even more. The main advantages of the FDTD method with respect to FEM are as mentioned above, the simplicity of the discretisation procedure, the low memory requirements, the explicit nature of the scheme... but the method is typically limited to a structured mesh. This leads to a loss of accuracy due to staircasing. A finer mesh is necessary to improve the accuracy, but the CFL condition requires a reduction of the time step and an increase in the computational costs. To improve the accuracy of the scheme in the case of curved interfaces non-uniform and unstructured mesh implementations have been suggested like the generalised Yee algorithm [51] or the Yee-like algorithm [20]. Unfortunately these methods are not as efficient as the original scheme [87]. Xie used another approach to generalise the Yee algorithm to unstructured meshes by employing a primal unstructured Delaunay mesh and its orthogonal Voronoi dual graph [144]. This method was initially limited to perfect electric conductors but in this work I was able to extend the method to isotropic, anisotropic, frequency dependent and chiral dielectrics [48, 49]. This allows me to model composites and metamaterials. I refer to this method as “UM-FDTD”, where UM stands for unstructured mesh. UM-FDTD preserves the advantages of the FDTD algorithm by significantly increasing the spatial and temporal step by using unstructured meshes to match a curved boundary. My results demonstrate that a 6 – 8 times coarser meshes can be employed leading to important savings with respect to memory and time. UM-FDTD is a generalisation of the classical Yee algorithm to unstructured meshes. Hence it simplifies to the classical method on a structured mesh. Thus it can naturally handle hybrid meshes without requiring any kind of interpolations between the structured and unstructured mesh and therefore no non-physical diffraction effects occur at different mesh interfaces. As edge and face based method it is not even limited to specific mesh elements like a hexahedron or tetrahedron. It can handle any kind of polyhedra. With the development of the UM-FDTD the advantages of an unstructured mesh method could be united with the simplicity and most of the other advantages of the FDTD method. Especially for 3D isotropic materials the simplicity of the implementation of UM-FDTD corresponds to a the implementation of a 1D FDTD scheme. For anisotropic materials it is however slightly more complicated as I will show later in this chapter.

Commercial Software

According to Cheng [29], after a keyword search in the Science Citation Index Expanded, the total number of journal publications of the three most common numerical methods in 2004 leads to about 60'000 results for the FEM, 19'000 for FDM and about 10'000 for BEM making it the third most used technique. These three methods therefore form the basis of most of the commercially available software tool in engineering ([25]). The softwares are first categorised in partial differential equations or integral technique solvers. For the first case, a volume mesh is needed whereas integral solvers require a surface mesh. A further classification can be done by regrouping the software as frequency or time domain methods. In the frequency domain, the FE method is typically used because it allows the use non-uniform meshes and can model complicated geometries. I however will only consider commercial software codes based upon the FDTD method. As mentioned before this techniques also allows the modelling of complex and inhomogenous structures, but doesn't create a larges set of linear equations and therefore doesn't require matrix solvers. The most popular FDTD commercial codes are probably CST Studio from CST, XFDTD from Remcom and Lumerical. For a more general overview, please refer to the paper by Su et al. [25]. These softwares are also able to model metamaterials demonstrating the importance of accurate modelling techniques of these materials for industrial applications. To improve the efficiency, conformal meshes are used, which account for subcell features, to reduce the stairstepping effect [149, 122, 38]. However the accuracy and stability can still not compete with those obtained by unstructured meshes. To our knowledge no FDTD method generalised to unstructured meshes is so far used in commercial software, which is one of the reasons for the development of UM-FDTD.

3.2. Pure scattered field formulation

The total and scattered field formulation allows me to generate an incident wave which appears to simulation as if the plane wave source is external to the simulation space e.g as if a wave has been generated at a great distance away. To establish this formalism I use the linearity of Maxwell's equation stating: If the fields \mathbf{E}_1 and \mathbf{E}_2 separately satisfy Maxwell's equations than $\mathbf{E}_{12} = \mathbf{E}_1 + \mathbf{E}_2$ also satisfies Maxwell's equations. This allows me to split the total electric field into an incident and scattered part, $\mathbf{E}_{tot} = \mathbf{E}_{inc} + \mathbf{E}_{scat}$. The analytically specified incident field corresponds to the field present in a region in the absence of any objects (dielectric or conductor). The incident field thus fulfills Maxwell's equations of free space.

$$\nabla \times \mathbf{E}_{inc} = -\mu_0 \frac{\partial \mathbf{H}_{inc}}{\partial t} \quad (3.1)$$

$$\nabla \times \mathbf{H}_{inc} = \varepsilon_0 \frac{\partial \mathbf{E}_{inc}}{\partial t} \quad (3.2)$$

The presence of a scatterer and the electromagnetic boundary conditions lead to the formation of the scattered field as the incident field interacts with the object. This

3.3. Classical 3D Yee algorithm

field must satisfy Maxwell's equation inside the scatterer with the medium parameters ε , μ , σ , σ_m as well as Maxwell's equations for free space outside the scatterer. The total field corresponds to the superposition of the incident and scattered field and has to obey within the scatterer the following equation

$$\nabla \times \mathbf{E}_{tot} = -\mu \frac{\partial \mathbf{H}_{tot}}{\partial t} - \sigma_m \mathbf{H}_{tot} \quad (3.3)$$

$$\nabla \times \mathbf{H}_{tot} = \varepsilon \frac{\partial \mathbf{E}_{tot}}{\partial t} + \sigma \mathbf{E}_{tot} \quad (3.4)$$

with $\varepsilon \neq \varepsilon_0$ and $\mu \neq \mu_0$. Using $\mathbf{E}_{tot} = \mathbf{E}_{inc} + \mathbf{E}_{scat}$ and $\mathbf{H}_{tot} = \mathbf{H}_{inc} + \mathbf{H}_{scat}$ I rewrite equation (3.3) and equation (3.4)

$$\nabla \times (\mathbf{E}_{inc} + \mathbf{E}_{scat}) = -\mu \frac{\partial (\mathbf{H}_{inc} + \mathbf{H}_{scat})}{\partial t} - \sigma_m (\mathbf{H}_{inc} + \mathbf{H}_{scat}) \quad (3.5)$$

$$\nabla \times (\mathbf{H}_{inc} + \mathbf{H}_{scat}) = \varepsilon \frac{\partial (\mathbf{E}_{inc} + \mathbf{E}_{scat})}{\partial t} + \sigma (\mathbf{E}_{inc} + \mathbf{E}_{scat}) \quad (3.6)$$

Subtracting equation (3.1) from equation (3.5) and equation (3.4) from equation (3.6) leads to

$$\nabla \times \mathbf{E}_{scat} = -\mu \frac{\partial \mathbf{H}_{scat}}{\partial t} - \sigma_m \mathbf{H}_{scat} - \left[(\mu - \mu_0) \frac{\partial \mathbf{H}_{inc}}{\partial t} + \sigma_m \mathbf{H}_{inc} \right] \quad (3.7)$$

$$\nabla \times \mathbf{H}_{scat} = \varepsilon \frac{\partial \mathbf{E}_{scat}}{\partial t} + \sigma \mathbf{E}_{scat} + \left[(\varepsilon - \varepsilon_0) \frac{\partial \mathbf{E}_{inc}}{\partial t} + \sigma \mathbf{E}_{inc} \right] \quad (3.8)$$

Rewriting equation (3.7) and equation (3.8) with the time derivatives on the left hand side leads to

$$\frac{\partial \mathbf{H}_{scat}}{\partial t} = -\frac{1}{\mu} \nabla \times \mathbf{E}_{scat} - \frac{\sigma_m}{\mu} \mathbf{H}_{scat} - \frac{\sigma_m}{\mu} \mathbf{H}_{inc} - \frac{\mu - \mu_0}{\mu} \frac{\partial \mathbf{H}_{inc}}{\partial t} \quad (3.9)$$

$$\frac{\partial \mathbf{E}_{scat}}{\partial t} = \frac{1}{\varepsilon} \nabla \times \mathbf{H}_{scat} - \frac{\sigma}{\varepsilon} \mathbf{E}_{scat} - \frac{\sigma}{\varepsilon} \mathbf{E}_{inc} - \frac{\varepsilon - \varepsilon_0}{\varepsilon} \frac{\partial \mathbf{E}_{inc}}{\partial t} \quad (3.10)$$

In the scattered field formulation the incident field is an analytically defined function. Therefore the only unknown is the scattered field.

3.3. Classical 3D Yee algorithm

For completeness and to illustrate the differences between the classical Yee algorithm and our Co-Volume scheme I derive the discretised update equations for a lossless dielectric.

3. Numerical Solution of Maxwell Equations

Starting with Faraday's law equation (2.2) and writing it in components

$$\frac{\partial H_x}{\partial t} = \frac{1}{\mu} \left(\frac{\partial E_z}{\partial y} - \frac{\partial E_y}{\partial z} \right) \quad (3.11)$$

$$\frac{\partial H_y}{\partial t} = \frac{1}{\mu} \left(\frac{\partial E_x}{\partial z} - \frac{\partial E_z}{\partial x} \right) \quad (3.12)$$

$$\frac{\partial H_z}{\partial t} = \frac{1}{\mu} \left(\frac{\partial E_y}{\partial x} - \frac{\partial E_x}{\partial y} \right) \quad (3.13)$$

similarly for Ampere's law equation (2.1) becomes

$$\frac{\partial E_x}{\partial t} = \frac{1}{\varepsilon} \left(\frac{\partial H_z}{\partial y} - \frac{\partial H_y}{\partial z} \right) \quad (3.14)$$

$$\frac{\partial E_y}{\partial t} = \frac{1}{\varepsilon} \left(\frac{\partial H_x}{\partial z} - \frac{\partial H_z}{\partial x} \right) \quad (3.15)$$

$$\frac{\partial E_z}{\partial t} = \frac{1}{\varepsilon} \left(\frac{\partial H_y}{\partial x} - \frac{\partial H_x}{\partial y} \right) \quad (3.16)$$

The electric field is updated at integer time steps n and the magnetic field at half integer time steps $n + \frac{1}{2}$. The electric field component E_a for $a = x, y, z$ is at half-integer steps for the a -location and integer for the other two components. For the magnetic field components it is the opposite. H_a for $a = x, y, z$ is at integer steps for the a -location and half-integer for the other two components.

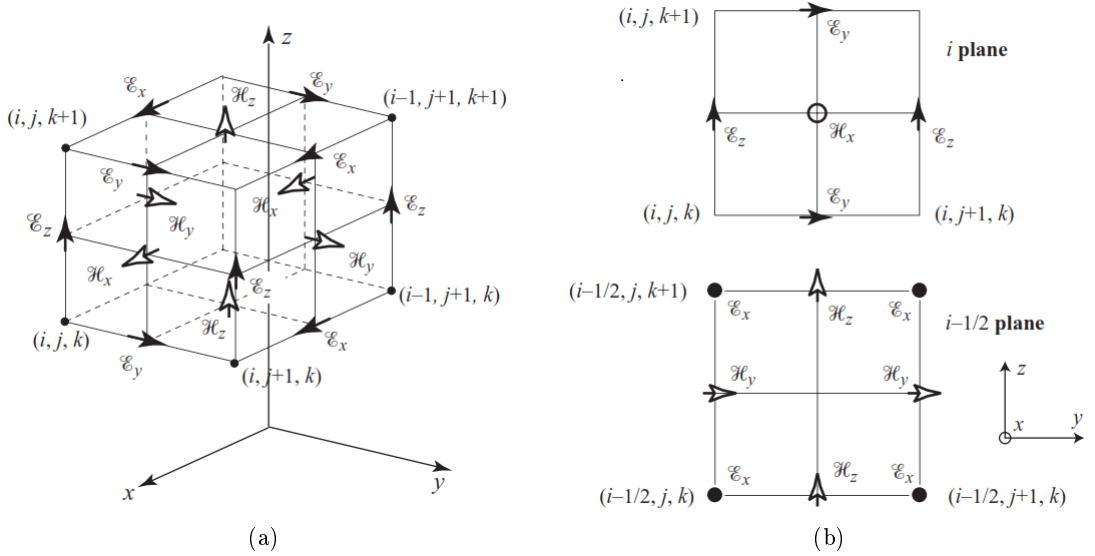


Figure 3.1.: (a) 3D Yee cell for a rectangular grid. ; (b) slices of the Yee cell at positions i and $i - \frac{1}{2}$. [118]

Applying the finite difference approximation for time and space as indicated as example

3.3. Classical 3D Yee algorithm

in equations (3.17) and (3.18)

$$\left. \frac{\partial E_z}{\partial t} \right|^{n+1/2} \simeq \frac{E_z^{n+1} - E_z^n}{\Delta t} \quad (3.17)$$

$$\frac{\partial E_y}{\partial z} \Big|^n \simeq \frac{E_y|_{i,j+\frac{1}{2},k+1}^n - E_y|_{i,j+\frac{1}{2},k}^n}{\Delta z} \quad (3.18)$$

to equations (3.11)-(3.16) leads after rearranging to the interleaved leap frog algorithm update equations

$$E_x|_{i+\frac{1}{2},j,k}^{n+1} = E_x|_{i+\frac{1}{2},j,k}^n + \frac{\Delta t}{\varepsilon_{i+\frac{1}{2},j,k}} \left[\frac{H_z|_{i+\frac{1}{2},j+\frac{1}{2},k}^{n+\frac{1}{2}} - H_z|_{i+\frac{1}{2},j-\frac{1}{2},k}^{n+\frac{1}{2}}}{\Delta y} - \frac{H_y|_{i+\frac{1}{2},j,k+\frac{1}{2}}^{n+\frac{1}{2}} - H_y|_{i+\frac{1}{2},j,k-\frac{1}{2}}^{n+\frac{1}{2}}}{\Delta z} \right] \quad (3.19)$$

$$E_y|_{i,j+\frac{1}{2},k}^{n+1} = E_y|_{i,j+\frac{1}{2},k}^n + \frac{\Delta t}{\varepsilon_{i,j+\frac{1}{2},k}} \left[\frac{H_x|_{i,j+\frac{1}{2},k+\frac{1}{2}}^{n+\frac{1}{2}} - H_x|_{i,j+\frac{1}{2},k-\frac{1}{2}}^{n+\frac{1}{2}}}{\Delta z} - \frac{H_z|_{i+\frac{1}{2},j+\frac{1}{2},k}^{n+\frac{1}{2}} - H_z|_{i-\frac{1}{2},j+\frac{1}{2},k}^{n+\frac{1}{2}}}{\Delta x} \right] \quad (3.20)$$

$$E_z|_{i,j,k+\frac{1}{2}}^{n+1} = E_z|_{i,j,k+\frac{1}{2}}^n + \frac{\Delta t}{\varepsilon_{i,j,k+\frac{1}{2}}} \left[\frac{H_y|_{i+\frac{1}{2},j,k+\frac{1}{2}}^{n+\frac{1}{2}} - H_y|_{i-\frac{1}{2},j,k+\frac{1}{2}}^{n+\frac{1}{2}}}{\Delta x} - \frac{H_x|_{i,j+\frac{1}{2},k+\frac{1}{2}}^{n+\frac{1}{2}} - H_x|_{i,j-\frac{1}{2},k+\frac{1}{2}}^{n+\frac{1}{2}}}{\Delta y} \right] \quad (3.21)$$

3. Numerical Solution of Maxwell Equations

$$H_x \Big|_{i,j+\frac{1}{2},k+\frac{1}{2}}^{n+\frac{1}{2}} = H_x \Big|_{i,j+\frac{1}{2},k+\frac{1}{2}}^{n-\frac{1}{2}} + \frac{\Delta t}{\mu_{i,j+\frac{1}{2},k+\frac{1}{2}}} \left[\frac{E_y \Big|_{i,j+\frac{1}{2},k+1}^n - E_y \Big|_{i,j+\frac{1}{2},k}^n}{\Delta z} - \frac{E_z \Big|_{i,j+1,k+\frac{1}{2}}^n - E_z \Big|_{i,j,k+\frac{1}{2}}^n}{\Delta y} \right] \quad (3.22)$$

$$H_y \Big|_{i+\frac{1}{2},j,k+\frac{1}{2}}^{n+\frac{1}{2}} = H_y \Big|_{i+\frac{1}{2},j,k+\frac{1}{2}}^{n-\frac{1}{2}} + \frac{\Delta t}{\mu_{i+\frac{1}{2},j,k+\frac{1}{2}}} \left[\frac{E_z \Big|_{i+1,j,k+\frac{1}{2}}^n - E_z \Big|_{i,j,k+\frac{1}{2}}^n}{\Delta x} - \frac{E_x \Big|_{i+\frac{1}{2},j,k+1}^n - E_x \Big|_{i+\frac{1}{2},j,k}^n}{\Delta z} \right] \quad (3.23)$$

$$H_z \Big|_{i+\frac{1}{2},j+\frac{1}{2},k}^{n+\frac{1}{2}} = H_z \Big|_{i+\frac{1}{2},j+\frac{1}{2},k}^{n-\frac{1}{2}} + \frac{\Delta t}{\mu_{i+\frac{1}{2},j,k+\frac{1}{2}}} \left[\frac{E_x \Big|_{i+\frac{1}{2},j+1,k}^n - E_x \Big|_{i+\frac{1}{2},j,k}^n}{\Delta y} - \frac{E_y \Big|_{i+1,j+\frac{1}{2},k}^n - E_y \Big|_{i,j+\frac{1}{2},k}^n}{\Delta x} \right] \quad (3.24)$$

Keep in mind that the electric field is updated at integer time steps $n \rightarrow n+1$ and spatial steps $i \rightarrow i+1$ and the magnetic field at half integer time steps $n - \frac{1}{2} \rightarrow n + \frac{1}{2}$ and spatial steps $i - \frac{1}{2} \rightarrow i + \frac{1}{2}$. The time step only changes when a derivative with respect to time is applied. In that case $n \rightarrow n+1$, the spatial grid points stay the same $i + \frac{1}{2} \rightarrow i + \frac{1}{2}$. Approximating a spatial derivative has no effect on the time step $n + \frac{1}{2} \rightarrow n + \frac{1}{2}$. Taking the derivative with respect to j for example, means, only the variation of the magnetic field in j direction is considered and therefore only j will change during the discretisation process $j - \frac{1}{2} \rightarrow j + \frac{1}{2}$. After discretising the derivatives with respect to space and time I rearrange the terms with respect to the electric or magnetic field components.

3.4. Modelling of isotropic dielectrics using the co-volume method

3.4.1. Problem formulation

The formulation employs the integral form of Maxwell's equations [144]. For a three dimensional lossy dielectric medium, Ampère's and Faraday's Laws are expressed, in scattered field formulation, as:

$$\int_A \varepsilon \frac{\partial}{\partial t} \mathbf{E}_{scat} d\mathbf{A} = \oint_{\partial A} \mathbf{H}_{scat} d\mathbf{l} - \frac{\partial}{\partial t} \int_A (\varepsilon - \varepsilon_0) \mathbf{E}_{inc} d\mathbf{A} - \int_A \sigma \mathbf{E}_{inc} d\mathbf{A} - \int_A \sigma \mathbf{E}_{scat} d\mathbf{A} \quad (3.25)$$

and

3.4. Modelling of isotropic dielectrics using the co-volume method

$$\int_A \mu \frac{\partial}{\partial t} \mathbf{H}_{scat} d\mathbf{A} = - \oint_{\partial A} \mathbf{E}_{scat} d\mathbf{l} - \frac{\partial}{\partial t} \int_A (\mu - \mu_0) \mathbf{H}_{inc} d\mathbf{A} \quad (3.26)$$

$$- \int_A \sigma_m \mathbf{H}_{inc} d\mathbf{A} - \int_A \sigma_m \mathbf{H}_{scat} d\mathbf{A}$$

The total fields are formed as the sum of the corresponding incident and scattered fields. To model a perfect electric conductor, the first term on the right side of equations (3.25,3.26) is sufficient. For modelling a non-lossy dielectric material the first two terms have to be considered and for a lossy dielectric material every term on the right side needs to be taken into account. In addition \mathbf{E}_{inc} , \mathbf{H}_{inc} and \mathbf{E}_{scat} , \mathbf{H}_{scat} represent respectively the incident electric and magnetic fields and scattered electric and magnetic fields. The incident field is assumed to be a plane wave illumination from the far field, which has the form $\mathbf{E}_{inc} = \mathbf{E}_0 \cos(\omega t - \mathbf{k} \cdot \mathbf{r})$, where \mathbf{E}_0 is the electric field vector, \mathbf{k} is the wave vector, \mathbf{r} is the position vector. From the known incident electric field, the incident magnetic field may be determined, using Faraday's Law, as

$$\mathbf{H}_{inc} = \frac{1}{\eta_0} \hat{\mathbf{k}} \times \mathbf{E}_{inc} \quad (3.27)$$

where $\hat{\mathbf{k}}$ is the unit wave vector and $\eta_0 = \sqrt{\mu_0/\varepsilon_0}$ is the impedance of free space.

3.4.2. Discrete equations

The Yee algorithm is a low operation count method for the solution of Ampère's Law and Faraday's Law. The algorithm is implemented on two mutually orthogonal meshes. For the present implementation, a primal tetrahedral mesh is generated using a Delaunay method [139]. The Voronoi diagram associated with this primal mesh is used to define a dual mesh. Each Voronoi face is a perpendicular bisector of the corresponding Delaunay edge and each Delaunay face is perpendicular to the corresponding Voronoi edge. It is assumed that the Delaunay mesh has N_e^D edges and that the Voronoi mesh has N_e^V edges. Thus each Delaunay edge has a perpendicular closed loop of Voronoi edges and similarly each Voronoi edge is surrounded by a closed loop of Delaunay edges. For the leapfrog scheme to be second order accurate, the unknowns are located at the midpoints of these edges. The unknown at the centre of the i^{th} Delaunay edge corresponds to the projection, $E_{scat,i}$, of the scattered electric field onto the direction of the edge. The unknown at the centre of the j^{th} Voronoi edge corresponds to the projection, $H_{scat,j}$, of the scattered magnetic field onto the direction of the edge.

Applying the central difference approximations to the fields according to the following

3. Numerical Solution of Maxwell Equations

equations

$$\int_A \varepsilon \frac{\partial}{\partial t} \mathbf{E}_{scat} d\mathbf{A} = \frac{\varepsilon (\mathbf{E}^{n+1} - \mathbf{E}^n) A^V}{\Delta t} + O[(\Delta t)^2] \quad (3.28)$$

$$\oint_{\partial A} \mathbf{E}_{scat} d\mathbf{l} \approx \sum_{k=1}^{M_j^D} E_{scat,i,j,k}^n l_{i,j,k}^D \quad (3.29)$$

$$\int_A \sigma \mathbf{E}_{scat} d\mathbf{A} \approx \sigma \mathbf{E}^{n+1/2} A^V = \frac{\sigma (\mathbf{E}^{n+1} + \mathbf{E}^n) A^V}{2} \quad (3.30)$$

$$\int_A \mu \frac{\partial}{\partial t} \mathbf{H}_{scat} d\mathbf{A} = \frac{\mu (\mathbf{H}^{n+1/2} - \mathbf{H}^{n-1/2}) A^D}{\Delta t} + O[(\Delta t)^2] \quad (3.31)$$

$$\oint_{\partial A} \mathbf{H}_{scat} d\mathbf{l} \approx \sum_{k=1}^{M_i^V} H_{scat,j,i,k}^{n+1/2} l_{j,i,k}^V \quad (3.32)$$

$$\int_A \sigma_m \mathbf{H}_{scat} d\mathbf{A} \approx \sigma_m \mathbf{H}^n A^D = \frac{\sigma (\mathbf{H}^{n+1/2} + \mathbf{H}^{n-1/2}) A^D}{2} \quad (3.33)$$

and applying them to Ampère's Law and Faraday's law leads to

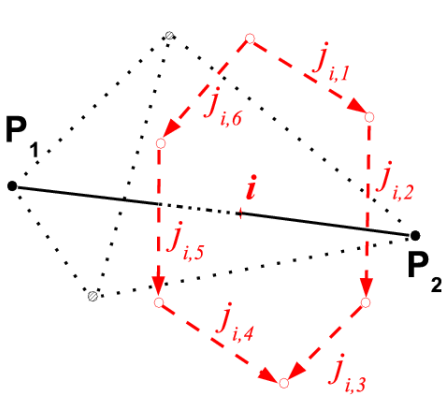
$$E_{scat,i}^{n+1} = \left(\frac{2\varepsilon - \sigma \Delta t}{2\varepsilon + \sigma \Delta t} \right) E_{scat,i}^n + \left(\frac{2\Delta t}{(2\varepsilon + \sigma \Delta t) A_i^V} \right) \left[\sum_{k=1}^{M_i^V} H_{scat,j,i,k}^{n+1/2} l_{j,i,k}^V - \sigma A_i^V E_{inc,i}^{n+1/2} - (\varepsilon - \varepsilon_0) A_i^V \frac{\partial}{\partial t} E_{inc,i}^{n+1/2} \right] \quad (3.34)$$

and

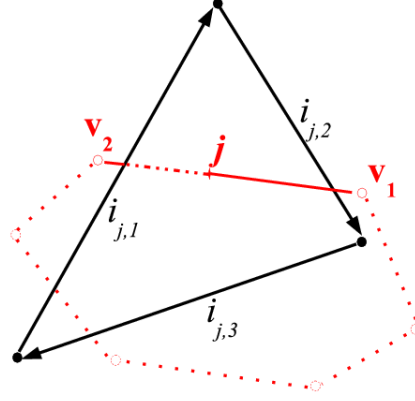
$$H_{scat,j}^{n+1/2} = \left(\frac{2\mu - \sigma_m \Delta t}{2\mu + \sigma_m \Delta t} \right) H_{scat,j}^{n-1/2} + \left(\frac{2\Delta t}{(2\mu + \sigma_m \Delta t) A_j^D} \right) \left[\sum_{k=1}^{M_j^D} E_{scat,i,j,k}^n l_{i,j,k}^D - \sigma_m A_j^D H_{inc,j}^n - (\mu - \mu_0) A_j^D \frac{\partial}{\partial t} H_{inc,j}^n \right] \quad (3.35)$$

where Δt denotes the time step, the superscript n denotes an evaluation at time level $t = n\Delta t$, l_i^D represents the length of the i^{th} Delaunay edge and A_i^V corresponds to the area of the Voronoi face spanned by the Voronoi edges surrounding Delaunay edge i . Similarly, l_j^V represents the length of the j^{th} Voronoi edge and A_j^D corresponds to the area of the Delaunay face spanned by the Delaunay edges surrounding Voronoi edge j . The numbers $j_{i,k}$, $k = 1, \dots, M_i^V$ refer to the M_i^V edges of the Voronoi face corresponding

to the i^{th} Delaunay edge, as illustrated in Figure 3.2a. Similarly, the numbers $i_{j,k}$, $k = 1, \dots, M_j^D$ refer to the M_j^D edges of the Delaunay face corresponding to the j^{th} Voronoi edge, as illustrated in Figure 3.2b.



(a) The i^{th} Delaunay edge, connecting Delaunay vertices p_1 and p_2 , and the corresponding Voronoi face, formed by the Voronoi edges $j_{i,1}, \dots, j_{i,6}$



(b) The j^{th} Voronoi edge, connecting Voronoi vertices v_1 and v_2 , and the corresponding Delaunay face, formed by the Delaunay edges $i_{j,1}, i_{j,2}, i_{j,3}$

Figure 3.2.: (a) Delaunay Edge and Voronoi face. ; (b) Voronoi Edge and Delaunay face.

These staggered equations are used to advance the solution in a leapfrog manner; with the magnetic field updated over the dual graph at the half time step, using equation (3.35), and the electric field updated over the primal graph at the full time step, using equation (3.34). At the interface boundaries, the material parameters in the equation are not constant over the area of integration, therefore the values of ϵ , μ , σ and σ_m are averaged at a dielectric interface, leading to the values ϵ_{av} , μ_{av} , σ_{av} and σ_{mav} . The evaluation of these averaged values is detailed in section 3.5.1.

3.5. Mesh generation

The main difference between our Co-Volume approach and the standard Yee algorithm is the generalisation of the method to unstructured meshes. Before investigating the requirements and challenges linked to the 3D unstructured mesh generation it is easier to first consider an example in 2D illustrating the principle and relation between the Voronoi and Delaunay mesh (Figure 3.3a). Firstly the space is filled with triangles forming the Delaunay mesh. Next, the circumcircle, a circle connecting the 3 corners of a triangle is drawn and the position of the circumcenter for each triangle is retained. If two circumcenters from neighbouring triangles are connected, they form a Voronoi edge. By construction, the Voronoi edge is the bisector of the Delaunay edge. This means a Voronoi edge is perpendicular to a Delaunay edge and it intersects it in the middle.

3. Numerical Solution of Maxwell Equations

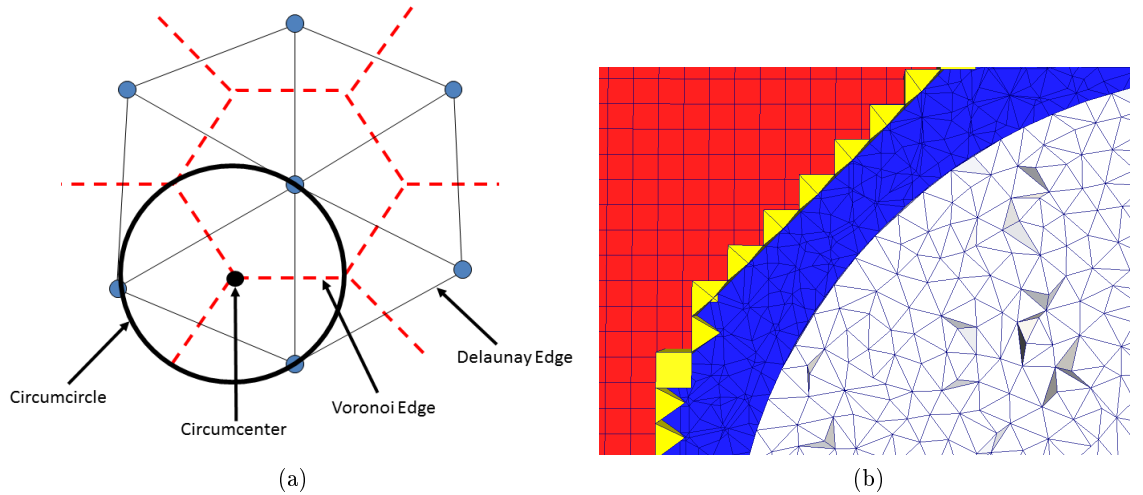


Figure 3.3.: (a) *Delaunay and Voronoi mesh in 2D.* ; (b) *Cut through hybrid mesh used to model sphere object. The displayed mesh consists of tetrahedra inside the sphere (white) and it's vicinity with few layers (blue). One layer of pyramids (yellow) links the tetrahedra to the hexahedra (red).*

This was only a very brief and simplified explanation about the relation of the primal Delaunay and its dual Voronoi mesh. In reality numerous challenges had to be overcome especially in $3D$. Not only employ an unstructured but a hybrid mesh is employed to represent the computational domain. Most of the free space region is filled with hexahedral elements. This is efficient in terms of managing the number of degrees of freedom required and enables a standard PML boundary condition to be implemented at the outer surface of the domain. Tetrahedral elements are used near to, and inside, scattering bodies. The tetrahedral and hexahedral elements are connected using pyramidal elements, which means that hanging edges may be avoided, as shown in Figure 3.3b. Mixed meshes of this type are readily generated using the cut cell technique detailed in [144]. Of importance here are the methods applied to ensure the quality of the elements in the unstructured tetrahedral mesh. Traditional automatic unstructured mesh generation methods, such as the advancing front technique [102] and the Delaunay triangulation [139], or their combination [47], do not guarantee the regularity of the edge lengths of the dual mesh and the absence of bad elements, e.g. for an acceptable Delaunay mesh, the corresponding Voronoi diagram is often highly irregular and can include some very short Voronoi edges. Methods based on improving mesh quality by swapping, reconnection and smoothing [127] cannot be used to guarantee suitable meshes [112]. To circumvent this problem, the approach adopted is to construct the unstructured mesh by employing a CVT \sim (central Voronoi tessellation) [42], with information provided from an ideal mesh. The CVT is a Voronoi tessellation whose generating points are the centroids of the corresponding Voronoi regions. All Voronoi and Delaunay edge lengths are required to be bounded from below, as the update equations will cease to be valid if some edges have zero length. For the classical Yee algorithm, on uniform Cartesian meshes, the stability

criterion is generally expressed as $c\Delta t \leq l/\sqrt{D}$, where $c = 1/\sqrt{\varepsilon\mu}$ is the speed of wave propagation in the medium l is the edge length in the mesh and D is the dimension of the simulation [126]. In contrast to finite element methods taking conductivities into account has no effect on the stability condition because only the amplitude changes but not the velocity. This will be demonstrated later in section 4.2.3. Extra care has to be taken for anisotropic materials because the speed of light differs in each direction. Therefore I choose the direction leading to the smallest time step. For heterogenous materials again the material parameters leading to the smallest time step are used. In the case of chiral materials the index of refraction is written as $n = \sqrt{\varepsilon\mu - \kappa^2}$ with κ the chirality. The chirality only has a small downsize effect on the time step. Nevertheless it seems that the chirality leads to the instabilities that are not linked to the time step. This phenomenon is investigated in subsections 4.4.3 and 4.4.4. For unstructured meshes, experience shows that $c\Delta t \leq S_f \min_{i,j}\{l_i^V, l_j^D\}$ is a practical stability criterion. In this expression, c is again the speed of wave propagation through the medium, Δt is the time step and l_i^V, l_j^D are the lengths of the Voronoi and Delaunay edges respectively. Here, S_f is a safety factor, that typically has a value roughly between 0.8 – 2 [144]. This value can be linked to the edge length depending on the type of element. An equilateral tetrahedron with edge length l has a height of $(\sqrt{6}/3)l = 0.81l$. An equilateral pyramid with edge length l has a height of $l/\sqrt{2}$ for hexahedra, l for hexahedra. Setting $l = 1$ leads to the corresponding Safety factors. I typically used a safety factor of 0.8. The smallest Voronoi or Delaunay edge length in the mesh is obtained through the use of the expression $\min_{i,j}\{l_i^V, l_j^D\}$. If two or more adjacent tetrahedral elements share the same circumsphere, the primal Delaunay mesh may be degenerate. In this case, the Voronoi edge connecting the circumcentres of neighbouring cells is of zero length. This difficulty is removed by merging these elements, as illustrated in Figure 3.4.

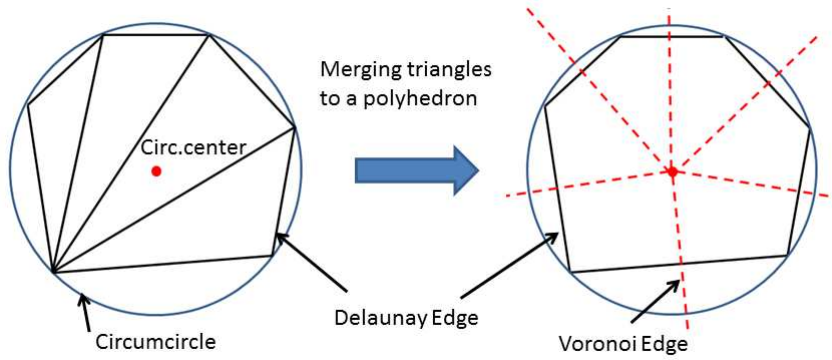


Figure 3.4.: An illustration, in 2D, of the merging process for cells sharing the same circumcentre.

It is also possible that elements with very small Voronoi edges will be created during the mesh generation process, which would influence the magnitude of the allowable time step. To avoid this difficulty, corresponding cells are merged if the distance between their

3. Numerical Solution of Maxwell Equations

circumcentres is below 10 % of the initial uniform element size of the Delaunay mesh, that is related to the characteristic wavelength. An additional requirement is that the centre of the circumsphere should lie inside each Delaunay tetrahedron. If this criterion is not met, a given Voronoi edge will not intersect with the corresponding Delaunay face and the approximation of the integral $\int_{\partial A} \mathbf{H} d\mathbf{l}$ cannot even guarantee first order accuracy. To avoid this problem, the requirement that a dual edge must be a bisector of the corresponding Delaunay face is relaxed, as illustrated for the 2D case in Figure 3.5. To get the bisectors of a triangle I consider three circles with the same radius r . Each circle is centred at one of the vertices A, B, C of the triangle. The radius has to be larger than half the length of the longest side of the triangle, i.e. $r > \text{distance}(A, B)/2$. To obtain the bisector of the edge AB , I connect the intersection points of the circles centred at A and B . This procedure is repeated for the other edges. The intersection point of the bisectors, the dashed line, is by definition the circumcentre $O1$ of the triangle. In the illustrated case, $O1$ is situated outside the triangle, leading to a bad element. The weighted Voronoi power diagram [138] leads to a shift in the location of the circumcentre of the element ABC , from position $O1$ to position $O2$ by changing the radius from $R2$ to $\overline{R2}$. The dotted-dashed lines intersecting at point $O2$ are no longer bisectors, as they do not cut each side of the element into equal segment, but they remain perpendicular to the respective edges.

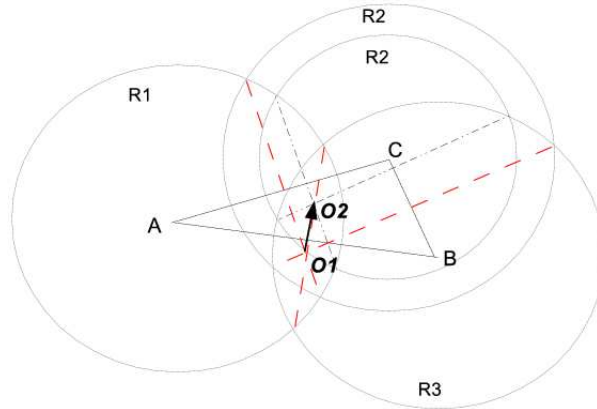


Figure 3.5.: *shifting the circumcenter from the outside to the inside of a triangle*

The relaxation of the bisection requirement allows us to generate unstructured meshes that meet the requirements of the leapfrog scheme. Additional requirements are that all Delaunay and Voronoi edges should be bounded above by a number that is not significantly greater than δ , which represents the side length of the cubes forming the Cartesian mesh; any deviation in the location of the midpoint of a Voronoi edge from the actual point of intersection with the corresponding Delaunay face should be minimised; any deviation in the location of the circumcentre of a tetrahedron from its centroid should also be minimised. The two most important requirements for securing a stable implementation of the leapfrog scheme are that all Voronoi and Delaunay edge lengths are

bounded from below and the centre of the circumsphere should lie inside each Delaunay tetrahedron. In practice, the other requirements have usually to be relaxed for complex three-dimensional geometries.

3.5.1. Boundary conditions

PEC boundary conditions

In a scattered field formulation, the condition

$$\mathbf{n} \times \mathbf{E}_{scat} = -\mathbf{n} \times \mathbf{E}_{inc} \quad (3.36)$$

is applied at the surface of a perfect electric conductor (PEC). Here, \mathbf{n} is the unit outward normal vector to the PEC surface. Without changing equations (3.45) and (3.46), I can strongly impose the electric field unknowns, at the set of edges forming the PEC interface, to satisfy the condition of equation (3.36). Within this leapfrog scheme, it is possible to model thin resistive or PEC sheets, by assigning the sheet conductivity only to the Delaunay edges forming the interface.

Far field boundary conditions

In scattering problems, the incident wave is assumed to be generated by a source located in the far field and the physical solution domain is infinite in extent. Nevertheless, the numerical simulation of the scattering problem is undertaken on a finite computational domain. For example, the computational domain employed for the problem of simulating scattering by an anisotropic dielectric sphere, located in free space, is illustrated in Figure 3.6. The infinite real physical domain has been truncated and, at the truncated outer computational boundary, the scattered field should consist of outgoing waves only. The modelling of this requirement is achieved by adding a wave damping perfectly matched layer (PML) [16] to the truncated exterior far-field boundary. In earlier work Morgan et al. [92], and El Hachemi et al. [44], have shown that it is convenient to represent the PML region with an assembly of regular hexahedral computational cells.

Dielectric interface boundary conditions

I present an easy but powerful averaging method for Dielectric and perfect electric conducting (PEC) interfaces suited for unstructured meshes. Usually in a scattered-field formulation PEC boundaries must be driven with the negative of the instantaneous incident field, in order to cancel out the field to zero. In the standard Yee algorithm based on a structured mesh, the three most common averaging techniques for material parameters at an interface between two dielectric of generic parameters a_1 and a_2 are:

$$\text{Arithmetic mean average} \quad : \quad a_{av} = (a_1 + a_2)/2 \quad (3.37)$$

$$\text{Harmonic mean average} \quad : \quad a_{av} = (2a_1a_2)/(a_1 + a_2) \quad (3.38)$$

$$\text{Geometric mean average} \quad : \quad a_{av} = \sqrt{a_1a_2} \quad (3.39)$$

3. Numerical Solution of Maxwell Equations

It has been reported in [65] that the geometric and harmonic means provide better accuracy for cell sizes in the range of $\lambda_0/10$ to $\lambda_0/20$, where λ_0 is the free-space wavelength, but both show lower convergence with smaller cell size. Meanwhile the arithmetic mean retains the second order convergence regardless of the grid resolution. Therefore I decided to use the arithmetic mean average and adapted it to unstructured meshes which do not necessarily have uniform cells. I will demonstrate shortly that our weighted averaging on an unstructured mesh corresponds to the arithmetic mean on a structured mesh.

Our averaging method does not require any change in equations (3.34) and (3.35). To illustrate the method consider a 3D isotropic dielectric object, e.g. a sphere, in free space, as represented in Figure 3.6. The material properties, ϵ and σ , associated to the electric field, are stored on the Delaunay edges and μ and σ_m associated to the magnetic field are stored on the Voronoi edges.

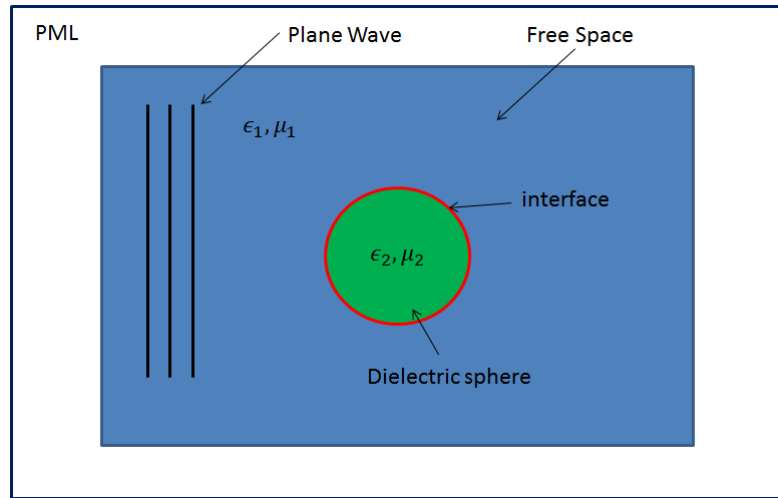


Figure 3.6.: *Simulation of scattering by a 3D dielectric sphere in free space.*

In Figure 3.7a and 3.7b I use the same colours as in Figure 3.6. Blue edges correspond to Delaunay edges in free space, green edges correspond to Delaunay edges inside the dielectric and red Delaunay edges form the interface between dielectric and free space. As can be seen in Figure 3.7a, which corresponds to Figure 3.2a, some of the Voronoi edges (black) surrounding a given Delaunay edge at the interface are in free space, whereas others are inside the dielectric or even intersect the interface

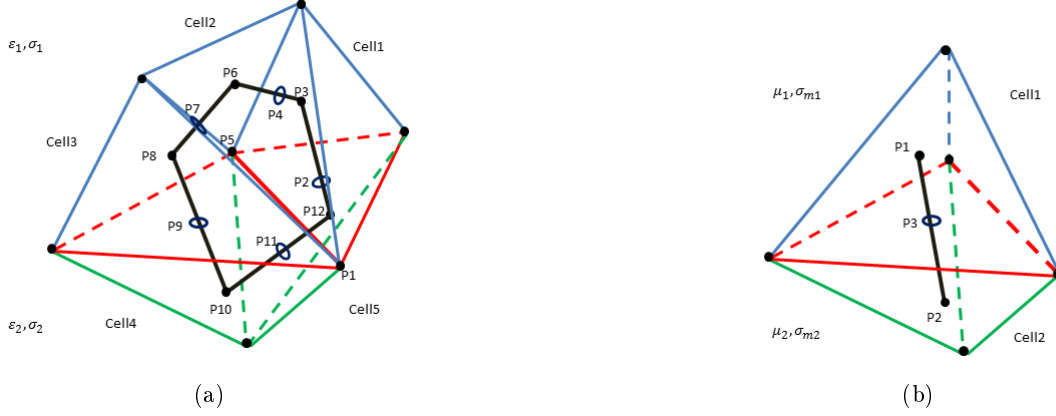


Figure 3.7.: Averaging of material properties at interfaces for : (a) Delaunay edges in free space in blue, within the dielectric in green, at interface in red. ; (b) Voronoi edges crossing triangles at the interface in black.

In equations (3.25) and (3.26) ε , μ , σ and σ_m are inside the integrals. I take them outside the integral for the discretised equations (3.34), (3.35) by averaging over the closed surface loop. For these Delaunay and Voronoi edges, the material properties are evaluated using the weighted average formulae

$$a_{avDel,i} = \frac{\sum_{k=1}^{2N_{Vor}} w_k a_{cell}}{\sum_{k=1}^{2N_{Vor}} w_k} \quad (3.40)$$

$$b_{avVor,j} = \frac{\sum_{k=1}^2 g_k b_{cell}}{\sum_{k=1} w_k} \quad (3.41)$$

When

equation (3.40) is used for averaging $a = \varepsilon$ and $a = \sigma$, the corresponding material parameter assigned to one of the cells surrounding Delaunay edge i is a_{cell} . The k^{th} volume spanned by the two endpoints of Delaunay edge i , the intersection point of the Voronoi edge with the Delaunay face and the position of the circumcentre of the cell is w_k . For example, in Figure 3.7a, w_1 would be the volume spanned by the points $P1$, $P5$, $P9$, $P8$ and, in free space, $a_{cell} = \varepsilon_1$ or $a_{cell} = \sigma_1$, w_2 would correspond to the volume spanned by the points $P1$, $P5$, $P9$, $P10$ and, inside the dielectric, $a_{cell} = \varepsilon_2$ or $a_{cell} = \sigma_2$. The averaged material parameter assigned to Delaunay edge i is $a_{avDel,i}$. Simply using the length between two points, like $P8$ and $P9$ for example as a weight instead of a volume, is not sufficient because although the distance between two points may be identical, the volumes might be very different depending on the cell. The volume averaging I use led to the best results. Equation (3.41) is used for averaging values of the parameters $b = \mu$ and $b = \sigma_m$ which are linked to the Voronoi edges. The length of a Voronoi edge inside a given cell is g_k , which corresponds to the distance between the intersection point of the Voronoi edge j with the Delaunay face and the circumcentre of the cell. For example, in Figure 3.7b, the distance between the points $P1$ and $P3$ is g_1 , and the coefficient $b_{cell} = \mu_1$ or $b_{cell} = \sigma_{m1}$. In the co-volume scheme we can also simulate a PEC by means of a resistive sheet, by assigning only to the Delaunay and Voronoi edges forming the

3. Numerical Solution of Maxwell Equations

interface a very high conductivity. I do not have to assign a conductivity to the edges inside the object, because the electric wave is already reflected at the interface. To prove that the weighted averaging on an unstructured mesh corresponds to the arithmetic mean on a structured mesh, I consider four cells (cubes) of a structured mesh and choose the Delaunay edge in the centre (magenta) in Figure 3.8a.

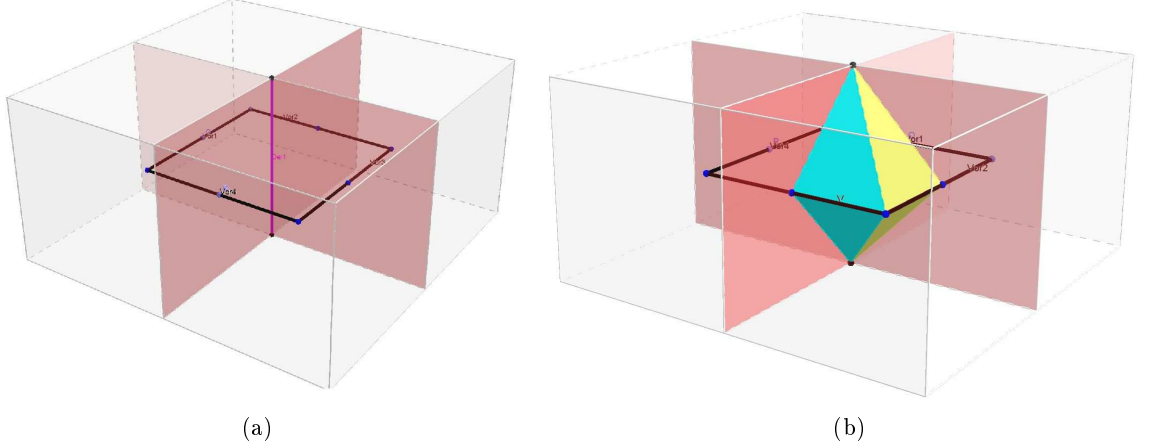
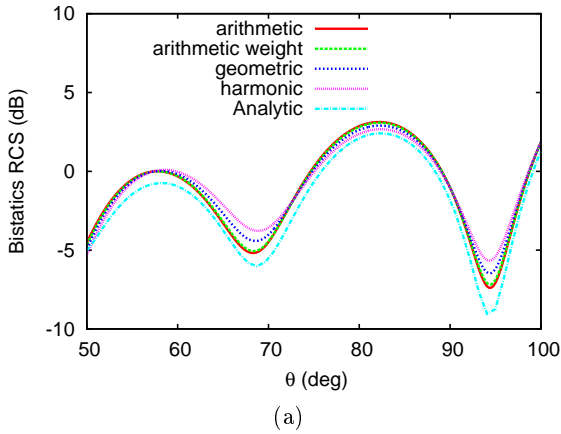


Figure 3.8.: *Averaging of material properties at interfaces for (a) Delaunay edge (magenta) surrounded by four Voronoi edges (dark red). ; (b) two sub-volumes (blue, yellow) of equal volume inside a given cell.*

This Delaunay edge is surrounded by four Voronoi edges (dark red) that connect the cell centre and passing through the centre of cube faces. Due to the structured uniform mesh, every cell has the same volume and, therefore, the two sub-volumes shown in blue and yellow in Figure 3.8b will also have equal volume. If I consider that two cells are located inside Dielectric (1) and two cells inside Dielectric (2), equation (3.40) becomes:

$$a_{avDel,i} = \frac{\sum_{k=1}^{2N_{Vor}} w_k a_{cell}}{\sum_{k=1}^{2N_{Vor}} w_k} \equiv \frac{\sum_{k=1}^{2N_{Vor}} w a_{cell}}{\sum_{k=1}^{2N_{Vor}} w} \equiv \frac{a_1 + a_2}{2} \quad (3.42)$$

I also investigated the accuracy of different averaging methods, namely the weighted arithmetic mean average (which I adopted for the unstructured mesh), the arithmetic (3.37), harmonic (3.38) and geometric (3.39) mean averages on an unstructured mesh.



Averaging Technique	L^2 Error
Weighted Arithmetic Mean	0.903 %
Arithmetic Mean	0.931 %
Geometric Mean	0.947 %
Harmonic Mean	0.948 %

(b)

Figure 3.9.: Results of a comparison of the use of different averaging methods across dielectric interface : (a) RCS calculations. ; (b) Relative L^2 Errors of each method.

I considered the problem of 2λ dielectric sphere illuminated by a monochromatic plane wave as described in section (4.2.3), then I computed the logarithmic L^2 error of the different averaging techniques of the RCS against the corresponding Mie solution. The results are represented in 3.9b. The relative error of all the methods varies only by about 0.05%. However differences can clearly be observed in Table 3.9a due to the logarithmic scale. It is apparent that the weighted arithmetic mean average gives the best results for an unstructured mesh, hence confirming our choice.

3.6. Modelling of anisotropic dielectrics

Analytical solutions to wave propagation problems in electromagnetics are mainly restricted to problems involving simple geometrical shapes and diagonal, uniaxial or biaxial, tensors [39][113]. Numerical techniques are required for the solution of the majority of problems, which involve arbitrary shaped objects. In earlier work [48], I demonstrated the capability of a generalised Yee algorithm adapted to unstructured meshes to accurately model the radar cross section (RCS) of arbitrarily shaped lossy dielectric objects. For isotropic cases our method shows significant savings with respect to memory and time with respect to the standard FDTD scheme due to the unstructured mesh I employ. Here, I describe the extension of the method to deal with anisotropic materials, such as composites.

There are generally two methods to deal with anisotropic materials. Firstly you use the constitutive equation to replace the displacement field in Maxwell's equations by the

3. Numerical Solution of Maxwell Equations

electric field [132]. Another possibility is to obtain the displacement field and afterwards use it in the constitutive equations. I adopt the latter method which has been proposed by [82]. This approach was originally presented within the context of a total field formulation, but the unstructured mesh extension adopted here employs a scattered field formulation.

3.6.1. Problem formulation

The integral form of Maxwell's equations is employed [144]. For a three dimensional lossy dielectric medium, Ampère's and Faraday's Laws are expressed, in a scattered field form, as

$$\int_A \left[\frac{\partial}{\partial t} + \bar{\sigma} \bar{\epsilon}^{-1} \right] \mathbf{D}_{scat} d\mathbf{A} = \oint_{\partial A} \mathbf{H}_{scat} d\mathbf{l} - \int_A (\bar{\epsilon} - \epsilon_0 \bar{I}) \frac{\partial \mathbf{E}_{inc}}{\partial t} d\mathbf{A} \quad (3.43)$$

$$- \int_A \bar{\sigma} \mathbf{E}_{inc} d\mathbf{A}$$

and

$$\int_A \left[\frac{\partial}{\partial t} + \bar{\sigma}_m \bar{\mu}^{-1} \right] \mathbf{B}_{scat} d\mathbf{A} = - \oint_{\partial A} \mathbf{E}_{scat} d\mathbf{l} - \int_A (\bar{\mu} - \mu_0 \bar{I}) \frac{\partial \mathbf{H}_{inc}}{\partial t} d\mathbf{A} \quad (3.44)$$

$$- \int_A \bar{\sigma}_m \mathbf{H}_{inc} d\mathbf{A}$$

I use the same convention as for the isotropic case, with the constitutive equations 2.10 and 2.9. The only difference is that from now on the material parameters are second order tensors.

3.6.2. Discrete equations

The same mesh and notation as for the isotropic dielectric case is used. When the leapfrog scheme is used for time discretisation, it will be second order accurate if the unknowns are located at the midpoints of these edges. The unknown at the centre of the i^{th} Delaunay edge corresponds to the projection, $(D_{scat,i}, E_{scat,i})$, of the scattered electric field onto the direction of the edge. The unknown at the centre of the j^{th} Voronoi edge corresponds to the projection, $(B_{scat,j}, H_{scat,j})$, of the scattered magnetic field onto the direction of the edge. In the scattered field formulation, the incident field is a known function, while the scattered field is unknown. At the interface boundaries, the material parameters in the equations (3.43) and (3.44) need to be averaged because the FDTD method approximation is continuous. Therefore, I average the values of $\bar{\epsilon}$, $\bar{\mu}$, $\bar{\sigma}$ and $\bar{\sigma}_m$ at a dielectric interface, leading to the values $\bar{\epsilon}_{av}, \bar{\mu}_{av}, \bar{\sigma}_{av}$ and $\bar{\sigma}_{m,av}$. The method for determining these averaged values is detailed in section 3.6.3. Direct discretisation

3.6. Modelling of anisotropic dielectrics

of Ampère's Law and Faraday's Law as described in section 3.4.2 then leads to the equations

$$D_{scat,i}^{n+1} = \langle \bar{a}_{\varepsilon+}^{-1} (\bar{a}_{\varepsilon-} \mathbf{D}_{scat}|_i + \mathbf{Z}_D|_i), \hat{\mathbf{e}}_i \rangle \quad (3.45)$$

$$B_{scat,j}^{n+1/2} = \left\langle \bar{a}_{\mu+}^{-1} \left(\bar{a}_{\mu-} \mathbf{B}_{scat}^{n-1/2} \Big|_j + \mathbf{Z}_B|_j \right), \hat{\mathbf{e}}_j \right\rangle \quad (3.46)$$

where $\langle \mathbf{F}, \hat{\mathbf{e}}_i \rangle$ denotes the dot product (projection) of any field vector \mathbf{F} along the i^{th} edge. The projection of the scattered electric field vector onto Delaunay edge i is denoted by $E_{scat,i}$, while $\mathbf{E}_{scat}|_i$ denotes the scattered electric field vector at the location of the i^{th} Delaunay edge. $\bar{a}_{\varepsilon+}$, $\bar{a}_{\mu+}$, $\mathbf{Z}_D|_i$, $\mathbf{Z}_B|_j$ are defined as follows

$$\bar{a}_{\varepsilon+} = \left(\bar{I} + \frac{\Delta t \bar{\sigma}_{av} \bar{\varepsilon}_{av}^{-1}}{2} \right)^{-1}, \quad \bar{a}_{\varepsilon-} = \left(\bar{I} - \frac{\Delta t \bar{\sigma}_{av} \bar{\varepsilon}_{av}^{-1}}{2} \right) \quad (3.47)$$

$$\bar{a}_{\mu+} = \left(\bar{I} + \frac{\Delta t \bar{\sigma}_{avm} \bar{\mu}_{av}^{-1}}{2} \right)^{-1}, \quad \bar{a}_{\mu-} = \left(\bar{I} - \frac{\Delta t \bar{\sigma}_{avm} \bar{\mu}_{av}^{-1}}{2} \right) \quad (3.48)$$

$$\begin{aligned} \mathbf{Z}_D|_i &= \Delta t \left[\left(\frac{1}{A_i^V} \sum_{k=1}^{M_i^V} H_{scat,j_i,k}^{n+1/2} l_{j_i,k}^V \right) \hat{\mathbf{e}}_i \right. \\ &\quad \left. - \left(\bar{\sigma}_{avm} \mathbf{H}_{inc}|_j - (\bar{\mu}_{av} - \mu_0 \bar{I}) \frac{\partial}{\partial t} \mathbf{H}_{inc}|_j \right) \right] \end{aligned} \quad (3.49)$$

$$\begin{aligned} \mathbf{Z}_B|_j &= \Delta t \left[\left(-\frac{1}{A_j^D} \sum_{k=1}^{M_j^D} E_{scat,i,j,k}^{n+1/2} l_{i,j,k}^D \right) \hat{\mathbf{e}}_j \right. \\ &\quad \left. - \left(\bar{\sigma}_{avm} \mathbf{H}_{inc}|_j - (\bar{\mu}_{av} - \mu_0 \bar{I}) \frac{\partial}{\partial t} \mathbf{H}_{inc}|_j \right) \right] \end{aligned} \quad (3.50)$$

Here, $B_{scat,j}^{n+1/2}$ and $D_{scat,i}^{n+1}$ are projections onto the Delaunay and Voronoi edges respectively, whereas the quantities $\mathbf{D}_{scat}|_i$, $\mathbf{E}_{inc}^{n+1/2}|_i$, and $\mathbf{B}_{scat}^{n-1/2}|_j$, $\mathbf{H}_{inc}|_j$ represent field vectors computed at the centre of the i^{th} Delaunay edge and the j^{th} Voronoi edge respectively. These field values have to be determined from their corresponding stored projections and this calculation, which is not direct, is described in detail in section 3.6.4. In contrast to the isotropic case, these equations cannot be updated in one step, as vector-matrix multiplications are involved, because it is not possible to have direct access to the full field vectors \mathbf{B} , \mathbf{H} , \mathbf{D} and \mathbf{E} at a given location. Nevertheless, approximated field vectors are obtained, which are required for the matrix-vector multiplication of the updating equations. Finally the resulting vectors are projected to the corresponding Delaunay edge \mathbf{e}_i or Voronoi edge \mathbf{e}_j . This updating process is explained in detail in Section 3.6.6.

3.6.3. Material interface boundary conditions

When the boundary is an interface between two different media, the update equations (3.43) and (3.44) require integration across the interface. These integrals are evaluated by assigning a weighted average value to the material parameters, based upon the mesh structure. In section 3.5.1, the material parameters at the interface are obtained by a weighted arithmetic mean average and compared the results produced with those obtained by using the arithmetic mean average, the harmonic mean average and the geometric mean average. I demonstrated that the weighted arithmetic mean average resulted in improved accuracy on unstructured meshes . Here, I adopt the same form of averaging, but applied to every component of the material parameter tensors. In the isotropic case, the scalar material properties, ε and σ , associated to the electric field, are stored on the Delaunay edges and the scalars μ and σ_m associated to the magnetic field are stored on the Voronoi edges. The adapted formules become

$$\varepsilon_{av_{q,l}}|_{Del,i} = \frac{\sum_{k=1}^{2M_i^V} w_k \varepsilon_{q,l}|_{Cell,k}}{\sum_{k=1}^{2M_i^V} w_k} \quad \sigma_{av_{q,l}}|_{Del,i} = \frac{\sum_{k=1}^{2M_i^V} w_k \sigma_{q,l}|_{Cell,k}}{\sum_{k=1}^{2M_i^V} w_k} \quad (3.51)$$

Here q and l can take the values 1, 2 or 3, corresponding to the x , y or z directions respectively, while M_i^V refers to the number of Voronoi edges surrounding a given Delaunay Edge i . As there are two sub-volumes associated to each Voronoi edge, I have to sum over $2M_i^V$ Voronoi edges. These account for the contribution of the material parameter assigned to each of the cells surrounding Delaunay edge $(.)_{Del,i}$, weighted by a coefficient w_k that corresponds to the volume spanned by the two endpoints of the Delaunay edge, the intersection point of the Voronoi edge with the Delaunay face and the position of the circumcentre of the cell. Each component of the tensors of magnetic permeability $\bar{\mu}$ and magnetic conductivity $\bar{\sigma}_m$, which are linked to the Voronoi edges, is obtained, by averaging, as

$$\mu_{av_{q,l}}|_{Vor,j} = \frac{\sum_{k=1}^2 g_k \mu_{q,l}|_{Cell_k}}{\sum_{k=1}^2 g_k} \quad \sigma_{m_{av_{q,l}}}|_{Vor,j} = \frac{\sum_{k=1}^2 g_k \sigma_{m_{q,l}}|_{Cell_k}}{\sum_{k=1}^2 g_k} \quad (3.52)$$

The lengths of the Voronoi edges, g_1 and g_2 , are the distances between the intersection point of the Voronoi edge $(.)_{Vor,j}$ with the Delaunay face and the circumcentre of the cell.

3.6.4. Obtaining approximated field vectors from edge projections

In Section 3.6.2 it was noted that the main difficulty with equations (3.45) and (3.46) are the matrix-vector multiplications. This is because of the projection based nature of

the co-volume updating scheme. The challenge is now to obtain the corresponding field vectors \mathbf{D}_{scat} and \mathbf{B}_{scat} and associate them with Delaunay edge i and Voronoi edge j respectively. Unfortunately, it is to my knowledge not possible to get exact full field vector components from field to edge projections. However, I can approximate the full field components at any location in the mesh. This is achieved by assuming that, in \mathbb{R}^3 , with a set of three orthogonal vectors $\mathbf{v}_1, \mathbf{v}_2, \mathbf{v}_3$, a general vector \mathbf{x} can be reconstructed as

$$\mathbf{x} = \sum_{i=1}^3 \mathbf{P}_{v_i} \quad (3.53)$$

in terms of the projections

$$\mathbf{P}_{v_i} = \frac{\langle \mathbf{x}, \mathbf{v}_i \rangle \mathbf{v}_i}{\|\mathbf{v}_i\|^2} \quad \text{for } i = 1, 2, 3 \quad (3.54)$$

As the mesh is assumed to be unstructured, I cannot use this method directly to obtain an exact field vector. The trivial solution would be to consider all the edges connected to one node, as depicted in Figure 3.10 (b), and solve a system of equations. This will give me a field vector at node n_1 . As one edge is always formed by two points, I do the same for point n_2 . Finally, the obtained field vectors are averaged and projected to the corresponding edge.

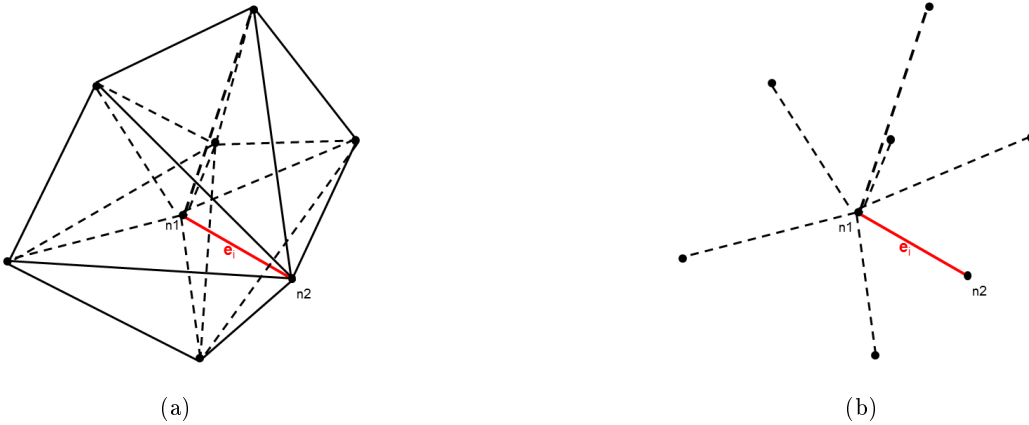


Figure 3.10.: Interpolation of the field vector at node n_1 : (a) Tetrahedra in the Delaunay mesh containing the point n_1 . ; (b) edges in the 3 Delaunay mesh containing the point n_1 .

For example, to obtain the displacement field vector \mathbf{D}_{scat} on the edge i , denoted by the red line in Figure 3.10 (a), I construct the set of equations

$$\bar{\bar{P}} \mathbf{D}_{scat} = (\mathbf{D}_{scat} \cdot \hat{\mathbf{e}}_i) \hat{\mathbf{e}}_i \quad (3.55)$$

3. Numerical Solution of Maxwell Equations

where

$$\bar{\bar{P}} = \begin{bmatrix} e_{i_x} e_{i_x} & e_{i_x} e_{i_y} & e_{i_x} e_{i_z} \\ e_{i_y} e_{i_x} & e_{i_y} e_{i_y} & e_{i_y} e_{i_z} \\ e_{i_z} e_{i_x} & e_{i_z} e_{i_y} & e_{i_z} e_{i_z} \end{bmatrix} \quad (3.56)$$

and $\hat{\mathbf{e}}_i$ is the normalised Delaunay edge vector corresponding to Delaunay edge i . The matrix $\bar{\bar{P}}$, based upon the x , y , z components of the vector $\hat{\mathbf{e}}_i$ and the projections $\mathbf{D}_{scat} \cdot \hat{\mathbf{e}}_i$ are known. The displacement field vector at a node belonging to Delaunay edge i is approximated by considering the sum of the system in equation (3.55) for each Delaunay edge connected to that node, as depicted in Figure 3.10 (b). In this case, the system

$$\bar{\bar{P}}' \mathbf{D}_{scat} = \sum_{q=1}^N (\mathbf{D}_{scat,q} \cdot \hat{\mathbf{e}}_q) \hat{\mathbf{e}}_q \quad (3.57)$$

is solved, with

$$\bar{\bar{P}}'_{l,m} = \sum_{q=1}^N \sum_{l=1}^3 \sum_{m=1}^3 e_{ql} e_{qm} \quad (3.58)$$

Here, \mathbf{D}_{scat} is the unknown vector, $\bar{\bar{P}}'$ and $\mathbf{D}_{scat,q} \cdot \hat{\mathbf{e}}_q$ are known, N is the number of Delaunay edges connected to the node and $e_{i_1} = e_{i_x}$, $e_{i_2} = e_{i_y}$ and $e_{i_3} = e_{i_z}$. This system of equations is solved locally, node by node, until an approximated field vector at all nodes of the Delaunay mesh is obtained. Finally, I link the computed field vector to the corresponding edges. A Delaunay edge is assumed to connect the two nodes n_1 and n_2 and the displacement field vector, associated to the Delaunay edge i , is obtained by averaging the electric field vectors at nodes n_1 and n_2 , i.e. $\mathbf{D}_{scat,i} = (\mathbf{D}_{scat,n_1} + \mathbf{D}_{scat,n_2})/2$. The same procedure is applied for approximating the magnetic flux vectors \mathbf{B}_{scat} , but using now the Voronoi edges. However, unlike the Cartesian Yee scheme, where each component of the field vectors has its own update equation, the approximations of the full vector fields obtained using this method are not good enough for time iterating the field components. It is found that error accumulation causes the algorithm to become unstable. In the following sections, I demonstrate how this difficulty may be circumvented.

3.6.5. Local orthogonal unit vectors

When using the integral formulation of Maxwell's equations, it is not the displacement field vector \mathbf{D}_{scat} that is updated, but rather its projection, $\mathbf{D}_{scat,i} = \mathbf{D}_{scat} \cdot \mathbf{e}_i$, onto a Delaunay edge \mathbf{e}_i . In the case of an isotropic material, the electric permittivity and the magnetic permeability are scalars, so that updating the fields only involves scalar multiplication between the field projections and the scalar material properties. For an anisotropic material, the integrals in Ampère's and Faraday's laws contain matrix-vector multiplications between material tensors ($\bar{\bar{\epsilon}}$, $\bar{\bar{\mu}}$, $\bar{\bar{\sigma}}$, $\bar{\bar{\sigma}}_m$) and the fields (\mathbf{D}_{scat} , \mathbf{B}_{scat}). To

deal with these matrix-vector multiplications, two linearly independent vectors are created for each Delaunay and Voronoi edge. Using the stabilised Gram-Schmidt orthonormalisation procedure, I generate three orthonormal vectors, as illustrated in Figure 3.11. The first vector \mathbf{e}_1 , to which the two linearly independent vectors ($\mathbf{e}'_2, \mathbf{e}'_3$) are added, remains unchanged during the whole process. Each set of three orthogonal vectors represents one local coordinate system, leading to as many local systems as Delaunay and Voronoi edges.

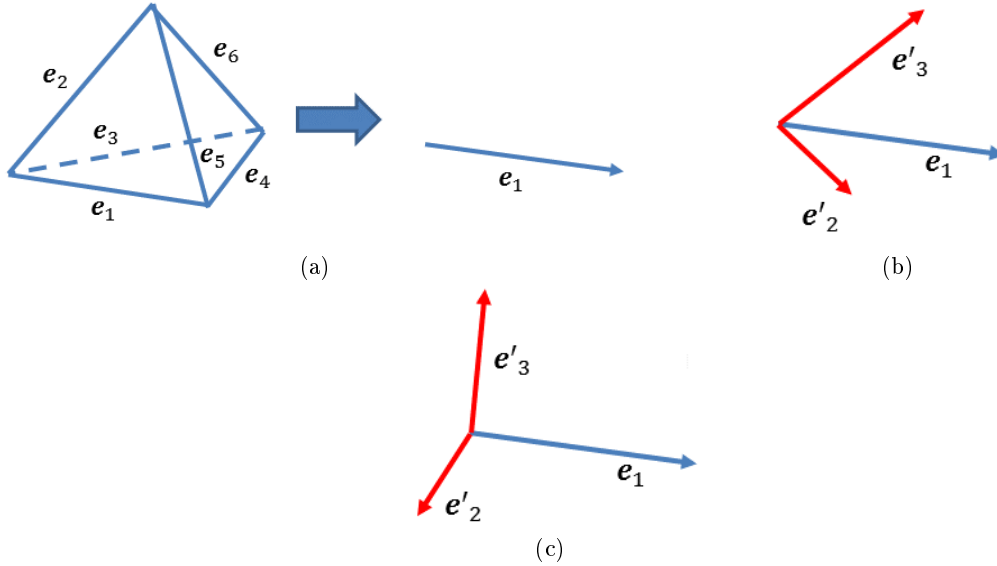


Figure 3.11.: *Generating the orthonormal local coordinate system.* (a) Consider Delaunay edge \mathbf{e}_1 from a given tetrahedron ; (b) Create two linear independent vectors \mathbf{e}'_2 and \mathbf{e}'_3 ; (c) Orthogonalisation of the vectors \mathbf{e}'_2 and \mathbf{e}'_3 with respect to \mathbf{e}_1 using the Gram Schmidt orthogonalisation procedure.

The discretisation, allows me to reconstruct approximated field vector components for each local coordinate system, using the field projections of the surrounding Delaunay or Voronoi edges, as explained in Section 3.6.4. The field vectors, obtained in this way, are projected onto the two orthogonal vectors forming the local frame. The first vector of each subset, which remains unchanged during the orthonormalisation procedure, can be immediately updated using the projection equation employed in the isotropic case. For this projection, no error is induced by the field averaging.

3.6.5.1. Coordinate transformation

The material tensors are expressed in the global reference frame formed by the orthonormal vectors $\hat{\mathbf{x}}$, $\hat{\mathbf{y}}$ and $\hat{\mathbf{z}}$. Three orthonormalised vectors $\hat{\mathbf{x}}'$, $\hat{\mathbf{y}}'$, $\hat{\mathbf{z}}'$ form the basis of each local coordinate system. The (\cdot) always refers to unit vectors and (\cdot') to vectors or vector components of the local coordinate system. The Jacobian matrix $\bar{\mathbf{J}}$, defined by

3. Numerical Solution of Maxwell Equations

$$\bar{\bar{\mathbf{J}}} = \begin{bmatrix} \frac{\partial x'}{\partial x} & \frac{\partial x'}{\partial y} & \frac{\partial x'}{\partial z} \\ \frac{\partial y'}{\partial x} & \frac{\partial y'}{\partial y} & \frac{\partial y'}{\partial z} \\ \frac{\partial z'}{\partial x} & \frac{\partial z'}{\partial y} & \frac{\partial z'}{\partial z} \end{bmatrix} \quad (3.59)$$

can be used to transform a vector, or a matrix, from the global to a local frame. Here (x', y', z') refers to the coordinate in the local coordinate system and (x, y, z) to the global coordinate system. Each component of the Jacobian can be interpreted as an amplification factor, describing how one coordinate in a given reference frame stretches, shrinks or rotates with respect to another coordinate in another reference frame. In our case, the Jacobian is pure a rotation matrix $\bar{\bar{\mathbf{J}}}_R$ which can be directly calculated as

$$\bar{\bar{\mathbf{J}}}_R = \begin{bmatrix} \hat{\mathbf{x}}' \cdot \hat{\mathbf{x}} & \hat{\mathbf{x}}' \cdot \hat{\mathbf{y}} & \hat{\mathbf{x}}' \cdot \hat{\mathbf{z}} \\ \hat{\mathbf{y}}' \cdot \hat{\mathbf{x}} & \hat{\mathbf{y}}' \cdot \hat{\mathbf{y}} & \hat{\mathbf{y}}' \cdot \hat{\mathbf{z}} \\ \hat{\mathbf{z}}' \cdot \hat{\mathbf{x}} & \hat{\mathbf{z}}' \cdot \hat{\mathbf{y}} & \hat{\mathbf{z}}' \cdot \hat{\mathbf{z}} \end{bmatrix} \quad (3.60)$$

Maxwell's equations are form invariant [24], which means that, in the local coordinate system, they may be expressed as

$$\mathbf{E}'(\mathbf{r}') = \left(\bar{\bar{\mathbf{J}}}_R^T \right)^{-1} \mathbf{E}(\mathbf{r}) \quad (3.61)$$

$$\mathbf{H}'(\mathbf{r}') = \left(\bar{\bar{\mathbf{J}}}_R^T \right)^{-1} \mathbf{H}(\mathbf{r}) \quad (3.62)$$

and a material parameter tensor, $\bar{\bar{\mathbf{M}}}$ say, is transformed into the local coordinate system using the operator transformation

$$\bar{\bar{\mathbf{M}}}'(\mathbf{r}') = \frac{\bar{\bar{\mathbf{J}}}_R \bar{\bar{\mathbf{M}}} \bar{\bar{\mathbf{J}}}_R^T}{\det(\bar{\bar{\mathbf{J}}}_R)} \quad (3.63)$$

The form invariance allows me to absorb the coordinate transformation completely into the material properties. Note that the determinant of the rotation matrix is unity, i.e. $\det(\bar{\bar{\mathbf{J}}}_R) = 1$.

3.6.6. Time updating scheme

As mentioned previously, equations (3.45) and (3.46) cannot be updated simultaneously, as the scattered field vectors \mathbf{D}_{scat} and \mathbf{B}_{scat} are not immediately available. In this section, the updating process will be explained in detail. For simplicity, I will restrict consideration to updating the electric field projection $E_{scat,i}^n$, as the magnetic field $H_{scat,j}^n$ will be similarly updated. Firstly I apply the coordinate transformation to the terms $\bar{\bar{a}}_{\varepsilon+}$, $\bar{\bar{a}}_{\varepsilon-}$ defined in equation (3.47) and $\bar{\bar{\varepsilon}}_{av}^{-1}$ from equation (3.46), so that

$$\bar{a}'_{\varepsilon+} = \bar{J}_R \left(\bar{I} + \frac{\Delta t \bar{\sigma}_{av} \bar{\varepsilon}_{av}^{-1}}{2} \right)^{-1} \bar{J}_R^T \quad (3.64)$$

$$\bar{a}'_{\varepsilon-} = \bar{J}_R \left(\bar{I} - \frac{\Delta t \bar{\sigma}_{av} \bar{\varepsilon}_{av}^{-1}}{2} \right) \bar{J}_R^T \quad (3.65)$$

$$\bar{\varepsilon}'_{av^{-1}} = \bar{J}_R \bar{\varepsilon}_{av}^{-1} \bar{J}_R^T \quad (3.66)$$

These are stored at the corresponding Delaunay edges before entering the time loop. Within the time iteration loop, I first calculate and store the right hand side of the equation (3.49) for each Delaunay edge $\hat{\mathbf{e}}_i$. This is readily accomplished, as the magnetic components in the circulation term $\sum_{k=1}^{M_i^V} H_{scat,j_i,k}^{n+0.5} l_{j_i,k}^V$ are available, from the previous iteration, and the full vector $\mathbf{E}_{inc,i}^{n+0.5}$ is also a known function. Before updating the projection $D_{scat,i}^n$ to $D_{scat,j}^{n+1}$, equation (3.57) is employed, to obtain the vectors \mathbf{D}_{scat}^n and \mathbf{Z}_D as defined above. These vectors are projected in each of the three orthogonal directions of every local frame, e.g. $\hat{\mathbf{e}}'_1 \equiv \hat{\mathbf{e}}_1$, $\hat{\mathbf{e}}'_2$, $\hat{\mathbf{e}}'_3$ from Figure 3.11, and the matrix vector multiplication is performed. Equation (3.46) in the local frame takes the vector form

$$\mathbf{D}'_{scat}{}^{n+1} = \bar{a}'_{\varepsilon+} [\bar{a}'_{\varepsilon-} \mathbf{D}'_{scat}{}^n + \mathbf{Z}'_D] \quad (3.67)$$

The constitutive equation allows me to retrieve the electric field projection. In practice, only the first line of $\bar{\varepsilon}_{av}^{-1}$ needs to be considered, due to the fact that the data storage is based upon field projections along the edges and not field vectors. As a result, the value

$$E_{scat,i}^{n+1} = \bar{\varepsilon}'_{av,11}{}^{-1} D'_{scat,e_1}{}^{n+1} + \bar{\varepsilon}'_{av,12}{}^{-1} D'_{scat,e_2}{}^{n+1} + \bar{\varepsilon}'_{av,13}{}^{-1} D'_{scat,e_3}{}^{n+1} \quad (3.68)$$

may be obtained. These values are used for updating the sum up curl term of equation (3.50) and then the magnetic field is updated in a similar manner.

3.7. Modelling of isotropic chiral material

Applications of isotropic metamaterials are smaller antennas, super lenses [150], polarisers, radomes or radar-cross section (RCS) reducing materials. Due to the causality condition (subsection 2.4.5) frequency-independent DNG metamaterials are not physically realisable [135]. Although the metamaterial under consideration is not necessary part of the DNG class, I decided to further generalise our method to frequency dependent materials. This is not a straightforward approach because the co-volume scheme is a time domain method, whereas the material parameters are frequency dependent functions. Therefore the material parameters need to be converted to the time domain using a convolution. The displacement field in time domain corresponds to

$$\mathbf{D}(\mathbf{r}, t) = \varepsilon_0 \varepsilon_\infty \mathbf{E}(\mathbf{r}, t) + \varepsilon_0 \int_0^t \mathbf{E}[\mathbf{r}, t - \tau] \chi_e(\mathbf{r}, \tau) d\tau \quad (3.69)$$

3. Numerical Solution of Maxwell Equations

Several methods exist to deal with frequency dependent materials in FDTD algorithms, namely the Auxiliary Differential Equation method [71, 69], the Piecewise Recursive convolution method [85, 72] and the Z-transform technique [123]. All three methods give comparable results. Nevertheless I decided to use the Z-transform because it is easy to implement and shows a better convergence close to the resonant frequency [80]. The Z-Transform is a common technique in signal processing and is the discrete version of the Laplace transform. Sullivan [123] had the idea to use this method to model frequency dependent materials. To my knowledge Demir et al. [37] were the first ones to model chiral materials in 3D using the finite-difference time domain method (FDTD) by taking into account the frequency dependence of all the material parameters (ε, μ, κ) using the Z-transform. In their method they only use first order approximations in the Z-Domain and derive the Z transform coefficients analytically. Pereda et al. [103] use another approach based upon the Padé approximants [5]. Using a bilinear transformation for calculating the Padé approximants they were able to preserve a second order accuracy in Z-Domain. In this work I generalise the method introduced by Pereda et al. to an unstructured mesh. To validate my results I compute the transmission and reflexion coefficients of a pulse through a 3D chiral slab in free space, I compute the rotation of the incident plane of polarisation after the slab and model the Radar-cross section of a sphere. Furthermore I investigate the stability behaviour of the algorithm with respect to different chiralities and meshes.

3.7.1. Problem formulation

For my update equations I use a mix between a scattered and total field formulation. This allows me to compute the reflexion and transmission coefficients in a single run compared to two runs required for the total field formulation. The integral form of Maxwell's equations is employed. For a three dimensional lossy dielectric medium, Ampère's and Faraday's laws are expressed, in a scattered field form, as

$$\int_{A^V} \frac{\partial \mathbf{D}_{scat}}{\partial t} d\mathbf{A} = \int_{\partial A^V} \mathbf{H}_{scat} d\mathbf{l} + \int_{A^V} (\varepsilon(\omega) - \varepsilon_0) \frac{\partial \mathbf{E}_{inc}}{\partial t} \quad (3.70)$$

$$\int_{A^D} \frac{\partial \mathbf{B}_{scat}}{\partial t} d\mathbf{A} = - \int_{\partial A^D} \mathbf{E}_{scat} d\mathbf{l} + \int_{A^D} (\mu(\omega) - \mu_0) \frac{\partial \mathbf{H}_{inc}}{\partial t} \quad (3.71)$$

for the calculation I need the displacement field \mathbf{D} and magnetic flux \mathbf{B} expressed as total fields where the total field is defined as the sum of the incident and scattered field (section 3.2). Equations (3.70) and (3.71) become

$$\int_{A^V} \frac{\partial \mathbf{D}_{tot}}{\partial t} d\mathbf{A} = \int_{\partial A^V} \mathbf{H}_{scat} d\mathbf{l} + \int_{A^V} \varepsilon_0 \frac{\partial \mathbf{E}_{inc}}{\partial t} \quad (3.72)$$

$$\int_{A^D} \frac{\partial \mathbf{B}_{tot}}{\partial t} d\mathbf{A} = - \int_{\partial A^D} \mathbf{E}_{scat} d\mathbf{l} + \int_{A^D} \mu_0 \frac{\partial \mathbf{H}_{inc}}{\partial t} \quad (3.73)$$

3.7. Modelling of isotropic chiral material

In contrast to the previous cases, the material parameters, the permittivity $\varepsilon(\omega)$, permeability $\mu(\omega)$ and the chiral parameter $\kappa(\omega)$ are now frequency dependent. For the permittivity and permeability a Lorentzian model is assumed, whereas the chirality follows a Condon model [128].

$$\varepsilon(\omega) = \varepsilon_\infty + \frac{(\varepsilon_s - \varepsilon_\infty)\omega_e^2}{\omega_e^2 + 2\omega_e\xi_e i\omega - \omega^2} \quad (3.74)$$

$$\mu(\omega) = \mu_\infty + \frac{(\mu_s - \mu_\infty)\omega_h^2}{\omega_h^2 + 2\omega_h\xi_h i\omega - \omega^2} \quad (3.75)$$

$$\hat{\kappa}(\omega) = i\kappa(\omega) = \frac{\tau_k\omega_k^2 i\omega}{\omega_k^2 + 2\omega_k\xi_k i\omega - \omega^2} \quad (3.76)$$

where ε_∞ , μ_∞ is the permittivity, permeability at the high frequency limit, ε_s , μ_s is the permittivity, permeability at the low frequency limit. ω_e , ω_h , ω_k are the resonance frequencies, ξ_e , ξ_h , ξ_k are the damping coefficients and τ_k is a coupling constant defining the magnitude of the chirality. Due to the frequency dependence of the material parameters we have to convert Ampere and Faraday's law to the frequency domain. This is achieved by replacing $\partial/\partial t$ by $j\omega$, leading to

$$\int_{A^V} j\omega \mathbf{D}_{tot} d\mathbf{A} = \int_{\partial A^V} \mathbf{H}_{scat} d\mathbf{l} + \int_{A^V} \varepsilon_0 j\omega \mathbf{E}_{inc} \quad (3.77)$$

$$\int_{A^D} j\omega \mathbf{B}_{tot} d\mathbf{A} = - \int_{\partial A^D} \mathbf{E}_{scat} d\mathbf{l} + \int_{A^D} \mu_0 j\omega \mathbf{H}_{inc} \quad (3.78)$$

The constitutive equations for a chiral material are derived from equations (2.58) and (2.59)

$$\mathbf{D}_{tot}(\omega) = \varepsilon(\omega)\mathbf{E}_{tot}(\omega) - i\kappa(\omega)\frac{1}{c}\mathbf{H}_{tot}(\omega) \quad (3.79)$$

$$\mathbf{B}_{tot}(\omega) = \mu(\omega)\mathbf{H}_{tot}(\omega) + i\kappa(\omega)\frac{1}{c}\mathbf{E}_{tot}(\omega) \quad (3.80)$$

Inserting equations (3.79) and (3.80) in equations (3.77) and (3.78) respectively, leads to

$$\begin{aligned} \int_{A^V} i\omega\varepsilon_\infty \mathbf{E}_{tot}(\omega) d\mathbf{A} &= \int_{\partial A^V} \mathbf{H}_{scat} d\mathbf{l} + \int_{A^V} \varepsilon_0 i\omega \mathbf{E}_{inc}(\omega) - \int_{A^V} i\omega(\varepsilon(\omega) - \varepsilon_\infty) \mathbf{E}_{tot}(\omega) d\mathbf{A} \\ &+ \int_{A^V} \frac{1}{c} i\omega \hat{\kappa}(\omega) \mathbf{H}_{tot}(\omega) d\mathbf{A} \end{aligned} \quad (3.81)$$

$$\begin{aligned} \int_{A^D} i\omega\mu_\infty \mathbf{H}_{tot}(\omega) d\mathbf{A} &= - \int_{\partial A^D} \mathbf{E}_{scat} d\mathbf{l} + \int_{A^D} \mu_0 i\omega \mathbf{H}_{inc}(\omega) - \int_{A^D} i\omega(\mu(\omega) - \mu_\infty) \mathbf{H}_{tot}(\omega) d\mathbf{A} \\ &- \int_{A^D} \frac{1}{c} i\omega \hat{\kappa}(\omega) \mathbf{E}_{tot}(\omega) d\mathbf{A} \end{aligned} \quad (3.82)$$

3. Numerical Solution of Maxwell Equations

where $\hat{\kappa}(\omega) = j\kappa(\omega)$. Introducing the following notation

$$\begin{aligned}
\mathbf{J}_{hh} &= i\omega(\mu(\omega) - \mu_\infty)\mathbf{H}_{tot}(\omega) \\
\mathbf{J}_{\kappa h} &= \frac{1}{c}i\omega\hat{\kappa}(\omega)\mathbf{H}_{tot}(\omega) \\
\mathbf{J}_{ee} &= i\omega(\varepsilon(\omega) - \varepsilon_\infty)\mathbf{E}_{tot}(\omega) \\
\mathbf{J}_{\kappa e} &= \frac{1}{c}i\omega\hat{\kappa}(\omega)\mathbf{E}_{tot}(\omega)
\end{aligned} \tag{3.83}$$

resulting in

$$\begin{aligned}
\int_{A^V} i\omega\varepsilon_\infty\mathbf{E}_{tot}(\omega)d\mathbf{A} &= \int_{\partial A^V} \mathbf{H}_{scat}d\mathbf{l} + \int_{A^V} \varepsilon_0 i\omega\mathbf{E}_{inc}(\omega) - \int_{A^V} \mathbf{J}_{ee}(\omega)d\mathbf{A} \\
&\quad + \int_{A^V} \mathbf{J}_{\kappa h}(\omega)d\mathbf{A}
\end{aligned} \tag{3.84}$$

$$\begin{aligned}
\int_{A^D} i\omega\mu_\infty\mathbf{H}_{tot}(\omega)d\mathbf{A} &= - \int_{\partial A^D} \mathbf{E}_{scat}d\mathbf{l} + \int_{A^D} \mu_0 i\omega\mathbf{H}_{inc}(\omega) - \int_{A^D} \mathbf{J}_{hh}(\omega)d\mathbf{A} \\
&\quad - \int_{A^D} \mathbf{J}_{\kappa e}(\omega)d\mathbf{A}
\end{aligned} \tag{3.85}$$

The incident field is assumed to be a monochromatic plane wave, generated by a source located in the far field, which has the form $\mathbf{E} = \mathbf{E}_0 \cos(\omega t - \mathbf{k} \cdot \mathbf{r})$.

3.7.2. Discrete equations and Z-Transform

To convert equations (3.84) and (3.85) from frequency to time domain the substitution $j\omega \rightarrow \frac{\partial}{\partial t}$ is employed. For the discretisation a second order central difference approximation is used. In our interleaved leapfrog scheme, the electric field projections are stored at integer time steps n and the magnetic field projections are stored at half-integer time steps $n + 1/2$ leading to the following approximations:

$$\frac{\partial \mathbf{E}}{\partial t} = \frac{\mathbf{E}^{n+1} - \mathbf{E}^n}{\Delta t} \tag{3.86}$$

$$\frac{\partial \mathbf{H}}{\partial t} = \frac{\mathbf{H}^{n+1/2} - \mathbf{H}^{n-1/2}}{\Delta t} \tag{3.87}$$

$$\mathbf{J}_{hh}^n = \frac{\mathbf{J}_{hh}^{n+1/2} + \mathbf{J}_{hh}^{n-1/2}}{2} \tag{3.88}$$

$$\mathbf{J}_{ee}^{n+1/2} = \frac{\mathbf{J}_{ee}^{n+1} + \mathbf{J}_{ee}^n}{2} \tag{3.89}$$

To convert a frequency dependent function to the Z-Domain the bilinear transformation is used

3.7. Modelling of isotropic chiral material

$$i\omega = \frac{2}{\Delta t} \frac{1 - Z^{-1}}{1 + Z^{-1}} \quad (3.90)$$

This allows us to express the equations (3.83) with second order accuracy in the Z-Domain by approximating it via Padé approximants $b_0^{ij}, b_1^{ij}, b_2^{ij}, a_1^{ij}, a_2^{ij}$ with $ij = ee, \kappa e, hh, \kappa h$. \mathbf{J}_{ee} becomes for example

$$\mathbf{J}_{ee} = \frac{b_0^{ee} + b_1^{ee} Z^{-1} + b_2^{ee} Z^{-2}}{1 + a_1^{ee} Z^{-1} + a_2^{ee} Z^{-2}} \quad (3.91)$$

Going back to the time domain is straightforward because Z^{-m} acts as an decrease operator in time. For example with $m = 1$, $Z^{-1} \mathbf{J}_{ee}^{n+1} = \mathbf{J}_{ee}^n$, I go back one time step. Rearranging equation (3.91) and using $Z^{-m} \mathbf{F}^n = \mathbf{F}^{n-m}$ with \mathbf{F} an arbitrary field leads to

$$\mathbf{J}_{ee}^{n+1} = \mathbf{W}_{ee}^n + b_0^{ee} \mathbf{E}^{n+1} \quad (3.92)$$

$$\mathbf{W}_{ee}^{n+1} = b_1^{ee} \mathbf{E}^{n+1} - a_1^{ee} \mathbf{J}_{ee}^{n+1} + b_2^{ee} \mathbf{E}^n - a_2^{ee} \mathbf{J}_{ee}^n \quad (3.93)$$

$$\mathbf{J}_{\kappa h}^{n+1/2} = \mathbf{W}_{\kappa h}^{n-1/2} + b_0^{\kappa h} \mathbf{H}^{n+1/2} \quad (3.94)$$

$$\mathbf{W}_{\kappa h}^{n+1/2} = b_1^{\kappa h} \mathbf{H}^{n+1/2} - a_1^{\kappa h} \mathbf{J}_{\kappa h}^{n+1/2} + b_2^{\kappa h} \mathbf{J}_{\kappa h}^{n-1/2} - a_2^{\kappa h} \mathbf{J}_{\kappa h}^{n-1/2} \quad (3.95)$$

$$\mathbf{J}_{hh}^{n+1/2} = \mathbf{W}_{hh}^{n-1/2} + b_0^{hh} \mathbf{H}^{n+1/2} \quad (3.96)$$

$$\mathbf{W}_{hh}^{n+1/2} = b_1^{hh} \mathbf{H}^{n+1/2} - a_1^{hh} \mathbf{J}_{hh}^{n+1/2} + b_2^{hh} \mathbf{H}^{n-1/2} - a_2^{hh} \mathbf{J}_{hh}^{n-1/2} \quad (3.97)$$

$$\mathbf{J}_{\kappa e}^{n+1} = \mathbf{W}_{\kappa e}^n + b_0^{\kappa e} \mathbf{E}^{n+1} \quad (3.98)$$

$$\mathbf{W}_{\kappa e}^{n+1} = b_1^{\kappa e} \mathbf{E}^{n+1} - a_1^{\kappa e} \mathbf{J}_{\kappa e}^{n+1} + b_2^{\kappa e} \mathbf{E}^n - a_2^{\kappa e} \mathbf{J}_{\kappa e}^n \quad (3.99)$$

Discretising equations (3.84) and (3.85) and using the above conventions leads to

$$\begin{aligned} \mathbf{E}_{tot}^{n+1} &= \mathbf{E}_{tot}^n + \frac{\Delta t}{\varepsilon_\infty A^V} \left[\sum_{k=1}^{M_i^V} H_{scat,j,i,k}^{n+1/2} l_{j,i,k}^V + \varepsilon_0 \frac{\partial \mathbf{E}_{inc}^{n+1/2}}{\partial t} A^V \right. \\ &\quad \left. - \mathbf{J}_{ee}^{n+1/2} A^V + \mathbf{J}_{\kappa h_{av}}^{n+1/2} A^V \right] \end{aligned} \quad (3.100)$$

$$\begin{aligned} \mathbf{H}_{tot}^{n+1/2} &= \mathbf{H}_{tot}^{n-1/2} + \frac{\Delta t}{\mu_\infty A^D} \left[- \sum_{k=1}^{M_j^D} E_{scat,i,j,k}^n l_{i,j,k}^D + \mu_0 \frac{\partial \mathbf{H}_{inc}^n}{\partial t} A^D \right. \\ &\quad \left. - \mathbf{J}_{hh}^n A^D - \mathbf{J}_{\kappa e_{av}}^n A^D \right] \end{aligned} \quad (3.101)$$

using equations (3.88) and (3.89) for replacing \mathbf{J}_{hh}^n and $\mathbf{J}_{ee}^{n+1/2}$ and furthermore using equations (3.92)-(3.99), equations (3.100) and (3.101) become

$$\begin{aligned} \mathbf{E}_{tot}^{n+1} &= \mathbf{E}_{tot}^n + \frac{\Delta t}{\varepsilon_\infty A^V} \left[\sum_{k=1}^{M_i^V} H_{scat,j,i,k}^{n+1/2} l_{j,i,k}^V + \varepsilon_0 \frac{\partial \mathbf{E}_{inc}^{n+1/2}}{\partial t} A^V \right. \\ &\quad \left. + \frac{-\mathbf{W}_{ee}^n - b_0^{ee} \mathbf{E}_{tot}^{n+1} - \mathbf{J}_{ee}^n}{2} A^V + \mathbf{J}_{\kappa h_{av}}^{n+1/2} A^V \right] \end{aligned} \quad (3.102)$$

3. Numerical Solution of Maxwell Equations

$$\begin{aligned} \mathbf{H}_{tot}^{n+1/2} = \mathbf{H}_{tot}^{n-1/2} + \frac{\Delta t}{\mu_\infty A^D} & \left[- \sum_{k=1}^{M_j^D} E_{scat,i,j,k}^n l_{i,j,k}^D + \mu_0 \frac{\partial \mathbf{H}_{inc}^n}{\partial t} A^D \right. \\ & \left. + \frac{-\mathbf{W}_{hh}^{n-1/2} - b_0^{hh} \mathbf{H}_{tot}^{n+1/2} - \mathbf{J}_{hh}^{n-1/2}}{2} A^D - \mathbf{J}_{\kappa e_{av}}^n A^D \right] \end{aligned} \quad (3.103)$$

Rearranging equations (3.102) and (3.103) to move \mathbf{E}_{tot}^{n+1} and $\mathbf{H}_{tot}^{n+1/2}$ to the left side lead to

$$\begin{aligned} \mathbf{E}_{tot}^{n+1} = \frac{1}{2\varepsilon_\infty + b_0^{ee} \Delta t} & \left[2\varepsilon_\infty \mathbf{E}_{tot}^n + \Delta t \left\{ 2 \left(\frac{1}{A^V} \sum_{k=1}^{M_i^V} H_{scat,j,i,k}^{n+1/2} l_{j,i,k}^V \right. \right. \right. \\ & \left. \left. \left. + \varepsilon_0 \frac{\partial \mathbf{E}_{inc}^{n+1/2}}{\partial t} A^V \right) - \mathbf{W}_{ee}^n - \mathbf{J}_{ee}^n + 2\mathbf{J}_{\kappa h_{av}}^{n+1/2} A^V \right\} \right] \end{aligned} \quad (3.104)$$

$$\begin{aligned} \mathbf{H}_{tot}^{n+1/2} = \frac{1}{2\mu_\infty + b_0^{hh} \Delta t} & \left[2\mu_\infty \mathbf{H}_{tot}^{n-1/2} + \Delta t \left\{ 2 \left(\frac{-1}{A^D} \sum_{k=1}^{M_j^D} E_{scat,i,j,k}^n l_{i,j,k}^D \right. \right. \right. \\ & \left. \left. \left. + \mu_0 \frac{\partial \mathbf{H}_{inc}^n}{\partial t} \right) - \mathbf{W}_{hh}^{n-1/2} - \mathbf{J}_{hh}^{n-1/2} - 2\mathbf{J}_{\kappa e_{av}}^n \right\} \right] \end{aligned} \quad (3.105)$$

This equation corresponds to the ones derived by [103]. Now I will adapt them to our unstructured mesh. Therefore I project all the vectors to the Delaunay edges e_i or Voronoi edges e_j with i, j an index for a Delaunay or Voronoi Edge respectively. The electric field vectors are projected to the Delaunay edges and the magnetic field vectors are projected to the Voronoi edges, leading finally to the update equations

$$\begin{aligned} E_{tot,i}^{n+1} = \frac{1}{2\varepsilon_\infty + b_0^{ee} \Delta t} & \left[2\varepsilon_\infty E_{tot,i}^n + \Delta t \left\{ 2 \left(\frac{1}{A^V} \sum_{k=1}^{M_i^V} H_{scat,j,i,k}^{n+1/2} l_{j,i,k}^V \right. \right. \right. \\ & \left. \left. \left. + \varepsilon_0 \frac{\partial E_{inc,i}^{n+1/2}}{\partial t} A^V \right) - W_{ee,i}^n - J_{ee,i}^n + 2J_{\kappa h,i_{av}}^{n+1/2} \right\} \right] \end{aligned} \quad (3.106)$$

$$\begin{aligned} H_{tot,j}^{n+1/2} = \frac{1}{2\mu_\infty + b_0^{hh} \Delta t} & \left[2\mu_\infty H_{tot,j}^{n-1/2} + \Delta t \left\{ 2 \left(\frac{-1}{A^D} \sum_{k=1}^{M_j^D} E_{scat,i,j,k}^n l_{i,j,k}^D \right. \right. \right. \\ & \left. \left. \left. + \mu_0 \frac{\partial H_{inc,j}^n}{\partial t} \right) - W_{hh,j}^{n-1/2} - J_{hh,j}^{n-1/2} - 2J_{\kappa e,j_{av}}^n \right\} \right] \end{aligned} \quad (3.107)$$

It is important to note that the field vectors are not first calculated and then projected to the edges, but equations (3.106) and (3.107) are applied directly. For a dispersive

non-chiral material $J_{\{\kappa e, j\}_{av}}$ and $J_{\{\kappa h, i\}_{av}}$ are equal to zero, leading to the simplicity of a 1D code for a 3D case. The difficulty of equations (3.106) and (3.107) lies in the coupling terms $J_{\kappa h, i_{av}}^{n+1/2}$ and $J_{\kappa e, j_{av}}^n$. In the co-volume scheme the electric field projections are stored on the Delaunay edges and the magnetic field projections on the Voronoi edges. But $\mathbf{J}_{\kappa h_{av}}^{n+1/2}$ depends on the magnetic field and has to be linked to the Delaunay edges and $\mathbf{J}_{\kappa e_{av}}^n$ depends on the electric field and has to be linked to the Voronoi edges. In Figure 3.12 I illustrate in the case of the electric field how to transfer it from the Delaunay to the Voronoi edges.

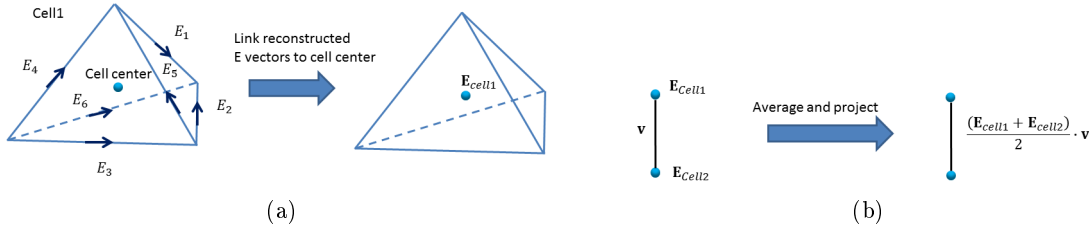


Figure 3.12.: *Associating electric field to Voronoi edges: (a) Reconstruct the electric field vector from its projections on the Delaunay edges and link this vector to the corresponding cell center. ; (b) average electric field vectors from cell centers linked to the same Voronoi edge \mathbf{v} and project them to the corresponding edge.*

In the case of a tetrahedra I have 6 Delaunay edges. On each edge an electric field projection E_i , $i = 1, \dots, 6$ is stored. Using these projections electric field vector \mathbf{E}_{Cell1} is reconstructed and linked to the cell center of the corresponding cell. A Voronoi edge connects cell centers of two neighboring cells. The same procedure is applied field reconstruction to the second cell. Finally the field vectors linked to the cell centers are averaged and projected to the corresponding Voronoi edge $([(\mathbf{E}_{Cell1} + \mathbf{E}_{cell2})/2] \cdot \mathbf{v})$. When the electric field is successfully linked to the voronoi edges $J_{\kappa e, i_{av}}^n$ is computed. The identical approach is used for the magnetic field. For additional informations on the reconstruction process of the field vectors from the projections please refer to subsection 3.6.4.

3.7.3. Boundary conditions

To satisfy the boundary conditions the same weighted averaging on the Padé approximants is applied as I used for the isotropic and anisotropic dielectric cases described in sections 3.5.1 and 3.6.3. Not all the Padé approximants are averaged, but only the coefficients on the numerator. To explain this I consider the case of the permeability associated to the Voronoi edges as illustrated in Figure 3.13.

3. Numerical Solution of Maxwell Equations

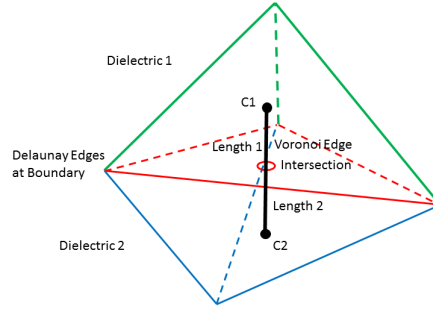


Figure 3.13.: Representation of a voronoi Edge and the corresponding cells.

Applying the bilinear transformation to $(\mu_\infty - \mu(\omega))$ leads to $(\mu_\infty - P(z))$ with

$$P(z) = \frac{b_0 + b_1 z^{-1} + b_2 z^{-2}}{1 + a_1 z^{-1} + a_2 z^{-2}} \quad (3.108)$$

The constitutive equation for the displacement flux becomes

$$\mathbf{B}(z)_i = \mu(z)\mathbf{H}(z)_i \quad (3.109)$$

$$\Leftrightarrow \mathbf{B}(z)_i = (\mu_\infty - P(z))\mathbf{H}(z)_i \quad (3.110)$$

where $i = 1, 2$ corresponds to dielectric medium 1 or 2. The average magnetic flux at the interface becomes

$$\mathbf{B}(z)_{av} = \frac{l_1 \mathbf{B}(z)_1 + l_2 \mathbf{B}(z)_2}{l_1 + l_2} \quad (3.111)$$

$$\Leftrightarrow \mathbf{B}(z)_{av} = \frac{l_1(\mu_{\infty,1} - P(z)_1)\mathbf{H}(z)_1 + l_2(\mu_{\infty,1} - P(z)_2)\mathbf{H}(z)_2}{(l_1 + l_2)} \quad (3.112)$$

$$\Leftrightarrow \mathbf{B}(z)_{av} = w_1(\mu_{\infty,1} - P(z)_1)\mathbf{H}(z)_1 + w_2(\mu_{\infty,2} - P(z)_2)\mathbf{H}(z)_2 \quad (3.113)$$

Where the length l of the Voronoi edge from the intersection point to the corresponding cell center acts as weight. Following equation 3.113, with $w_i = l_i/(l_1 + l_2)$, we see that only the numerator of $P(z)$ is multiplied by the weight.

3.7.4. Updating scheme

1. Magnetic field loop. Calculation of $H_{scat,j}^{n+1/2}$

- a) Reconstruct \mathbf{E}_{scat}^n from Delaunay edges and project it to the Voronoi edges leading to $E_{scat,j}^n$
- b) add the incident field to obtain the total field vector $E_{tot,j}^n = E_{scat,j}^n + E_{inc,j}^n$
- c) compute $J_{ke,j}^n$ with equations (3.98) and (3.99)

- d) calculate $H_{tot,j}^{n+1/2}$ using equation (3.107)
 - e) compute $J_{hh,j}^{n+1/2}$ using equations (3.96) and (3.97)
 - f) compute $H_{scat,j}^{n+1/2} = H_{tot,j}^{n+1/2} - H_{inc,j}^{n+1/2}$
2. Electric field loop. Calculation of $E_{scat,i}^{n+1}$
- a) Reconstruct $\mathbf{H}_{scat}^{n+1/2}$ from Voronoi edges and project it to the Delaunay edges leading to $H_{scat,i}^{n+1/2}$
 - b) add the incident field to obtain the total field vector $H_{tot,i}^{n+1/2} = H_{scat,i}^{n+1/2} + H_{inc,i}^{n+1/2}$
 - c) compute $J_{kh,i}^{n+1/2}$ with equations (3.94) and (3.95)
 - d) calculate $E_{tot,i}^{n+1}$ using equation (3.106)
 - e) compute $J_{ee,i}^{n+1}$ using equations (3.92) and (3.93)
 - f) compute $E_{scat,i}^{n+1} = E_{tot,i}^{n+1} - E_{inc,i}^{n+1}$

3.8. Modelling of bi-anisotropic materials

The electromagnetic modelling of bi-anisotropic materials is a very challenging task because all the methods developed so far have to be combined because the material parameters are frequency dependent second order tensors with a non zero chirality tensor $\varepsilon(\omega), \mu(\omega), \kappa(\omega) \rightarrow \bar{\bar{\varepsilon}}(\omega), \bar{\bar{\mu}}(\omega), \bar{\bar{\kappa}}(\omega)$. The applications for bianisotropic materials may be similar to those of chiral materials but they allow an additional control of the material properties due to the anisotropy. Possible applications are radomes [130], waveguides [145, 22, 23], polarisers[105], backward wave media [128] or cloaking devices [58]. I am interested in modelling a material based upon small (with respect to the wavelength) metallic omega inclusions periodically arranged in a dielectric matrix to compare with experiments. This algorithm is mainly based upon the work of Nayyeri [95], but I adapted it to allow me to model also frequency dependent composites. In this case the chirality should be zero.

3.8.1. Problem formulation

As for the bianisotropic case I consider the constitutive equations

$$\begin{aligned} \mathbf{D}_{tot}(\omega) &= \bar{\bar{\varepsilon}}(\omega) \mathbf{E}_{tot}(\omega) - \frac{i}{c} \bar{\bar{\kappa}}(\omega) \mathbf{H}_{tot}(\omega) \\ \mathbf{B}_{tot}(\omega) &= \bar{\bar{\mu}}(\omega) \mathbf{H}_{tot}(\omega) + \frac{i}{c} \bar{\bar{\kappa}}^T(\omega) \mathbf{E}_{tot}(\omega) \end{aligned}$$

3. Numerical Solution of Maxwell Equations

where all the material parameters are second order tensors. For the material parameters I assume the following frequency dependence as suggested by [128]

$$\bar{\bar{\epsilon}}(\omega) = \epsilon_0 \left(\bar{\bar{\epsilon}}_\infty + \frac{\omega_\epsilon^2}{\omega_\epsilon^2 - \omega^2 + i2\omega_\epsilon \xi_\epsilon \omega} (\bar{\bar{\epsilon}}_s - \bar{\bar{\epsilon}}_\infty) \right) \quad (3.114)$$

$$\bar{\bar{\mu}}(\omega) = \mu_0 \left(\bar{\bar{\mu}}_\infty + \frac{\omega^2}{\omega_\mu^2 - \omega^2 + i2\omega_\mu \xi_\mu \omega} (\bar{\bar{\mu}}_s - \bar{\bar{\mu}}_\infty) \right) \quad (3.115)$$

$$\hat{\bar{\bar{\kappa}}} = i\bar{\bar{\kappa}}(\omega) = i \frac{\omega_\kappa^2 \omega}{\omega_\kappa^2 - \omega^2 + i2\omega_\kappa \xi_\kappa \omega} \bar{\bar{\tau}}_\kappa \quad (3.116)$$

Where ω_ϵ , ω_μ , ω_κ the resonance frequencies, ξ_ϵ , ξ_μ , ξ_κ the dampings, $\bar{\bar{\epsilon}}_s$, $\bar{\bar{\mu}}_s$, $\bar{\bar{\epsilon}}_\infty$, $\bar{\bar{\mu}}_\infty$ typically diagonal tensors representing the low frequency (static) and high frequency limit respectively. $\bar{\bar{\tau}}_\kappa$ is the magnetoelectric coupling coefficient matrix. For the omega inclusions a reciprocal model is assumed, meaning $\bar{\bar{\epsilon}}$, $\bar{\bar{\mu}}$ are symmetric and $\bar{\bar{\kappa}} = -\bar{\bar{\kappa}}^T$. According to [128], for a low density of omega particles the material is best described by the equations (3.114)-(3.116) where the permittivity follows a Lorentz and the chirality a Condon model. Consider that the suggested permeability has a ω^2 frequency dependence in the numerator in contrast to the Lorentz model. For a plane wave propagating in z direction with $\mathbf{E}(z=0) = E_0 \hat{\mathbf{x}}$, $\mathbf{H}(z=0) = -H_0 \hat{\mathbf{y}}$ with normal incidence on a bianisotropic material, in $\bar{\bar{\kappa}}$ the only non zero element is $\kappa_{x,y}$ or $-\kappa_{y,x}$.

$$\hat{\mathbf{x}} = \begin{pmatrix} 1 \\ 0 \\ 0 \end{pmatrix}, \quad \hat{\mathbf{y}} = \begin{pmatrix} 0 \\ 1 \\ 0 \end{pmatrix}, \quad \hat{\mathbf{z}} = \begin{pmatrix} 0 \\ 0 \\ 1 \end{pmatrix}$$

To create an omega material with its optical axis rotated by the Euler angles α , β , γ with respect to the propagation vector I define the rotation matrix as follows.

$$\bar{\bar{U}} = \begin{pmatrix} \cos(\alpha) & -\sin(\alpha) & 0 \\ \sin(\alpha) & \cos(\alpha) & 0 \\ 0 & 0 & 1 \end{pmatrix} \times \begin{pmatrix} 1 & 0 & 0 \\ 0 & \cos(\beta) & -\sin(\beta) \\ 0 & \sin(\beta) & \cos(\beta) \end{pmatrix} \begin{pmatrix} \cos(\gamma) & -\sin(\gamma) & 0 \\ \sin(\gamma) & \cos(\gamma) & 0 \\ 0 & 0 & 1 \end{pmatrix}$$

The material parameters in the rotated coordinates are calculated according to

$$\begin{aligned} \bar{\bar{\epsilon}}_{rotated} &= \bar{\bar{U}}^T \bar{\bar{\epsilon}} \bar{\bar{U}} \\ \bar{\bar{\mu}}_{rotated} &= \bar{\bar{U}}^T \bar{\bar{\mu}} \bar{\bar{U}} \\ \bar{\bar{\kappa}}_{rotated} &= \bar{\bar{U}}^T \bar{\bar{\kappa}} \bar{\bar{U}} \end{aligned}$$

Instead of using the method of Nayyeri [95] which is actually an adapted version of Demir [37] for the omega inclusions I decided to generalise the method suggested by Pereda [103]. Therefore I directly take the equations (3.100) and (3.101) from the isotropic chiral material and adapt them to a bianisotropic material.

$$\begin{aligned} \mathbf{E}_{tot}^{n+1} &= \mathbf{E}_{tot}^n + \bar{\bar{\epsilon}}_\infty^{-1} \Delta t \left[\frac{1}{A^V} \sum_{k=1}^{M_i^V} H_{scat,j_i,k}^{n+0.5} l_{j_i,k}^V + \epsilon_0 \frac{\partial \mathbf{E}_{inc}^{n+1/2}}{\partial t} \right. \\ &\quad \left. - \mathbf{J}_{ee,tot}^{n+1/2} + \mathbf{J}_{\kappa h_{av},tot}^{n+1/2} \right] \end{aligned} \quad (3.117)$$

3.8. Modelling of bi-anisotropic materials

$$\mathbf{H}_{tot}^{n+1/2} = \mathbf{H}_{tot}^{n-1/2} + \bar{\mu}_{\infty}^{-1} \Delta t \left[-\frac{1}{A^D} \sum_{k=1}^{M_j^D} E_{scat,i_j,k}^n l_{i_j,k}^D + \mu_0 \frac{\partial \mathbf{H}_{inc}^n}{\partial t} - \mathbf{J}_{hh,tot}^n - \mathbf{J}_{\kappa e_{av},tot}^n \right] \quad (3.118)$$

Where \mathbf{J}_{hh} , $\mathbf{J}_{\kappa h}$, \mathbf{J}_{ee} , $\mathbf{J}_{\kappa e}$ are defined as follows

$$\mathbf{J}_{hh,tot}^{n+1/2} = i\omega(\bar{\mu}(\omega) - \bar{\mu}_{\infty})\mathbf{H}_{tot}^{n+1/2}(\omega) \quad (3.119)$$

$$\mathbf{J}_{\kappa h,tot}^{n+1/2} = \frac{1}{c} i\omega \hat{\kappa}(\omega) \mathbf{H}_{tot}^{n+1/2}(\omega) \quad (3.120)$$

$$\mathbf{J}_{ee,tot}^{n+1} = i\omega(\bar{\varepsilon}(\omega) - \bar{\varepsilon}_{\infty})\mathbf{E}_{tot}^{n+1}(\omega) \quad (3.121)$$

$$\mathbf{J}_{\kappa e,tot}^{n+1} = \frac{1}{c} i\omega \hat{\kappa}^T(\omega) \mathbf{E}_{tot}^{n+1}(\omega) \quad (3.122)$$

The electric field is defined at integer and the magnetic field at half-integer time steps.

$$\mathbf{J}_{hh}^n = \frac{\mathbf{J}_{hh}^{n+1/2} + \mathbf{J}_{hh}^{n-1/2}}{2} \quad (3.123)$$

$$\mathbf{J}_{ee}^{n+1/2} = \frac{\mathbf{J}_{ee}^{n+1} + \mathbf{J}_{ee}^n}{2} \quad (3.124)$$

I use the Z-transform suggested by Sullivan to convert frequency dependent tensors to the Z and later to the time domain, but this time I derive the coefficients analytically using the table 3.1. I cannot use the bilinear transformation because due to the second order tensor material parameters it is not possible to simply extract the fields \mathbf{E}_{tot}^{n+1} , $\mathbf{H}_{tot}^{n+1/2}$ as I did it in equations (3.102) and (3.103) .

Frequency Domain	Z Domain
$F(\omega) = \frac{\beta}{(\rho^2 + \beta^2) + j2\rho\omega - \omega^2}$	$F(z) = \frac{e^{-\rho\Delta t} \sin(\beta\Delta t) z^{-1}}{1 - 2e^{-\rho\Delta t} \cos(\beta) z^{-1} + e^{-2\rho\Delta t} z^{-2}}$
$F(\omega) = \beta$	$F(z) = \frac{\beta}{\Delta t}$
$i\omega F(\omega)$	$\left(\frac{1-z^{-1}}{\Delta t}\right) F(z)$
$\omega^2 F(\omega) = -(i\omega)^2 F(\omega)$	$-\left(\frac{1-z^{-1}}{\Delta t}\right)^2 F(z)$
$i\omega\omega^2 F(\omega) = -(i\omega)^3 F(\omega)$	$-\left(\frac{1-z^{-1}}{\Delta t}\right)^3 F(z)$

Table 3.1.: Analytical Z-Transform. ρ , β are constants

I assume that only the elements of $\bar{\varepsilon}_s$, $\bar{\varepsilon}_{\infty}$, $\bar{\mu}_s$, $\bar{\mu}_{\infty}$ and $\bar{\tau}_{\kappa}$ are anisotropic but the frequency responses

$$\frac{\omega_{\varepsilon}^2}{\omega_{\varepsilon}^2 - \omega^2 + i2\omega_{\varepsilon}\xi_{\varepsilon}\omega}, \quad \frac{\omega_{\mu}^2}{\omega_{\mu}^2 - \omega^2 + i2\omega_{\mu}\xi_{\mu}\omega}, \quad \frac{\omega_{\kappa}^2\omega}{\omega_{\mu}^2 - \omega^2 + i2\omega_{\mu}\xi_{\mu}\omega} \quad (3.125)$$

3. Numerical Solution of Maxwell Equations

of equations (3.114)-(3.116) are independent upon the directions. To update equation (3.117) and (3.118) I have to update \mathbf{J}_{hh} , $\mathbf{J}_{\kappa h}$, \mathbf{J}_{ee} , $\mathbf{J}_{\kappa e}$ from equation (3.121). Therefore I actually have to find the Z-transform of equations (3.125) instead of equations (3.114)-(3.116). In the Z-Domain the constitutive equation are defined as

$$\mathbf{D}(z) = \bar{\bar{\epsilon}}(z) \mathbf{E}(z) \Delta t - \frac{1}{c} i \bar{\bar{\kappa}}(z) \mathbf{H}(z) \Delta t \quad (3.126)$$

$$\mathbf{B}(z) = \bar{\bar{\mu}}(z) \mathbf{H}(z) \Delta t + \frac{1}{c} i \bar{\bar{\kappa}}^T(z) \mathbf{E}(z) \Delta t \quad (3.127)$$

in contrast to his first paper [123] where the time step Δt was included in the definition of the Z transform, in a later publication [124] Sullivan removed the factor from the definition and added it in the constitutive equation to guarantee mathematical consistency. I first determine the analytical pade coefficients of $i\omega(\bar{\bar{\epsilon}}(\omega) - \bar{\bar{\epsilon}}_\infty)$

$$F_\epsilon(\omega) = i\omega(\bar{\bar{\epsilon}}(\omega) - \bar{\bar{\epsilon}}_\infty) \quad (3.128)$$

$$= i\omega \frac{\omega_\epsilon}{\sqrt{1 - \xi_\epsilon^2}} (\bar{\bar{\epsilon}}_s - \bar{\bar{\epsilon}}_\infty) \quad (3.129)$$

$$\frac{\omega_\epsilon \sqrt{1 - \xi_\epsilon^2}}{(\omega_\epsilon \xi_\epsilon)^2 + (\omega_\epsilon \sqrt{1 - \xi_\epsilon^2})^2 + i\omega 2\omega_\epsilon \xi_\epsilon - \omega^2} \quad (3.130)$$

$$F_\epsilon(z) = \frac{\omega_\epsilon}{\sqrt{1 - \xi_\epsilon^2}} \left(\frac{1 - z^{-1}}{\Delta t} \right) (\bar{\bar{\epsilon}}_s - \bar{\bar{\epsilon}}_\infty) \quad (3.131)$$

$$\frac{e^{-\omega_\epsilon \xi_\epsilon \Delta t} \sin(\omega_\epsilon \sqrt{1 - \xi_\epsilon^2} \Delta t) z^{-1}}{1 - 2e^{-\omega_\epsilon \xi_\epsilon \Delta t} \cos(\omega_\epsilon \sqrt{1 - \xi_\epsilon^2} \Delta t) z^{-1} + e^{-2\omega_\epsilon \xi_\epsilon \Delta t} z^{-2}} \quad (3.132)$$

$$= \frac{C_{\epsilon 1} z^{-1} - C_{\epsilon 1} z^{-2}}{1 - C_{\epsilon 2} z^{-1} + C_{\epsilon 3} z^{-2}} (\bar{\bar{\epsilon}}_s - \bar{\bar{\epsilon}}_\infty) \quad (3.133)$$

$$F_\kappa(\omega) = i\omega \frac{1}{c} \hat{\bar{\bar{\kappa}}}(\omega) \quad (3.134)$$

$$= \frac{1}{c} (i\omega)^2 \frac{\omega_\kappa}{\sqrt{1 - \xi_\kappa^2}} \bar{\bar{\tau}}_\kappa \quad (3.135)$$

$$\frac{\omega_\kappa \sqrt{1 - \xi_\kappa^2}}{(\omega_\kappa \xi_\kappa)^2 + (\omega_\kappa \sqrt{1 - \xi_\kappa^2})^2 + i\omega 2\omega_\kappa \xi_\kappa - \omega^2} \quad (3.136)$$

$$F_\kappa(z) = - \left(\frac{1 - z^{-1}}{\Delta t} \right)^2 \frac{1}{c} \frac{\omega_\kappa}{\sqrt{1 - \xi_\kappa^2}} \bar{\bar{\tau}}_\kappa \quad (3.137)$$

$$\frac{e^{-\omega_\kappa \xi_\kappa \Delta t} \sin(\omega_\kappa \sqrt{1 - \xi_\kappa^2} \Delta t) z^{-1}}{1 - 2e^{-\omega_\kappa \xi_\kappa \Delta t} \cos(\omega_\kappa \sqrt{1 - \xi_\kappa^2} \Delta t) z^{-1} + e^{-2\omega_\kappa \xi_\kappa \Delta t} z^{-2}} \quad (3.138)$$

$$= \frac{-C_{\kappa 1} z^{-1} + 2C_{\kappa 1} z^{-2} C_{\kappa 1} z^{-3}}{1 - C_{\kappa 2} z^{-1} + C_{\kappa 3} z^{-2}} \bar{\bar{\tau}}_\kappa \quad (3.139)$$

3.8. Modelling of bi-anisotropic materials

because $\mathbf{J}_{\kappa h}$ and $\mathbf{J}_{\kappa e}$ only appear at time step $n + 1/2$ and n in equations (3.117) and (3.118) for this case I can also use the bilinear transformation as before

$$i\omega = \frac{2}{\Delta t} \frac{1 - Z^{-1}}{1 + Z^{-1}}$$

and rewrite

$$F_{\kappa}(\omega) = i\omega \frac{1}{c} \hat{\kappa}(\omega) \rightarrow F_{\kappa}(z) = \frac{1}{c} \frac{b_0 + b_1 z^{-1} + b_2 z^{-2}}{1 + a_1 z^{-1} + a_2 z^{-2}} \bar{\bar{\kappa}}$$

$$\begin{aligned} F_{\mu}(\omega) &= i\omega(\bar{\mu}(\omega) - \bar{\mu}_{\infty}) \\ &= -(i\omega)^3 \frac{1}{\omega_{\mu} \sqrt{1 - \xi_{\mu}^2}} (\bar{\mu}(\omega) - \bar{\mu}_{\infty}) \\ &\quad \frac{\omega_{\mu} \sqrt{1 - \xi_{\mu}^2}}{(\omega_{\mu} \xi_{\mu})^2 + (\omega_{\mu} \sqrt{1 - \xi_{\mu}^2})^2 + i\omega 2\omega_{\mu} \xi_{\mu} - \omega^2} \\ F_{\mu}(z) &= -\left(\frac{1 - z^{-1}}{\Delta t}\right)^3 \frac{1}{\omega_{\mu} \sqrt{1 - \xi_{\mu}^2}} (\bar{\mu}(\omega) - \bar{\mu}_{\infty}) \\ &\quad \frac{e^{-\omega_{\mu} \xi_{\mu} \Delta t} \sin(\omega_{\mu} \sqrt{1 - \xi_{\mu}^2} \Delta t) z^{-1}}{1 - 2e^{-\omega_{\mu} \xi_{\mu} \Delta t} \cos(\omega_{\mu} \sqrt{1 - \xi_{\mu}^2} \Delta t) z^{-1} + e^{-2\omega_{\mu} \xi_{\mu} \Delta t} z^{-2}} \\ &= \frac{-C_{\mu 1} z^{-1} + 3C_{\mu 1} z^{-2} - 3C_{\mu 1} z^{-3} + C_{\mu 1} z^{-4}}{1 - C_{\mu 2} z^{-1} + C_{\mu 3} z^{-2}} (\bar{\mu}(\omega) - \bar{\mu}_{\infty}) \end{aligned}$$

with all the coefficients defined as

$$C_{\varepsilon 1} = \frac{\omega_{\varepsilon} e^{-\omega_{\varepsilon} \xi_{\varepsilon} \Delta t} \sin(\omega_{\varepsilon} \sqrt{1 - \xi_{\varepsilon}^2} \Delta t)}{\Delta t \sqrt{1 - \xi_{\varepsilon}^2}} \quad (3.140)$$

$$C_{\varepsilon 2} = 2e^{-\omega_{\varepsilon} \xi_{\varepsilon} \Delta t} \cos(\omega_{\varepsilon} \sqrt{1 - \xi_{\varepsilon}^2} \Delta t) \quad (3.141)$$

$$C_{\varepsilon 3} = e^{-2\omega_{\varepsilon} \xi_{\varepsilon} \Delta t} \quad (3.142)$$

$$C_{\mu 1} = \frac{e^{-\omega_{\mu} \xi_{\mu} \Delta t} \sin(\omega_{\mu} \sqrt{1 - \xi_{\mu}^2} \Delta t)}{\Delta t^3 \omega_{\mu} \sqrt{1 - \xi_{\mu}^2}} \quad (3.143)$$

$$C_{\mu 2} = 2e^{-\omega_{\mu} \xi_{\mu} \Delta t} \cos(\omega_{\mu} \sqrt{1 - \xi_{\mu}^2} \Delta t) \quad (3.144)$$

$$C_{\mu 3} = e^{-2\omega_{\mu} \xi_{\mu} \Delta t} \quad (3.145)$$

3. Numerical Solution of Maxwell Equations

$$C_{\kappa 1} = \frac{\omega_{\kappa} e^{-\omega_{\kappa} \xi_{\kappa} \Delta t} \sin\left(\omega_{\kappa} \sqrt{1 - \xi_{\kappa}^2} \Delta t\right)}{\Delta t^2 c \sqrt{1 - \xi_{\kappa}^2}} \quad (3.146)$$

$$C_{\kappa 2} = 2e^{-\omega_{\kappa} \xi_{\kappa} \Delta t} \cos\left(\omega_{\kappa} \sqrt{1 - \xi_{\kappa}^2} \Delta t\right) \quad (3.147)$$

$$C_{\kappa 3} = e^{-2\omega_{\kappa} \xi_{\kappa} \Delta t} \quad (3.148)$$

$$b_0 = \frac{4\omega_{\kappa}^2}{\omega_{\kappa}^2 \Delta t^2 + 4\Delta t \omega_{\kappa} \xi_{\kappa} + 4} \quad (3.149)$$

$$b_1 = -2b_0 \quad (3.150)$$

$$b_2 = b_0 \quad (3.151)$$

$$a_1 = \frac{2\omega_{\kappa}^2 \Delta t^2 - 8}{\omega_{\kappa}^2 \Delta t^2 + 4\Delta t \omega_{\kappa} \xi_{\kappa} + 4} \quad (3.152)$$

$$a_2 = \frac{\omega_{\kappa}^2 \Delta t^2 - 4\Delta t \omega_{\kappa} \xi_{\kappa} + 4}{\omega_{\kappa}^2 \Delta t^2 + 4\Delta t \omega_{\kappa} \xi_{\kappa} + 4} \quad (3.153)$$

With all these definitions the equations 3.121 become

$$\mathbf{J}_{hh,tot}^{n+1/2} = \frac{-C_{\mu 1} z^{-1} + 3C_{\mu 1} z^{-2} - 3C_{\mu 1} z^{-3} + C_{\mu 1} z^{-4}}{1 - C_{\mu 2} z^{-1} + C_{\mu 3} z^{-2}} (\bar{\mu}_s - \bar{\mu}_{\infty}) \mathbf{H}_{tot}^{n+1/2} \quad (3.154)$$

$$\mathbf{J}_{\kappa h,tot}^{n+1/2} = \frac{1}{c} \frac{b_0 + b_1 z^{-1} + b_2 z^{-2}}{1 + a_1 z^{-1} + a_2 z^{-2}} \bar{\tau}_{\kappa} \mathbf{H}_{tot}^{n+1/2}(\omega) \quad (3.155)$$

$$\mathbf{J}_{ee,tot}^{n+1} = \frac{C_{\varepsilon 1} z^{-1} - C_{\varepsilon 1} z^{-2}}{1 - C_{\varepsilon 2} z^{-1} + C_{\varepsilon 3} z^{-2}} (\bar{\varepsilon}_s - \bar{\varepsilon}_{\infty}) \mathbf{E}_{tot}^{n+1}(\omega) \quad (3.156)$$

$$\mathbf{J}_{\kappa e,tot}^{n+1} = \frac{1}{c} \frac{b_0 + b_1 z^{-1} + b_2 z^{-2}}{1 + a_1 z^{-1} + a_2 z^{-2}} \bar{\tau}_{\kappa}^T \mathbf{E}_{tot}^{n+1}(\omega) \quad (3.157)$$

$$\begin{aligned} \mathbf{J}_{hh,tot}^{n+1/2} &= -C_{\mu 1} (\bar{\mu}_s - \bar{\mu}_{\infty}) \mathbf{H}_{tot}^{n-1/2} + 3C_{\mu 1} (\bar{\mu}_s - \bar{\mu}_{\infty}) \mathbf{H}_{tot}^{n-3/2} \\ &\quad - 3C_{\mu 1} (\bar{\mu}_s - \bar{\mu}_{\infty}) \mathbf{H}_{tot}^{n-5/2} + C_{\mu 1} (\bar{\mu}_s - \bar{\mu}_{\infty}) \mathbf{H}_{tot}^{n-7/2} \\ &\quad + C_{\mu 2} \mathbf{J}_{hh,tot}^{n-1/2} - C_{\mu 3} \mathbf{J}_{hh,tot}^{n-3/2} \end{aligned} \quad (3.158)$$

$$\begin{aligned} \mathbf{J}_{\kappa h,tot}^{n+1/2} &= \frac{1}{c} \left(b_0 \bar{\tau}_{\kappa} \mathbf{H}_{tot}^{n+1/2} + b_1 \bar{\tau}_{\kappa} \mathbf{H}_{tot}^{n-1/2} + b_2 \bar{\tau}_{\kappa} \mathbf{H}_{tot}^{n-3/2} \right) \\ &\quad - a_1 \mathbf{J}_{\kappa h,tot}^{n-1/2} - a_2 \mathbf{J}_{\kappa h,tot}^{n-3/2} \end{aligned} \quad (3.159)$$

$$\begin{aligned} \mathbf{J}_{ee,tot}^{n+1} &= C_{\varepsilon 1} (\bar{\varepsilon}_s - \bar{\varepsilon}_{\infty}) \mathbf{E}_{tot}^n - C_{\varepsilon 1} (\bar{\varepsilon}_s - \bar{\varepsilon}_{\infty}) \mathbf{E}_{tot}^{n-1} \\ &\quad + C_{\varepsilon 2} \mathbf{J}_{ee,tot}^n - C_{\varepsilon 3} \mathbf{J}_{ee,tot}^{n-1} \end{aligned} \quad (3.160)$$

$$\begin{aligned} \mathbf{J}_{\kappa e,tot}^{n+1} &= \frac{1}{c} \left(b_0 \bar{\tau}_{\kappa}^T \mathbf{E}_{tot}^{n+1} + b_1 \bar{\tau}_{\kappa}^T \mathbf{E}_{tot}^n + b_2 \bar{\tau}_{\kappa}^T \mathbf{E}_{tot}^{n-1} \right) \\ &\quad - a_1 \mathbf{J}_{\kappa e,tot}^n - a_2 \mathbf{J}_{\kappa e,tot}^{n-1} \end{aligned} \quad (3.161)$$

3.8. Modelling of bi-anisotropic materials

By comparing the Lorentz model with the one suggested by [128] with the ω^2 dependence I figured out that for dampings $\xi_\mu \leq 0.1$ they nearly show the same behaviour. If I take a damping suggested by [95] of $\xi_\mu = 0.5$ the differences become more important as can be seen in Figure 3.14.

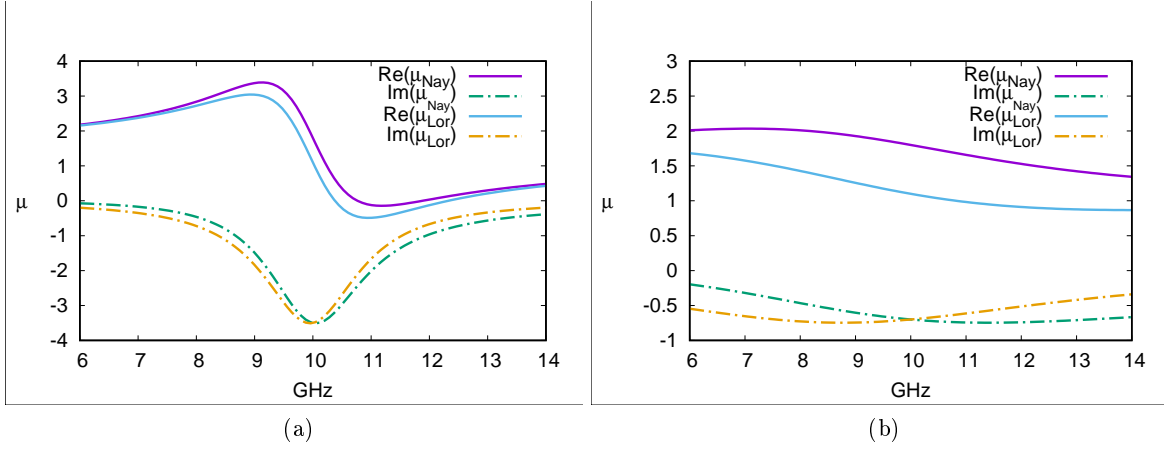


Figure 3.14.: Comparison of permeability model suggested by Nayyeri and the Lorentz model (a) $\xi_\mu = 0.1$; (b) $\xi_\mu = 0.5$

If I change however the frequency independent term in equation (3.115) from μ_s to μ_∞ , even for higher dampings, the functions become much more similar or even identical especially at the resonance frequency, our region of interest.

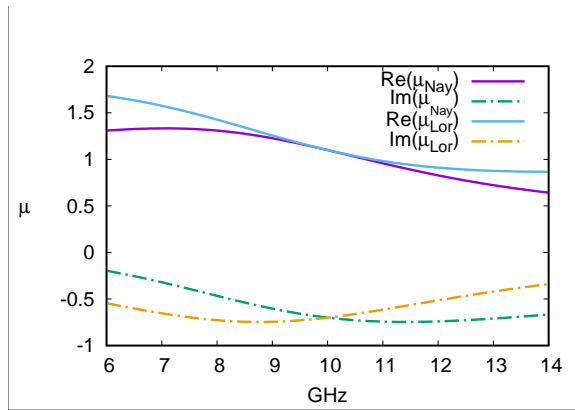


Figure 3.15.: Replacing the constant term μ_s by μ_∞ by maintaining a high damping of $\xi_\mu = 0.5$

I am actually not sure if the frequency independent term μ_s is correct because in other publications like in [128] or [41] a simple constant is used whereas the ω^2 dependence is

3. Numerical Solution of Maxwell Equations

maintained. Pereda on the other hand directly assumed a Lorentz model for both, the electric and magnetic field [103]. The reader might wonder why I do not simply consider a ω^2 dependence. The reason becomes obvious by considering equation 3.154. As you can see the ω^2 dependence forces me to go to the fourth order in the Z-Domain whereas the Lorentz model only requires second order. This reduces the number of arrays and it allows me to use a larger timestep because the ω^2 dependence forced Nayyeri to use a very small time step of $\Delta t = \Delta x / (20c_0)$ to guarantee the stability of the scheme. Where Δx is the edge length of a cubic cell. For completeness, the corresponding parameters and equations in the Z-Domain for the Lorentz permittivity are.

$$C_{\mu 1} = \frac{\omega_{\mu} e^{-\omega_{\mu} \xi_{\mu} \Delta t} \sin\left(\omega_{\mu} \sqrt{1 - \xi_{\mu}^2} \Delta t\right)}{\Delta t \sqrt{1 - \xi_{\mu}^2}} \quad (3.162)$$

$$C_{\mu 2} = 2e^{-\omega_{\mu} \xi_{\mu} \Delta t} \cos\left(\omega_{\mu} \sqrt{1 - \xi_{\mu}^2} \Delta t\right) \quad (3.163)$$

$$C_{\mu 3} = e^{-2\omega_{\mu} \xi_{\mu} \Delta t} \quad (3.164)$$

$$\mathbf{J}_{hh,tot}^{n+1/2} = \frac{-C_{\mu 1} z^{-1} - C_{\mu 1} z^{-2}}{1 - C_{\mu 2} z^{-1} + C_{\mu 3} z^{-2}} (\bar{\mu}_s - \bar{\mu}_{\infty}) \mathbf{H}_{tot}^{n+1/2} \quad (3.165)$$

$$\begin{aligned} \mathbf{J}_{hh,tot}^{n+1/2} &= C_{\mu 1} (\bar{\mu}_s - \bar{\mu}_{\infty}) \mathbf{H}_{tot}^{n-1/2} - C_{\mu 1} (\bar{\mu}_s - \bar{\mu}_{\infty}) \mathbf{H}_{tot}^{n-3/2} \\ &\quad + C_{\mu 2} \mathbf{J}_{hh,tot}^{n-1/2} - C_{\mu 3} \mathbf{J}_{hh,tot}^{n-3/2} \end{aligned} \quad (3.166)$$

To fulfill the boundary conditions only the coefficients on the numerator are averaged as in 3.7.3. Due to the anisotropy I cannot directly update the equations (3.117) and (3.118) because the method is based upon field projections and not field vectors. To solve this issue I have to create two additional orthogonal vectors for each Delaunay and Voronoi Edge to store additional informations. This procedure is explained in detail in 3.6.4 and 3.6.5. Each set of three orthogonal vectors creates a local coordinate system. Our material parameters have to be expressed in this local system. Therefore I apply the coordinate tranformation and a material parameter tensor, $\bar{\bar{M}}$ say, is transformed into the local coordinate system $\bar{\bar{M}}'$ using the operator transformation (identical to equation (3.63))

$$\bar{\bar{M}}'(\mathbf{r}') = \frac{\bar{\bar{J}}_R \bar{\bar{M}} \bar{\bar{J}}_R^T}{\det(\bar{\bar{J}}_R)} \quad (3.167)$$

where $\bar{\bar{J}}_R$ is the Jacobian matrix which is nothing else than a rotation matrix in our case due to the orthogonality of the local coordinate system. " ' " refers to the local coordinate system. For an omega material with its optical axis rotated by the Euler angles α, β, γ I apply equation 3.167 of course on the rotated materials parameters $\bar{\bar{\epsilon}}_{rotated}, \bar{\bar{\mu}}_{rotated}, \bar{\bar{\kappa}}_{rotated}$.

3.8.2. Update equations

Before solving equations (3.117) and (3.118) it is easier to rewrite them as

$$\mathbf{E}_{tot}^{n+1} = \mathbf{E}_{tot}^n + \bar{\varepsilon}_\infty^{-1} \mathbf{F} \mathbf{E}_{tot}^{n+1/2} \quad (3.168)$$

$$\mathbf{H}_{tot}^{n+1/2} = \mathbf{H}_{tot}^{n-1/2} + \bar{\mu}_\infty^{-1} \mathbf{F} \mathbf{H}_{tot}^n \quad (3.169)$$

$$\mathbf{F} \mathbf{E}_{tot} = \Delta t \left[\frac{1}{AV} \sum_{k=1}^{M_i^V} H_{scat,j_i,k}^{n+0.5} l_{j_i,k}^V + \varepsilon_0 \frac{\partial \mathbf{E}_{inc}^{n+1/2}}{\partial t} - \mathbf{J}_{ee,tot}^{n+1/2} + \mathbf{J}_{kh,tot}^{n+1/2} \right] \quad (3.170)$$

$$\mathbf{F} \mathbf{H}_{tot} = \Delta t \left[-\frac{1}{AD} \sum_{k=1}^{M_j^D} E_{scat,i_j,k}^n l_{i_j,k}^D + \mu_0 \frac{\partial \mathbf{H}_{inc}^n}{\partial t} - \mathbf{J}_{hh,tot}^n - \mathbf{J}_{ke,tot}^n \right] \quad (3.171)$$

Several things should be taken into account before updating equations (3.168), (3.169). First of all, the field vectors have to be projected on the corresponding normalised Delaunay or Voronoi edges denoted by $\hat{\mathbf{e}}_i$ and $\hat{\mathbf{e}}_j$. The vectors \mathbf{E}_{tot} , $\mathbf{F} \mathbf{E}_{tot}$, $\partial \mathbf{E}_{inc} / \partial t$, $\mathbf{J}_{ee,tot}$ and $\mathbf{J}_{khav,tot}$ are linked to the Delaunay edges and \mathbf{H}_{tot} , $\mathbf{F} \mathbf{H}_{tot}$, $\partial \mathbf{H}_{inc} / \partial t$, $\mathbf{J}_{hh,tot}$ and $\mathbf{J}_{keav,tot}$ to the Voronoi edges respectively. The projection of the total electric field vector \mathbf{E} at time step n to a unit vector \mathbf{e}_j is for example denoted as $E_{tot,j}^n = \langle \mathbf{E}_{tot}^n, \hat{\mathbf{e}}_j \rangle$ with $\langle \rangle$ the dot product. $\mathbf{J}_{kh,tot}$ needs to be associated to the Delaunay edges which is not directly possible because the magnetic field projections are linked to the Voronoi edges. The same problem rises for $\mathbf{J}_{ke,tot}$ which needs to be linked to the Voronoi edges but depends upon the electric field projections linked to the Delaunay edges. To solve this problem, I use the same method as in the isotropic chiral case (subsection 3.7.2). Furthermore, during the updating several matrix vector multiplication have to be calculated, for example in equation (3.161) where the magnetoelectric coupling matrix, expressed in local coordinates, $\bar{\tau}_\kappa^T$ is multiplied by \mathbf{E}_{tot}^{n+1} . In our projection based algorithm this multiplication cannot be executed directly, therefore I apply the same method as in the anisotropic case (section 3.6.6). I generate for each Voronoi or Delaunay edge two additional vectors labelled as e'_2 , e'_3 or v'_2 , v'_3 dependent if they belong to a Delaunay or Voronoi edge respectively (3.6.5). The three vectors together form a local coordinate system. The material parameter matrices are expressed with respect to this coordinate system using equation (3.167). Then I reconstruct a field vector according to (3.6.4). This vector is then projected to the two newly generated vectors e'_2 , e'_3 or v'_2 , v'_3 . The original edge e_1 , v_1 is updated using the standard update equation to reduce additional errors. Finally instead of computing $(\bar{\mu}'_s - \bar{\mu}'_\infty) \mathbf{H}_{tot}^{n-1/2}$ with $\mathbf{H}_{tot}^{n-1/2}$ currently linked to a cell center I compute $(\bar{\mu}'_s - \bar{\mu}'_\infty)_{11} H'_{tot,v_1}{}^{n-1/2} + (\bar{\mu}'_s - \bar{\mu}'_\infty)_{12} H'_{tot,v'_2}{}^{n-1/2} + (\bar{\mu}'_s - \bar{\mu}'_\infty)_{13} H'_{tot,v'_3}{}^{n-1/2}$ resulting

3. Numerical Solution of Maxwell Equations

in a simple scalar I associate to the original Voronoi edge v_1 , with v'_2, v'_3 the two additionally generated edges. In $(\bar{\mu}'_s - \bar{\mu}'_\infty)_{lm}$, lm refers to the element in the l th row and m th column in the matrix expressed in the local coordinate system and $H^{n-1/2}_{tot, v'_2}$ is the total magnetic field projected to the edge v'_2 . Everytime a matrix vector multiplication has to be done we have to follow the procedure I explained.

3.8.3. Updating scheme

Herein by Delaunay vertexes I refer to all the points of the Delaunay mesh whereas the cell centers are the vertexes of the Voronoi mesh.

Calculation of $H^{n+1/2}_{scat, j}$ from equation (3.169)

1. loop over the cells

- a) Reconstruct $\mathbf{H}^{n-1/2}_{scat}$ from the projections of the Voronoi mesh and associate it to the cell center.
- b) Reconstruct \mathbf{E}^n_{scat} from the projections of the Delaunay mesh and associate it to the cell center.

The difference between the reconstruction of $\mathbf{H}^{n-1/2}_{scat}$ and \mathbf{E}^n_{scat} is that the field projections of $\mathbf{H}^{n-1/2}_{scat}$ from which I reconstruct the corresponding vector are associated to the Voronoi Edges. In this case I use the same procedure as explained in the anisotropic section 3.6.4 and link the vector naturally to the cell center. For \mathbf{E}^n_{scat} it is different because it needs to be reconstructed from the Delaunay edges. To link it to the cell centers we use the method as described in the isotropic chiral case illustrated in Figure 3.12

1. Magnetic field loop over the Voronoi Edges.

- a) Calculate the Curl $\sum_{k=1}^{M_i^V} H^{n+0.5}_{scat, j_i, k} l^V_{j_i, k}$ needed in (3.170)
- b) Compute $\bar{\mu}_0 \partial \mathbf{H}^{n+1/2}_{inc} / \partial t$ and project to the Voronoi edges. It is also possible to directly compute the projection $\mu_0 \partial \mathbf{H}^{n+1/2}_{inc, i} / \partial t$ because $\bar{\mu}_0 = \mu_0 \bar{I}$ and in our formulation the incident field is always an analytical function which we define, therefore we do not have to reconstruct it from projections.
- c) Take \mathbf{E}^n_{scat} reconstructed in the previous loop and associated to the cell center. Define \mathbf{E}^n_{inc} , compute $\mathbf{E}^n_{tot} = \mathbf{E}^n_{scat} + \mathbf{E}^n_{inc}$ and project it to the original Voronoi edge and the two additional ones.
- d) Compute $\bar{\gamma}_\kappa^T \mathbf{E}^n_{tot}$ needed in $\mathbf{J}^n_{\kappa e, tot}$
- e) Calculate the projection $J^n_{\kappa e, tot, j}$
- f) Define $\mathbf{H}^{n-1/2}_{inc}$ and with $\mathbf{H}^{n-1/2}_{scat}$ (reconstructed before) compute $\mathbf{H}^{n-1/2}_{tot} = \mathbf{H}^{n-1/2}_{scat} + \mathbf{H}^{n-1/2}_{inc}$

- g) To compute $(\bar{\mu}'_s - \bar{\mu}'_\infty) \mathbf{H}_{tot}^{n-1/2}$ required in $\mathbf{J}_{hh,tot,av}^n = (\mathbf{J}_{hh,tot}^{n+1/2} + \mathbf{J}_{hh,tot}^{n-1/2})/2$ project $\mathbf{H}_{tot}^{n-1/2}$ to the original Voronoi edge and the two additionally generated edges associated to each Voronoi edge. Now compute $(\bar{\mu}'_s - \bar{\mu}'_\infty)_{11} H'_{tot,v_1}{}^{n-1/2} + (\bar{\mu}'_s - \bar{\mu}'_\infty)_{12} H'_{tot,v_2}{}^{n-1/2} + (\bar{\mu}'_s - \bar{\mu}'_\infty)_{13} H'_{tot,v_3}{}^{n-1/2}$ where v_1 refers to the original Voronoi edge and v_2, v_3 to the two additionally generated edges forming all together a local coordinate system. In $(\bar{\mu}'_s - \bar{\mu}'_\infty)_{lm}$, lm refers to the element in the l th row and m th column in the matrix expressed in the local coordinate system and $H'_{tot,v'_2}{}^{n-1/2}$ is the total magnetic field projected to the edge v'_2 .
- h) Compute $J_{hh,tot,j}^n$
- i) Compute $FH_{tot,j}^n$
- j) Add the projection $J_{\kappa e,tot,j}^n$ to $FH_{tot,j}^n$
2. loop over the cells
- a) Reconstruct \mathbf{FH}_{tot}^n from the Voronoi edges v_j and link it to the cell center
3. Loop over Voronoi edges
- a) Project \mathbf{FH}_{tot}^n to the two additional edges linked to Voronoi edge v_j .
- b) Compute $\bar{\mu}^{-1} \mathbf{FH}_{tot}^n$ needed in equation (3.169)
- c) Update equation (3.169) leading to $H_{tot,j}^{n+1/2}$. Compute $H_{inc,j}^{n+1/2}$ (known analytically) to obtain the scattered field projections $H_{scat,j}^{n+1/2} = H_{tot,j}^{n+1/2} - H_{inc,j}^{n+1/2}$. We need $H_{scat,j}^{n+1/2}$ to calculate the curl in equation (3.170) correctly.

Calculation of $E_{scat,i}^{n+1}$ from equation (3.168)

1. loop over the Delaunay edges
- a) Compute the curl $\sum_{k=1}^{M_j^D} E_{scat,i_{j,k}}^n l_{i_{j,k}}^D$ needed in equation (3.171)
2. loop over the vertexes of the Delaunay mesh
- a) Reconstruct \mathbf{E}_{scat}^n from the projections of the Delaunay mesh and associate it to the Delaunay vertexes.
- b) Reconstruct $\mathbf{H}_{scat}^{n-1/2}$ from the projections of the Voronoi mesh and associate it to the Delaunay vertexes.

The difference between the reconstruction of \mathbf{E}_{scat}^n and $\mathbf{H}_{scat}^{n-1/2}$ is that the field projections of \mathbf{E}_{scat}^n from which we reconstruct the corresponding vector are associated to the Delaunay edges. In this case we use the same procedure as explained in the anisotropic section 3.6.4 and link the vector naturally to the Delaunay vertex. For $\mathbf{H}_{scat}^{n-1/2}$ it is different because we reconstruct this one from the Voronoi edges. To link it to the Delaunay

3. Numerical Solution of Maxwell Equations

vertexes we use the method as described in the isotropic chiral case illustrated in Figure 3.12 adapted to the magnetic field.

1. Electric field loop over the Delaunay Edges. Calculation of $E_{scat,i}^{n+1}$ using equation (3.168)
 - a) Compute $\bar{\epsilon}_0 \partial \mathbf{E}_{inc}^{n+1/2} / \partial t$ and project to the Voronoi edges. It is also possible to directly compute the projection $\mu_0 \partial \mathbf{H}_{inc,i}^{n+1/2} / \partial t$ because $\bar{\mu}_0 = \mu_0 \bar{I}$ and in our formulation the incident field is always an analytical function which we define, therefore we do not have to reconstruct it from projections.
 - b) Take $\mathbf{H}_{scat}^{n+1/2}$ reconstructed in the previous loop associated to the Delaunay vertex. Define $\mathbf{H}_{inc}^{n+1/2}$, compute $\mathbf{H}_{tot}^{n+1/2} = \mathbf{H}_{scat}^{n+1/2} + \mathbf{H}_{inc}^{n+1/2}$ and project it to the original Delaunay edge and the two additional ones.
 - c) Compute $\bar{\tau}_\kappa \mathbf{H}_{tot}^{n+1/2}$ needed in $\mathbf{J}_{\kappa h,tot}^{n+1/2}$
 - d) Calculate the projection $J_{\kappa h,tot,i}^{n+1/2}$
 - e) Define \mathbf{E}_{inc}^n and with \mathbf{E}_{scat}^n (reconstructed before) compute $\mathbf{E}_{tot}^n = \mathbf{E}_{scat}^n + \mathbf{E}_{inc}^n$
 - f) To compute $(\bar{\epsilon}'_s - \bar{\epsilon}'_\infty) \mathbf{E}_{tot}^n$ required in $\mathbf{J}_{ee,tot,av}^{n+1/2} = (\mathbf{J}_{ee,tot}^{n+1} + \mathbf{J}_{ee,tot}^n) / 2$ project \mathbf{E}_{tot}^n to the original Delaunay edge and the two additionally generated edges associated to each Delaunay edge. Now compute $(\bar{\epsilon}'_s - \bar{\epsilon}'_\infty)_{11} E'_{tot,e_1} + (\bar{\epsilon}'_s - \bar{\epsilon}'_\infty)_{12} E'_{tot,e'_2} + (\bar{\epsilon}'_s - \bar{\epsilon}'_\infty)_{13} E'_{tot,e'_3}$ where e_1 refers to the original Delaunay edge and e'_2, e'_3 to the two additionally generated edges forming all together a local coordinate system. In $(\bar{\epsilon}'_s - \bar{\epsilon}'_\infty)_{lm}$, lm refers to the element in the l th row and m th column in the matrix expressed in the local coordinate system and E'_{tot,e'_2} is the total magnetic field projected to the edge v'_2 .
 - g) Compute $J_{ee,tot,i}^{n+1/2}$
 - h) Compute $FE_{tot,j}^{n+1/2}$
 - i) Add the projection $J_{\kappa h,tot,i}^{n+1/2}$ to $FE_{tot,i}^{n+1/2}$
2. Loop over the Delaunay vertexes
 - a) Reconstruct $\mathbf{FE}_{tot}^{n+1/2}$ from the Delaunay edges e_i and link it to the Delaunay vertexes
3. Loop over Delaunay edges
 - a) Project $\mathbf{FE}_{tot}^{n+1/2}$ to the two additional edges linked to Delaunay edge e_j .
 - b) Compute $\bar{\epsilon}^{-1} \mathbf{FE}_{tot}^n$ needed in equation (3.168)
 - c) Update equation (3.168) leading to $E_{tot,i}^{n+1}$. Compute $E_{inc,i}^{n+1}$ (known analytically) to obtain the scattered field projections $E_{scat,i}^{n+1} = E_{tot,i}^{n+1} - E_{inc,i}^{n+1}$. We need $E_{scat,i}^{n+1}$ to calculate the curl in equation (3.171) correctly.

4. Code Validation and Numerical Examples

In this chapter we present all the numerical examples to validate our Co-Volume method for different kinds of materials. Typical benchmark tests are the computation of the radar cross section (RCS) of a sphere or the transmission of an electromagnetic pulse through a slab of a dielectric material, because analytical solutions are available for these cases. I start with the results of an isotropic lossy dielectric material, followed by the results of an anisotropic lossy material. Until now the material parameters were frequency independent. For the modelling of an isotropic chiral material the frequency dependence and chirality have to be taken into account. I finish this chapter by validating the method that allows me to model bi-anisotropic materials, where the material parameters become second order tensors with frequency dependent entries.

4.1. Radar cross section and transmission

4.1.1. Radar cross section

The radar cross section (RCS) corresponds to the amount of scattered power from a target towards a radar. The bi-static RCS which, in contrast to the mono-static RCS, is a function of aspect angle and bi-static angle. The scattered wave is decomposed into 2 parts. One part has the same polarization as the transmitted signal and is referred to as co-polarised, while the other part has an orthogonal polarisation state compared to the transmitted signal and is referred to as cross-polarised. In scattering experiments, the radar cross section is of practical interest because an analytical solution is available for certain simple cases. To obtain the required far field information from the computed near field data, a near to far field transformation procedure [14] is employed. To achieve this, a closed collection surface, S , completely enclosing the scatterer, is constructed and, when steady state conditions have been achieved, a further cycle is computed. During this cycle, the harmonic solution produced by the time domain solver is used to calculate the phasor amplitudes \check{E} and \check{H} which enable fictitious electric and magnetic currents to be defined on S . Using the surface equivalence theorem, the components of the scattered electric field in the far field are determined [91]. With these values, the distribution of the radar cross-section is computed as

$$\chi = \lim_{r \rightarrow \infty} 4\pi r^2 \frac{|\check{E}_{scat,\theta}|^2 + |\check{E}_{scat,\phi}|^2}{|\check{E}_{inc,\theta}|^2 + |\check{E}_{inc,\phi}|^2} \quad (4.1)$$

4. Code Validation and Numerical Examples

where (r, θ, ϕ) denotes a standard spherical polar coordinate system. For the results presented here, the collection surface, S , is taken to be the surface formed in the mesh by removing all but the first three layers of tetrahedra that are attached to the scattering surface. The quantity χ defined in equation (4.1) is used to compute

$$RCS(\theta, \phi) = 10 \log_{10}(\chi) \quad (4.2)$$

which is the RCS in dB.

4.1.2. Transmission

In one of the numerical examples, a pulse is sent through a dielectric radome representing the nose of an aircraft, protecting the radar equipment. Radomes are used to protect radar systems from weather or to conceal antenna electronic equipment from the public view. Typically, a material that minimally attenuates the electromagnetic signal transmitted or received by the antenna is used. The transmission is evaluated as

$$T(f) = 20 \log_{10} \left\| \frac{\mathcal{F}[E_{tot}(\mathbf{r}_0, t)]}{\mathcal{F}[E_{inc}(\mathbf{r}_0, t)]} \right\| \quad (4.3)$$

which corresponds to the ratio of the amplitude of the total electric field divided by the amplitude of the incident electric field at a point \mathbf{r}_0 inside the radome.

4.2. Isotropic lossy material

4.2.1. Comparison between standard FDTD and co-volume method

In order to show the advantages of using the co-volume method compared to the standard Yee's algorithm, I consider two regular structured meshes with spacing of $\lambda/15$ and $\lambda/60$. Figure 4.1 shows the two staircase surfaces of the sphere for the coarse and fine meshes. I compare their Bistatic RCS with the results computed by the co-volume method, using a conforming unstructured mesh with global spacing of $\lambda/15$. Throughout the thesis I compute the RCS of sphere with a size similar to the wavelength, typically with a electrical length of 2λ . I restrict myself to these cases because the method has already been extensively tested for other shapes and higher electrical lengths like a 15λ PEC sphere, a 10λ PEC aircraft or a 170λ waveguide [144][111].

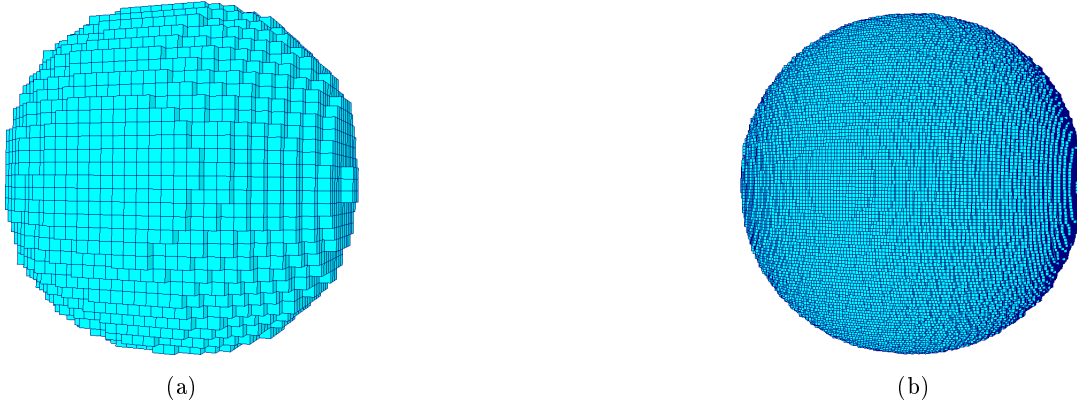


Figure 4.1.: Structured sphere's surface meshes (a) $\lambda/15$ spacing ; (b) $\lambda/60$ spacing

First, I considered the case of a plane wave scattered by a 2λ PEC sphere. The accuracy of our method and the ones from standard Yee's scheme are checked against the analytical Mie solution.

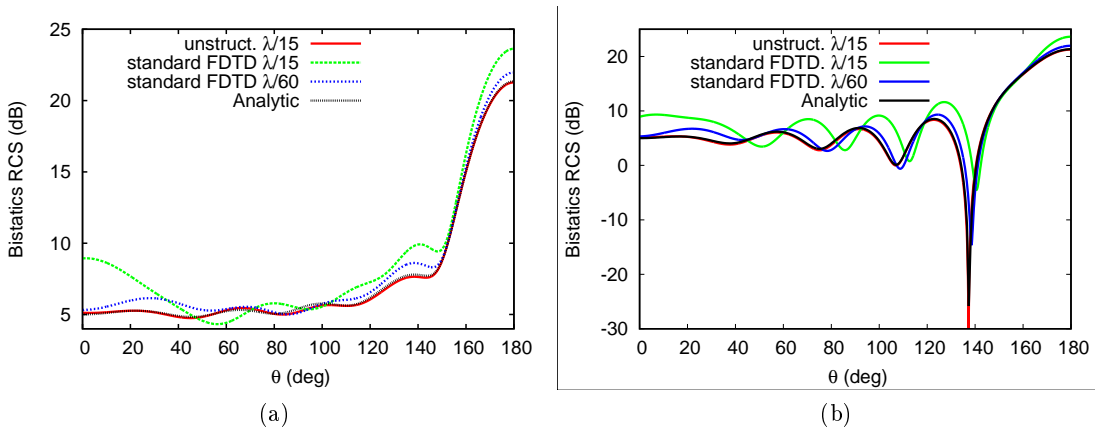


Figure 4.2.: *Scattering of a plane wave by a PEC sphere of electrical length 2λ comparing the co-volume and standard FDTD method: (a) co-polarised RCS distribution; (b) cross-polarised RCS distribution*

Figure 4.2 shows, for both co-polarised and cross-polarised, that even a structured mesh with very fine spacing $\lambda/60$ does not achieve the accuracy of the conformal unstructured mesh of spacing $\lambda/15$.

4. Code Validation and Numerical Examples

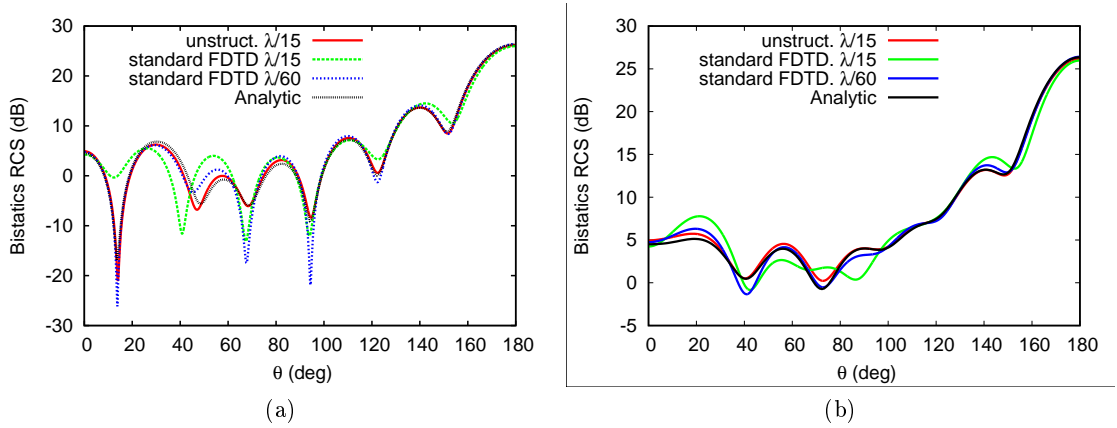


Figure 4.3.: *Scattering of a plane wave by a dielectric sphere of electrical length 2λ comparing the co-volume and standard FDTD method, for the case $\varepsilon = 2$, $\mu = 1$, $\sigma = \sigma_m = 0$: (a) co-polarised RCS distribution; (b) cross-polarised RCS distribution*

A finer structured mesh is clearly required to achieve comparable results to those produced by the geometry conforming co-volume method. A similar comparison was also carried out for the case of 2λ dielectric sphere, as shown in Figure 4.3. It is also clear that much finer structured meshes are required to overcome the effect of the staircase that structure grids introduce near the geometry. In addition, the increased resolution by a factor of 4, has led to an increase in size of the volume mesh, by a factor of 64. This resulted in the use of a time step that was four time smaller and an increase in the CPU requirement by a factor of 256. The relative L2 errors corresponding to the figures 4.2 and 4.3 are represented in table 4.1a and 4.1b. It can be seen that the method shows better results for the PEC than for the dielectric case. Nevertheless the L^2 error of an RCS should be considered with care because the RCS varies on the logarithmic scale from -5 to 30 dB. Hence a relatively small deviation from the analytical solution in the vicinity of 180° has a much higher impact on the L^2 error as a deviation at a relatively small angle. Nevertheless the challenge is to capture the small oscillations as good as possible arising for our testcase between $0^\circ - 120^\circ$. So, although the L^2 error of the $\lambda/15$ unstructured mesh is higher for the dielectric case compared to the $\lambda/60$ structured mesh (Table 4.1b), the co-volume method gives better results for low angles.

relative L^2 Error	co-polarised	cross-polarised
standard FDTD $\lambda/15$	54.80 %	50.75 %
standard FDTD $\lambda/60$	15.18 %	14.04 %
unstructured $\lambda/15$	2.99 %	2.77 %

(a)

relative L^2 Error	co-polarised	cross-polarised
standard FDTD $\lambda/15$	12.63 %	12.75 %
standard FDTD $\lambda/60$	1.41 %	1.39 %
unstructured $\lambda/15$	4.68 %	4.66 %

(b)

Table 4.1.: Relative L2-Error with respect to different meshes computed in linear scale of (a) PEC sphere ; (b) Dielectric sphere

4.2.2. Convergence of the leapfrog scheme

The centered leap frog scheme is known to be second order on an ideal mesh. To evaluate the order of convergence on a general unstructured mesh, I chose the example of a dielectric sphere of radius $1m$ with relative electric permittivity $\epsilon_r = 2$, relative magnetic permeability $\mu_r = 1$, electric and magnetic conductivities $\sigma = \sigma_m = 0 S/m$, excited using a plane wave with a wavelength of $1 m$. Several meshes with global spacing of 4, 8, 15 and 20 cells per wavelength (in free space) are generated. For each mesh, after 20 cycles the numerical solution of the RCS is compared to the analytical distribution using the L^2 error. The tangent of the fitted line will give us the rate of convergence. Figure 4.4a shows an order of convergence of 1.59 for the co-polarised RCS whereas Figure 4.4b shows an order of convergence of 1.48 for the cross-polarised RCS. Averaging the two tangents leads to an order of convergence of 1.54.

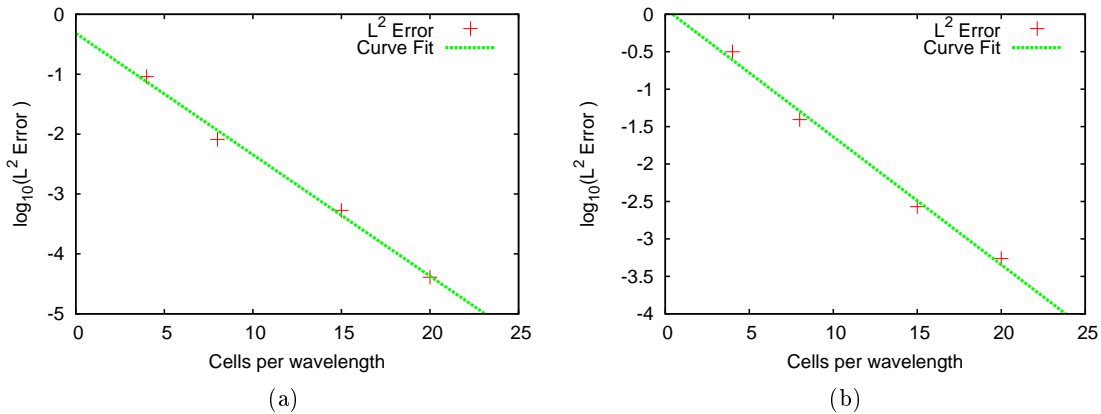


Figure 4.4.: Order of convergence of the scheme using the L^2 error for varying number of cells per wavelength (a) co polarised (b) cross polarised

4.2.3. Scattering by a spherical object

The initial examples involve spherical scatterers and have analytical solutions for the RCS that can be used to validate the numerical distribution computed using equation(4.2). The meshes employed in the simulations for modelling the spherical objects have between 15 and 20 degrees of freedom per wavelength, λ , in free space. This level of resolution will decrease in a dielectric, e.g. with a relative electric permittivity of $\varepsilon_r = 2$ the mesh resolution reduces to 10 degrees of freedom per wavelength. Past experience has shown that, with a co-volume method of this type, reasonable results are obtained provided a mesh resolution of at least 8 degrees of freedom per wavelength is employed. Such a low grid resolution is sufficient for this scheme, in which the field vectors are stored at the center of the faces. As there are in general about four times more degrees of freedom than points, the co-volume method needs four times less cells compared to a finite element method. In each case, the calculated RCS represents the cross and co-polarised scattered waves. Due to the spherical symmetry, only the RCS from 0 – 180 degrees is represented. All the computations were performed using a single processor comparable to an Intel core *i7*. For all the examples, the PML has a thickness of 10 layers of hexahedra. The space between the inner boundary of the PML and the object surface is filled with either 7 or 8 cells. The first examples involve scattering of a plane wave with wavelength $\lambda = 1 m$, propagating in x direction, by a sphere, of radius $1 m$.

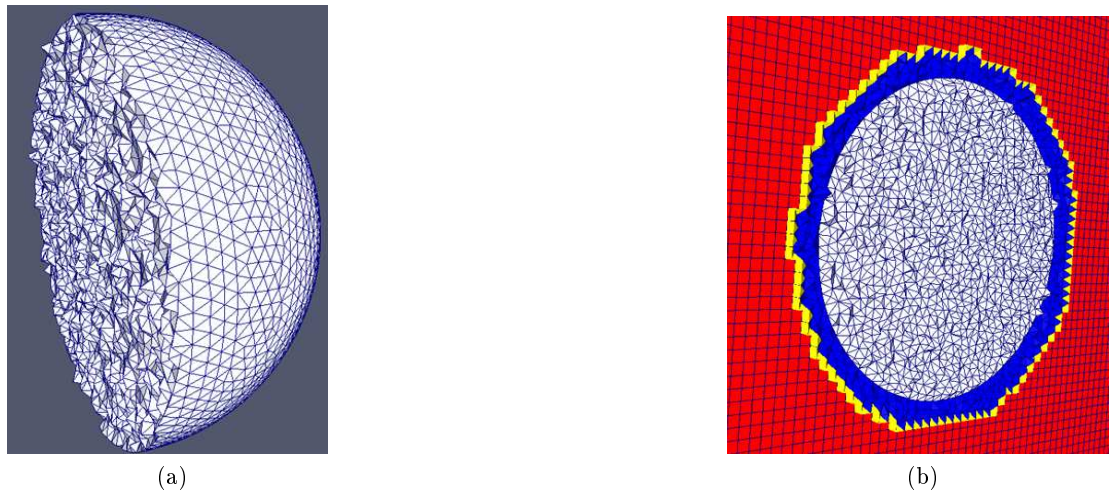


Figure 4.5.: (a) View of a cut through the discretised dielectric sphere. (b) Detail of a cut through the mesh showing the different cell types.

A view of a cut through the mesh used to represent the sphere is given in Figure 4.5a and Figure 4.5b. The white cells lie inside the sphere and consist exclusively of tetrahedra. Outside the sphere, there are a few layers of tetrahedra, shown in blue, connected to the red hexahedra using a layer of yellow pyramids. In total, the mesh contains 451355 cells, 989069 Delaunay edges and 1138930 Voronoi edges. When the object is considered to be a dielectric sphere, the relative electric permittivity is $\varepsilon_r = 2$, the relative magnetic

4.2. Isotropic lossy material

permeability is $\mu_r = 1$ and the conductivities are $\sigma = \sigma_m = 0 \text{ S/m}$. The solution is advanced through 20 cycles of the incident wave using 328 time steps per cycle, with the computation requiring 1.6 minutes per cycle. If not indicated differently, I use the same number of time steps for all the dielectric test cases computed on the $\lambda/15$ mesh of the sphere. By comparing with the analytical solution I observed that the steady state is reached for all the presented test cases after the indicated number of cycles. The computed bi-static RCS distributions are shown to be in good comparison with the analytical solution for this problem in Figure 4.6. The corresponding L^2 errors for the co- and cross-polarised RCS are 4.68 % and 4.66 % respectively.

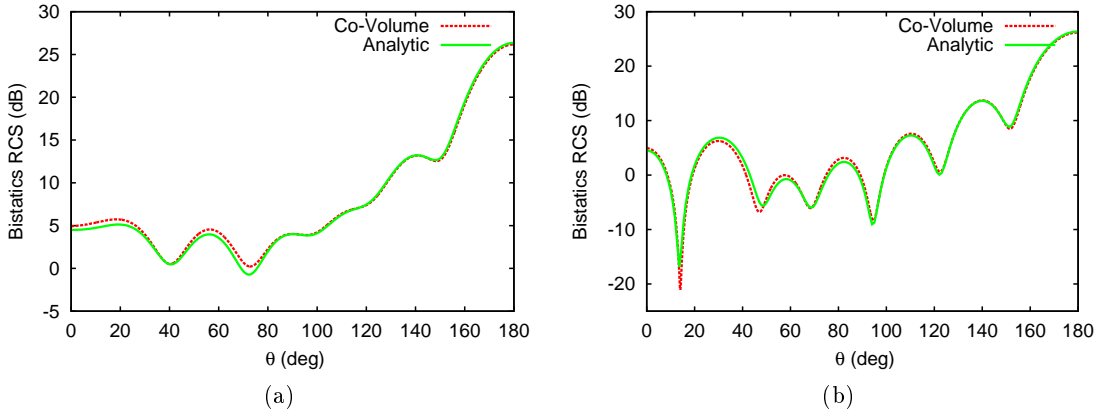


Figure 4.6.: *Scattering of a plane wave by a dielectric sphere of electrical length 2λ with $\varepsilon_r = 2$, $\mu_r = 1$ and $\sigma = \sigma_m = 0 \text{ S/m}$; (a) co-polarised RCS distribution; (b) cross-polarised RCS distribution*

Next, I use the same mesh, representing a sphere with the same relative electric permittivity $\varepsilon_r = 2$ and relative magnetic permeability $\mu_r = 1$, but the electric conductivity is set to $\sigma = 0.7 \text{ S/m}$.

4. Code Validation and Numerical Examples

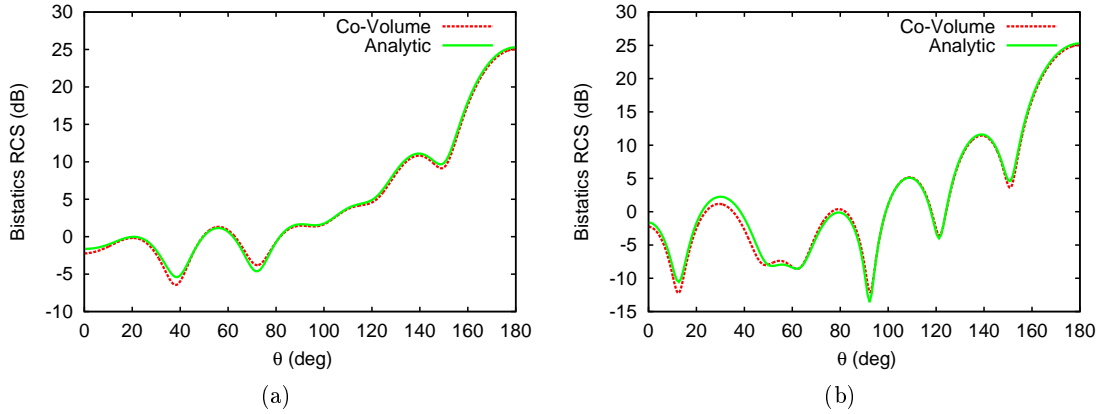


Figure 4.7.: Scattering of a plane wave by a dielectric lossy sphere of electrical length 2λ with $\varepsilon_r = 2$, $\mu_r = 1$ and $\sigma = 0.7 S/m$, $\sigma_m = 0 S/m$: (a) co-polarised RCS distribution; (b) cross-polarised RCS distribution

The solution is again advanced through 20 cycles and the computed bi-static RCS results are shown to be in good agreement with the analytical solution in Figure 4.7. The corresponding L^2 errors for the co- and cross- polarised RCS are 6.49 % and 6.35 % respectively. For the case of a PEC sphere, I have chosen to model the problem by using the same mesh and setting the value of the electric conductivity to $\sigma = 10^6 S/m$, with a relative electric permittivity $\varepsilon_r = 1$ and relative magnetic permeability $\mu_r = 1$. In this case, no specific PEC boundary condition is required. The distribution of the analytical solution of the RCS for a PEC sphere is seen to be in excellent agreement with the numerical solution in Figure 4.8.

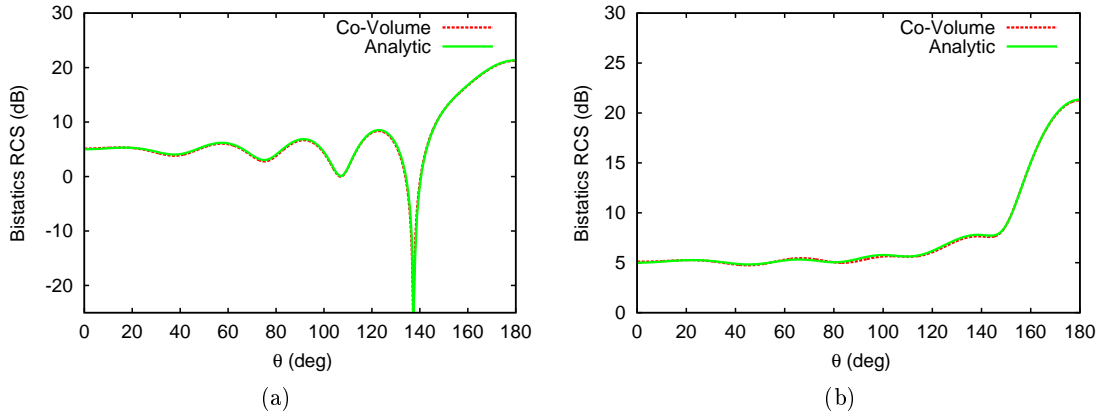


Figure 4.8.: Scattering of a plane wave by a PEC sphere of electrical length 2λ with $\varepsilon_r = 1, \mu_r = 1, \sigma = \sigma_m = 10^6 S/m$; (a) co-polarised RCS distribution; (b) cross-polarised RCS distribution.

As mentioned earlier, the presence of a resistive sheet on the surface of the object can be easily simulated by assigning only to the Delaunay and Voronoi Edges forming the interface a specific conductivity, permeability or permittivity.

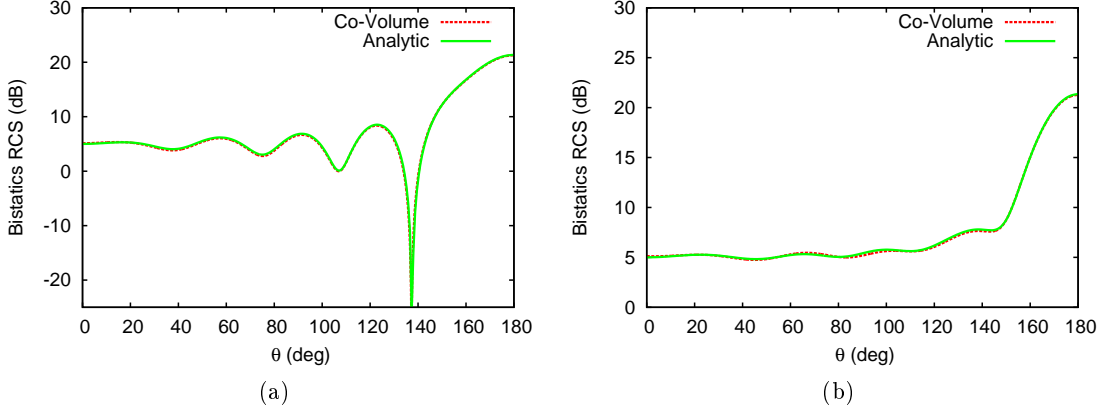


Figure 4.9.: *Scattering of a plane wave by sphere covered with a resistive sheet of conductivity $\sigma = \sigma_m = 10^6 S/m$: (a) co-polarised RCS distribution; (b) cross-polarised RCS distribution*

For those edges, I choose very high conductivity, $\sigma = 10^6 S/m$, this allows to model a PEC sphere by the means of highly conducting resistive sheets. No ϵ_r and μ_r has to be specified inside the sphere because the plane wave is totally reflected from the highly conducting surface. Figure 4.9 proves the excellent agreement between the analytical of PEC sphere and numerical solution of a sphere covered by a high conductive resistive sheet. Convergence tests performed for these examples showed that RCS results within a 3 dB tolerance can be obtained using an element size of $\lambda/15$, 9 cycles of the incident wave and 206 time steps per cycle. These computations required only 1.1 minutes per cycle on a single processor. The L^2 errors for the RCS represented in Figure 4.8 and 4.9 for the co- and cross-polarised RCS are for both cases 1.64 % and 1.69 % respectively.

4.2.3.1. Scattering by a coated spherical object

The next examples involve scattering of a plane wave with wavelength $\lambda = 1 m$, propagating in the x direction, by a coated spherical object, of electrical length (2λ) with a radius of $0.5 m$ and a uniform dielectric coating of thickness $0.5 m$ as represented in Figure 4.10.

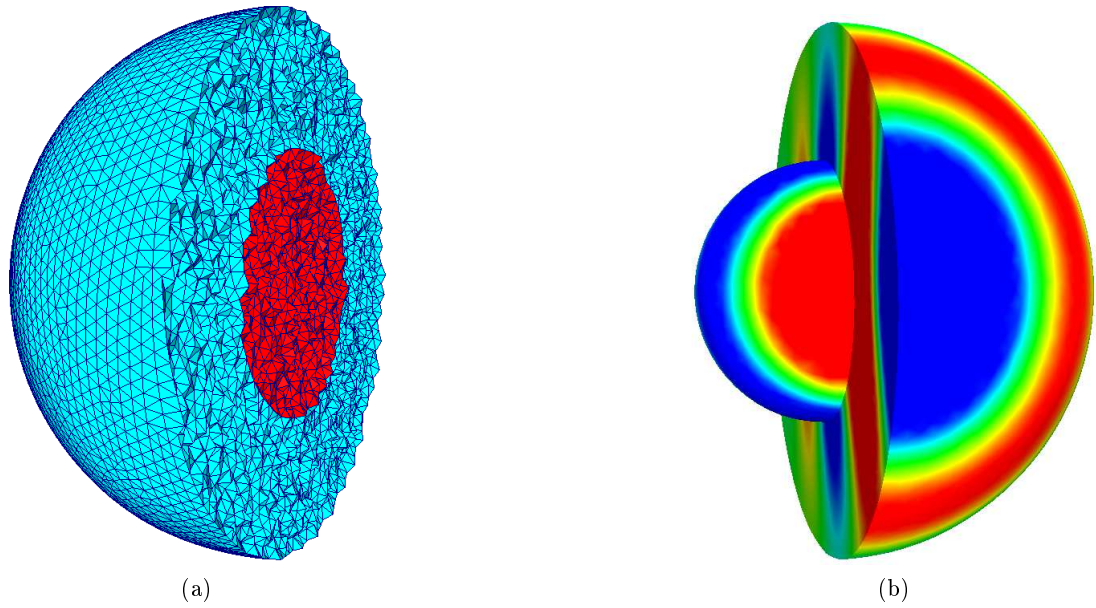


Figure 4.10.: *Cut through a coated sphere (a) View of the mesh used to represent a coated dielectric sphere, with the blue cells representing the coating and the red cells the dielectric.; (b) Graphical representation of the scattered field for the coated dielectric sphere*

For these examples the PML has a thickness of 10 layers of hexahedra elements. The smallest distance between the inner boundary of the PML and the object surface is filled with 8 cells. The mesh consists of 876116 cells, 1673527 Delaunay and 2076019 Voronoi edges respectively. For the first case, a PEC sphere, with parameters $\epsilon_r = 1$, $\mu_r = 1$, $\sigma = 10^6 S/m$, $\sigma_m = 0 S/m$, is coated with a spherical dielectric, with parameters $\epsilon_r = 2$, $\mu_r = 1$, $\sigma = \sigma_m = 0 S/m$. The computed bi-static RCS distribution is seen to be in good agreement with the analytical distribution in Figure 4.11. The corresponding L^2 errors for the co- and cross-polarised RCS are 1.06 % and 1.09 % respectively.

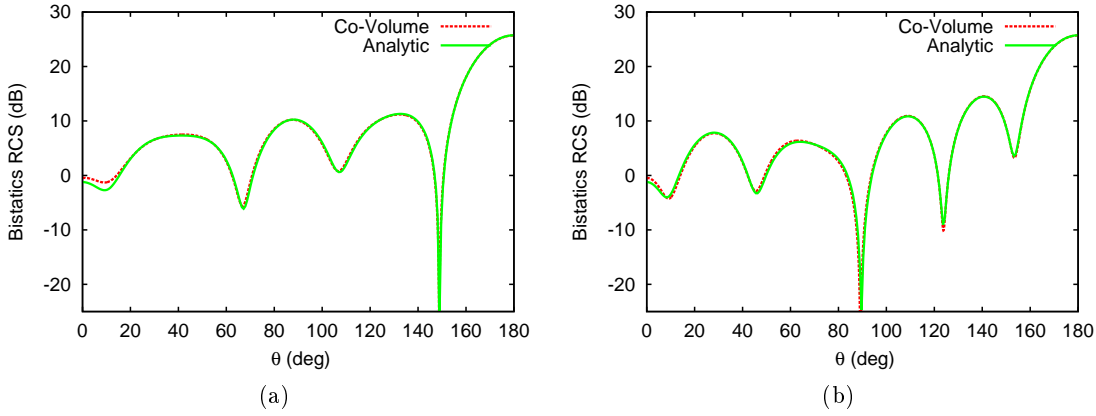


Figure 4.11.: Scattering of a plane wave by a coated PEC sphere of electrical length 2λ : (a) co-polarised RCS distribution; (b) cross-polarised RCS distribution

For the second case, a PEC sphere, with parameters $\epsilon_r = 1$, $\mu_r = 1$, $\sigma = 10^6 S/m$, $\sigma_m = 0 S/m$, is coated with a conducting dielectric, with parameters $\epsilon_r = 2$, $\mu_r = 1$, $\sigma = 0.7 S/m$ and $\sigma_m = 0 S/m$. The computed bistatic RCS distribution is seen to be in good agreement with the analytical distribution in Figure 4.12. The corresponding L^2 errors for the co- and cross-polarised RCS are 1.02 % and 1.04 % respectively.

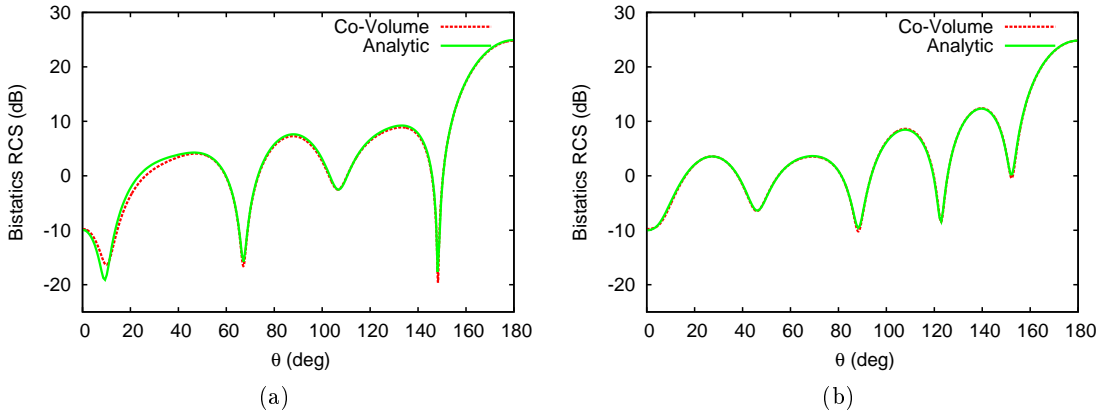


Figure 4.12.: Scattering of a plane wave by a PEC sphere coated with a conducting dielectric of total electrical length 2λ : (a) co-polarised RCS distribution; (b) cross-polarised RCS distribution

The scatterer is now replaced by a dielectric sphere of radius $0.5 m$, characterised by the parameters $\epsilon_r = 2$, $\mu_r = 1$, $\sigma = \sigma_m = 0 S/m$, with a uniform dielectric coating of thickness $0.5 m$, characterised by the parameters $\epsilon_r = 1.5$, $\mu_r = 1$, $\sigma = \sigma_m = 0 S/m$. The computed bi-static RCS distribution is seen to be in good agreement with the analytical

4. Code Validation and Numerical Examples

distribution in Figure 4.13 with the corresponding L^2 errors for the co- and cross-polarised RCS of 1.31 % and 1.28 % respectively.

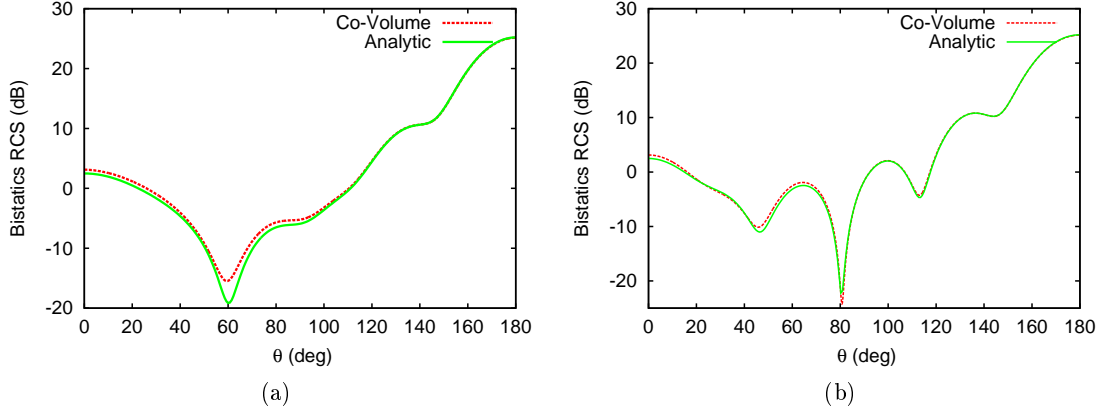


Figure 4.13.: *Scattering of a plane wave by a coated dielectric sphere of electrical length 2λ : (a) co-polarised RCS distribution; (b) cross-polarised RCS distribution*

4.2.3.2. Transmission of a narrow band pulse

The final example demonstrates the use of the method in a predictive mode and involves the calculation of the transmission efficiency of a dielectric radome. The radome consists of half an ellipsoid, with a lateral radius of 0.5 m , a length of 1 m and a thickness of 0.05 m . The ellipsoid is constructed of Ipar Plexiglass, with a relative electric permittivity $\epsilon_r = 2.59$ and a loss tangent $\sigma = 0.015\text{ S/m}$. Radomes of this type are commonly employed on subsonic aircraft. The narrow band pulse

$$E_y(\mathbf{r}, t) = e^{-(t-\mathbf{k}\cdot\mathbf{r}/\omega)^2/2\tau^2} \sin(\omega t - \mathbf{k} \cdot \mathbf{r}) \quad (4.4)$$

is used to illuminate the radome, where τ denotes the pulse width, \mathbf{k} is the the wave vector and \mathbf{r} is the general position vector. Figure 4.14a shows the details of the mesh. The yellow elements form the radome structure and Figure 4.14b shows contours of the electric component E_y of the pulse. The employed mesh represented in Figure 4.14c has 40 degrees of freedom per wavelength and the PML has a thickness of 10 layers of hexahedral elements. The smallest distance between the inner boundary of the PML and the object surface corresponds to 8 cells. The mesh contains 876314 cells, 1673283 Delaunay edges and 2076114 Voronoi edges. I illuminate the radome with a 1.2 GHz narrowband pulse with a pulse width of $1 \times 10^{-9}\text{ s}$.

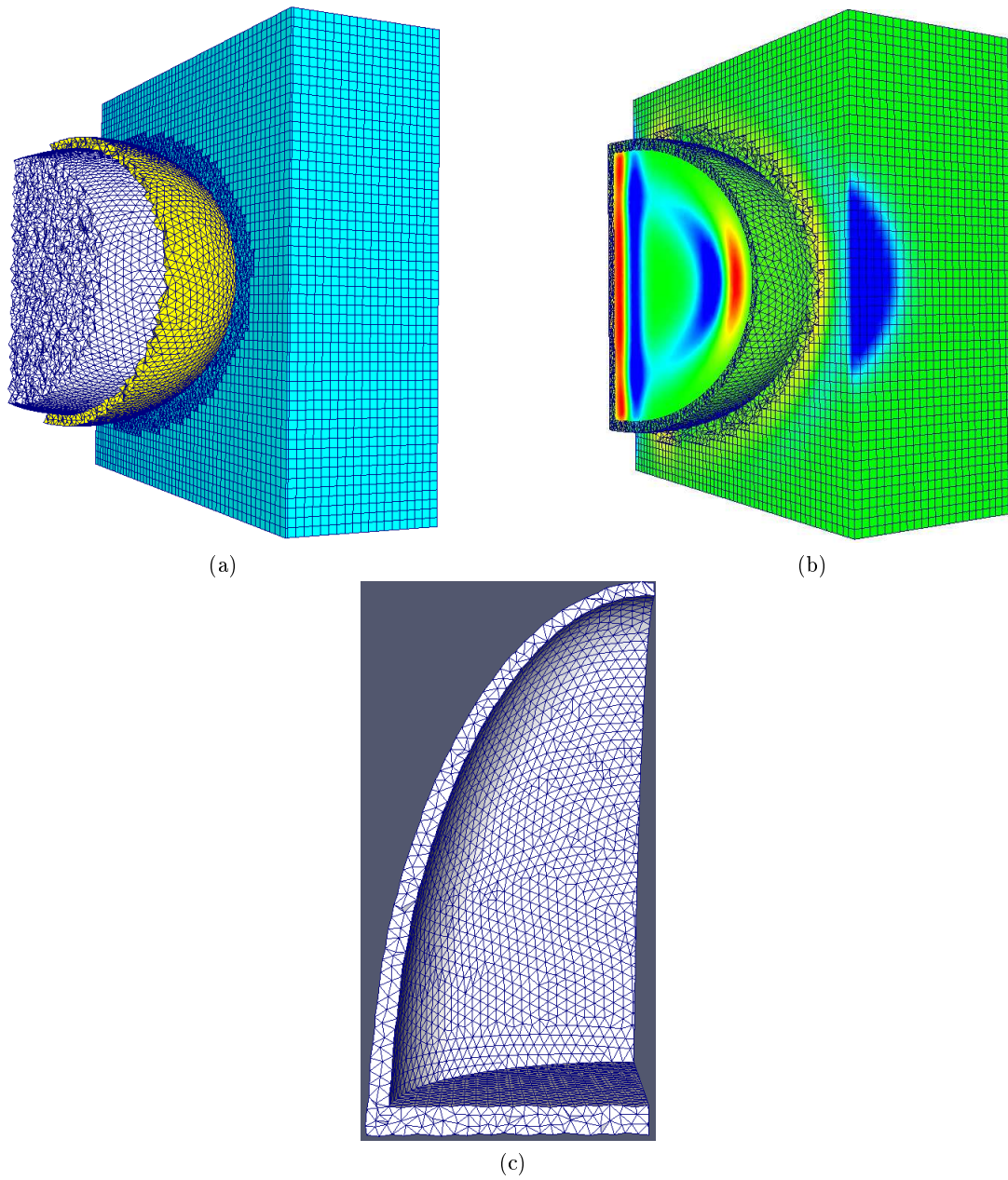


Figure 4.14.: (a) View of the coarse mesh used for the radome example, with the yellow cells representing the dielectric and the white and blue cells representing free space.; (b) Graphical representation of the scattered field induced by an EM pulse (c) mesh with 40 degrees of freedom per wavelength

The transmission calculated using equation (4.3) can be seen in Figure (4.15).

4. Code Validation and Numerical Examples

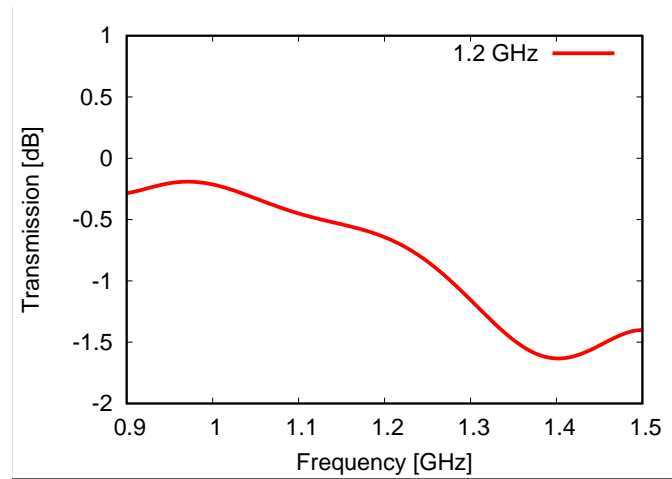


Figure 4.15.: Transmission of a Narrowband pulse centered at 1.2GHz , through a dielectric radome with 40 degrees of freedom per wavelength

4.3. Numerical Validation for anisotropic lossy objects

4.3.1. Scattering on sphere

A series of examples, involving scattering of an incident plane wave by an anisotropic sphere, is included here to demonstrate the numerical performance of the algorithm that has been described. The algorithm is validated by comparing the results produced with those obtained from the open source program Discrete Dipole Scattering (DDSCAT) [40], which is an implementation of the frequency domain discrete dipole approximation [46]. The incident wave has free space wavelength $\lambda_0 = 1 \text{ m}$ and it propagates in the x direction. In each case, the electrical length of the sphere is $2\lambda_0$.

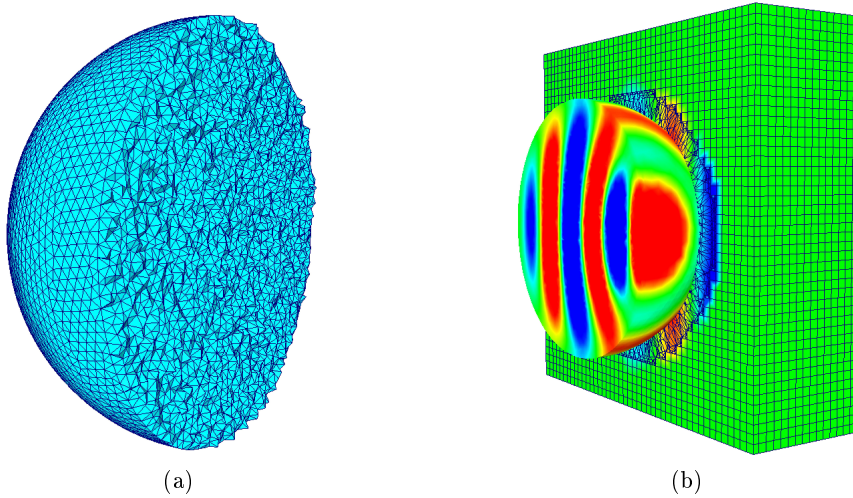


Figure 4.16.: *Scattering by a dielectric anisotropic sphere: (a) cut through the mesh used to represent the sphere; (b) contours of E_y on a cut through the computational domain.*

The mesh employed is illustrated in Figure 4.16 and has an average edge length of $\lambda_0/20$. For each example, the PML region is located at a minimum distance of λ_0 from the scatterer and the PML is discretised using 10 layers of hexahedra. The minimum distance between the inner boundary of the PML and the surface of the scatterer is represented by 8 cells. The complete mesh consists of 876,116 cells, 1,673,527 Delaunay edges and 2,076,019 Voronoi edges. For the anisotropic case, it is estimated that a mesh spacing of $\lambda_0/20$ should be sufficient. As I include a test case with full anisotropic tensors for both electric and magnetic properties, I decided to use the same mesh for all the test cases.

4.3.1.1. Magnetically uniaxial non-lossy anisotropic sphere

The first test case involves an uniaxial permeability tensor and is devised to check the updating of the magnetic field projections. For the sphere, the material parameters

4. Code Validation and Numerical Examples

$$\bar{\bar{\epsilon}}_r = \begin{bmatrix} 1 & 0 & 0 \\ 0 & 1 & 0 \\ 0 & 0 & 1 \end{bmatrix}, \bar{\bar{\sigma}} = \begin{bmatrix} 0 & 0 & 0 \\ 0 & 0 & 0 \\ 0 & 0 & 0 \end{bmatrix}, \bar{\bar{\mu}}_r = \begin{bmatrix} 1.5 & 0 & 0 \\ 0 & 1.5 & 0 \\ 0 & 0 & 2.0 \end{bmatrix}, \bar{\bar{\sigma}}_m = \begin{bmatrix} 0 & 0 & 0 \\ 0 & 0 & 0 \\ 0 & 0 & 0 \end{bmatrix}$$

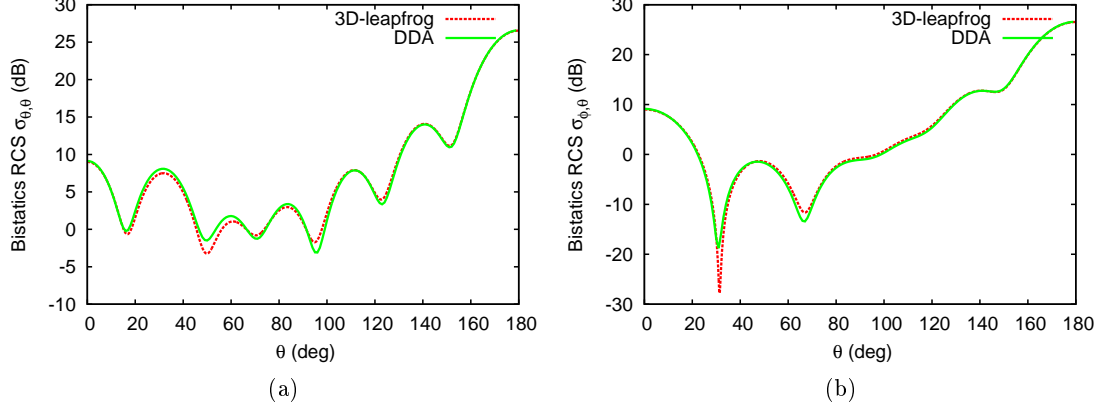


Figure 4.17.: *Scattering of a plane wave by a dielectric sphere of electrical length 2λ with anisotropic permeability: (a) co-polarised RCS distribution; (b) cross-polarised RCS distribution.*

are used. In this case the only term in equation (??) that involves matrix multiplication is $(\bar{\bar{\mu}}_{av} - \mu_0 \bar{\bar{I}}) \frac{\partial}{\partial t} \mathbf{H}_{inc}^n|_j$. The matrices $\bar{\bar{a}}'_{\mu+}$ and $\bar{\bar{a}}'_{\mu-}$ reduce to the unit matrix and the update of magnetic field from the constitutive equation (3.68) only requires multiplication by the coefficient $(\bar{\bar{\mu}}_{av}^{-1})_{11}$. Figure 4.17 shows the computed distributions of both the cross-polarised ($\sigma_{\theta\phi}$) and the co-polarised ($\sigma_{\theta\theta}$) RCS compared with the distributions obtained from using the discrete dipole approximation (DDA). It can be seen that the RCS distributions are in excellent agreement, apart from the differences in the troughs, which are typical of comparisons between time-domain and frequency-domain approximations. The corresponding L^2 errors for the co- and cross-polarised RCS are 1.22 % and 1.13 % respectively.

4.3.1.2. Electrically uniaxial non-lossy anisotropic sphere

This test case involves a uniaxial permittivity tensor, to check on the updating of the electric field projections. For this case, the material parameter values

$$\bar{\bar{\epsilon}} = \begin{bmatrix} 1.5 & 0 & 0 \\ 0 & 1.5 & 0 \\ 0 & 0 & 2.0 \end{bmatrix}, \bar{\bar{\sigma}} = \begin{bmatrix} 0 & 0 & 0 \\ 0 & 0 & 0 \\ 0 & 0 & 0 \end{bmatrix}, \bar{\bar{\mu}} = \begin{bmatrix} 1 & 0 & 0 \\ 0 & 1 & 0 \\ 0 & 0 & 1 \end{bmatrix}, \bar{\bar{\sigma}}_m = \begin{bmatrix} 0 & 0 & 0 \\ 0 & 0 & 0 \\ 0 & 0 & 0 \end{bmatrix}$$

are used for the sphere.

4.3. Numerical Validation for anisotropic lossy objects

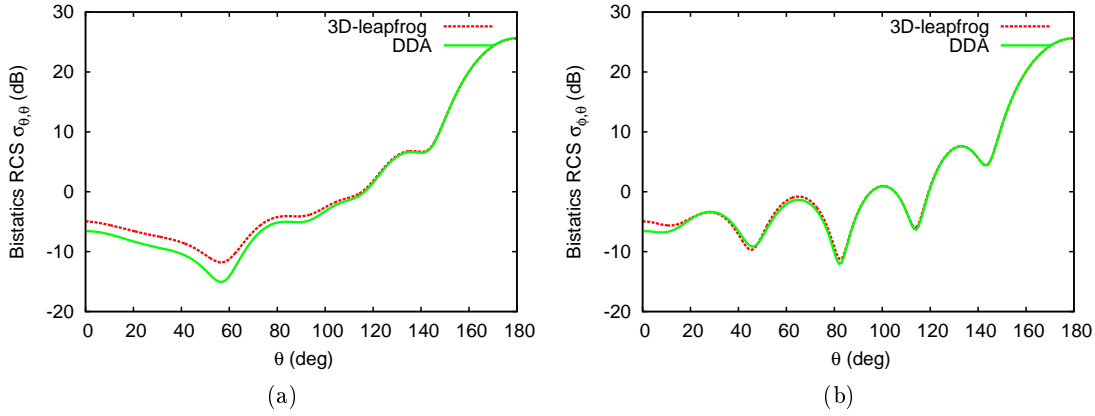


Figure 4.18.: *Scattering of a plane wave by a dielectric sphere of electrical length 2λ with anisotropic permittivity: (a) co-polarised RCS distribution ; (b) cross-polarised RCS distribution.*

In this case the only term that require matrix multiplication in equation (??) is $(\bar{\bar{\epsilon}}_{av} - \epsilon_0 \bar{\bar{I}}) \frac{\partial \mathbf{E}_{inc}^{n+0.5}}{\partial t} \Big|_j$, as the other matrices $\bar{a}'_{\epsilon+}$ and $\bar{a}'_{\epsilon-}$ reduce to the unit matrix. The update of the electric field from the constitutive equation (3.68) only involves multiplication by the coefficient $(\bar{\bar{\epsilon}}_{av}^{-1})_{11}$. Figure 4.18 shows good agreement between the computed RCS distributions and those produced with the DDA method. There seems to be a big difference between our solution and the solution from DDA for the co-polarised RCS distribution in Figure 4.18 (a) but this is mainly due to the logarithmic scaling I am using highlighting even small differences between the results because the corresponding L2-Errors for the co-and cross-polarised RCS are only 1.37 % and 1.33 % respectively.

4.3.2. Electrically lossy anisotropic sphere

The next example involves an anisotropic permittivity tensor, together with electric conductivity. The material parameters

$$\bar{\bar{\epsilon}} = \begin{bmatrix} 1.3 & 0 & 0 \\ 0 & 1.6 & 0 \\ 0 & 0 & 2.0 \end{bmatrix} \quad \bar{\bar{\sigma}} = \begin{bmatrix} 0.3 & 0 & 0 \\ 0 & 0.5 & 0 \\ 0 & 0 & 0.7 \end{bmatrix} \quad \bar{\bar{\mu}} = \begin{bmatrix} 1 & 0 & 0 \\ 0 & 1 & 0 \\ 0 & 0 & 1 \end{bmatrix} \quad \bar{\bar{\sigma}}_m = \begin{bmatrix} 0 & 0 & 0 \\ 0 & 0 & 0 \\ 0 & 0 & 0 \end{bmatrix}$$

are employed.

4. Code Validation and Numerical Examples

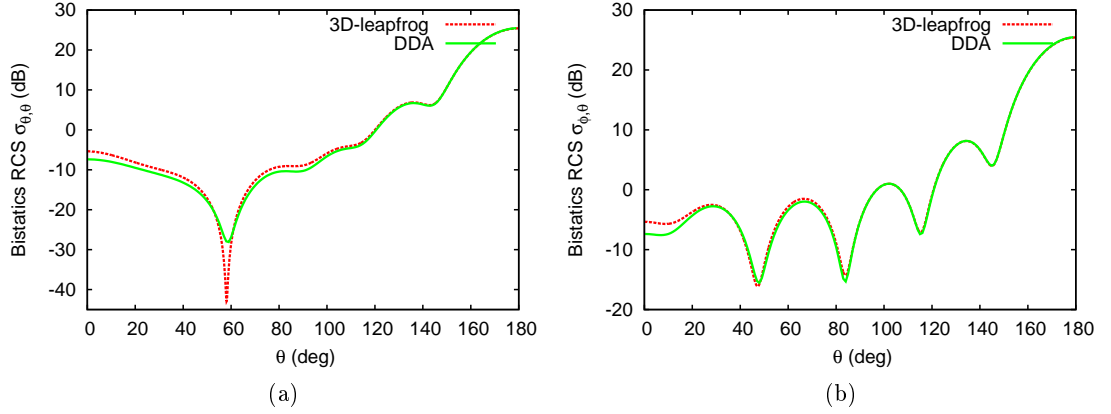


Figure 4.19.: *Scattering of a plane wave by a dielectric sphere of electrical length 2λ with anisotropic permittivity and electrical conductivity: (a) co-polarised RCS distribution; (b) cross-polarised RCS distribution.*

In this case, the matrix multiplications are required in equation (??) and the time updating scheme described in Section 3.6.6 was used. The RCS distributions computed with the 3D-leapfrog and with the DDA scheme are compared in Figure 4.19. Steady state conditions were attained in the time domain approach after ten cycles of the incident wave leading to L^2 errors for the co and cross polarised RCS of 1.15 % and 1.09 % respectively.

4.3.3. Magnetically lossy anisotropic sphere

For the next example, I consider an anisotropic permeability tensor, together with magnetic conductivity. The sphere, in this case, is characterised by the material parameters

$$\bar{\bar{\epsilon}} = \begin{bmatrix} 1 & 0 & 0 \\ 0 & 1 & 0 \\ 0 & 0 & 1 \end{bmatrix}, \bar{\bar{\sigma}} = \begin{bmatrix} 0 & 0 & 0 \\ 0 & 0 & 0 \\ 0 & 0 & 0 \end{bmatrix}, \bar{\bar{\mu}} = \begin{bmatrix} 1.3 & 0 & 0 \\ 0 & 1.6 & 0 \\ 0 & 0 & 2 \end{bmatrix}, \bar{\bar{\sigma}}_m = \begin{bmatrix} 0.3 & 0 & 0 \\ 0 & 0.5 & 0 \\ 0 & 0 & 0.7 \end{bmatrix}$$

4.3. Numerical Validation for anisotropic lossy objects

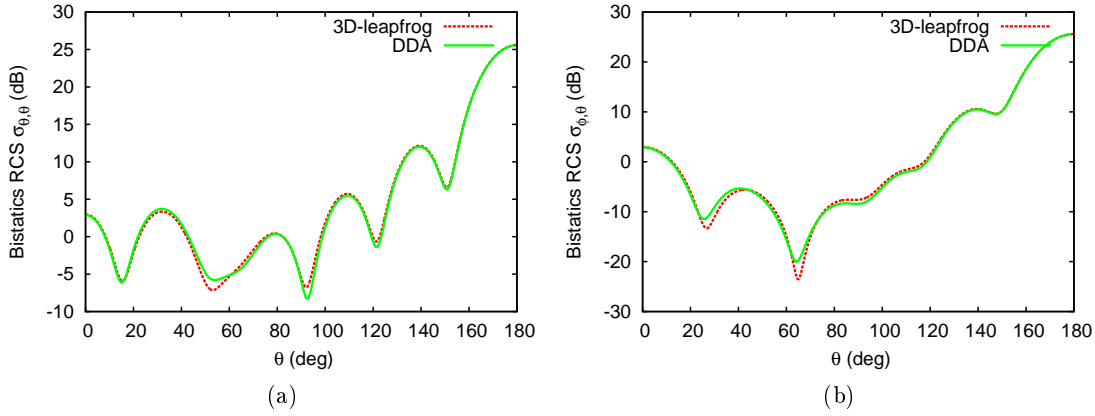


Figure 4.20.: *Scattering of a plane wave by a dielectric sphere of electrical length 2λ with anisotropic permeability and magnetic conductivity: (a) co-polarised RCS distribution; (b) cross-polarised RCS distribution.*

In this example, matrix multiplication is required in equation (??) and the scheme described in Section 3.6.6 was used for the magnetic field update. The time domain solver reached steady state after ten cycles of the incident wave. The comparison between the RCS distributions computed with the current time domain approach and frequency domain method is given in Figure 4.20. The corresponding L^2 errors for the co-and cross-polarised RCS are 0.41 % and 0.39 % respectively.

4.3.4. Computational cost of the anisotropic model

The next example includes the use of full anisotropic tensors for both electric and magnetic properties. The sphere is characterised by the parameters

$$\bar{\bar{\epsilon}} = \begin{bmatrix} 1.3 & 0 & 0 \\ 0 & 1.6 & 0 \\ 0 & 0 & 2.0 \end{bmatrix} \quad \bar{\bar{\sigma}} = \begin{bmatrix} 0.3 & 0 & 0 \\ 0 & 0.5 & 0 \\ 0 & 0 & 0.7 \end{bmatrix} \quad \bar{\bar{\mu}} = \begin{bmatrix} 1.2 & 0 & 0 \\ 0 & 1.4 & 0 \\ 0 & 0 & 1.8 \end{bmatrix} \quad \bar{\bar{\sigma}}_m = \begin{bmatrix} 0.4 & 0 & 0 \\ 0 & 0.3 & 0 \\ 0 & 0 & 0.5 \end{bmatrix}$$

Comparison with DDA results is not possible in this case, as the DDA code only allows for the modelling of non-magnetic materials. To investigate the time penalty that results from the use of the anisotropic model, two simulations were performed on the same mesh. In the first example, the sphere was taken to be an isotropic lossy dielectric material, with $\mu > 1$, $\epsilon > 1$, $\sigma > 0$, $\sigma_m > 0$. In the second example, the sphere was modelled as an anisotropic lossy dielectric material, so that $\bar{\bar{\mu}} \neq \mu_r \bar{\bar{I}}$, $\bar{\bar{\epsilon}} \neq \epsilon_r \bar{\bar{I}}$, $\bar{\bar{\sigma}} > \bar{\bar{0}}$, $\bar{\bar{\sigma}}_m > \bar{\bar{0}}$. It was found that the computational cost for the example involving the anisotropic sphere was ten times the cost of the solution for the isotropic sphere. This extra cost mainly arises from equation (3.57), which implies a requirement to solve a system of three equations for each Voronoi and Delaunay node.

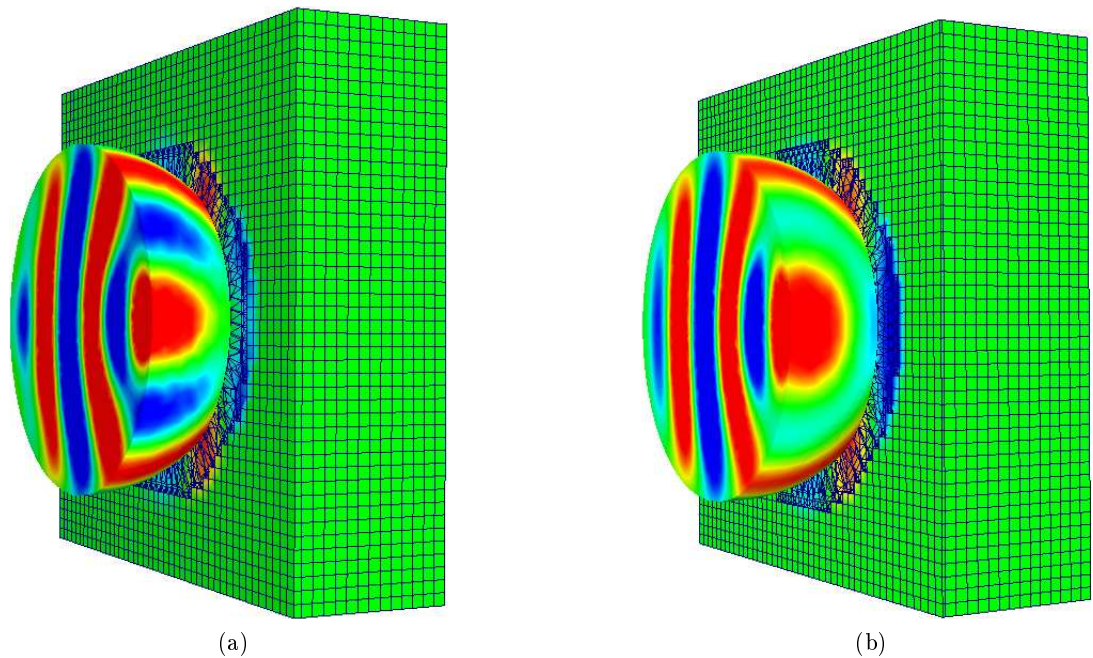


Figure 4.21.: *Scattering of a plane wave by a fully anisotropic dielectric sphere of electrical length 2λ : (a) contours of H_z shown on a cross-section through the mesh; (b) contours of E_y shown on a cross section through the mesh.*

Considering these additional costs, is this scheme competitive when compared to the standard FDTD method? In my first paper [48], I showed that the accuracy of this scheme, with a $\lambda/15$ unstructured mesh, compares favorably with that of the standard FDTD method, with a $\lambda/90$, $\lambda/120$ structured mesh, for objects of curved shape. This means that comparable results are obtained when using a mesh that is 6 to 8 times coarser. This is of course only valid for objects of high curvature with respect to the wavelength. For objects of very high electrical lengths, e.g a 20λ sphere, the curvature becomes less and less important and at a given point UM-FDTD will be outperformed by the standard Yee algorithm. The smaller a standard FDTD Yee's cell has 12 edges and 6 faces where the electric and magnetic field components are stored respectively. This corresponds to 18 degrees of freedom. Discretising one Yee's cell requires 6 tetrahedra, in the worst case scenario, leading to 19 edges and 14 faces. As the electric field projections are stored at the Delaunay edges and the magnetic field projections at Voronoi edges intersecting with the faces, this sums up to 33 degrees of freedom. Although the number of degrees of freedom have nearly doubled, this is more than compensated by the fact that I use a mesh that is, at least, 6 times coarser. Furthermore, because I am working in three dimensions, this should also be taken into account, This implies that, for the same volume, an unstructured mesh with 33 degrees of freedom produces the same accuracy as a structured mesh with $6^3 \times 6 = 1296$ degrees of freedom.

The extra operations, needed for averaging and reconstructing the vectors described in

section 3.6.4, imply a cost penalty. For each node, 18 averaging operations for each field, in addition to 3×3 operations of vector reconstruction for each edge are required. For the 6 tetrahedra lying inside one cube, the number of operations will be $2 \times 8 \times 18 + 9 \times (19 + 14) = 585$ for all degrees of freedom, taking into account the 19 electric field vectors and 14 magnetic field vectors. For one cell of a Cartesian mesh, 8 operations are required for averaging the two offset components of a field vector, leading to 48 extra operations on one cell node or 144 per Yee's cell. However, in this case dealing with curved boundaries, to achieve the same level of accuracy, the standard scheme will actually cost $6^3 \times 48 = 10368$ operations per same computational volume whereas the co-volume method only needs 585 operations.

4.3.5. Transmission of a narrow band pulse

As final example, I evaluate the transmission efficiency of a pulse through a radome made of anisotropic dielectric containing conducting fibers. The radome consists of half an ellipsoid, with a lateral radius of 0.5 m , a length of 1 m and a thickness of 0.05 m . Figure 4.22 and Figure 4.24 display a radome mesh with 20 points per wavelength. This mesh is only used for visualisation, as it is too coarse for a 1 GHz pulse. For the actual simulation, a finer mesh with 40 points per wavelength is used to guarantee enough degrees of freedom per wavelength inside the dielectric. In [48], I showed that the number of element layers employed to represent a given thickness of material has no impact on the results, provided that I meet the minimum number of points per wavelength requirement.

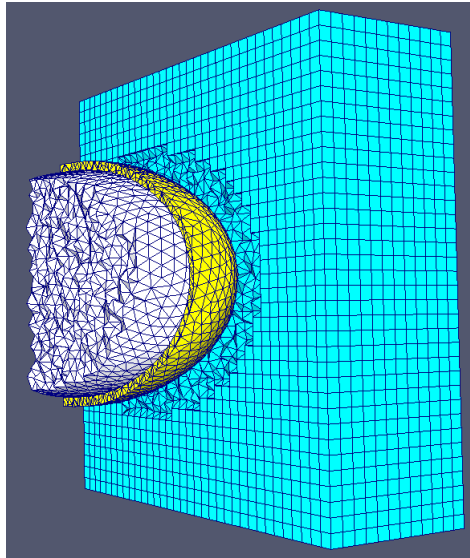


Figure 4.22.: Radome (yellow) in free space (white, blue)

The incident plane wave used to illuminate the Radome is a narrow band pulse (equation (4.4)). Composites are harder to model than standard anisotropic materials, due to the inner structure, e.g orientation of the fibers.

4. Code Validation and Numerical Examples

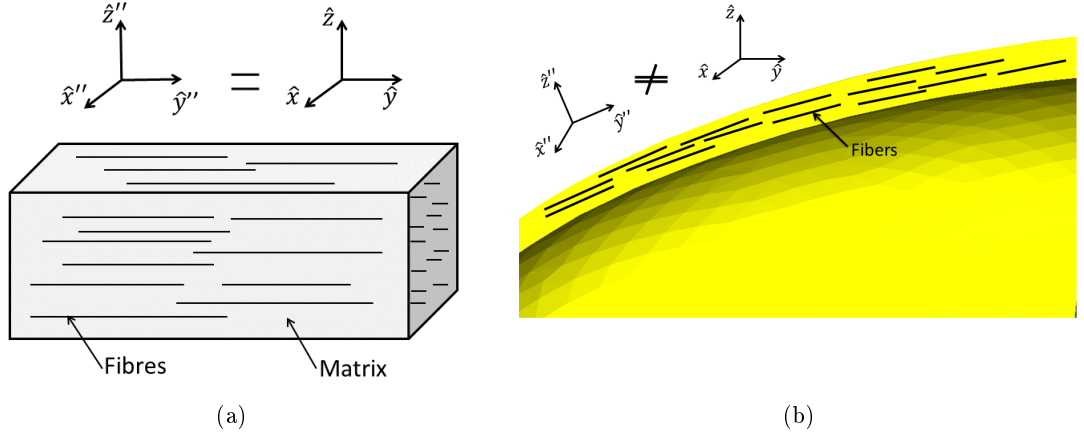


Figure 4.23.: *Composite material: (a) material frame (b) Distance between cell centers and material frame located at surface*

In Figure 4.23 (a) I illustrate a cut through a composite slab with the fibers oriented in the $\hat{\mathbf{y}}''$ direction. Due to the specific orientation of the slab, the material frame $(\hat{\mathbf{x}}'', \hat{\mathbf{y}}'', \hat{\mathbf{z}}'')$ and the global frame $(\hat{\mathbf{x}}, \hat{\mathbf{y}}, \hat{\mathbf{z}})$ are identical. In the case of the curved shell of a radome, the situation is more complicated, as the orientation of the fibers changes in space. In this case, for each location on the shell, there exist a material frame which, in general, differs from the global frame as illustrated in Figure 4.23 (b). In the previous sections, the coordinate transformation has only been used to pass from a global frame $(\hat{\mathbf{x}}, \hat{\mathbf{y}}, \hat{\mathbf{z}})$ to a local frame linked to each Voronoi or Delaunay edge $(\hat{\mathbf{x}}', \hat{\mathbf{y}}', \hat{\mathbf{z}}')$. For a composite, firstly a coordinate transformation from the material frame, linked to the orientation of the fibers, $(\hat{\mathbf{x}}'', \hat{\mathbf{y}}'', \hat{\mathbf{z}}'')$ to the global frame $(\hat{\mathbf{x}}, \hat{\mathbf{y}}, \hat{\mathbf{z}})$ is required. Afterwards I pass from the global frame to a local frame linked to each Voronoi or Delaunay edge, according to $(\hat{\mathbf{x}}', \hat{\mathbf{y}}', \hat{\mathbf{z}}')$. $(\hat{\mathbf{x}}'', \hat{\mathbf{y}}'', \hat{\mathbf{z}}'') \rightarrow \bar{\bar{J}}_{R1} \rightarrow (\hat{\mathbf{x}}, \hat{\mathbf{y}}, \hat{\mathbf{z}}) \rightarrow \bar{\bar{J}}_{R2} \rightarrow (\hat{\mathbf{x}}', \hat{\mathbf{y}}', \hat{\mathbf{z}}')$. Here, $\bar{\bar{J}}_{Ri}$, $i = 1, 2$, are the two transformation matrices, where $\bar{\bar{J}}_{R2}$ is identical to $\bar{\bar{J}}_R$ from equation (3.60). First, I have to create an orthonormal material frame. As in the preceding sections, an orthonormal system simplifies the coordinate transformation because the transformation matrix becomes a simple rotation matrix. The procedure here is illustrated in Figure 4.24(a). Initially, I only consider the Voronoi edges at the dielectric interface. Each Voronoi edge (Vor1, blue) crossing the face of a tetrahedron is surrounded by three Delaunay edges. I select two of these edges, (Del_1, Del_2) . By construction, they are parallel to the surface. Using the cross product, I create a vector $\mathbf{x}'' = Del_1 \times Del_2$ perpendicular to the dielectric surface. Finally, I take the cross product to obtain the vector $\mathbf{y}'' = \mathbf{z}'' \times Del_1$ and assign $\mathbf{z}'' = Del_1$. After normalising, I end up with one orthonormal material frame $(\hat{\mathbf{x}}'', \hat{\mathbf{y}}'', \hat{\mathbf{z}}'')$ for each face of the dielectric interface. The next step consists in linking the material frame to the cells inside the composite. To achieve this, I compare the distance between the intersection points of a Voronoi edge with the interface and the circumcenter of all cells C_1 inside the dielectric. After finding

4.3. Numerical Validation for anisotropic lossy objects

the smallest distance, I link the local material frame ($\hat{\mathbf{x}}', \hat{\mathbf{y}}', \hat{\mathbf{z}}'$) from the surface to the corresponding cell. This process is illustrated in Figure 4.24 (b).

$$\bar{\bar{J}}_{R1} = \begin{bmatrix} \mathbf{x}'' \cdot \mathbf{x} & \mathbf{x}'' \cdot \mathbf{y} & \mathbf{x}'' \cdot \mathbf{z} \\ \mathbf{y}'' \cdot \mathbf{x} & \mathbf{y}'' \cdot \mathbf{y} & \mathbf{y}'' \cdot \mathbf{z} \\ \mathbf{z}'' \cdot \mathbf{x} & \mathbf{z}'' \cdot \mathbf{y} & \mathbf{z}'' \cdot \mathbf{z} \end{bmatrix} \quad \bar{\bar{J}}_{R2} = \begin{bmatrix} \mathbf{x}' \cdot \mathbf{x} & \mathbf{x}' \cdot \mathbf{y} & \mathbf{x}' \cdot \mathbf{z} \\ \mathbf{y}' \cdot \mathbf{x} & \mathbf{y}' \cdot \mathbf{y} & \mathbf{y}' \cdot \mathbf{z} \\ \mathbf{z}' \cdot \mathbf{x} & \mathbf{z}' \cdot \mathbf{y} & \mathbf{z}' \cdot \mathbf{z} \end{bmatrix}$$

A typical material parameter tensor $\bar{\bar{M}} = \bar{\bar{\epsilon}}, \bar{\bar{\sigma}}, \bar{\bar{\mu}}, \bar{\bar{\sigma}}_m$ is now defined with respect to the material frame ($\hat{\mathbf{x}}'', \hat{\mathbf{y}}'', \hat{\mathbf{z}}''$) and linked to the cells inside the dielectric. The first coordinate transformation converts the material parameters, from the material to the global frame, according to

$$\bar{\bar{M}} = \frac{\bar{\bar{J}}_{R1} \bar{\bar{M}}'' \bar{\bar{J}}_{R1}^T}{\det(\bar{\bar{J}}_{R1})}$$

The second coordinate transformation converts the parameters from the global to the local frame and this process has already been described in the preceding sections. Considering, for example, equations (3.47,3.48), the material parameters $\bar{\bar{\epsilon}}, \bar{\bar{\sigma}}, \bar{\bar{\mu}}, \bar{\bar{\sigma}}_m$ have to be replaced by $\bar{\bar{\epsilon}}'', \bar{\bar{\sigma}}'', \bar{\bar{\mu}}'', \bar{\bar{\sigma}}_m''$. This is true for each equations in which the material parameters appear.

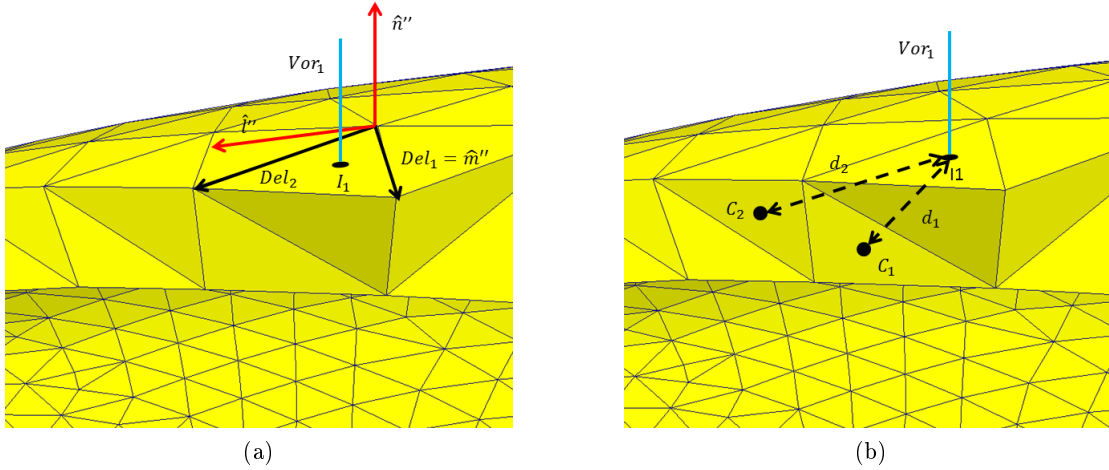


Figure 4.24.: Radome of composite material: (a) Construction of orthonormal material frame (b) Distance between cell centers and material frame located at surface

Our radome is characterised by the material parameters

$$\bar{\bar{\epsilon}}'' = \begin{bmatrix} 2.59 & 0 & 0 \\ 0 & 2.59 & 0 \\ 0 & 0 & 4.7 \end{bmatrix} \quad \bar{\bar{\sigma}}'' = \begin{bmatrix} 100 & 0 & 0 \\ 0 & 100 & 0 \\ 0 & 0 & 10 \end{bmatrix} \quad \bar{\bar{\mu}}'' = \begin{bmatrix} 1 & 0 & 0 \\ 0 & 1 & 0 \\ 0 & 0 & 1 \end{bmatrix} \quad \bar{\bar{\sigma}}_m'' = \begin{bmatrix} 0 & 0 & 0 \\ 0 & 0 & 0 \\ 0 & 0 & 0 \end{bmatrix}$$

4. Code Validation and Numerical Examples

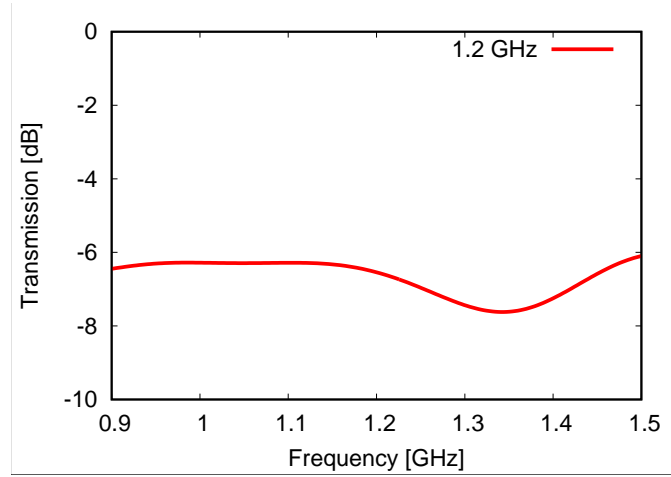


Figure 4.25.: *Transmission of 1.2 GHz pulse through a radome made out of a composite dielectric*

Due to the orientation of the fibers, the properties of our composite are the same in the $\hat{\mathbf{m}}''$ and the $\hat{\mathbf{l}}''$ directions, but differ along the $\hat{\mathbf{n}}''$ axis. For our material parameters, this means that $\bar{M}(1,1)'' = \bar{M}(2,2)'' \neq \bar{M}(3,3)''$, and the other components are 0, for $\bar{\epsilon}'', \bar{\sigma}''$ and $\bar{\mu}'' = \bar{I}$ and $\bar{\sigma}_m'' = 0$. Typically, a material that minimally attenuates the electromagnetic signal transmitted or received by the antenna is used. The transmission is evaluated using equation (4.3) which corresponds to the ratio of the amplitude of the total electric field divided by the amplitude of the incident electric field at a point \mathbf{r}_0 inside the radome. The transmission of 1.2 GHz narrowband pulse through a composite radome is represented in Figure 4.25.

4.4. Numerical validation for isotropic chiral material

To validate my algorithm I compute the transmission coefficients of an EM pulse through a chiral slab and the variation of the angle of the plane of polarisation of the incident field. For both cases I use a structured mesh to model a dielectric slab of dimensions $0.3\text{ m} \times 0.3\text{ m} \times 0.1\text{ m}$ in x, y, z dimension. A thickness of 0.1 m corresponds to 40 cells.

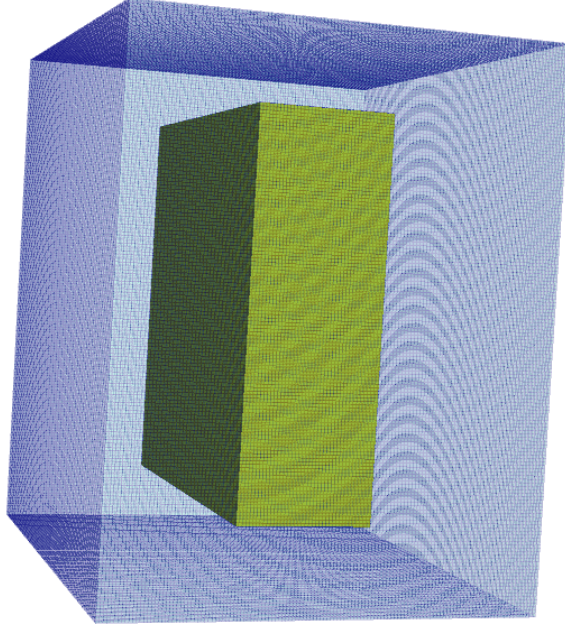


Figure 4.26.: *Chiral slab (yellow) in free space (blue)*

4.4.1. Rotation of the plane of polarisation

As mentioned in the introduction the chirality induces a rotation of the plane of polarisation of the incident field (ORD) if the chirality is a real number. In the case of a complex number the plane of polarisation is rotated and the polarisation changes (CD). To validate our results I currently only consider the real part of the chirality. In this case the rotation of the angle can be computed according to the following formula

$$\Phi = \text{Re}(\kappa)\omega L \quad (4.5)$$

With Φ the variation of the angle, $\text{Re}(\kappa)$ the real part of the chirality, ω the angular frequency of the incident wave and L the thickness of the slab [66]. I use the slab in free space as depicted in Figure 4.26. To numerically compute the variation of the angle I use the Fourier transform, which allows me to compute the variation of the amplitude without the time dependence. Therefore I choose a point of the Delaunay mesh behind (with respect to the incident wave) the chiral slab and take the fourier transform of

4. Code Validation and Numerical Examples

the y versus the Fourier transform of the x component of the electric field for a wave propagating in z direction.

$$\Phi_{num} = \frac{FT(\mathbf{E}_y)}{FT(\mathbf{E}_x)} \quad (4.6)$$

and compare them with the analytical computed angle Φ .

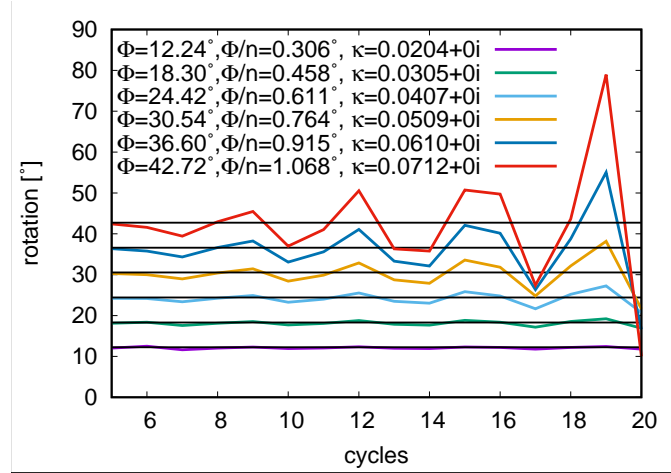


Figure 4.27.: *Rotation of the plane of polarisation for 6 different chiralities over time. The black line corresponds to the analytical value.*

According to Figure 4.27, for chiralities below $\kappa = 0.0407$ the scheme appears to be stable and the numerically computed angle of rotation of the plane of polarisation matches well the analytical solution. For higher chiralities the angle of rotation starts varying significantly over time. It seems that the chirality leads to an instability of the algorithm if the imaginary part of the chirality is too high. This instability and the stabilising effect of damping ($Im(\kappa) \neq 0$) is investigated in subsection 4.4.3 and 4.4.4

4.4.2. Reflection and transmission on a chiral slab

I compute the transmission and reflection coefficients of a chiral slab in free space. The derivation of this expression can be found in all details in [66]. I will only give the transmission and reflection coefficients for a bi-isotropic slab of infinite height and width with a finite thickness L between two bi-isotropic media. Medium 1 extends from $z \in]-\infty, -L[$, the bi-isotropic slab from $z \in [-L, 0[$ and medium 3 from $z \in [0, +\infty[$.

4.4. Numerical validation for isotropic chiral material

Defining the following parameters:

$$Z_L = \eta_{3\pm} \quad (4.7)$$

$$Z^+ = \eta_{2\pm} = \eta_2 e^{\mp j\vartheta_2} \quad (4.8)$$

$$Z^- = \eta_{2\mp} = \eta_2 e^{\pm j\vartheta} \quad (4.9)$$

$$Z^+ + Z^- = 2\eta_2 \cos(\vartheta_2) \quad (4.10)$$

$$Z^+ - Z^- = \mp 2j\eta_2 \sin(\vartheta_2) \quad (4.11)$$

$$\beta^+ = k_{2\pm} = k_2 (\cos(\vartheta_2) \pm \kappa_{2r}) \quad (4.12)$$

$$\beta^- = k_{2\mp} = k_2 (\cos(\vartheta_2) \mp \kappa_{2r}) \quad (4.13)$$

$$\beta = k_2 \cos(\vartheta_2) \quad (4.14)$$

$$\eta_i = \sqrt{\frac{\mu_i}{\varepsilon_i}} \quad (4.15)$$

$$\chi_{r,i} = \sin(\vartheta_i) \quad (4.16)$$

$$\kappa_{r,i} = \kappa_i / n_i \quad (4.17)$$

$$n_i = \sqrt{\frac{\mu_i \varepsilon_i}{\mu_0 \varepsilon_0}} \quad (4.18)$$

$$\varepsilon_+ = \varepsilon (\cos(\vartheta) + \kappa_r) e^{j\vartheta} \quad (4.19)$$

$$\varepsilon_- = \varepsilon (\cos(\vartheta) - \kappa_r) e^{-j\vartheta} \quad (4.20)$$

With κ_r the relative chirality, n the index of refraction, χ_r the relative Tellegen parameter which equals 0 in chiral media, η the impedance and $i = 1, 2, 3$ the index for the corresponding region.

$$Z_{in\pm} = \eta_2 \frac{\eta_{3\pm} \cos(\vartheta_2 \mp k_2 L \cos(\vartheta_2)) + j\eta_2 \sin(k_2 L \cos(\vartheta_2))}{\eta_2 \cos(\vartheta_2 \pm k_2 L \cos(\vartheta_2)) + j\eta_{3\pm} \sin(k_2 L \cos(\vartheta_2))} \quad (4.21)$$

The corresponding reflection coefficients at the interface are

$$R_{co} = \frac{Z_{in+} Z_{in-} \cos(2\vartheta_1) - \eta_1^2 + j\eta_1 (Z_{in+} - Z_{in-}) \sin(\vartheta_1)}{Z_{in+} Z_{in-} + \eta_1^2 + \eta_{1+} Z_{in+} + \eta_{1-} Z_{in-}} \quad (4.22)$$

$$R_{cr} = -\frac{jZ_{in+} Z_{in-} \sin(2\vartheta_1) + \eta_1 (Z_{in+} - Z_{in-}) \cos(\vartheta_1)}{Z_{in+} Z_{in-} + \eta_1^2 + \eta_{1+} Z_{in+} + \eta_{1-} Z_{in-}} \quad (4.23)$$

$$T_{\pm\pm} = \frac{2\eta_2 \eta_3 \cos(\vartheta_1) \cos(\vartheta_2) e^{\pm j(\vartheta_1 - \vartheta_3)} e^{\mp j\kappa_r k_2 L}}{\eta_2 (\eta_{1\mp} \cos(\Psi_{\pm}) + \eta_{3\pm} \cos(\Psi_{\mp})) + j(\eta_2^2 + \eta_{1\mp} \eta_{3\pm}) \sin(k_2 L \cos(\vartheta_2))} \quad (4.24)$$

$$T_{co} = \frac{1}{2} (T_{++} + T_{--}) \quad (4.25)$$

$$T_{cr} = -\frac{j}{2} (T_{++} - T_{--}) \quad (4.26)$$

with $\Psi_{\pm} = \vartheta_2 \pm k_2 L \cos(\vartheta_2)$. In my case medium 1 and 3 are free space and the slab is not bi-isotropic but only chiral. Therefore the Tellegen parameter equals 0. An in y

4. Code Validation and Numerical Examples

direction linearly polarised narrowband pulse propagating in z direction is send towards the slab.

$$\mathbf{E}_y(\mathbf{r}, t) = e^{-(t-\mathbf{k}\cdot\mathbf{r}/\omega)^2/2\tau^2} \sin(\omega t - \mathbf{k} \cdot \mathbf{r}) \quad (4.27)$$

Our material parameters are $\varepsilon_s = 1.8 \varepsilon_0$, $\varepsilon_\infty = 1.6 \varepsilon_0$, $\mu_s = 1.1 \mu_0$, $\mu_\infty = 1.0 \mu_0$, $\omega_e = \omega_h = \omega_k = 2\pi \times 3.5 \text{ GHz}$, $\xi_e = 0.14$, $\xi_h = 0.12$, $\xi_k = 0.1$ and $\tau_k = 1 \text{ ps}$. The thickness of the slab is 0.1 m and is made out of 40 cells, leading to a spatial discretisation $\Delta z = 0.0025 \text{ m}$. To compute the frequency dependent reflection I chose a point p_1 of the mesh in free space just in front of the slab. For the transmission coefficient I chose another point p_2 slightly behind the slab. Next I reconstruct the electric field vector at the corresponding points and use the Fourier transformation to get a time independent response. I compute the co-polarised reflection coefficient R_{co} , the co-polarised transmission coefficient T_{co} and the cross-polarised transmission coefficient T_{cr} according to

$$R_{co} = \frac{FT(\mathbf{E}_{scat,y,p1})}{FT(\mathbf{E}_{inc,y,p1})} \quad (4.28)$$

$$T_{co} = \frac{FT(\mathbf{E}_{scat,y,p2})}{FT(\mathbf{E}_{inc,y,p2})} \quad (4.29)$$

$$T_{cr} = \frac{FT(\mathbf{E}_{scat,x,p2})}{FT(\mathbf{E}_{inc,y,p2})} \quad (4.30)$$

R_{cr} equals zero and T_{cr} would be zero for a non chiral material.

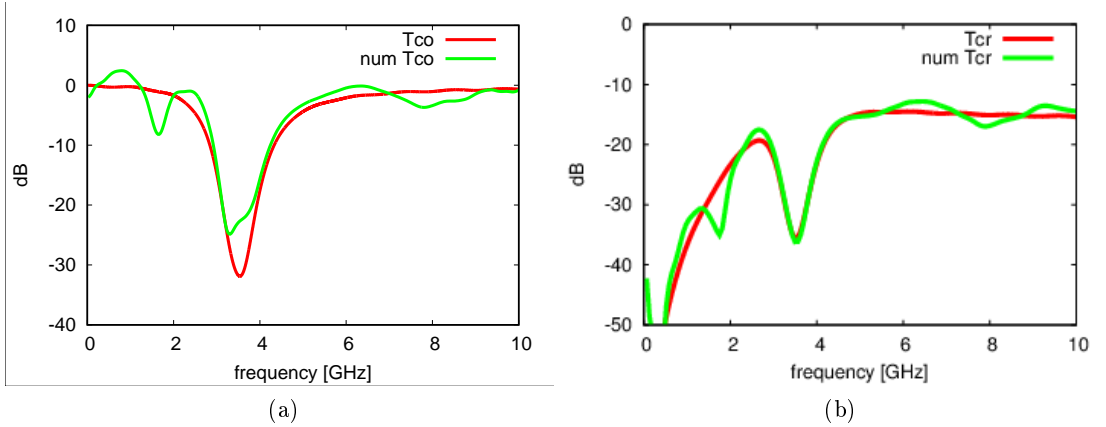
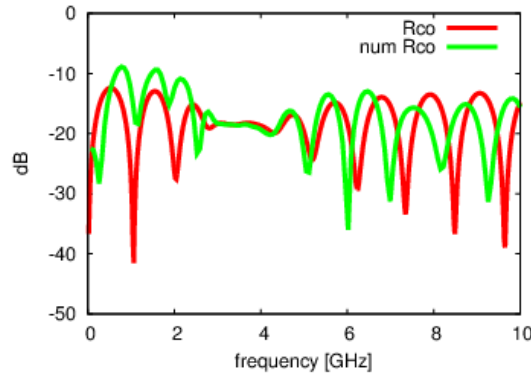


Figure 4.28.: Analytical vs Numerical Transmission coefficients (a) T_{co} ; (b) T_{cr}


 Figure 4.29.: Analytical vs Numerical Reflection coefficients R_{co}

As expected T_{cr} differs from zero. Furthermore the results agree reasonably well in the vicinity of the resonance frequency. The differences between the analytical and numerical results are probably due to two reasons. First of all, the analytical model assumes a slab with infinite extension in the directions perpendicular to the propagation of light. Which is clearly not the case for my slab. Applying periodic boundary conditions (which are not yet implemented in my code) to model an infinite slab should already improve the results. Furthermore, the numerical dispersion inherent to the scattered field formulation leads to a shift in the peaks for the reflection coefficient.

4.4.3. Numerical stability without damping

During my simulations I observed that an increase in the chirality leads to an instability of the algorithm. To understand this instability let's consider again equation (4.5). L corresponds to the thickness and can also be expressed as $L = n\Delta z$ with n the number of cells along the z direction (thickness) of our slab. Δz is the edge length of a given cell. Instead of considering the overall rotation of the plane of polarisation, I normalise it to a single cell, leading to :

$$\Phi_{cell} = \frac{\Phi}{n} = \kappa\omega\Delta z \quad (4.31)$$

To investigate the instabilities I set $\xi_k = 0$ which leads to a vanishing imaginary part in the chirality. Then I run the algorithm for 20 cycles on two different meshes and compute the angle Φ_{cell} . The results start at the 5th cycle because no steady state is achieved before (at least not for the fine mesh). Both meshes represent the same slab with the same dimension. Only the spatial step Δz differs. The finer mesh has $\Delta z = 0.0025 m$ and the coarser $\Delta z = 0.003 m$. To visualise the deviation of the computed from the expected angle I calculate the relative error $(x_{ana} - x_{num})/x_{num}$ with x_{ana} the analytical value and a_{num} the numerically computed value. The results are represented in Figure 4.30.

4. Code Validation and Numerical Examples

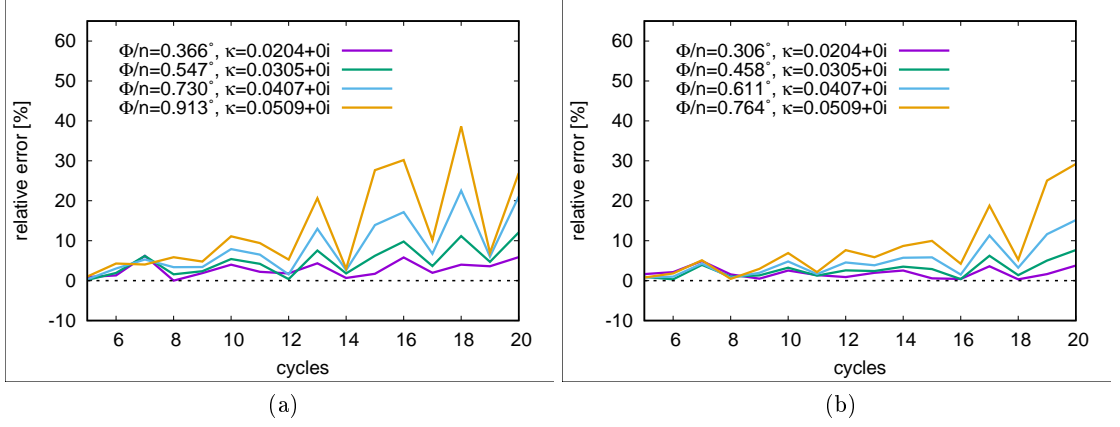


Figure 4.30.: Relative Error of the numerically computed rotation of the plane of polarisation with increasing chirality compared to analytical values for two meshes (a) mesh with $\Delta z = 0.003$ (b) mesh with $\Delta z = 0.0025$ m

From Figure 4.30 (a) and (b) it can be clearly seen that for the same chirality the oscillations increase with increasing spatial step Δz . To further investigate the effect of the spatial step Δz , I kept the chirality constant and used meshes with different spatial sizes ($\Delta z = 0.0025$ m, 0.003 m, 0.004 m, 0.005 m) where the dimension of the slab remained the same. Increasing the spatial step Δz leading to an increase in Φ_{cell} for coarser meshes (Figure 4.31a). I use the same time step of 2.9 ps for all the meshes. For another test I use the same mesh ($\Delta z = 0.003$) but reduce the time step (Figure 4.31b).

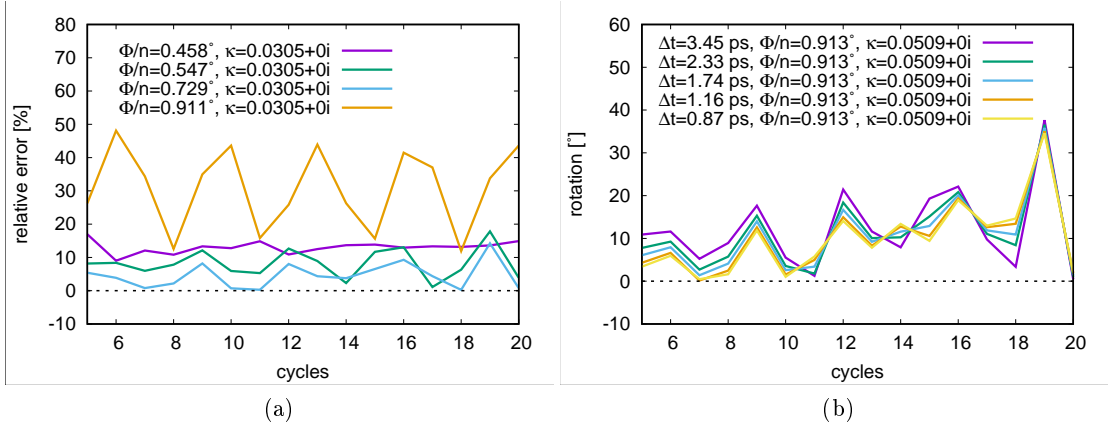


Figure 4.31.: Effect on mesh refinement and time steps on the results (a) same chirality, different meshes (b) same mesh, different time step

From Figure 4.31a I observe that for $\kappa = 0.0305$ I only obtain a stable result for $\Phi/n = 0.458^\circ$ at an error of roughly 10%. For all the other, coarser meshes, the solution varies

significantly. By analysing Figure 4.31b it appears that a decrease of the time step only has a minor effect on the stability. I can conclude that the chirality induced instabilities are directly linked to the spatial discretisation and do not strongly depend on the time step. For $Im(\kappa) = 0$, according to my results, the condition $\Phi/n < 0.45$ should be fulfilled to obtain a stable solution. To verify these results I considered the publication of Pereda [103]. Their parameters are: $\omega = 2\pi \times 8GHz$, $\tau_k = 5 \times 10^{-12}s$, $\omega_k = 2\pi \times 3.5GHz$, $\xi_k = 0.1$ leading to $\kappa = -0.059 - i0.006$. Only considering the real part of the chirality, with $\Delta z = 0.001m$ this leads to $\Phi_{Cell} = 0.57^\circ$. I had further discussions with Ana Grande [103]. She gave me additional results. For $Re(\kappa) = 0.17$, $\Delta z = 0.2 \times 10^{-3}m$ and a slab with a thickness of $L = 500\Delta z$ I get $\Phi_{Cell} = 0.49^\circ$. In contrast to my testcases so far, Ana Grande and Pereda considered materials with $Im(\kappa) \neq 0$. Therefore I continue to investigate the effect of damping $Im(\kappa) \neq 0$ on the stability of the algorithm.

4.4.4. Numerical stability with damping

In this section I demonstrate the stabilising effects of damping induced imaginary part of the chirality. Therefore I used a coupling coefficient $\tau_k = 2 \times 10^{-12}s$ which leads without damping ($\xi_k = 0$) to very strong instabilities in the scheme. For a constant τ_k I increase the damping ($\xi_k = 0.01, 0.025, 0.5, 0.1$) and plot as before Φ over 20 cycles. Furthermore I computed the real and imaginary parts of the chirality for different damping coefficients. Figure 4.32 shows a stable scheme for Φ_{Cell} , which before lead to instabilities in the undamped case. It appears that as long as $Im(\kappa) \geq Re(\kappa)/15$ the scheme is stable.

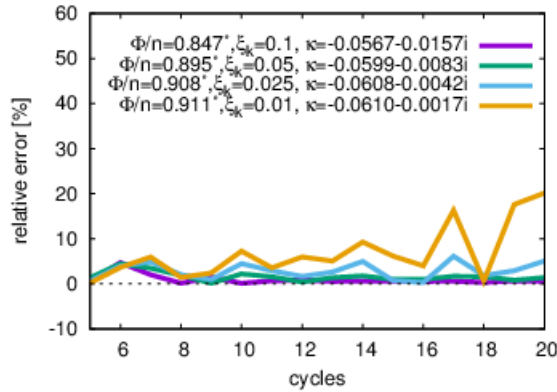


Figure 4.32.: relative error of computed angle over 20 cycles

But in this case I am not dealing with a pure ORD because due to the imaginary part the polarisation also changes. For $\tau_k = 2 \times 10^{-12}s$, $\omega_k = 2\pi \times 3.5GHz$, and varying ξ_k , the real and imaginary part of the chirality are displayed in Figure 4.33.

4. Code Validation and Numerical Examples

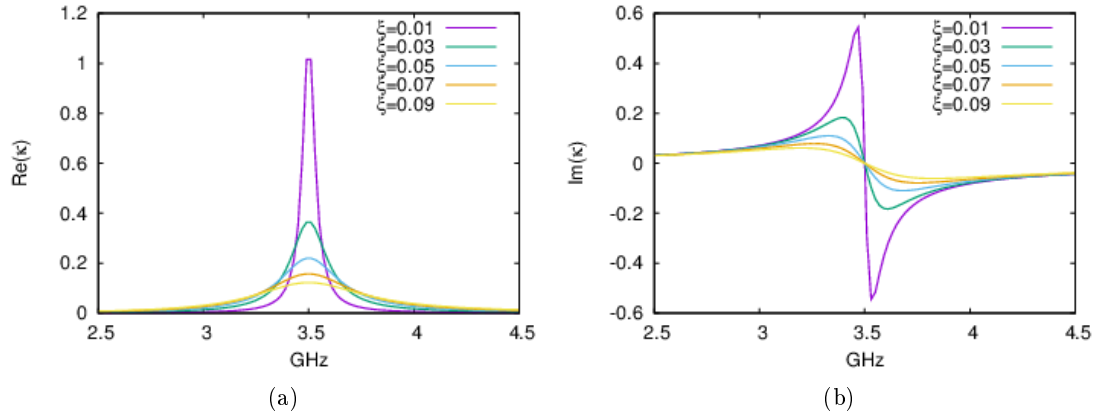


Figure 4.33.: *Real and imaginary part of the chirality for varying damping factors (a) Real part of the chirality ; (b) imaginary part of the chirality*

My results demonstrate a successful implementation of the algorithm for modelling isotropic chiral media. Furthermore the stabilising effects of the damping have been investigated.

4.5. Numerical validation for bi-anisotropic media

For bi-anisotropic media not only the numerical methods but also the analytical solutions become increasingly complex. Although there exist an analytical solution developed by Rikte [106] I am still working on the implementation. Meanwhile, I validate my method in two steps. First of all I do not consider the chirality tensor by setting all its components to zero. The algorithm now models an anisotropic frequency dependent material. Next I use DDscat [40] as for the anisotropic case because it can handle diagonal complex material parameters. As benchmark test I compute the bistatic RCS of a sphere

4.5.1. Radar cross section on anisotropic dispersive sphere

To validate my algorithm I compute the RCS (equation (4.2)) of a 2λ sphere. Where I used exactly the same mesh as for the isotropic case (Figure 4.5a) on which a plane wave with $\lambda = 1\text{ m}$ is incident. In my algorithm I assume a Lorentz model dispersion relation for the permittivity and permeability

$$\begin{aligned}\bar{\bar{\epsilon}}(\omega) &= \epsilon_0 \left(\bar{\bar{\epsilon}}_\infty + \frac{\omega_\epsilon^2}{\omega_\epsilon^2 - \omega^2 + j2\omega_\epsilon\xi_\epsilon\omega} (\bar{\bar{\epsilon}}_s - \bar{\bar{\epsilon}}_\infty) \right) \\ \bar{\bar{\mu}}(\omega) &= \mu_0 \left(\bar{\bar{\mu}}_\infty + \frac{\omega^2}{\omega_\mu^2 - \omega^2 + j2\omega_\mu\xi_\mu\omega} (\bar{\bar{\mu}}_s - \bar{\bar{\mu}}_\infty) \right)\end{aligned}$$

4.5.1.1. Isotropic permittivity

For the first case, I decided to use identical entries for $\varepsilon_{\infty,ii}$ and $\varepsilon_{s,ii}$ with $i = 1, 2, 3$ and no frequency dependence at all for the permeability. This corresponds to an isotropic dispersive material.

$$\bar{\varepsilon}_{\infty} = \varepsilon_0 \begin{pmatrix} 1.6 & 0 & 0 \\ 0 & 1.6 & 0 \\ 0 & 0 & 1.6 \end{pmatrix}, \quad \bar{\varepsilon}_s = \varepsilon_0 \begin{pmatrix} 2 & 0 & 0 \\ 0 & 2 & 0 \\ 0 & 0 & 2 \end{pmatrix}, \quad \bar{\mu}(\omega) = \mu_0 \begin{pmatrix} 1 & 0 & 0 \\ 0 & 1 & 0 \\ 0 & 0 & 1 \end{pmatrix}$$

$$\omega_{\varepsilon} = 0.6 \text{ GHz}, \quad \xi_{\varepsilon} = 0.4$$

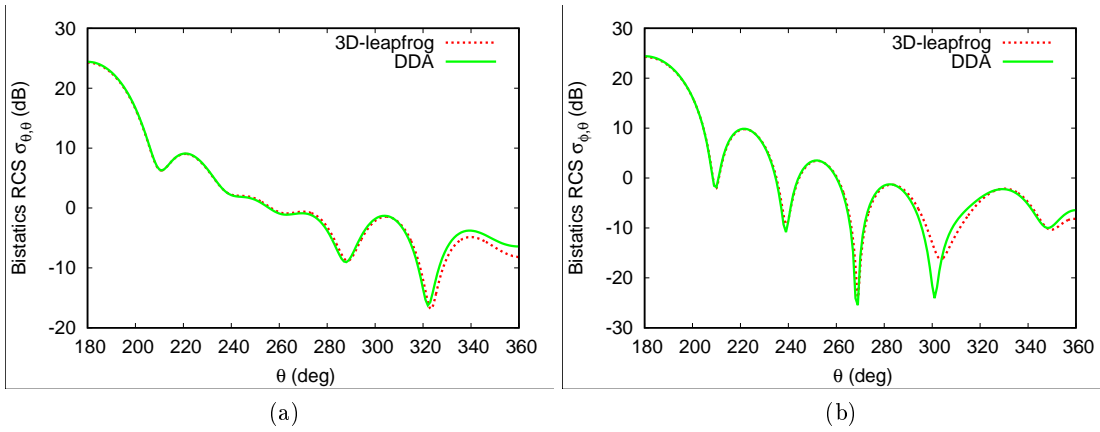


Figure 4.34.: *Scattering of a plane wave by a dielectric sphere of electrical length 2λ with anisotropic dispersive permittivity: (a) co-polarised RCS distribution; (b) cross-polarised RCS distribution.*

Overall a very good agreement between the RCS for both polarisations is obtained (Figure 4.34). The corresponding L2-Errors for the co and cross polarised RCS are 2.94 % and 2.96 % respectively.

4.5.1.2. Anisotropic permittivity

For the second case, the entries on the diagonal of the matrices $\bar{\varepsilon}_{\infty}$ and $\bar{\varepsilon}_s$ differ from each other. As in the example before no frequency dependence for the permeability is assumed.

$$\bar{\varepsilon}_{\infty} = \varepsilon_0 \begin{pmatrix} 1.6 & 0 & 0 \\ 0 & 1.4 & 0 \\ 0 & 0 & 1.7 \end{pmatrix}, \quad \bar{\varepsilon}_s = \varepsilon_0 \begin{pmatrix} 2.1 & 0 & 0 \\ 0 & 1.9 & 0 \\ 0 & 0 & 2.0 \end{pmatrix}, \quad \bar{\mu}(\omega) = \mu_0 \begin{pmatrix} 1 & 0 & 0 \\ 0 & 1 & 0 \\ 0 & 0 & 1 \end{pmatrix}$$

$$\omega_{\varepsilon} = 0.6 \text{ GHz}, \quad \xi_{\varepsilon} = 0.4$$

4. Code Validation and Numerical Examples

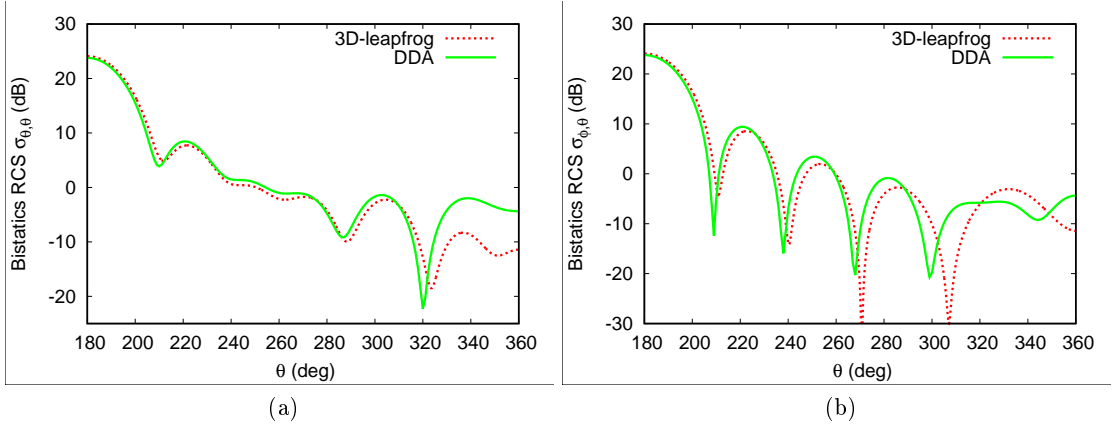


Figure 4.35.: *Scattering of a plane wave by a dielectric sphere of electrical length 2λ with anisotropic dispersive permittivity: (a) co-polarised RCS distribution; (b) cross-polarised RCS distribution.*

The co-polarised RCS of our 3D-leapfrog scheme and the DDA solution match well over the whole angular range except for the last 30 degrees. The cross-polarised RCS on the other hand shows a slight shift in the dips between my solution and the DDA approximation (Figure 4.35). The corresponding L2-Errors for the co and cross polarised RCS are 11.19 % and 11.22 % respectively.

4.5.1.3. Isotropic permeability

This time I removed the frequency dependence of the permittivity and use identical elements for entries of the permeability matrix. This corresponds to an isotropic dispersive material with respect to the permeability

$$\bar{\mu}_\infty = \begin{pmatrix} 1.6 & 0 & 0 \\ 0 & 1.6 & 0 \\ 0 & 0 & 1.6 \end{pmatrix}, \bar{\mu}_s = \begin{pmatrix} 2.0 & 0 & 0 \\ 0 & 2.0 & 0 \\ 0 & 0 & 2.0 \end{pmatrix}, \bar{\epsilon}(\omega) = \epsilon_0 \begin{pmatrix} 1 & 0 & 0 \\ 0 & 1 & 0 \\ 0 & 0 & 1 \end{pmatrix}$$

$$\omega_\mu = 0.6 \text{ GHz}, \xi_\mu = 0.4$$

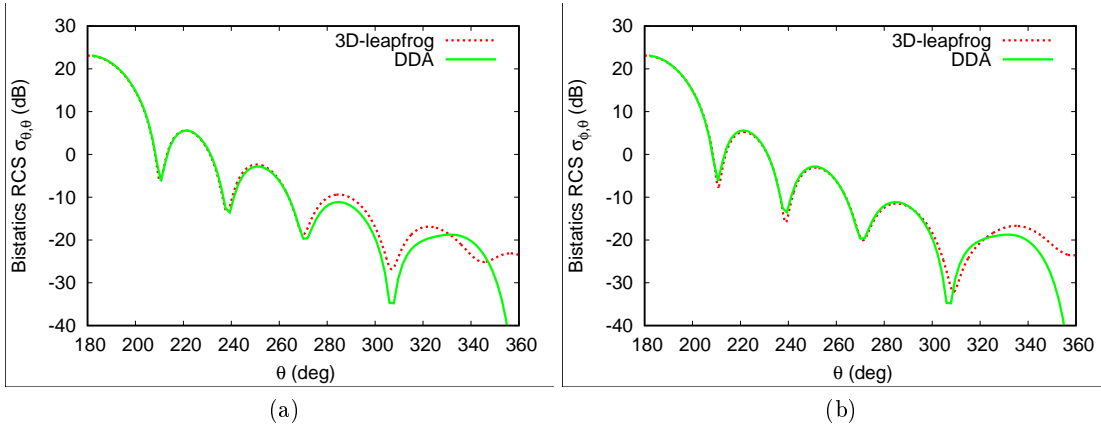


Figure 4.36.: *Scattering of a plane wave by a dielectric sphere of electrical length 2λ with anisotropic dispersive permittivity: (a) co-polarised RCS distribution; (b) cross-polarised RCS distribution.*

Again a good agreement for both polarisations is observed. Only at the end of the angular range around -30dB the solutions start to diverge slightly from each other. The corresponding L2-Errors for the co and cross polarised RCS are 11.74 % and 11.74 % respectively.

4.5.1.4. Anisotropic permeability

As last test case we defined a matrix where the entries on the diagonal of the matrices $\bar{\mu}_\infty$ and $\bar{\mu}_s$ differ from each other.

$$\bar{\epsilon}(\omega) = \epsilon_0 \begin{pmatrix} 1 & 0 & 0 \\ 0 & 1 & 0 \\ 0 & 0 & 1 \end{pmatrix} \quad \bar{\mu}_\infty = \mu_0 \begin{pmatrix} 1.6 & 0 & 0 \\ 0 & 1.9 & 0 \\ 0 & 0 & 1.7 \end{pmatrix}, \quad \bar{\mu}_s = \mu_0 \begin{pmatrix} 2.1 & 0 & 0 \\ 0 & 1.9 & 0 \\ 0 & 0 & 2.0 \end{pmatrix}$$

$$\omega_\mu = 0.6 \text{ GHz}, \quad \xi_\mu = 0.4$$

4. Code Validation and Numerical Examples

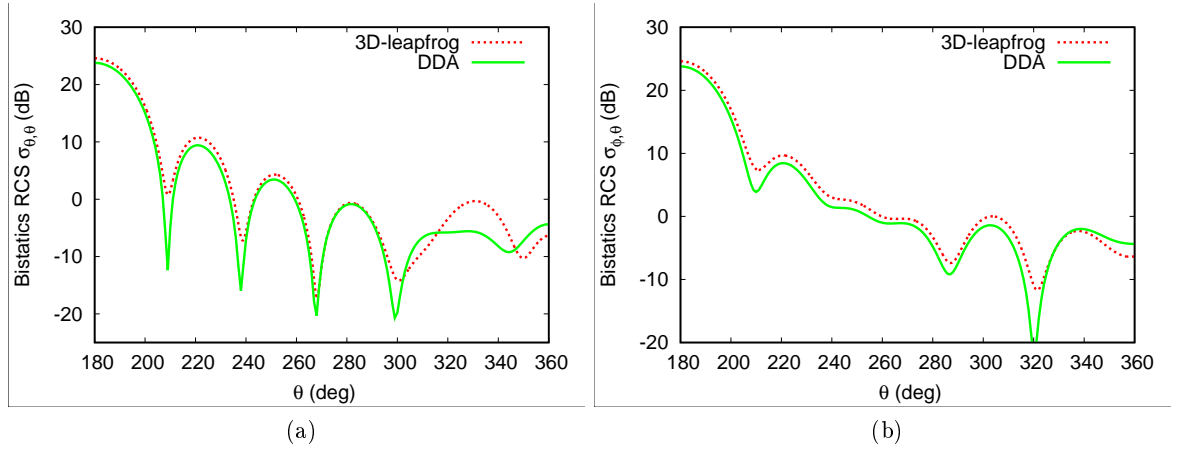


Figure 4.37.: *Scattering of a plane wave by a dielectric sphere of electrical length 2λ with anisotropic dispersive permittivity: (a) co-polarised RCS distribution; (b) cross-polarised RCS distribution.*

In contrast to the results for anisotropic permittivity, depicted in Figure 4.35, this time no shift of the peak occurs. The two solutions agree quite well except again for the last 40 degrees for the co-polarised solution. The corresponding L2-Errors for the co and cross polarised RCS are 11.13 % and 11.13 % respectively. Unfortunately I can only compare my results with another numerical method because an analytical solution for frequency dependent anisotropic materials does not exist. Therefore it is not clear which method is more or less accurate. Although the L2 errors appears to be relatively high the shapes of the RCS agree quite well in most of the cases.

4.5.1.5. isotropic chiral vs bi-anisotropic

To validate the implementation of the magnetoelectric coupling tensor I decided to compare the bi-anisotropic with the isotropic chiral solution. Therefore we use diagonal tensors with identical entries on the diagonal.

$$\begin{aligned} \bar{\bar{\mu}}_{\infty} &= \mu_0 \begin{pmatrix} 1.0 & 0 & 0 \\ 0 & 1.0 & 0 \\ 0 & 0 & 1.0 \end{pmatrix}, \bar{\bar{\mu}}_s = \mu_0 \begin{pmatrix} 1.1 & 0 & 0 \\ 0 & 1.1 & 0 \\ 0 & 0 & 1.1 \end{pmatrix}, \quad \omega_{\mu} = 2\pi \times 3.5 \text{ GHz}, \quad \xi_{\mu} = 0.12 \\ \bar{\bar{\epsilon}}_{\infty} &= \epsilon_0 \begin{pmatrix} 1.6 & 0 & 0 \\ 0 & 1.6 & 0 \\ 0 & 0 & 1.6 \end{pmatrix}, \bar{\bar{\epsilon}}_s = \epsilon_0 \begin{pmatrix} 1.8 & 0 & 0 \\ 0 & 1.8 & 0 \\ 0 & 0 & 1.8 \end{pmatrix}, \quad \omega_{\epsilon} = 2\pi \times 3.5 \text{ GHz}, \quad \xi_{\epsilon} = 0.14 \\ \bar{\bar{\tau}}_{\kappa} &= \frac{1}{c} \begin{pmatrix} 0.0003 & 0 & 0 \\ 0 & 0.0003 & 0 \\ 0 & 0 & 0.0003 \end{pmatrix}, \quad \omega_{\kappa} = 2\pi \times 3.5 \text{ GHz}, \quad \xi_{\kappa} = 0.1 \end{aligned}$$

4.5. Numerical validation for bi-anisotropic media

for the isotropic case

$$\begin{aligned}\mu_\infty &= \mu_0, \mu_s = \mu_0 1.1, \omega_\mu = 2\pi \times 3.5 \text{ GHz}, \xi_\mu = 0.12 \\ \varepsilon_\infty &= \varepsilon_0 1.6, \varepsilon_s = \varepsilon_0 1.8, \omega_\varepsilon = 2\pi \times 3.5 \text{ GHz}, \xi_\varepsilon = 0.14 \\ \tau_\kappa &= \frac{1}{c} 0.003, \omega_\kappa = 2\pi \times 3.5 \text{ GHz}, \xi_\kappa = 0.1\end{aligned}$$

The incoming plane wave with optical axis along z direction has an angular frequency of $\omega = 5 \text{ GHz}$. If the implementation of the bi-anisotropic algorithm is correct we expect the same results as for the isotropic chiral algorithms. For the simulation I used a slab with lateral extension $x = y = 0.3 \text{ m}$ and a thickness of $d = 0.1 \text{ m}$ in z direction. Figures 4.38 and 4.39 demonstrate the correct implementation of my algorithm.

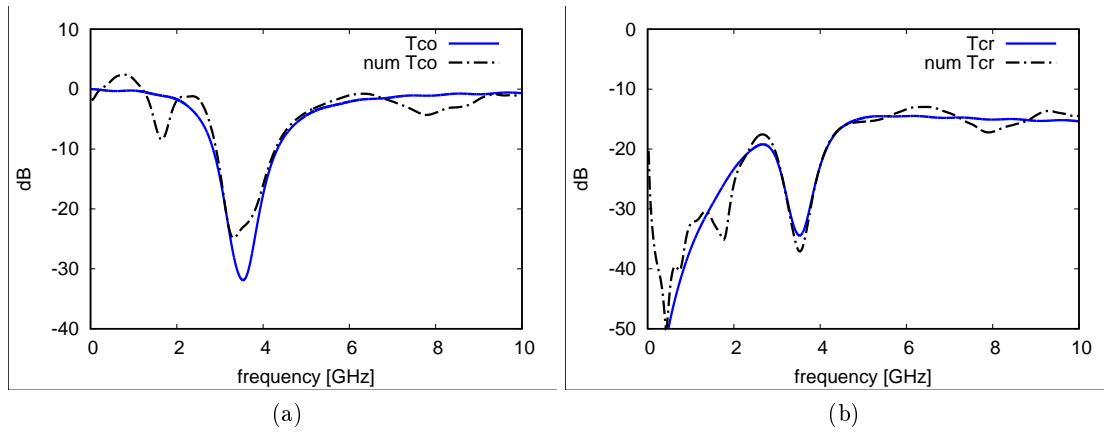


Figure 4.38.: Analytical isotropic chiral vs Numerical bi-anisotropic transmission coefficients (a) T_{co} ; (b) T_{cr}

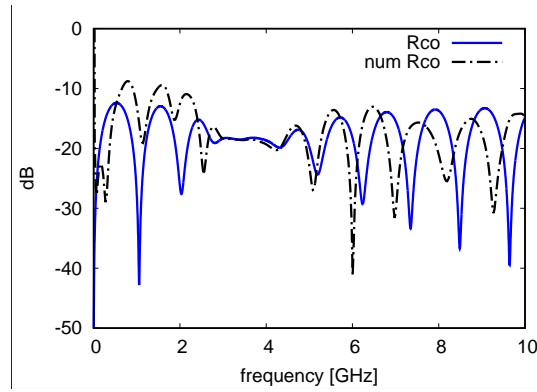


Figure 4.39.: Analytical isotropic chiral vs Numerical bi-anisotropic reflection coefficients R_{co}

Part II.

Multiscale Approach for Metamaterial Modelling

5. Micro to Macro Approach

Due to its microstructure composites and metamaterials cannot be modelled in the same way as simple dielectric materials like glass. The orientation of its constituents makes the composite anisotropic, meaning the index of refraction depends on the orientation of the fibers. The same is true for the metamaterial where the index of refraction depends upon the orientation and arrangement of the unit cells. Imagine, modelling VLF (very low frequency) radiation, typically in the frequency range from $3 - 30 \text{ kHz}$. Such antennas are used for communication in submarines because the radiated waves may penetrate between $10 \text{ m} - 30 \text{ m}$ deep into the ocean. This leads to a free space wavelength of $\lambda_0 = 1000 \text{ m} - 10 \text{ km}$. To model an object, most of the numerical methods require the creation of a mesh to represent the object. The mesh needs to be fine enough to capture all the phenomena of interest and at the same time be as coarse as possible to reduce the computational costs. As example, for a finite difference time domain algorithm which is based upon a structured mesh, the FDTD grid cell (for free space simulations) should be at least $\lambda_0/10$. This corresponds to a cell with an edge length of $100 \text{ m} - 1 \text{ km}$, which is much longer than the antennas and even longer than most of the submarines. Using a very fine mesh is in this case however a poor alternative because the computational costs would be tremendous. Instead a technique called “thin-wire approximation” [125] which allows the modelling of sub-cell structures is applied. Similar problems occur for the modelling of metamaterials consisting of a periodic array of wires and rings (Figure 5.1). In this case it is not possible to model every single unit cell separately. At this point multiscale techniques can be used to circumvent the typically required fine meshes and to reduce the sometimes tremendous computational costs. The idea behind these methods is to predict the behavior of a given material at a large scale by only performing calculations on a smaller scale, as single unit cell for example. Multiscale techniques can be roughly divided into two classes, analytical and numerical homogenisation techniques. The analytical techniques may be used for two component composites but quickly reach their limitations for metamaterials. Concerning the numerical homogenisation techniques, I decided to divide them in two classes, “direct” and “indirect” techniques. As direct technique I classify a method where the material parameters can be directly calculated from the electric and magnetic fields by field averaging. This typically involves inverting the constitutive equations as suggested by Wu or Pendry [143, 101]. In an indirect method, the material parameters are not directly deduced from the field quantities. Such methods typically involve the scattering parameters introduced in subsection 6.4 and a retrieval algorithm to compute the material parameters from the S-parameters 6.8. This procedure is identical to the experimental method, with the exception that the S parameters are computed numerically. Li, Chen and Smith presented such methods for metamaterials [77, 78, 28, 120]. In this chapter I briefly recall the analytical homogenisation techniques

Multiscale Approach

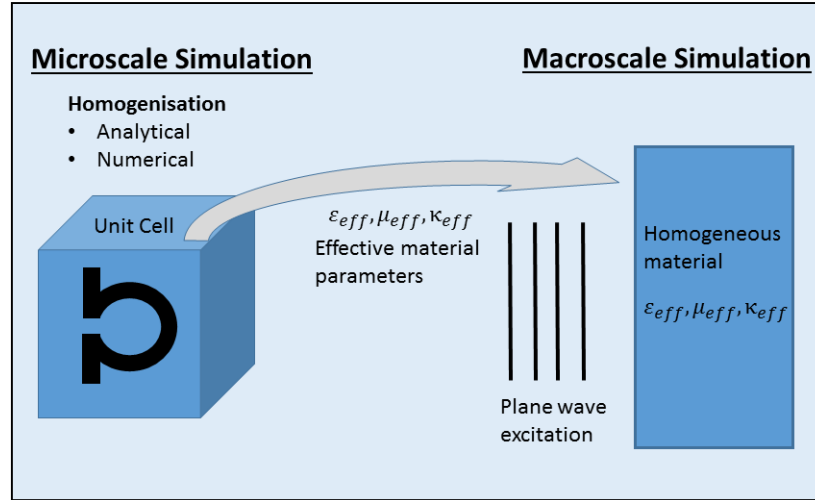


Figure 5.1.: *Schematic representation of the multiscale approach*

and their limitations, before I focus on a indirect and direct numerical homogenisation technique.

5.1. Analytical microscale homogenisation techniques

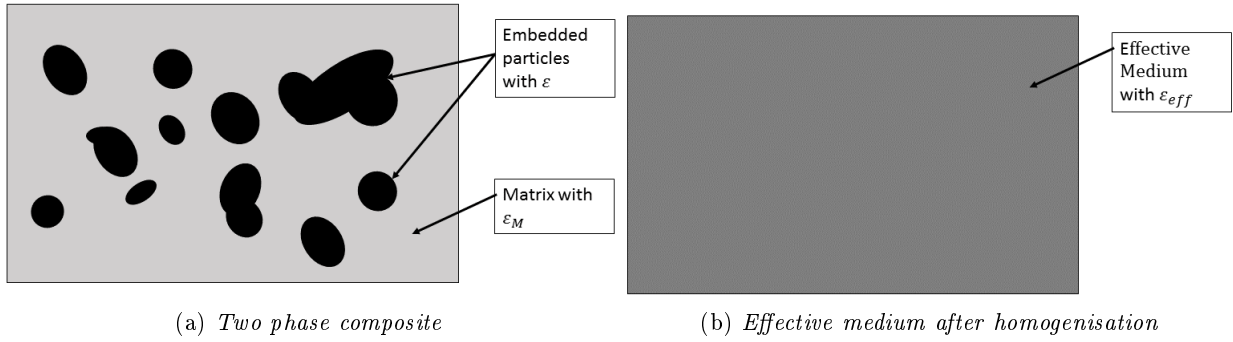
For composites very simple mixing formulas have been established over the last century by Maxwell Garnett [50], Bruggemann [21], Looyenga [85] and Bergman [17]. The Maxwell Garnett (equation (5.1)), Bruggeman (equation (5.2)) and Looyenga (equation (5.3)) equations only rely upon one single parameter to compute the effective permittivity of a two component composite, namely the volume fraction V_f defined as the volume of the embedded particles divided by the total volume. Due to this simplifications the first three mentioned methods can only be applied in some special cases.

$$\frac{\varepsilon_{eff} - \varepsilon_M}{\varepsilon_{eff} + 2\varepsilon_M} = V_f \frac{\varepsilon - \varepsilon_M}{\varepsilon + 2\varepsilon_M} \quad (5.1)$$

$$(1 - V_f) \frac{\varepsilon_M - \varepsilon_{eff}}{\varepsilon_M + 2\varepsilon_{eff}} = -V_f \frac{\varepsilon - \varepsilon_{eff}}{\varepsilon + 2\varepsilon_{eff}} \quad (5.2)$$

$$\varepsilon_{eff}^{1/3} = V_f \varepsilon^{1/3} + (1 - V_f) \varepsilon_M^{1/3} \quad (5.3)$$

Where ε is the permittivity of the embedded particles, ε_M is the permittivity of the matrix (Figure 5.2a) and ε_{eff} the permittivity of the effective medium after the homogenisation (Figure 5.2b).

Figure 5.2.: *Effective medium from a two phase composite*

The Maxwell Garnett model is suited for systems with low volume fractions of embedded particles with particles far away from each other. The Bruggeman theory is equivalent to Maxwell Garnett for low volume fractions. Above $V_f = 1/3$ the embedded particles are assumed to be partially connected. The Looyenga formulation on the other hand assumes a percolation for any volume fraction.

The Bergmann representation of effective dielectric functions is the most general form of effective medium approaches.

$$\varepsilon_{eff} = \varepsilon_M \left(1 - V_f \int_0^1 \frac{g(n, V_f)}{t - n} dn \right)$$

where

$$t = \frac{\varepsilon_M}{(\varepsilon_M - \varepsilon)} \quad (5.4)$$

The function $g(n, V_f)$ is the spectral density function holding all the topological details of the microgeometry. Unfortunately $g(n, V_f)$ cannot simply be computed analytically. Experiments were conducted to match the theoretical optical spectra with the experimental ones by adjusting $g(n, V_f)$. As mentioned, those methods relying on simple analytic mixing formulas have their limitations, especially if metallic inclusions are considered instead of dielectric ones, which is the case for metamaterials. A purely numerical solution to the homogenization of metamaterials appears to be a much better approach for the modelling of metamaterials.

5.2. Numerical microscale techniques

Compared to analytical methods numerical homogenisation techniques have the advantage not to be limited to the quasi static regime, low volume fractions or the shape of the inclusions [56]. I will mainly focus on methods that have been designed for metamaterials. These techniques are based upon three main pillars. Field averaging, the retrieval of effective parameters from scattering and periodic boundary conditions. To illustrate the procedure of field averaging and effective parameter retrieval I consider a publication

5. Micro to Macro Approach

from 1999 by Pendry et al. [101] were they investigated the effective permeability of several periodic artificially magnetic structures. To allow the retrieval of an effective permittivity the unit cell should be much smaller than the incoming wavelength in the material ($a \ll \lambda$). Pendry et al. suggest a field averaging which follows directly from the integral form of Maxwell's equation. They average every component of \mathbf{H} along each of the three axes of a unit cell, leading to

$$\begin{aligned}(H_{avg})_x &= \frac{1}{a} \int_{\mathbf{r}=(0,0,0)}^{\mathbf{r}=(a,0,0)} \mathbf{H} \cdot d\mathbf{r} \\ (H_{avg})_y &= \frac{1}{a} \int_{\mathbf{r}=(0,0,0)}^{\mathbf{r}=(0,a,0)} \mathbf{H} \cdot d\mathbf{r} \\ (H_{avg})_z &= \frac{1}{a} \int_{\mathbf{r}=(0,0,0)}^{\mathbf{r}=(0,0,a)} \mathbf{H} \cdot d\mathbf{r}\end{aligned}$$

\mathbf{B} is averaged over each face of the unit cell. Where the corresponding surfaces A_x, A_y, A_z are spanned by the vectors $\mathbf{y}, \mathbf{z}; \mathbf{x}, \mathbf{z}; \mathbf{x}, \mathbf{y}$, resulting in

$$(B_{avg})_{x,y,z} = \frac{1}{a^2} \int_{A_{x,y,z}} \mathbf{B} \cdot d\mathbf{A}$$

To obtain the effective material parameters the constitutive equation $\mathbf{B} = \mu\mathbf{H}$ and the effective fields \mathbf{B}_{avg} and \mathbf{H}_{avg} are used leading to

$$\begin{aligned}\mu_{eff,x} &= \frac{(B_{avg})_x}{\mu_0 (H_{avg})_x} \\ \mu_{eff,y} &= \frac{(B_{avg})_y}{\mu_0 (H_{avg})_y} \\ \mu_{eff,z} &= \frac{(B_{avg})_z}{\mu_0 (H_{avg})_z}\end{aligned}$$

To reduce the computational costs instead of meshing all the unit cells of the a periodic metamaterial it is more efficient to model a single unit cell and to apply periodic boundary conditions. In the frequency domain these conditions are implemented by Bloch functions. This method is known as the eigenfrequency method and is for example used in an algorithm developed by Smith [120]. Pendry assumed that the size of a unit cell (defined by a) is negligible with respect to the incoming wave. According to Smith [120] this is however not the case for most of the metamaterials to date. Therefore he adapted the method from Pendry and generalised it to chiral materials. He showed that the retrieved material parameters needs to be corrected, which works well for an empty unit cells but leads to an approximation for a metamaterial. My method doesn't need this correction. Furthermore instead of using a linear polarised wave to retrieve the material parameters I use a circular polarised one, which allows me to retrieve all the parameters perpendicular to the optical axis.

5.2.1. Indirect microscale parameter retrieval

This method is based upon the calculation of the S-parameters that are related to the complex reflection and transmission coefficients. From them, one can retrieve the material parameters. Typically, the metamaterials considered in the methods so far are all non chiral. In this case only two effective material parameters have to be identified, the permittivity and permeability. For the chiral material however the chirality also needs to be determined. Therefore I use a method by Chen [28, 26]. For the simulation I only consider a unit cell of the metamaterial surrounded by a layer of free space and a PML (Absorbing boundary condition (ABC)) on both sides along the optical axis as depicted in Figure 5.3. I use periodic boundary conditions (PBC) perpendicular to the direction of propagation to create an infinitely extended slab in lateral direction. The thickness along the optical axis still corresponds to a single unit cell.

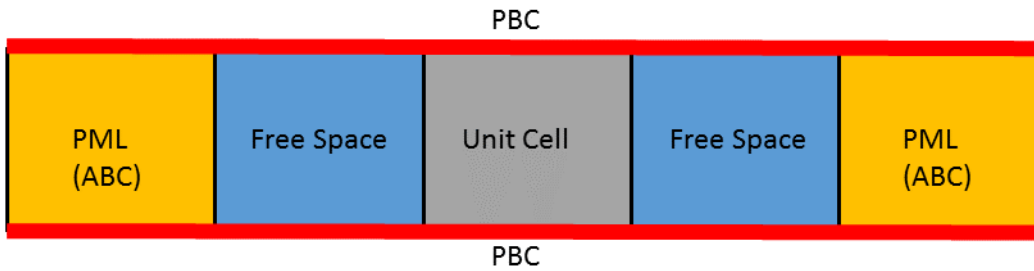


Figure 5.3.: *Unit cell surrounded by free space and PML along the optical axis*

Algorithm procedure

1. I set two ports, an emitting and a receiving port to record the S-parameters. The ports are located between the PML and free space. After running the simulation I obtain the S-parameters.
2. From the S-parameters I compute the material parameters using the same retrieval algorithm as described in section 6.8.
3. In the next step I use an optimisation algorithm giving me the best match between the computed material parameters and the corresponding Lorentz or Condon model. The materials parameters are complex functions, and the retrieved parameters (ε_∞ , ε_s , ω_ε , ξ_ε ...) have to match the real and imaginary part of the model. Therefore I use the open source library for nonlinear optimisation (NLOpt). From this library I use an evolutionary algorithm for global optimisation, namely ESCH, developed by Carlos Henrique da Silva Santo's [34].
4. These parameters (ε_∞ , ε_s , ω_ε , ξ_ε ...) obtained from the optimisation algorithm are the input for my UM-FDTD program which allows the simulation of bi-anisotropic media (section 3.8). With this program I model the experimental slab with the

5. Micro to Macro Approach

same dimensions $7\text{ cm} \times 15\text{ cm} \times 15\text{ cm}$ as in the experiment. Remember, the S parameters I obtained at the beginning correspond to those of slab with an infinite lateral extension but with a finite thickness of a single unit cell, therefore they differ from the experimental data.

5. From this simulation I obtain the S-parameters from the transmission and reflection and compare them directly with the experimental S-parameters.

My material parameters are tensors. Therefore I have to change the orientation of the incident field vectors with respect to the unit cell to get all the elements of the material parameter matrices. The element in the permittivity matrix along the optical axis is set to the permittivity of the matrix material. I used a frequency domain code, for instance COMSOL. To validate this method, the configuration depicted in Figure 5.3 is used. The unit cell is a simple dielectric, with the same, constant, permittivity as the matrix material (FR4). From this setup I compute the S-parameters. The ports required for computing the scattering parameters are placed at the interface between the free space and the PML. In contrast to the magnitude, the phase of the numerical S-parameters needs to be corrected by an angle $\Phi_{corr} = k_0(c_0/l_{fs})$ to compensate for the free space region. Where $l_{fs} = l_{fs,1} + l_{fs,2}$ is the total length of the free space and $l_{fs,i}$, $i = 1, 2$ the free space region on each side of the dielectric and k_0 is the free space wavenumber. Correcting the phase leads to a perfect agreement between numerical and analytical S-parameters as illustrated in Figure 5.4. This correction is obviously also required for the unit cell of the metamaterial and the results are presented in subchapter 8.1.1.

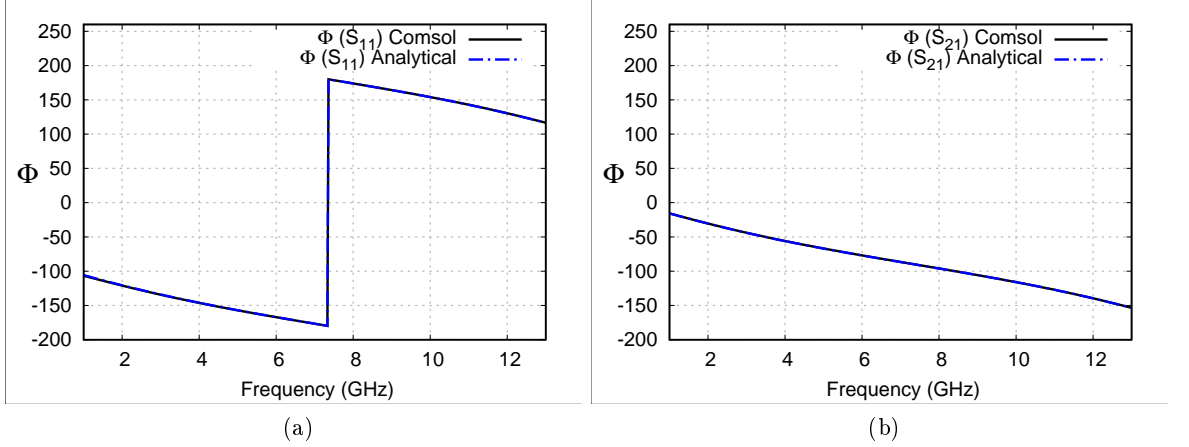


Figure 5.4.: Phase of S_{11} and S_{21} corrected by $\Phi_{add} = k_0(c_0/l_{fs})$ for transmitting and receiving ports located at the interface between the dielectric and free space (a) $|S_{11}|$; (b) $|S_{21}|$

I use the retrieval algorithm for the bianisotropic material and obtain the expected permittivity of 4.5 with the loss tangent of 0.004 S/m as depicted in Figure 5.5

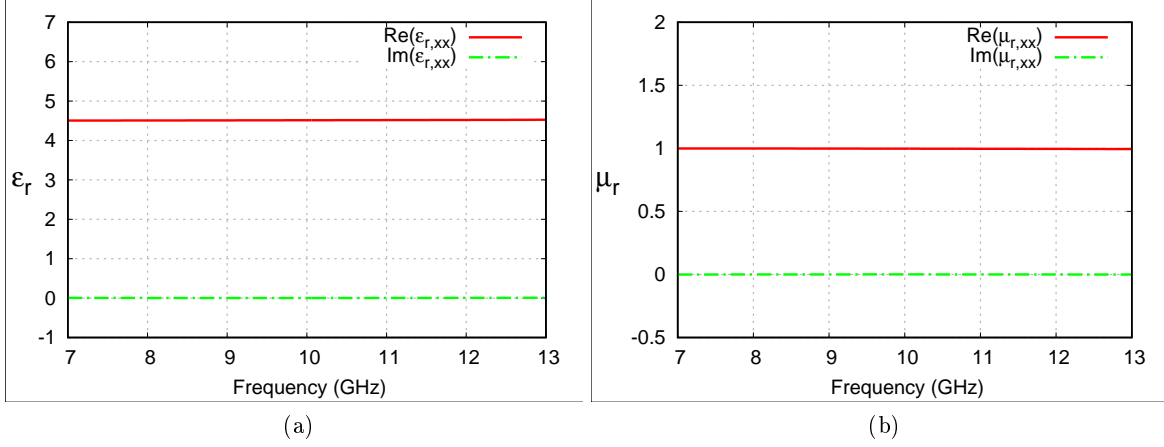


Figure 5.5.: Material parameters of FR4 after phase correction (a) relative permittivity ; (b) relative permeability

5.2.2. Direct mean field technique

The constitutive equations for a bi-anisotropic material are defined as in equations (2.64) and (2.65). We only consider the chiral case, therefore the Tellegen parameter $\bar{\chi}$ is not considered. For a reciprocal bi-anisotropic, $\bar{\epsilon}$ and $\bar{\mu}$ are symmetric tensors and $\bar{\xi} = -\bar{\zeta}^T = -i/c\bar{\kappa}^T$ where. Writing equations (2.64) and (2.65) for every component leads to

$$\begin{aligned}
 D_x &= \epsilon_{xx}E_x + \epsilon_{xy}E_y + \epsilon_{xz}E_z - \frac{i}{c}(\kappa_{xx}H_x + \kappa_{xy}H_y + \kappa_{xz}H_z) \\
 D_y &= \epsilon_{yx}E_x + \epsilon_{yy}E_y + \epsilon_{yz}E_z - \frac{i}{c}(\kappa_{yx}H_x + \kappa_{yy}H_y + \kappa_{yz}H_z) \\
 D_z &= \epsilon_{zx}E_x + \epsilon_{zy}E_y + \epsilon_{zz}E_z - \frac{i}{c}(\kappa_{zx}H_x + \kappa_{zy}H_y + \kappa_{zz}H_z) \quad (5.5)
 \end{aligned}$$

$$\begin{aligned}
 B_x &= \frac{i}{c}(\kappa_{xx}E_x + \kappa_{xy}E_y + \kappa_{xz}E_z) + \mu_{xx}H_x + \mu_{xy}H_y + \mu_{yz}H_z \\
 B_y &= \frac{i}{c}(\kappa_{yx}E_x + \kappa_{yy}E_y + \kappa_{yz}E_z) + \mu_{yx}H_x + \mu_{yy}H_y + \mu_{yz}H_z \quad (5.6) \\
 B_z &= \frac{i}{c}(\kappa_{zx}E_x + \kappa_{zy}E_y + \kappa_{zz}E_z) + \mu_{zx}H_x + \mu_{zy}H_y + \mu_{zz}H_z
 \end{aligned}$$

If the wave is propagating in x direction with electric field in z and magnetic field in y direction equation (5.5) and (5.6) become

$$D_z = \epsilon_{zz}E_z - \frac{i}{c}\kappa_{zy}H_y \quad (5.7)$$

$$B_y = \mu_{yy}H_y + \frac{i}{c}\kappa_{yz}E_z \quad (5.8)$$

5. Micro to Macro Approach

To determine the components of $\bar{\varepsilon}$, $\bar{\mu}$, $\bar{\kappa}$ I use the property that the components of $\bar{\varepsilon}$, $\bar{\mu}$ differ for a right or a left hand circular polarised wave.

According to Lindell [66], for a bi-isotropic medium the constitutive correspond to equations (2.62) and (2.63). Lindell suggests to use the wavefields \mathbf{E}_+ , \mathbf{E}_- and \mathbf{H}_+ , \mathbf{H}_- instead of the electric and magnetic fields directly. They are linked to each other via

$$\mathbf{E} = \mathbf{E}_+ + \mathbf{E}_- \quad (5.9)$$

$$\mathbf{H} = \mathbf{H}_+ + \mathbf{H}_- \quad (5.10)$$

The wavefield decomposition of an electromagnetic field in a bi-isotropic medium is based upon the two following postulates:

1. Each of the two wavefields \mathbf{E}_+ , \mathbf{H}_+ and \mathbf{E}_- , \mathbf{H}_- sees the bi-isotropic medium as an equivalent isotropic medium with respective medium parameters μ_+ , ε_+ and μ_- , ε_-
2. The two wavefields are independent: they do not couple in a homogeneous bi-isotropic medium.

Next the equivalent parameters are defined as

$$\eta_+ = i \frac{\xi}{\varepsilon_+ - \varepsilon} = i \frac{\mu_+ - \mu}{\varsigma} \quad (5.11)$$

$$\eta_- = -i \frac{\xi}{\varepsilon_- - \varepsilon} = -i \frac{\mu_- - \mu}{\varsigma} \quad (5.12)$$

leading to

$$\varepsilon_+ = \varepsilon (1 + \kappa_r) \quad (5.13)$$

$$\varepsilon_- = \varepsilon (1 - \kappa_r) \quad (5.14)$$

$$\mu_+ = \mu (1 + \kappa_r) \quad (5.15)$$

$$\mu_- = \mu (1 - \kappa_r) \quad (5.16)$$

With the constitutive equations

$$\mathbf{D}_\pm = \varepsilon_\pm \mathbf{E}_\pm$$

$$\mathbf{B}_\pm = \mu_\pm \mathbf{H}_\pm$$

where $\kappa_r = \kappa / \sqrt{\varepsilon_r \mu_r}$ is the relative chirality and the $+$, $-$ refers to a right hand circular polarised and left hand circular polarised wave if I am looking along the direction of propagation of the incident wave. The different material parameters are obtained by

combining the equations (5.13)-(5.16) to

$$\varepsilon = \frac{\varepsilon_+ + \varepsilon_-}{2} \quad (5.17)$$

$$\kappa_r = \frac{\varepsilon_+ - \varepsilon_-}{2\varepsilon} = \frac{\varepsilon_+ - \varepsilon_-}{\varepsilon_+ + \varepsilon_-} \quad (5.18)$$

$$\mu = \frac{\mu_+ + \mu_-}{2} \quad (5.19)$$

$$\kappa_r = \frac{\mu_+ - \mu_-}{2\mu} = \frac{\mu_+ - \mu_-}{\mu_+ + \mu_-} \quad (5.20)$$

I assume that these statements can be generalised to the bi-anisotropic medium where the material parameters become second order tensors because each equation should still hold indepently for every component of the matrix.

$$\bar{\bar{\varepsilon}}_{eff} = \frac{1}{2} (\bar{\bar{\varepsilon}}_{eff,+} + \bar{\bar{\varepsilon}}_{eff,-}) \quad (5.21)$$

$$\bar{\bar{\mu}}_{eff} = \frac{1}{2} (\bar{\bar{\mu}}_{eff,+} + \bar{\bar{\mu}}_{eff,-}) \quad (5.22)$$

$$\bar{\bar{\kappa}}_r = (\bar{\bar{\varepsilon}}_{eff,+} + \bar{\bar{\varepsilon}}_{eff,-})^{-1} (\bar{\bar{\varepsilon}}_{eff,+} - \bar{\bar{\varepsilon}}_{eff,-}) \quad (5.23)$$

$$\bar{\bar{\kappa}}_r = (\bar{\bar{\mu}}_{eff,+} + \bar{\bar{\mu}}_{eff,-})^{-1} (\bar{\bar{\mu}}_{eff,+} - \bar{\bar{\mu}}_{eff,-}) \quad (5.24)$$

Algorithm procedure

To obtain the effective material parameters I first illuminate the unit cell with a right hand polarised and afterwards a left hand polarised wave. The optical axis is oriented along the x axis and the wave rotates in the x, y plane.

$$\mathbf{E}(\mathbf{r}, t) = \begin{pmatrix} 0 \\ \pm iE_0 \\ E_0 \end{pmatrix} e^{i(\mathbf{k} \cdot \mathbf{r} - \omega t)}$$

In this direct homogenisation approach I require the volume average of the field vectors over two unit cells. The first cell corresponds to the unit cell of the metamaterial consisting of a metallic inclusion inside a matrix cube. The fields $\{\mathbf{D}_+\}$, $\{\mathbf{B}_+\}$, $\{\mathbf{D}_-\}$, $\{\mathbf{B}_-\}$ are calculated inside these cells, where $\langle \rangle$ refers to the volume average of the field vectors over an unit cell. As reference I use a unit cell with the same dimension and the same dielectric material but without the inclusion, leading to $\{\mathbf{E}_+\}$, $\{\mathbf{H}_+\}$, $\{\mathbf{E}_-\}$, $\{\mathbf{H}_-\}$. From these quantities I can calculate the matrices $\bar{\bar{\varepsilon}}_{eff,+}$ and $\bar{\bar{\varepsilon}}_{eff,-}$ which I write as $\bar{\bar{\varepsilon}}_{eff,\pm}$ by taking the ratio of the different field components.

$$\bar{\bar{\varepsilon}}_{eff,\pm} = \begin{pmatrix} \frac{\langle D_{x,\pm} \rangle}{\langle E_{x,\pm} \rangle} & \frac{\langle D_{x,\pm} \rangle}{\langle E_{y,\pm} \rangle} & \frac{\langle D_{x,\pm} \rangle}{\langle E_{z,\pm} \rangle} \\ \frac{\langle D_{y,\pm} \rangle}{\langle E_{x,\pm} \rangle} & \frac{\langle D_{y,\pm} \rangle}{\langle E_{y,\pm} \rangle} & \frac{\langle D_{y,\pm} \rangle}{\langle E_{z,\pm} \rangle} \\ \frac{\langle D_{z,\pm} \rangle}{\langle E_{x,\pm} \rangle} & \frac{\langle D_{z,\pm} \rangle}{\langle E_{y,\pm} \rangle} & \frac{\langle D_{z,\pm} \rangle}{\langle E_{z,\pm} \rangle} \end{pmatrix} \quad (5.25)$$

5. Micro to Macro Approach

From equations (5.21) the effective permittivity tensor can be calculated. It should however be noted that only the elements on the diagonal correspond to the effective permittivity. If I apply this method to a simple isotropic or anisotropic material $\varepsilon_+ = \varepsilon_-$. The off-diagonal elements are residua from the coupling, which can be calculated from equation (5.23). This time only the off diagonal elements should be considered for a bi-anisotropic material. To compute the effective permeability I proceed in the same way as before by calculating this time the matrices $\bar{\bar{\mu}}_{eff,\pm}$ using equation (5.22).

$$\bar{\bar{\mu}}_{eff,\pm} = \begin{pmatrix} \frac{\{B_{x,\pm}\}}{\{H_{x,\pm}\}} & \frac{\{B_{x,\pm}\}}{\{H_{y,\pm}\}} & \frac{\{B_{x,\pm}\}}{\{H_{z,\pm}\}} \\ \frac{\{B_{y,\pm}\}}{\{H_{x,\pm}\}} & \frac{\{B_{y,\pm}\}}{\{H_{y,\pm}\}} & \frac{\{B_{y,\pm}\}}{\{H_{z,\pm}\}} \\ \frac{\{B_{z,\pm}\}}{\{H_{x,\pm}\}} & \frac{\{B_{z,\pm}\}}{\{H_{y,\pm}\}} & \frac{\{B_{z,\pm}\}}{\{H_{z,\pm}\}} \end{pmatrix} \quad (5.26)$$

From these matrices, using equations (5.21)-(5.24) I deduce the material parameters $\bar{\varepsilon}$, $\bar{\mu}$, $\bar{\kappa}$. The results are presented in subsection 8.1.2. This method offers two advantages compared to the “indirect” method. First of all the computational requirements are much lower because no free space region or PML is required. Secondly, the effective material parameters are calculated directly. There is no need to first compute the S-parameters and then using an algorithm to compute the material parameters.

6. Experimental Characterisation of Material Properties

6.1. Introduction

There exist several experimental methods to extract the permittivity and permeability of a material. They all have their advantages and disadvantages mainly depending upon the sample material, size and temperature. In my experiment I am not only interested in retrieving the permittivity and the permeability but also the chirality adding an additional constraint for the experimental setup. After introducing several experimental techniques and justifying my choice, I explain in detail our setup and the corresponding calibration and measurement techniques. Furthermore I give a brief introduction to the scattering parameters (S-parameters) from which the permittivity and permeability may be computed using a retrieval algorithm. To test my setup with isotropic dielectrics I use the NRW (Nicolson-Ross-Weir) algorithm [96]. For the metamaterials I need an adapted version of the NRW algorithm as suggested by Chen [28, 26].

6.2. Review of experimental procedures for the characterisation of material properties

To retrieve the material parameters three methods based upon transmission and reflection are commonly used. I will briefly explain the advantages and disadvantages of these methods especially with respect to measurements of metamaterials because this adds additional restrictions to the setup. This section is mainly based upon the techniques used in [90], [54] and [4].

Transmission/Reflection line method

The transmission and reflection method is commonly used to determine the permittivity and permeability of dielectric materials. For a non-chiral material commercially available rectangular waveguides could be used. But due to the rotatory dispersion occurring in chiral samples circular waveguide components are required which are not commercially available. By referring to Figure 6.1, the circular measurement cell including the chiral sample is located at (2). A rectangular to circular waveguide transition (located at (1)) feeds the signal from the vector network analyser (VNA) to the sample. A chiral sample will rotate the plane of polarisation which can be measured using a rotatable transition (located at (3)).

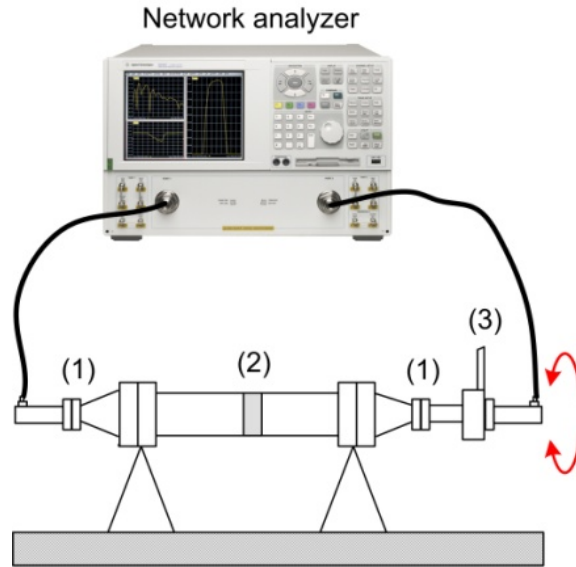


Figure 6.1.: *Illustration of circular waveguide setup.*

The advantage of this system is its small size and that the measurements are well shielded from external interferences. A disadvantage is the sensitivity to local density variations in the sample which may cause fluctuations in the measurements. Air gaps between the sample and the waveguide walls will further influence the results. Therefore the sample has to be artificially shaped to fit tightly into the waveguide which may be challenging. These problems may be overcome by averaging through several sample orientations and by precise sample manufacturing. Furthermore, unwanted higher modes may propagate in the sample. In this case inversion equations cannot be developed.

Resonator technique

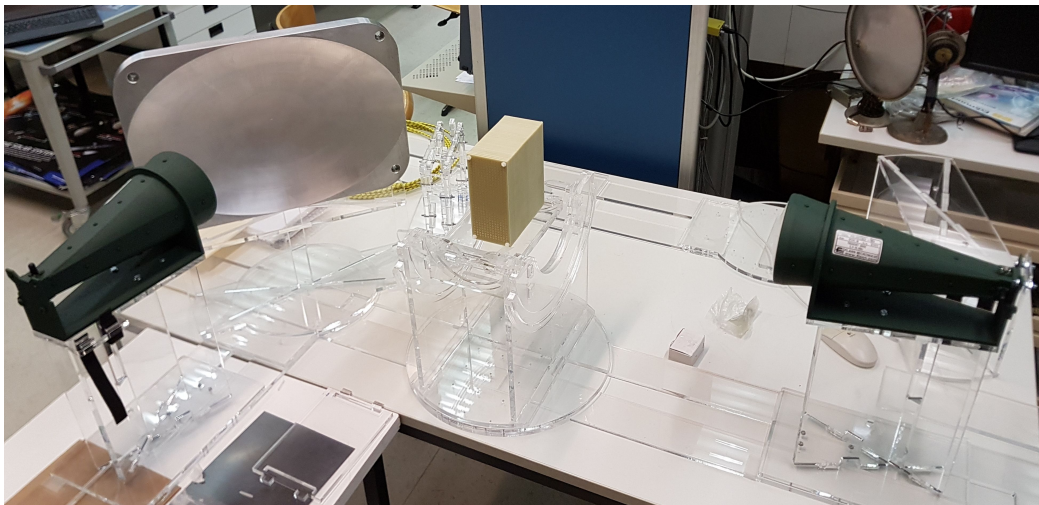
The resonator technique is the most suitable method for obtaining high precision measurements of non-chiral media. With this method two quantities are measured: the resonant frequency and the quality factor. It cannot be used for chiral media as this would at least require three independent quantities for a full characterisation. Furthermore the sample would be so small that the material could not be considered as homogeneous. So until now no resonator technique for the studies of chiral materials has been implemented experimentally.

Free space technique

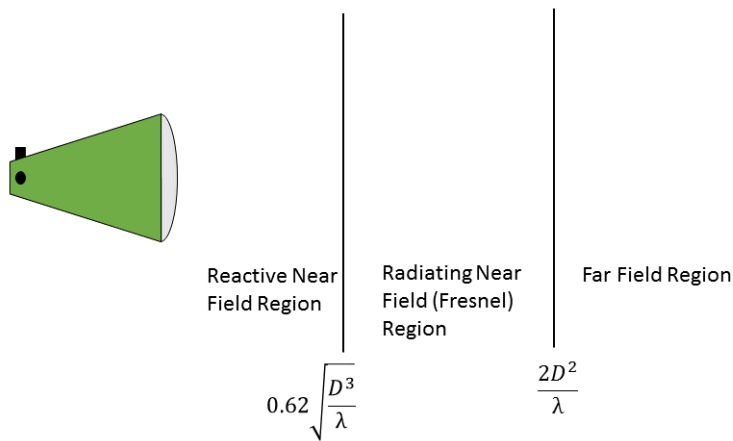
A free wave setup (Figure 6.2a) consists of a transmitting and receiving antenna, a VNA (to generate and measure the reflected and transmitted signal) and a sample holder. The sample should be located in the far field of the antenna. To reduce the diffraction effects at the edges of the sample the beam width should be decreased by a focussing lens or an ellipsoidal mirror. Simply positioning the sample closer to the antenna is a

6.2. Review of experimental procedures for the characterisation of material properties

bad solution for two reasons. First of all, the effects of multiple reflections between the sample and antenna are enhanced, introducing additional errors in the measurement. Furthermore, the plane wave assumption is not valid anymore, because we are not in the far field, making the development of inversion equations to extract material parameters impossible. In Figure 6.2b the different field regions are illustrated. Where D is the aperture of the antenna and λ the wavelength. In the reactive near field region the electric and magnetic fields are out of phase by 90 degrees to each other. In the far field region, the radiation pattern does not change its shape with distance, the fields are orthogonal to each other and in phase. In this region the plane wave assumption is valid. In the radiating near field region observe a mixture between the reactive rear field and far field region is observed. Especially the radiation pattern may vary with distance.



(a)



(b)

Figure 6.2.: (a) *Experimental setup* ; (b) *Different field regions*

6. *Experimental Characterisation of Material Properties*

A focussing device like a dielectric lens [76] or an ellipsoidal mirror [86] solves these two issues, it even allows one to reduce the size of the sample if the beam is focused well enough. Although the wave becomes a Gaussian behind the focal point, the plane wave assumption still holds. The free space technique offers several advantages :

1. A gap between the sample and the waveguide wall leads to the excitation of higher order modes induced by the inhomogenities due to the fabrication process. In the free wave setup this problem does not exist.
2. For cavities or waveguides the samples have to be cut properly according to the shape of the waveguide to limit the gap between the dielectric and the walls. This leads to additional constraints on the size and the fabrication process of the sample. Not every material may be machined precisely enough. For the free wave setup relatively large samples are required. Diffraction effects at the edges of the sample are negligible if the minimum transverse dimension of the sample is greater than three times the beam width at the focus [54].
3. Measurements based upon the free wave technique are non-destructive and contactless and are therefore suited for dielectric measurements at high temperature.
4. Suited for high frequency measurements

The disadvantages are :

1. Multiple reflections between antenna and surface of the sample causing errors in the measurement, although these reflections may be identified in the time domain.
2. Relatively large and flat samples are required. To further reduce diffraction effects at the edge of the sample a focussing device should be used. The size of the sample should nevertheless still be about three times the diameter of the beam at the focal point.
3. Care must be taken by the thickness of the sample. Depending on the thickness the reflected field is too weak to allow an accurate measurement of the phase resulting in important measurement errors.

To obtain accurate measurements the system has to be correctly calibrated. There exist several calibration standards. The most common are TRL (THROUGH, REFLECT, LINE) and GRL (GATED, REFLECT, LINE). To further increase the accuracy time gating is applied. The calibration eliminates the effects of the cable and antenna and significantly improves the quality of the measurement. The free space technique is my method of choice because it is without any further modifications suited for the dielectric characterisation of metamaterials and all the components are commercially available.

6.3. Free space measurement setup

The vector network analyser (Model ZVK from Rohde and Schwarz) generates the signal and measures the magnitude and phase of the complex S (scattering) parameters. I use

the Flann DP-240 Dual Polarised Horn as transmitting and receiving antennas. The antennas are mounted on rails in order to allow us to change their distance from the sample and thus to reposition the focal point (Figure 6.2a). The ellipsoidal mirror has been specially designed for the DP-240 antennas for a frequency range of $4.5 - 18 \text{ GHz}$. The 3 dB -width of the beam on the mirror focus is 13 cm at 4.5 GHz and 2.6 cm at 18 GHz . Rojo et al. [108] proved that for the frequency range of interest a sample diameter of 15 cm is large enough to avoid diffraction effects. Figure 6.2a also shows the mirror fabricated by the research service of the University of Murcia (Spain). The dimensions are $490 \times 350 \times 50 \text{ mm}$ and has been designed according to [108]. One of the main advantages of this setup is the large frequency range from $4.5 - 18 \text{ GHz}$. Previously two setups were needed [55] one for the X Band ($8.2 - 12.4 \text{ GHz}$) and another for the Ku band ($12.4 - 18 \text{ GHz}$). They required different antennas, mirrors and waveguides. Furthermore, as mentioned before, the use of a mirror instead of dielectric lenses prevents the effect of multiple reflection due to the lenses. I placed the mirror at a distance of 25 cm with respect to the transmitting antenna. The distance between the mirror and sample and between the sample and the receiving antenna is 45 cm in both cases

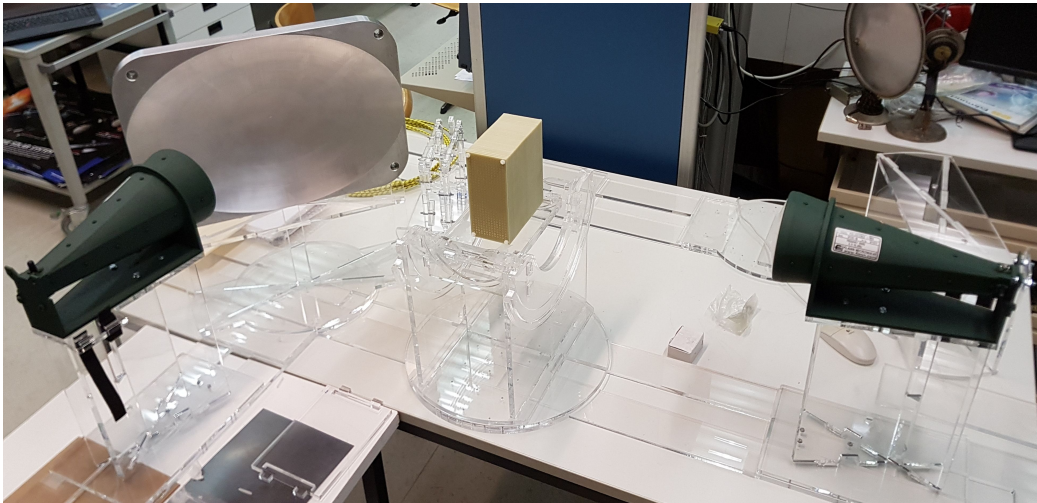


Figure 6.3.

6.4. Scattering parameters

This subsection, mainly based upon [1] gives only a brief summary about the scattering parameters. For more information please refer to Kurokawa [75]. The S (scattering) parameters are the key quantities to calculate the electromagnetic properties of a material. This theory is based upon a linearity assumption. If a circuit consists of linear elements it can mathematically be represented by a set of linear equations. The idea is to put complicated circuits into a black box, take two pairs of nodes defined by voltages and currents and link them via two linear equations. These parameters are automatically computed by the vector network analyser. The S parameters are complex numbers cor-

6. Experimental Characterisation of Material Properties

responding to the magnitude and phase of a signal. They are commonly displayed in matrix form with the number of rows and columns equal to the number of ports. For two ports the matrix is

$$\bar{\bar{S}} = \begin{pmatrix} S_{11} & S_{12} \\ S_{21} & S_{22} \end{pmatrix} \quad (6.1)$$

For the matrix element S_{ij} , the subscript j corresponds to the input (excited) and i to the output port respectively. S_{11} refers to the ratio of the signal that reflects from port one to the amplitude of the signal incident on port one. S_{21} means the response at port 2 due to an incident signal at port 1. Parameters along the diagonal of $\bar{\bar{S}}$ correspond to the reflection coefficients because they only take into account what happens at one port. Off-diagonal elements on the other hand correspond to the transmission coefficients because they refer to what happens at one port when it is excited by a signal incident at another port. I will only concentrate on 2 port systems as illustrated in Figure 6.4 because they are the most common used. For each port there is an incoming and emitted wave, therefore each port is shown as 2 nodes. The S parameters are expressed with respect to the reference impedance Z_0 .

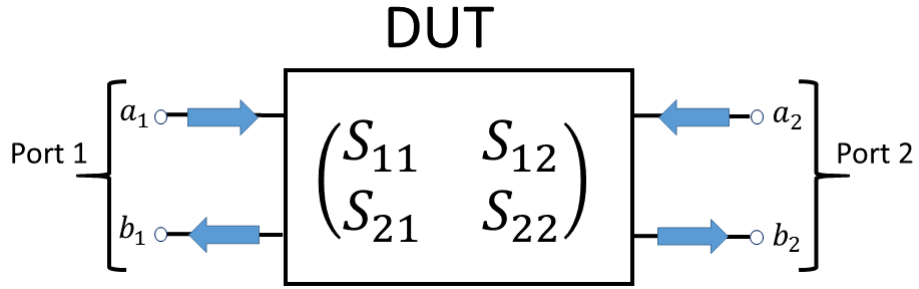


Figure 6.4.: 2 port system.

The link between input a_i , $i = 1, 2$ and output signal b_j , $j = 1, 2$ is given by

$$\begin{pmatrix} b_1 \\ b_2 \end{pmatrix} = \begin{pmatrix} S_{11} & S_{12} \\ S_{21} & S_{22} \end{pmatrix} \begin{pmatrix} a_1 \\ a_2 \end{pmatrix} \quad (6.2)$$

$$\Leftrightarrow \begin{matrix} b_1 \\ b_2 \end{matrix} = \begin{matrix} S_{11}a_1 + S_{12}a_2 \\ S_{21}a_1 + S_{22}a_2 \end{matrix} \quad (6.3)$$

The different S parameters may be obtained by setting the value of the incident signal a_i , $i = 1, 2$ to 0 leading to

$$\begin{aligned} S_{11}|_{a_2=0} &= b_1/a_1 \\ S_{12}|_{a_1=0} &= b_1/a_2 \\ S_{21}|_{a_2=0} &= b_2/a_1 \\ S_{22}|_{a_1=0} &= b_2/a_2 \end{aligned} \quad (6.4)$$

To measure S_{ii} for example, a signal at port i is injected and the reflected signal is measured at port i . For this specific case no signal is injected into port 2, so $a_j = 0$,

$i \neq j$. To measure S_{ij} , a signal is injected at port j and the response is measured at port i . S parameters are commonly expressed in decibels (dB).

$$S_{ij}(\text{dB}) = 20 \log [S_{ij}(\text{magnitude})] \quad (6.5)$$

Power ratios are expressed as $10 \log(x)$, but here voltage ratios are used, where the power P is linked to voltage U by $P = U^2/R$, with R the resistance. Keeping in mind a property of logarithmic calculus, $10 \log(x^2) = 20 \log(x)$, the difference between the two definitions becomes obvious. The VNA saves the information in a “touchstone” file. For a two-port VNA the file ends with “s2p”.

6.5. Time Gating

Time gating is a crucial part of the measuring process, but it needs to be used with care. Therefore I use some of the slides from keysight (formerly known as Agilent) FieldFox Handheld Education Series Part 4 [64] to give a brief introduction of the concept. The S parameters measured by a VNA are expressed in the frequency domain. For some application this is unfortunately not the most suited representation, therefore the time domain may be more appropriate. This is illustrated in Figure 6.5 where the S_{11} parameter of a device under test is represented. As a reminder, the S_{11} parameter corresponds to the reflected signal (emitted at port 1 and measured at port 1). Considering Figure 6.6, it becomes clear that each peak in the time domain corresponds to a specific reflected signal of the DUT (Device under test).

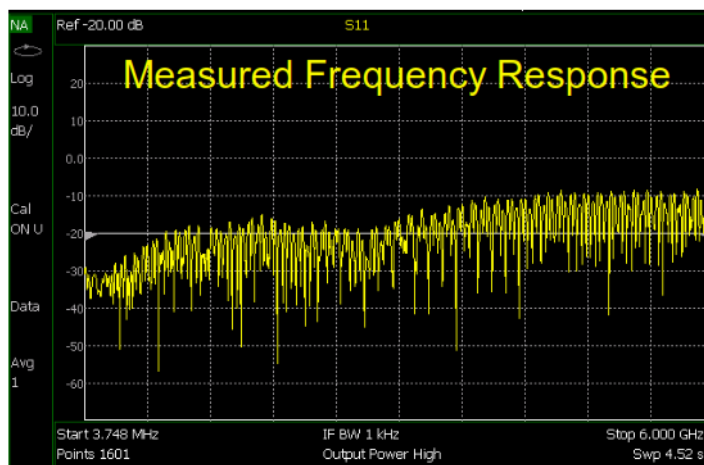


Figure 6.5.: *frequency response of a coax device under test.*

6. Experimental Characterisation of Material Properties

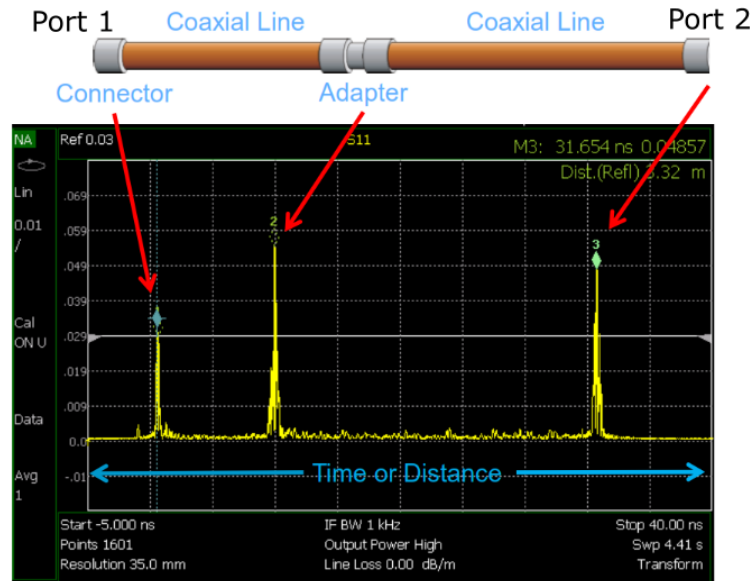


Figure 6.6.: Time domain response and identification of the different reflection peaks, due to non-continuities, with the corresponding parts of a coaxial line.

For the S_{11} parameter of a coax adapter connected to a waveguide which is connected to a horn antenna a characteristic response as illustrated in Figure 6.7 is obtained. This measurement allows me to clearly identify the effect of the coaxial adapter and the horn antenna. In this figure the setup has already been calibrated to remove the effects of the cable.

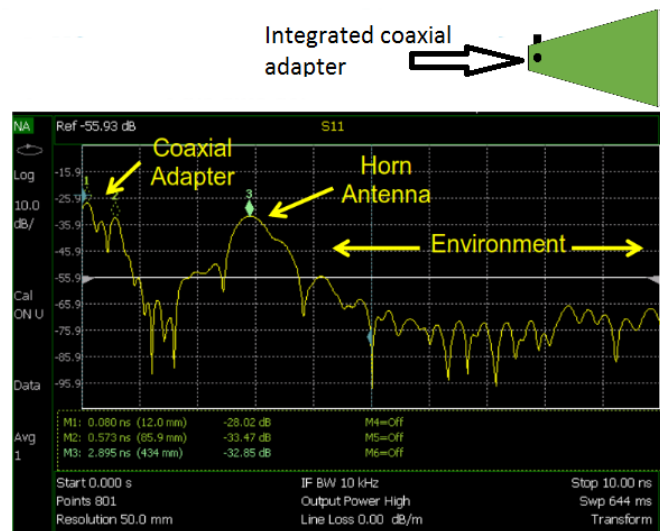


Figure 6.7.: Time Domain response of a coax adapter and antenna

6.5. Time Gating

The time domain even allows me to identify and characterise further components, as the reflection of a metal plate I put in various positions in front of the antenna. This effect will be used during the calibration I present later.

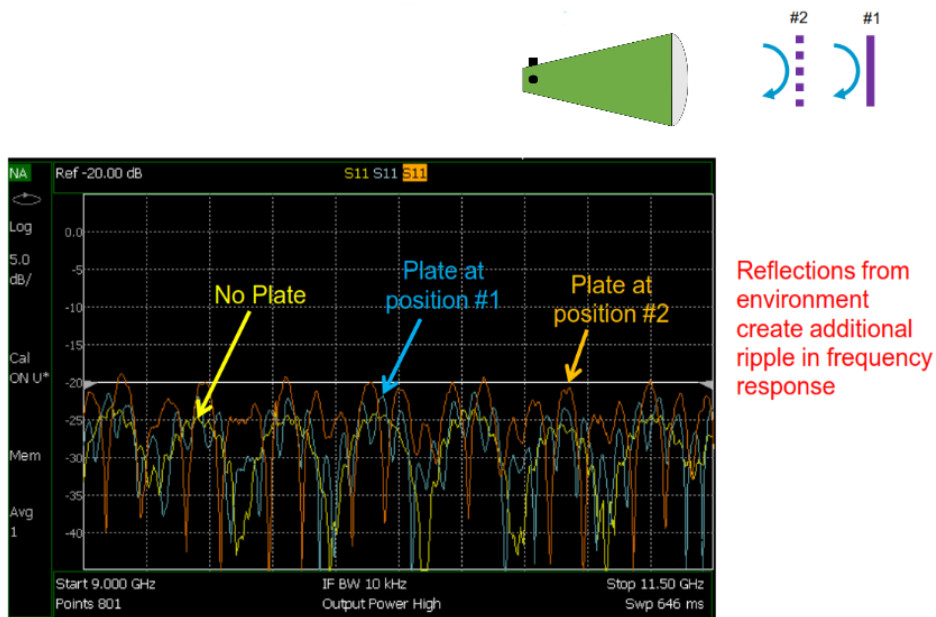


Figure 6.8.: *Frequency domain response of the effect of a metal plate located at two different positions.*

In Figure 6.8 the effect of the metal plate on the frequency response depending on the position becomes obvious. Unfortunately in the frequency domain this is not very helpful. In the time domain however an additional peak appears in Figure 6.9 which has not been present before in Figure 6.7. The peaks corresponding to the reflection of the coax adapter and the horn antenna remain the same.

6. Experimental Characterisation of Material Properties

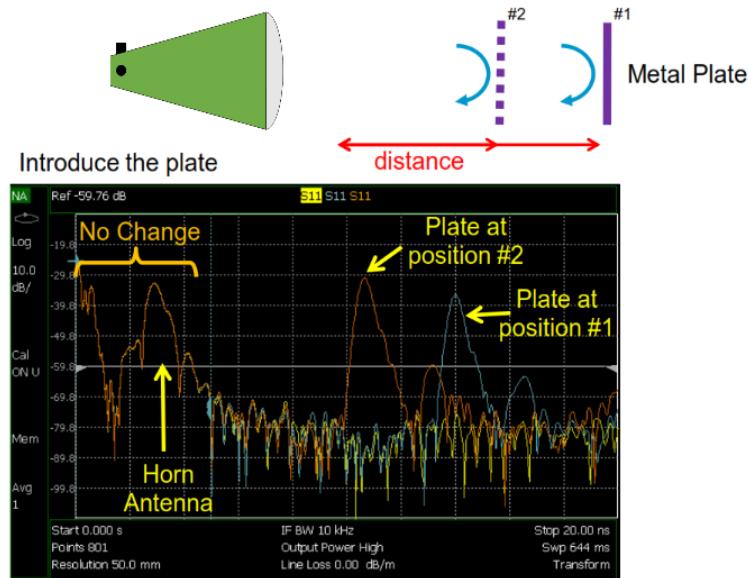


Figure 6.9.: Time domain response of the effect of a metal plate located at two different positions.

To remove the effect of the antenna, to only consider the effect of the metal plate or generally the DUT a technique called time gating is applied. Time gating allows me to remove or include responses in time. This is schematically illustrated in Figure 6.10. There exist different kind of gatings and care has to be taken to choose the best suited one. Generally a “hamming” or “hanning” window is used. Time gating involves a convolution and it may also lead to undesirable effects, like ringing (appearance of many small side lobes caused by frequency truncation), the signal has to be normalised and so on. For more information please refer to the agilent or keysight Application note 1287-12 “Time Domain Analysis Using a Network Analyzer”.

Time Gating

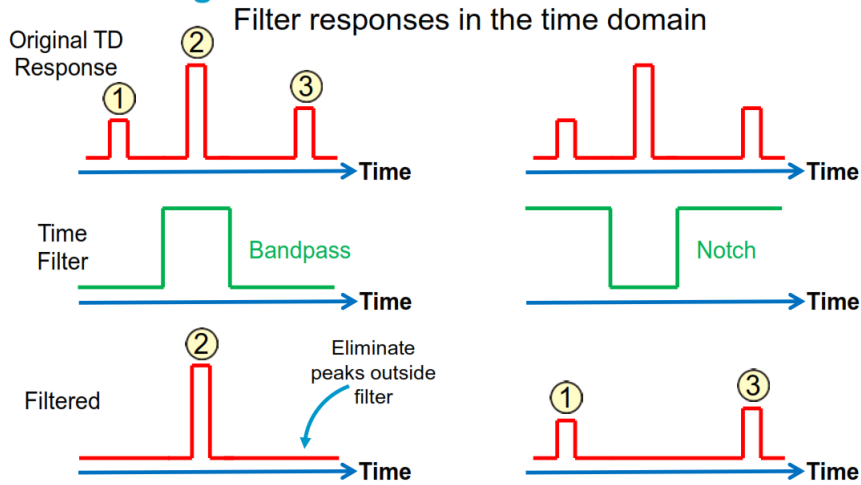


Figure 6.10.: Time Gating using a band pass or notch.

In Figure 6.11 a band pass filter is applied to the signal caused by the coax adapter and horn antenna. The effect of ringing is clearly visible in the “environment” part of the time gated signal. Figure 6.12 shows the effect of the time gating in the frequency domain. The gated signal is now much smoother compared to the ungated one.

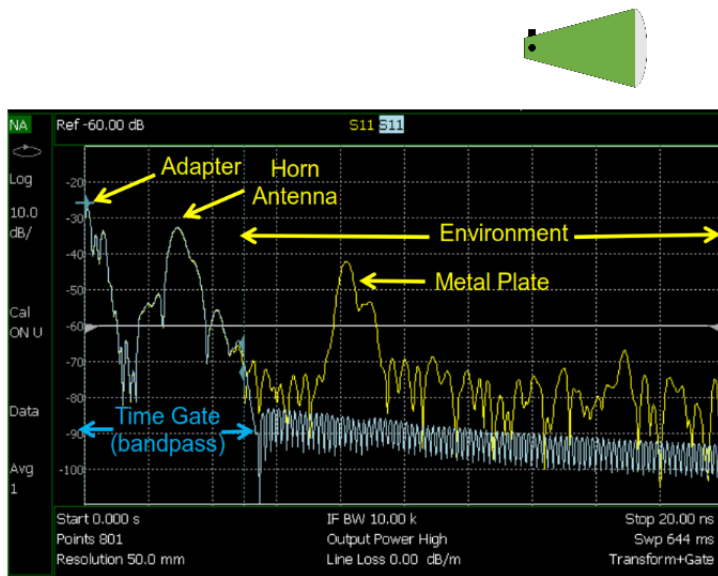


Figure 6.11.: Frequency domain representation of band pass filtered signal of a coax adapter and horn antenna.

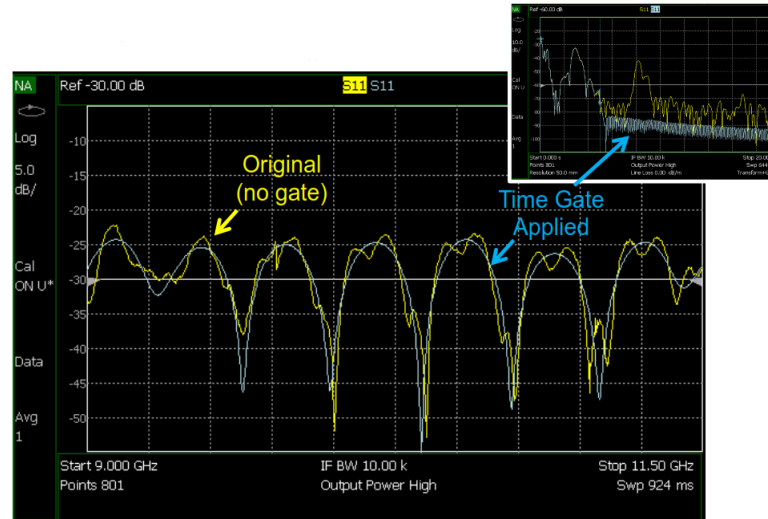


Figure 6.12.: Comparison between an ungated and a gated signal in the frequency domain.

6.6. Review of calibration techniques of the free space setup

Before a measurement I need to calibrate the system to eliminate the effects of the cable, antennas and multiple reflections. There exist many different calibration techniques. I explain the most common ones and go into detail about their advantages and disadvantages for free space measurement systems. Most of these techniques require a symmetric setup, therefore I already plan to add a second mirror to my setup to compare the effects of different calibration techniques. For simplicity I draw the antennas in the following figures with a dielectric lens as focussing device, although I use an ellipsoidal mirror instead of lenses.

TRM

TRM [19] stands for THROUGH, REFLECT and MATCH as depicted in Figure 6.13. The THROUGH standard is obtained with an air DUT (Device Under Test) between the antennas. For the REFLECT, a metal plate of known thickness has to be placed between the antennas. To achieve the MATCH a broadband absorber has to be added. The advantage of this technique is that the antennas do not have to be moved during calibration. The disadvantage is that it is very difficult to find a perfect broadband absorber for free space, therefore limiting the use of this calibration technique.

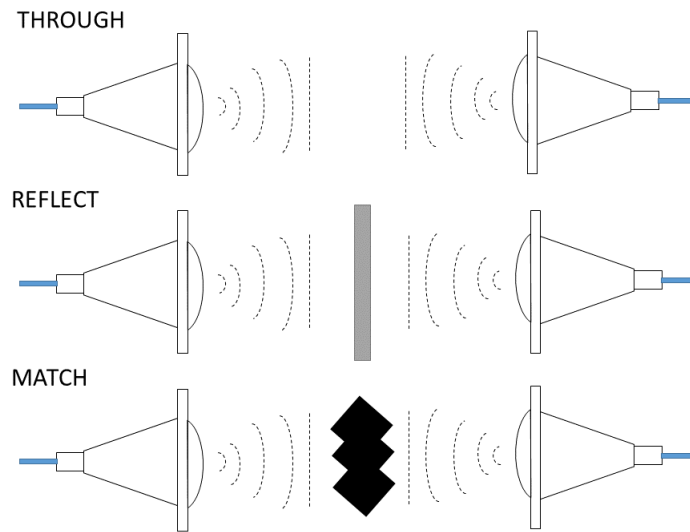


Figure 6.13.

TRL

The TRL calibration for free space measurement systems has been developed by Ghodgaonkar [54]. The acronym TRL stands for THROUGH, REFLECT and LINE. After the calibration of the VNA the reference planes are located at the end of the coaxial lines. TRL is then used as a second pier calibration to determine the error parameters describing the influence of the coaxial adapter, antenna and free-space up to the sample surface. Correcting the measured data with the inverse of this error terms moves the reference planes at the sample surface. To realise a THROUGH, the antennas have to be distanced by twice the focal length. For the REFLECT, a metal plate has to be placed at the focal planes of the transmission and receiving antenna respectively and the port 2 antenna must be moved back by the thickness of the metal plate. After this measurement, the antenna has to be moved back to its original position. Finally, for the LINE, the focal planes of transmit and receive antenna have to be separated by a quarter of the free-space wavelength at the center of the frequency band. Afterwards they have to be moved back to the original position. As can be seen, this method involves a lot of mechanical movements of the antennas leading to important errors if no highly precise positioning fixtures are used. The higher the working frequency the harder the calibration of the free space system. Nevertheless for our frequency range this method could be applicable. For more information please refer to the publication of Rocha [107]. It may be quite challenging to program this algorithm on your own. If no commercial software is available (or too expensive) I recommend downloading a scilab extension called “Microwave Toolbox” doing a complete TRL calibration from <http://www.microwave.fr/products.html>. This program has been written by Tibault Reveyrand.

6. Experimental Characterisation of Material Properties

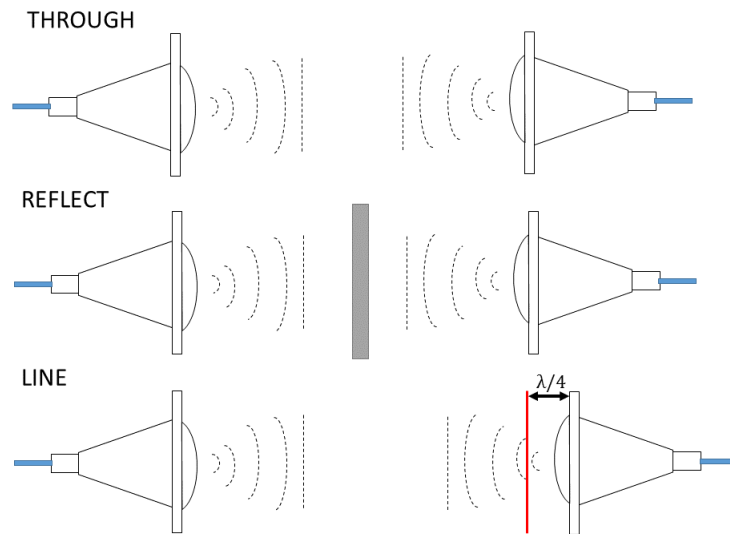
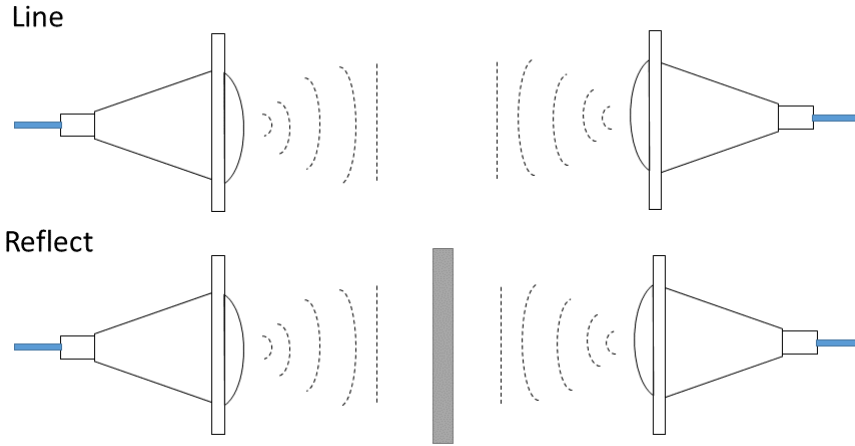


Figure 6.14.: *TRL calibration.*

GRL

The GRL calibration (Figure 6.15) has been developed by Bartley and Begley [15]. GRL stands for GATED, REFLECT, LINE (the LINE in this case is actually a THROUGH because the antennas are not moved). The advantage of this method is, that no movement of the antennas is required. Before measuring the LINE and REFLECT, the response of the antennas is time gated. This method has been reported to give the highest accuracy [15]. Unfortunately no software compatible with our VNA exists and as for the other methods this calibration requires a symmetric setup. Therefore I am currently working on my own implementation. In the mean time I use another calibration technique which is explained below.


 Figure 6.15.: *GRL calibration.*

Normalisation based calibration

The previous calibration methods require a symmetric setup whereas I currently use an asymmetric one. In the future I plan to add a second mirror in front of the receiving antenna to increase the power received by the antenna and to make it symmetric. Then I will use the GRL calibration. In the mean time, for my setup I adapt a calibration method suggested by Munoz [94] consisting of actually two calibrations. In their setup, Munoz had a coaxial adapter connected to a transmission line which was connected to a horn and adapted a TRL calibration for this. In the DP-240 antenna, the coax adapter is already integrated, simplifying the calibration for me. As a first calibration TOSM (THROUGH, OPEN, SHORT, MATCH) is used to remove the effect of the cable by moving the reference plane from the ports of the VNA to the end of the cable, connected to the antenna. The aim of the second calibration is to shift the reference planes to the sample surface. Therefore I first do a measurement without sample (like a THROUGH in the previous calibration techniques) and measure the $S_{21}THROUGH$. To filter out the effects from the antennas, edge diffraction effects and unwanted reflections, a time gating is applied around the transmitted signal. Next, I place a metal plate in the sample holder and measure the $S_{11}REFLECT$ and apply a time gating around the reflected signal. These two measurements act as reference signals. I place the sample in the sample holder making sure that its front face (directed towards the transmitting antenna) is located at the same position as the front face of the metal plate used during the calibration. I measure the $S_{11}DUT$ and $S_{21}DUT$ and time gate the signal as explained in subsection 6.7. Normalisation with respect to the reference measurements leads to

$$S_{11}DUT_{Norm} = \frac{S_{11}DUT}{S_{11}REFLECT} \quad (6.6)$$

$$S_{21}DUT_{Norm} = \frac{S_{21}DUT}{S_{21}THROUGH} \quad (6.7)$$

6. Experimental Characterisation of Material Properties

These parameters can now be represented in polar coordinates. The $S_{11}DUT_{Norm}$ phase has to be increased by $+\pi$ to revert the phase change introduced by measuring the REFLECT (metal plate). Furthermore I have to subtract a phase of k_0L from the $S_{21}DUT_{Norm}$. Leading to

$$S_{11}DUT_{Norm} = |S_{11}DUT_{Norm}| e^{i(\Phi_{11}+\pi)} \quad (6.8)$$

$$S_{21}DUT_{Norm} = |S_{21}DUT_{Norm}| e^{i(\Phi_{21}-k_0L)} \quad (6.9)$$

where Φ_{i1} is the measured phase of $S_{i1}DUT_{Norm}$, $i = 1, 2$, k_0 is the free space wavevector and L the thickness of the sample. This calibration method has the advantage that I do not have to move the antenna, reducing measurement errors.

6.7. Practical considerations

It is quite delicate to get reasonable results out of these measurements as I had to figure out during many failures. As hints for other people here is some useful advice:

- Ensure that the chosen frequency range for the measurement is not too small if you want to time gate, because the peak of the signal in the time domain will be broader the smaller the selected frequency band. When the signal in the time domain becomes too broad all multiple reflections are hidden in it and a reasonable time gating is not possible anymore. For our measurement a bandwidth of 1.2 GHz was too small. Our signal in the time domain had an extension of 3 ns (at the bottom) which corresponds to about a distance of 90 cm in free space (a lot if you only have a sample of a thickness of 1 cm). Proper time gating is not possible in this case. On the other hand, a too large frequency range results in a very narrow peak in the time domain which has not enough measurement points for an accurate reconstruction of the signal in frequency domain after time gating. I got satisfying results with a frequency band width of $4 - 6\text{ GHz}$ but our VNA (ZVK from Rohde and Schwarz) is also quite old and measures only 1601 points over the whole frequency range. Newer VNAs measure up to 100'000 points. In this case the time gating of even narrower pulses should be fine.
- Do not use a too small time gate. Always keep in mind that for a time gate band pass filter you set to zero all the points outside the gate. With a limited number of points, if the gate is too small, you may end up with only very few measurement points from which the signal is reconstructed in the frequency domain. Several test measurements should be conducted to verify the effect of time gating. In my experiment, I applied a time gate (Figure 6.16a) including the whole peak (main signal). Of course this only makes sense by choosing the right frequency range avoiding a too broad response in the time domain. Small time gates (Figure 6.16b) should be used with care because too much information may be lost.

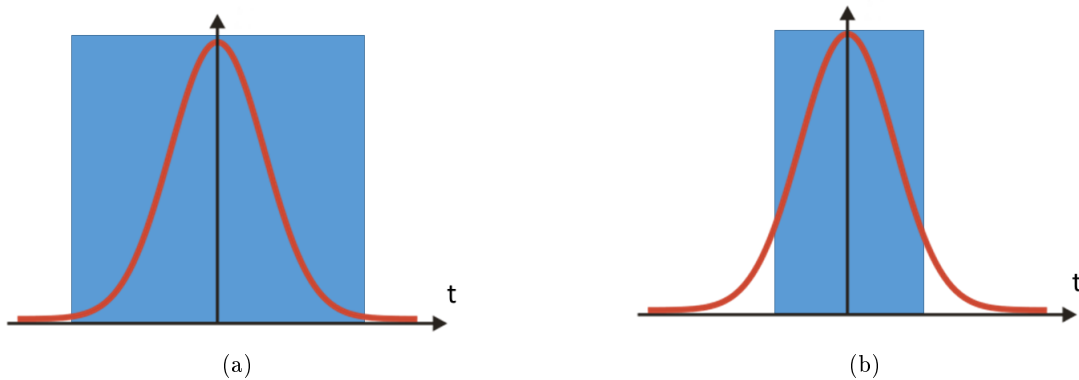


Figure 6.16.: Applying time gates of different widths (blue) on a given response in time domain (a) Large gate. ; (b) Narrow gate.

- Do not gate asymmetrically. If you use a time gate, try to gate symmetrically with the center of the gate at the maximum of the peak. By gating asymmetrically (Figure 6.17) I observed a change in the phase with respect to a symmetrically applied gate.

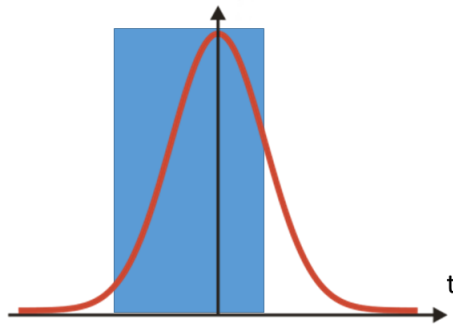


Figure 6.17.: *asymmetric time gating (blue) with respect to the peak.*

- Care has to be taken during the measurement of low loss materials like PMMA. If $|S_{11}| < 0.2$ our VNA is not able anymore to retrieve the correct phase [94], leading to a dip or peak in the retrieved permittivity and permeability. Even by increasing the power of the VNA the problem may persist.

6.8. Dielectric properties from S-parameters

In 1970 Nicolson and Ross [96] and Weir [141] in 1974 developed a method for the extraction of the dielectric properties of a material from the S-parameters, known as Nicholson-Ross-Weir (NRW) algorithm. Today there exist different methods to extract

6. Experimental Characterisation of Material Properties

the material parameters. A nice overview including some examples and the limitations of the different methods can be found in the Rohde and Schwarz application Note [4]. Here I start with the NRW algorithm and explain some of the difficulties and how to deal with them. I assume a linearly polarised plane wave with angular frequency ω normally incident on a planar sample of infinite lateral extension and finite thickness d situated in free space (Figure 6.18). For characterising losses, instead of the imaginary part, the loss tangent, defined as the ratio between the imaginary and real part $\tan\delta = (.)''/(.)'$ is commonly used.

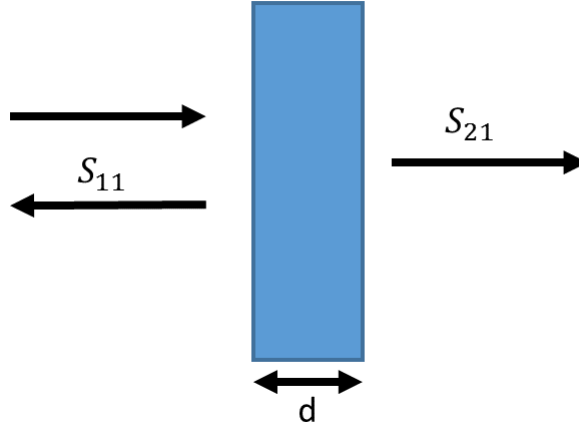


Figure 6.18.: *S-parameters of a planar dielectric sample in free space.*

The S_{11} and S_{21} parameters are linked to the phase shift function T and the interface reflection coefficient Γ by the following equations:

$$S_{11} = \frac{\Gamma(1 - T^2)}{1 - \Gamma^2 T^2} \quad (6.10)$$

$$S_{21} = \frac{T(1 - \Gamma^2)}{1 - \Gamma^2 T^2} \quad (6.11)$$

T and Γ are given by

$$\Gamma = \frac{(\eta - \eta_0)}{(\eta + \eta_0)} = \frac{(z_{in} - 1)}{(z_{in} + 1)} \quad (6.12)$$

$$T = e^{-\gamma d} \quad (6.13)$$

where $z_{in} = \eta/\eta_0$ is the normalised characteristic impedance, $\eta = \sqrt{\mu/\varepsilon}$ the impedance for the sample, $\eta_0 = \sqrt{\mu_0/\varepsilon_0}$ the free space impedance and γ the propagation constant of the sample

6.8. Dielectric properties from S-parameters

$$\gamma = \gamma_0 \sqrt{\varepsilon \mu} = \alpha + i\beta \quad (6.14)$$

$$z_{in} = \sqrt{\frac{\mu_r}{\varepsilon_r}} \quad (6.15)$$

where $\gamma_0 = i2\pi/\lambda_0 = i\omega/c_0$ represents the propagation constant of free space and λ_0 the free space wavelength, ω the angular frequency and c_0 the speed of light in free space. α is the attenuation factor and β the phase factor. From equation (6.10) and equation (6.11) Γ is derived as

$$\Gamma = K \pm \sqrt{K^2 - 1} \quad (6.16)$$

where

$$K = \frac{S_{11}^2 - S_{21}^2 + 1}{2S_{11}} \quad (6.17)$$

$$T = \frac{S_{11} + S_{21} - \Gamma}{1 - (S_{11} + S_{21})\Gamma} \quad (6.18)$$

In equation (6.16) the plus or minus sign is chosen such that $|\Gamma| < 1$. Rewriting equation (6.13) leads to

$$\gamma = \ln\left(\frac{1}{T}\right)/d \quad (6.19)$$

Keeping in mind that T is a complex number, leading to multiple values of γ , and can be written as

$$T = |T| e^{i\phi} \quad (6.20)$$

where ϕ is the phase leading to

$$\gamma = \ln\left(\frac{1}{|T|}\right)/d + i\left(\frac{2\pi m - \phi}{d}\right) \quad (6.21)$$

$$= -\frac{\ln(|T|)}{d} + i\left(\frac{2\pi m - \phi}{d}\right) \quad (6.22)$$

$$= \alpha + i\beta \quad (6.23)$$

where $m = 0, \pm 1, \pm 2, \dots$

In contrast to the real part of γ , the imaginary part is not single valued. Using equation (6.12) and equation (6.15), leads to

$$\sqrt{\frac{\mu_r}{\varepsilon_r}} = \frac{(1 + \Gamma)}{(1 - \Gamma)} \quad (6.24)$$

From equation (6.14) and equation (6.24), I obtain

6. Experimental Characterisation of Material Properties

$$\varepsilon_r = \frac{\gamma}{\gamma_0} \left(\frac{1 - \Gamma}{1 + \Gamma} \right) = \frac{\gamma}{i\omega z_{in}} \quad (6.25)$$

$$\mu_r = \frac{\gamma}{\gamma_0} \left(\frac{1 + \Gamma}{1 - \Gamma} \right) = \frac{\gamma z_{in}}{i\omega} \quad (6.26)$$

due to the multiple values of the imaginary part of γ , ε_r and μ_r are also not unique. This is especially a problem for thick samples. The phase constant β corresponds to the imaginary part of γ .

$$\beta = 2\pi/\lambda \quad (6.27)$$

where λ is the wavelength in the sample material. From equation (6.21) and equation (6.27) I obtain

$$\frac{d}{\lambda} = m - \frac{\phi}{2\pi} \quad (6.28)$$

For $m = 0$ and $-2\pi < \phi < 0$, d/λ is between 0 and 1. If the sample thickness is chosen to be smaller than λ the values of ε , μ are unique and correspond to $m = 0$. The ambiguity problem occurs if $d > \lambda$. The effects of a wrong initial value of m on the material parameters and how to find the correct value are explained in the appendix C. In the case of a low loss material another much easier method to compute the electric permittivity only requiring the transmission S_{21} [94] may be used. This method assumes $\mu_r = 1$ and a loss tangent $\tan\delta_\varepsilon < 0.01$ and leads to two formulas, one for the parallel (\parallel) another for the perpendicular \perp polarisation with respect to the plane of incidence.

$$\begin{aligned} \varepsilon_{r\parallel} &= \frac{-(R+1) - \sqrt{(R+1)^2 + (R+1)(R-1)\sin^2(2\theta)}}{2(R-1)\cos^2(\theta)} \\ \varepsilon_{r\perp} &= \frac{1 + R\cos(2\theta)}{1 - R} \\ R &= \sqrt{\frac{(1 - |S_{21}|^2)}{\sin^2\Phi_{21}}} \end{aligned} \quad (6.29)$$

where θ is the angle of incidence and Φ_{21} the phase of S_{21} . R is defined as in equation (6.29) for θ below the Brewster angle, otherwise a minus sign precedes the root. I only do measurements at normal incidence ($\theta = 0$). In this case $\varepsilon_{\parallel} = \varepsilon_{\perp}$. This formula and implementation is much easier than the NRW algorithm, reducing the possibility of errors. To compare the accuracy of our measured S parameters I compute the analytical S parameters according to Arslanagic [8].

$$S_{11} = \frac{(1 - T^2)(\eta^2 - \eta_0^2)}{(\eta + \eta_0)^2 - (\eta - \eta_0)^2 T^2} \quad (6.30)$$

$$S_{21} = \frac{4\eta\eta_0 T}{(\eta + \eta_0)^2 - (\eta - \eta_0)^2 T^2} \quad (6.31)$$

where $\eta = \sqrt{\mu/\varepsilon}$ is the impedance inside the dielectric, $T = e^{-ikd}$ is the phase shift function and η_0 , the impedance of free space, d the thickness of the slab and $k = \omega^2\varepsilon\mu$ the wavevector. For an isotropic material $S_{11} = S_{22}$ and $S_{21} = S_{12}$.

6.9. Retrieval of constitutive parameters from a bi-anisotropic metamaterial

In subsection 6.8 I used the NRW algorithm to retrieve $\varepsilon(\omega)$, $\mu(\omega)$ from an isotropic dielectric material with the help of the S-parameters. My metamaterial is however bi-anisotropic, this means the materials parameters become 2nd order tensors. Furthermore another parameters has to be determined, the chirality $\kappa(\omega)$. This subsection is based upon the publications of Li et al. [77, 78] and Chen et al. [28, 26]. Assuming a reciprocal material and a harmonic time dependence $e^{-i\omega t}$, where ω is the angular frequency, the constitutive equation to describe a bi-anisotropic material is

$$\begin{aligned}\mathbf{D} &= \bar{\varepsilon} \cdot \mathbf{E} + \bar{\xi} \cdot \mathbf{H} \\ \mathbf{B} &= \bar{\mu} \cdot \mathbf{H} + \bar{\zeta} \cdot \mathbf{E}\end{aligned}$$

where

$$\begin{aligned}\bar{\varepsilon} &= \varepsilon_0 \begin{pmatrix} \varepsilon_{xx}(\omega) & 0 & 0 \\ 0 & \varepsilon_{yy}(\omega) & 0 \\ 0 & 0 & \varepsilon_{zz}(\omega) \end{pmatrix}, \quad \bar{\mu} = \mu_0 \begin{pmatrix} \mu_{xx}(\omega) & 0 & 0 \\ 0 & \mu_{yy}(\omega) & 0 \\ 0 & 0 & \mu_{zz}(\omega) \end{pmatrix} \\ \bar{\xi} &= -i\frac{1}{c} \begin{pmatrix} 0 & 0 & 0 \\ 0 & 0 & 0 \\ 0 & \kappa_{zy} & 0 \end{pmatrix}, \quad \bar{\zeta} = i\frac{1}{c} \begin{pmatrix} 0 & 0 & 0 \\ 0 & 0 & \kappa_{yz} \\ 0 & 0 & 0 \end{pmatrix}\end{aligned}$$

Where where c is the speed of light. Reciprocal means $\bar{\varepsilon}$, $\bar{\mu}$ are symmetric and $\bar{\zeta} = -\bar{\xi}^T = i/c\bar{\kappa}$. $\bar{\zeta}$ and $\bar{\xi}$ depend upon the the material under investigation (section 2.11). For a bi-axial medium, they are defined as above. I assume a plane wave polarised in z direction propagating with wavevector \mathbf{k} in x direction interacting, with a bi-anisotropic material, only ε_{zz} , μ_{yy} and $\kappa_{zy} = \kappa_{yz} = \kappa$ are active. The other four components will not be involved. To retrieve the active material parameters I make use of the fact that the characteristic impedance inside a bi-anisotropic material has different values for the wave propagating in the two opposite directions of the x axis. The propagation of the incident wave with respect to the Omega particle and the bi-anisotropic slab are illustrated in Figure 6.19 (a) and Figure 6.19 (b) respectively.

6. Experimental Characterisation of Material Properties

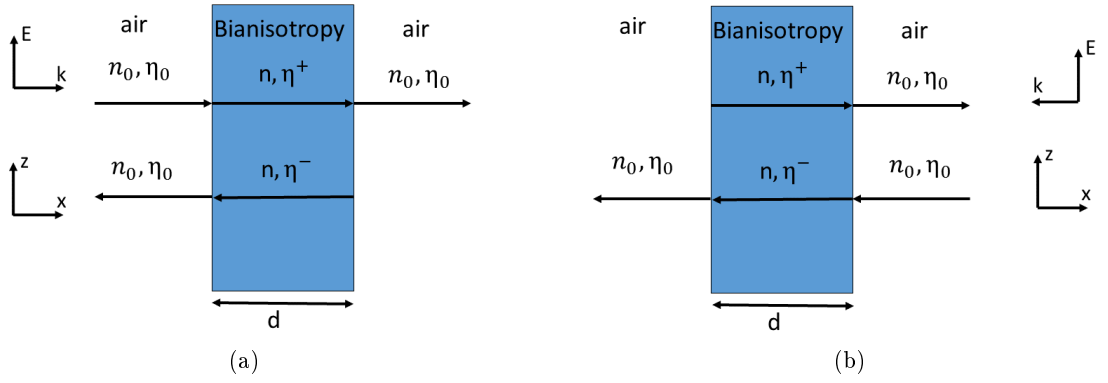


Figure 6.19.: (a) wavevector \mathbf{k} parallel to \mathbf{x} ; (b) wavevector \mathbf{k} anti-parallel to \mathbf{x} .

The wave traveling in the $\pm x$ direction leads to the impedances

$$\eta^+ = \frac{\mu_{yy}}{n + i\kappa} \quad , \quad \eta^- = \frac{\mu_{yy}}{n - i\kappa} \quad (6.32)$$

where n is the refractive index

$$n = \pm \sqrt{\varepsilon_{zz}\mu_{yy} - \kappa^2} \quad (6.33)$$

In contrast to the retrieval of the material parameters of an isotropic dielectric material which only required the S_{11} and S_{21} parameter, the change of the impedance with the direction requires the determination of three S parameters, namely the S_{11} , S_{21} and S_{22} . S_{12} is identical to S_{21} . The analytical form of the S parameters for a wave propagating in $+x$ direction is

$$S_{11} = \frac{2i \sin(nk_0d) [n^2 + (\kappa_0 + i\mu)^2]}{[(\mu_{yy} + n)^2 + \kappa^2] e^{-ink_0d} - [(\mu_{yy} - n)^2 + \kappa^2] e^{ink_0d}} \quad (6.34)$$

$$S_{21} = \frac{4\mu_{yy}n}{[(\mu_{yy} + n)^2 + \kappa^2] e^{-ink_0d} - [(\mu_{yy} - n)^2 + \kappa^2] e^{ink_0d}} \quad (6.35)$$

where d is the thickness of the homogeneous (Omega particles much smaller than wavelength) bi-anisotropic slab and k_0 is the wavenumber in free space. If the wave is propagating in the $-x$ direction the remaining S parameters become

$$S_{22} = \frac{2i \sin(nk_0d) [n^2 + (\kappa_0 - i\mu_{yy})^2]}{[(\mu_{yy} + n)^2 + \kappa^2] e^{-ink_0d} - [(\mu_{yy} - n)^2 + \kappa^2] e^{ink_0d}} \quad (6.36)$$

$$S_{12} = \frac{4\mu_{yy}n}{[(\mu_{yy} + n)^2 + \kappa^2] e^{-ink_0d} - [(\mu_{yy} - n)^2 + \kappa^2] e^{ink_0d}} \quad (6.37)$$

6.9. Retrieval of constitutive parameters from a bi-anisotropic metamaterial

As can be seen $S_{12} = S_{21}$, but $S_{11} \neq S_{22}$. This leads us to three independent equations for the three unknowns (n, μ_y, κ) . The refractive index is linked to the S parameters via

$$\cos(nk_0d) = \frac{1 - S_{11}S_{22} + S_{21}^2}{2S_{21}} \quad (6.38)$$

For a passive medium, $n = n' + in''$ must obey the condition that $n'' \geq 0$. After retrieving n the other parameters can be calculated using $z_{in,\pm}$ from equation (6.42)

$$\kappa = In \frac{(z_{in,-} + z_{in,+})}{(z_{in,-} - z_{in,+})} \quad (6.39)$$

$$\mu_{yy} = (n - i\kappa) z_{in,+} \quad (6.40)$$

$$\varepsilon_{zz} = \frac{(n + i\kappa)}{z_{in,+}} \quad (6.41)$$

To retrieve the material parameters ε_{zz} , μ_{yy} , κ I use the algorithm suggested by Chen et al. [28, 26]. The S_{11} , S_{21} and interface reflection coefficient Γ are defined as in equations (6.10), (6.11). Only the phase T is defined slightly different

$$T = e^{ink_0d}$$

where n is the refractive index, k_0 the wavenumber in free space and d the thickness of the slab. The normalised characteristic impedance z_{in} and the refractive index n are obtained by inverting equations (6.10) and (6.11) leading to

$$z_{in,\pm} = \frac{(S_{11} - S_{22}) \pm \sqrt{(1 - S_{11}S_{22} + S_{12}S_{21})^2 - 4S_{12}S_{21}}}{(1 - S_{11})(1 - S_{22}) - S_{12}S_{21}} \quad (6.42)$$

$$T = X \pm i\sqrt{1 - X^2} \quad (6.43)$$

where

$$X = \frac{1 - S_{11}S_{22} + S_{21}^2}{2S_{21}} \quad (6.44)$$

To determine the sign of equations (6.42) and (6.43) the passive medium condition is used leading to the requirements

$$z'_{in} \geq 0 \quad (6.45)$$

$$n'' \geq 0 \quad (6.46)$$

From equation (6.43) the refractive index n is obtained.

$$n = \frac{1}{k_0L} \{ [\ln(T)]'' + 2m\pi - i[\ln(T)]' \} \quad (6.47)$$

where m is an integer related to the branch index of n' . As before the real part of n is therefore not uniquely determined. To solve this problem I employ again the phase unwrapping method. To determine the sign of z_{in} and n equations (6.45) and (6.46)

6. Experimental Characterisation of Material Properties

are usually used. Unfortunately this method may fail if z'_{in} and n'' are close to zero. Therefore Chen et al. suggest to use the fact that n and z_{in} are related to determine the correct signs. To determine the correct sign of Z_{in} two cases needs to be distinguished. Therefore a small positive number δ is defined. If $|z'_{in}| \geq \delta$ equation (6.45) is used. If $|z_{in}| < \delta$, the sign of z_{in} is determined so that the corresponding refractive index n has a non-negative imaginary part, or equivalently $|T| \leq 1$. After obtaining the value of z_{in} equation (6.48) is applied

$$T = e^{ink_0d} = \frac{S_{21}}{1 - S_{11} \frac{Z_{in}-1}{Z_{in}+1}} \quad (6.48)$$

to avoid the sign ambiguity in equation (6.43).

6.10. Metamaterial with metallic omega inclusions

The advantage of metamaterials in general or pseudochiral materials specifically are the ability to tune the electromagnetic properties of a material by slightly changing the unit cells. I decided to build our metamaterial based upon metallic omega inclusions for two reasons. First of all it is a relatively simple structure because the wire and split ring are combined in one structure and not spatially separated as in the metamaterial designed by Smith 2.17a2.17b. Furthermore, although the shape seems simple, it leads to the coupling of the electric and magnetic field making it bi-anisotropic if the unit cells are arranged correctly. My omega inclusions have dimensions similar to those used by Aydin [11] (Figure 6.20a) because they show a resonance between $10\text{ GHz} - 11\text{ GHz}$ which lies in the working range of my free space setup. The main difference between my and Aydin's structure is that I use sharp edges at the gap whereas the edges of Aydin's structure are rounded off. The omegas are made out of copper and has dimensions: $r = 1.19\text{ mm}$, $w = 0.45\text{ mm} \pm 20\text{ }\mu\text{m}$ and $L = 1.8\text{ mm}$. The FR4 circuit boards and the copper have a thickness of 1.6 mm and $30\text{ }\mu\text{m}$ respectively.

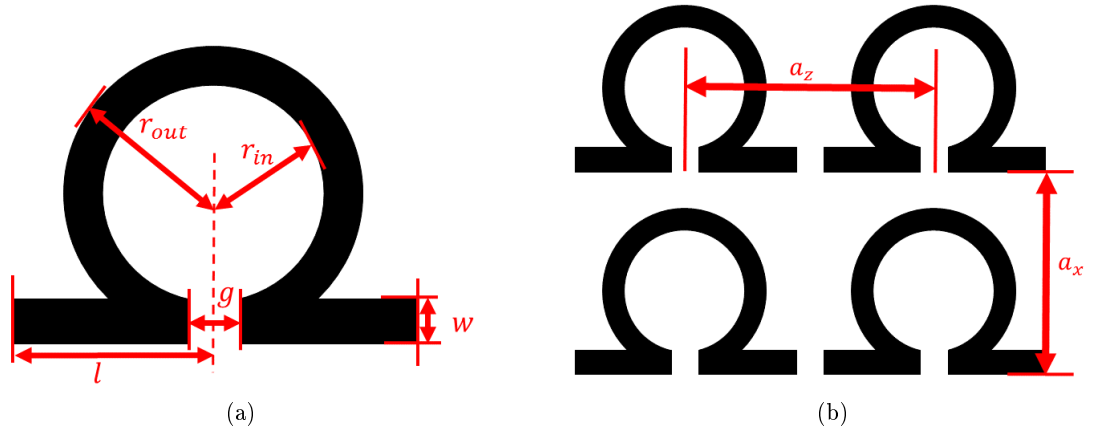


Figure 6.20.: (a) size of single Omega particle. ; (b) Periodicity of array of Omega cells.

6.10. Metamaterial with metallic omega inclusions

The omega pattern is obtained by etching the copper that is deposited on a FR4 substrate. The dimensions of the FR4 slab in x, y, z direction is $70\text{ mm} \times 1.6\text{ mm} \times 150\text{ mm}$ (Figure 6.21). The number of omega structures on an FR4 substrate in x and y direction are 13 and 32.

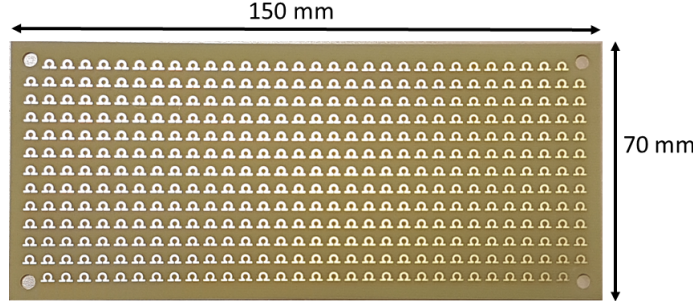


Figure 6.21.: *Periodic arrangement of omega structures on FR4 substrate*

To create a bi-anisotropic slab we pile the printed circuit boards (PCBs) up, therefore the number of Omega structures in z direction depends upon the number of FR4 substrates. One FR4 substrate with copper Omega structures is always followed by two FR4 slabs without Omega structures. This procedure is repeated until the desired extension of the slab is achieved. In total I ordered 32 FR4 slabs with Omega pattern and 62 without Omega pattern. The dimension of the final slab in x, y, z direction is $70\text{ mm} \times 150\text{ mm} \times 150\text{ mm}$. According to [108] these lateral dimensions guarantee that there are no diffraction effects at the boundary of the slab in the desired frequency range if we use the ellipsoidal mirror to focus the incident beam. The interested reader can find the effects of different kinds of Omega inclusions with respect to size and orientation on the transmission, reflection in the publications by Aydin [11, 10] and Li [77, 78]. Using the lumped element equivalent circuit model [128] the capacitance (C_0), inductance (L_0), resonance frequency (ω_0), resistance (R_0) can be expressed as:

$$\omega_0 = \frac{1}{\sqrt{L_0 C_0}} \quad (6.49)$$

$$R_0 = \sqrt{\frac{\omega_0 \mu_0}{2\sigma}} \frac{2r_{in}}{w} \quad (6.50)$$

$$L_0 = \mu_0 r_{in} \left[\log \left(\frac{16r_{in}}{w} \right) - 2 \right] \quad (6.51)$$

$$C_0 = \frac{\pi l \varepsilon_0 \varepsilon_m}{\log(4l/w)} \quad (6.52)$$

where ε_m is the matrix relative permittivity, σ is the metal conductivity, r_{out} , r_{in} , l are defined in Figure 6.20a. Using equations (6.49)-(6.52) from Tretyakov [128] the capacitance (C_0), inductance (I_0), resonance frequency (ω_0), resistance (R_0) of a unit cell are calculated. The parameters are given in Figure 6.20a. $r_{out} = 1.19\text{ mm}$, $L =$

6. Experimental Characterisation of Material Properties

1.8 mm, $w = 0.45$ mm and $g = 0.3$ mm leading

$$C_0 = 82.13 \mu F$$

$$L_0 = 2.61 nH$$

$$R_0 = 142.65 m\Omega$$

$$f_0 = 10.87 GHz$$

This result is only valid for a single unit cell. If the Omega structures are arranged periodically with $a_x = a_y = a_z = 4.8$ mm as illustrated in Figure 6.20b, we expect a stop band of roughly 1 GHz close to ω_0 because of the coupling between all the inclusions.

7. Experimentally Measured Material Parameters

In this chapter I present first the results for a simple isotropic dielectric, which were mainly used to test the setup and calibration, before showing the retrieved material parameters of the bi-anisotropic metamaterial.

7.1. Experimental validation for an isotropic dielectric

To test my experimental setup, calibration and retrieval algorithm I used PMMA (poly(methyl methacrylate)) also referred to as acrylic glass or “plexiglas” and polystyrene. In the literature, the real part of the permittivity for PMMA varies between $2.50 - 2.64$ at 10 GHz and the loss tangent is of the order of 10^{-2} [94]. Similarly polystyrene has a relative permittivity of 2.54 at 10 GHz and a loss tangent of 0.00033 [93]. Our samples have at least a lateral dimension of $15\text{ cm} \times 15\text{ cm}$ to avoid refraction effects on the boundaries. The minimum thickness of the sample should correspond to around 20% of the incoming wavelength inside the dielectric. Measurements of samples with different thicknesses are recommended if the order of magnitude of the material parameters are not known at all. For the following measurements I used a step sweep mode with 1601 frequency points and averaging of 30 sweeps from $8\text{ GHz} - 14\text{ GHz}$ for a perpendicular polarised incident wave and a power of -10 dBm . I define perpendicular and parallel polarisation with respect to the plane spanned by the incident and reflected wavevector from the mirror. According to Munoz et al. [94] the magnitude of the parallel polarised signal is usually weaker than the perpendicular polarised signal. The lower the signal, the higher the measurement uncertainties, especially for the S_{11} parameter, therefore I only use the perpendicular polarisation. For all the measurement the 500 MHz at the beginning and end of the frequency band should not be considered because they are severely affected by the time gating. This also has to be taken into account in the retrieval algorithm because the time gating affects the phase in this region leading to an incorrect phase unwrapping. In the retrieval algorithm, if necessary I simply neglected the first measurement points to guarantee a correct phase unwrapping.

I first measured the material parameters for a 2.94 mm PMMA sample. This is already the thinnest sample I can measure for an estimated relative permittivity of roughly $\epsilon'_r = 2.5$. The results are presented in Figure 7.1. The top horizontal black line at $\epsilon'_r = 2.55$ corresponds to the averaged real part of the permittivity for different values from the literature. The second black line indicates 0 . A good agreement between the measured and expected values is observed.

7. Experimentally Measured Material Parameters

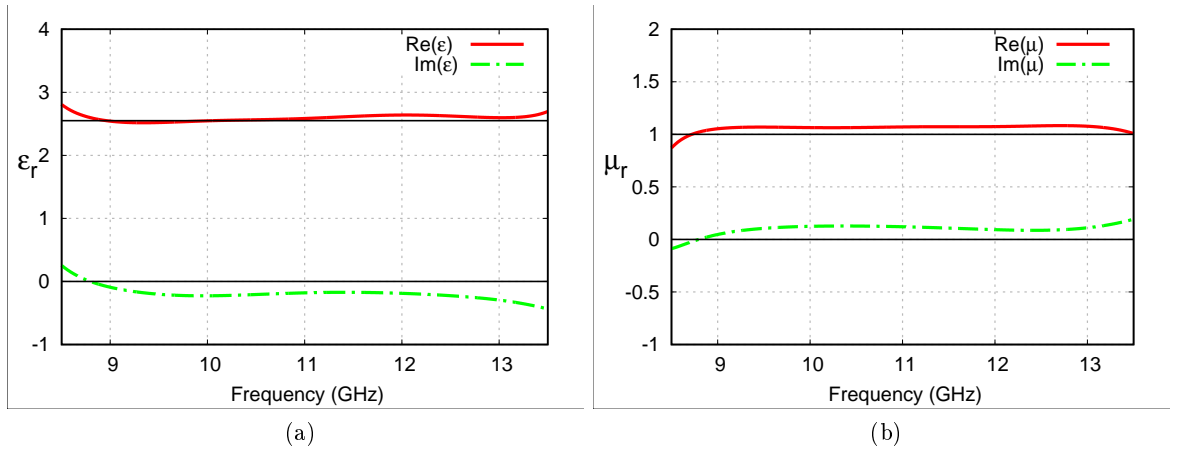


Figure 7.1.: Material parameters for a 2.94 mm PMMA sample from NRW algorithm (a) relative permittivity ; (b) relative permeability

In the next step I repeated the measurement but this time with a 10 mm thick PMMA sample (Figure 7.2). As before, the 500 MHz at the beginning and at the end are not considered because of the time gating. Nevertheless from 8.5 GHz – 10.5 GHz I observe important fluctuations in the material parameters. This problem rises because $|S_{11}| < 0.2$ leading to high uncertainties in the measurement of the S_{11} phase. $|S_{11}|$ reaches a minimum when the sample thickness corresponds to one half of the wavelength inside the sample. This is exactly the case for our frequency range and the 10 mm PMMA sample.

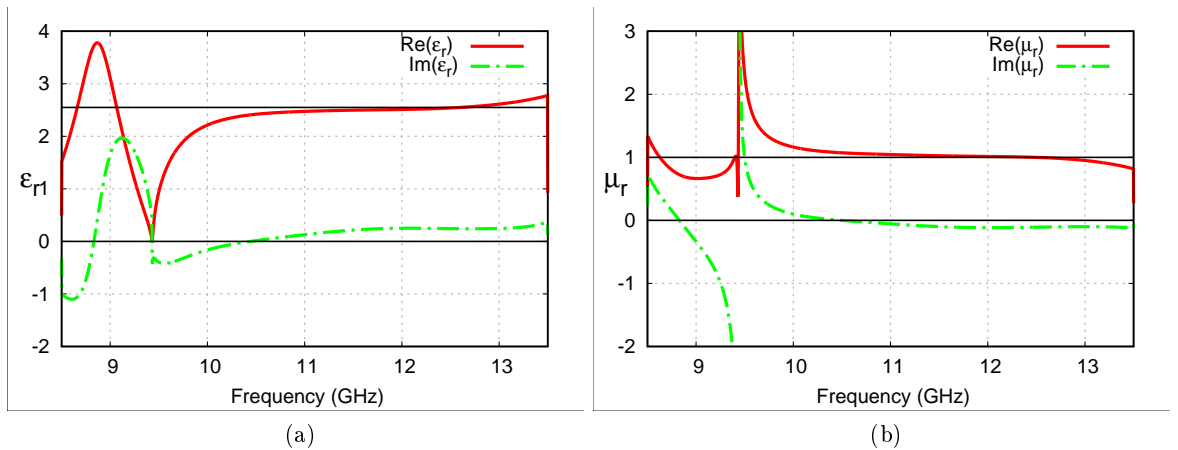


Figure 7.2.: Material parameters for a 10 mm PMMA sample NRW algorithm (a) relative permittivity ; (b) relative permeability

In Figure 7.3 we see that for the 2.94 mm PMMA sample $|S_{11}|$ is always well above 0.2,

7.1. Experimental validation for an isotropic dielectric

whereas this is not the case at all for the 10 mm PMMA sample. The region where $|S_{11}| < 0.2$ and where strong fluctuations appear in the retrieved material parameters are exactly overlapping. To proof that the measurements are correct I compute the $|S_{11}|$ parameter analytically for the 2.94 mm and 10 mm PMMA sample by assuming $\epsilon_r = (2.55 + i0.0)$ and $\mu_r = (1.0 + i0.0)$. These curves are perfectly overlapping in the frequency range not affected by the time gating.

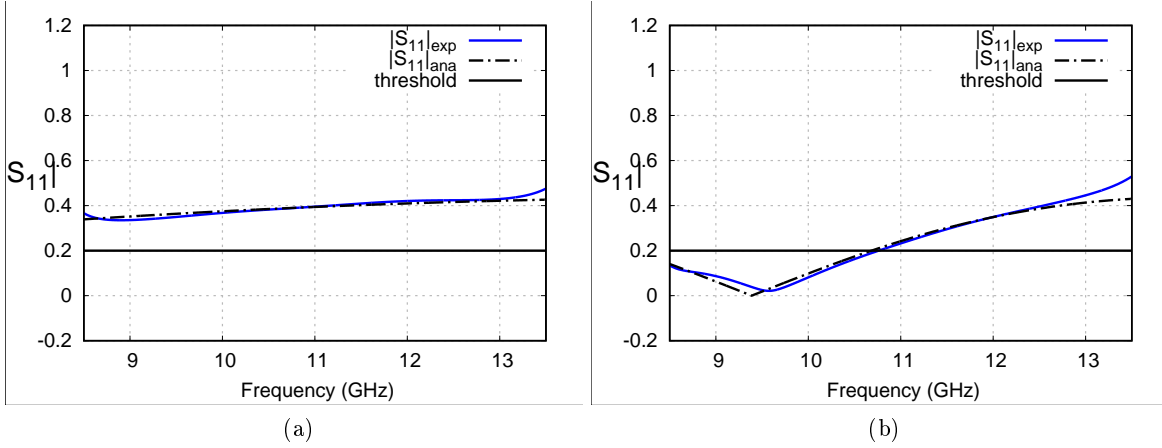


Figure 7.3.: Comparison of experimental and analytical S_{11} for (a) 2.94 mm thick PMMA sample ; (b) 10 mm thick PMMA sample

Furthermore, I used a 3 mm thick slab of polystyrene and measured the material parameters from 8 GHz – 14 GHz. Due to the effect of time gating I display only the frequency range from 8.5 GHz – 13.5 GHz.

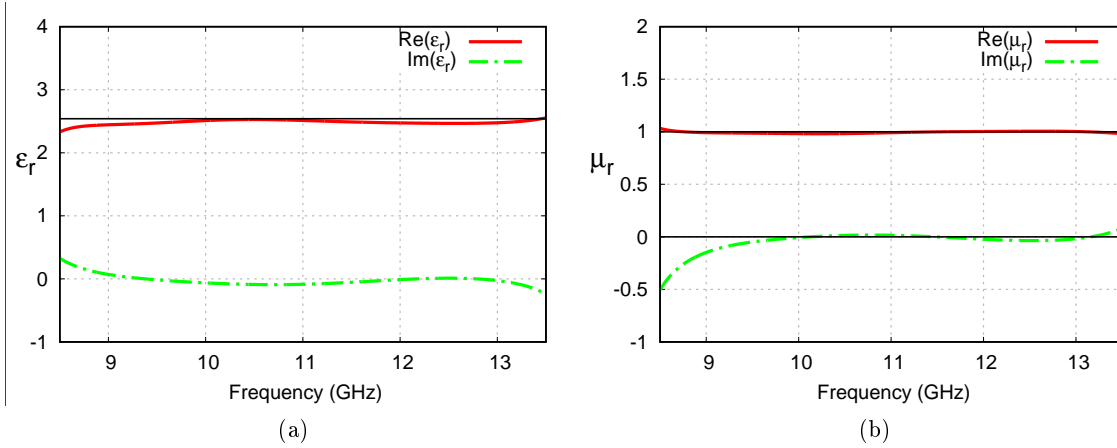


Figure 7.4.: Material parameters for a 3 mm polystyrene sample NRW algorithm (a) complex permittivity ; (b) complex permeability

7. Experimentally Measured Material Parameters

In the literature [93], the relative permittivity at 10 GHz is indicated as 2.54 with a loss tangent of 0.00033. The results I obtained are represented in Figure 7.4 and they match very well with the expected values, although up to 7% errors should be taken into account [94]. As a final verification I use the low loss retrieval method because this formula and implementation is much easier than the NRW algorithm, reducing the possibility of errors. I computed ε_{\perp} again for the same polystyrene and PMMA sample of 3 mm and 2.94 mm respectively. The results are depicted in Figure 7.5. For the PMMA slab the expected permittivity of 2.55 at 10 GHz is obtained whereas the permittivity of polystyrene is with this method slightly higher as expected. Nevertheless the results are comparable if the errors are considered.

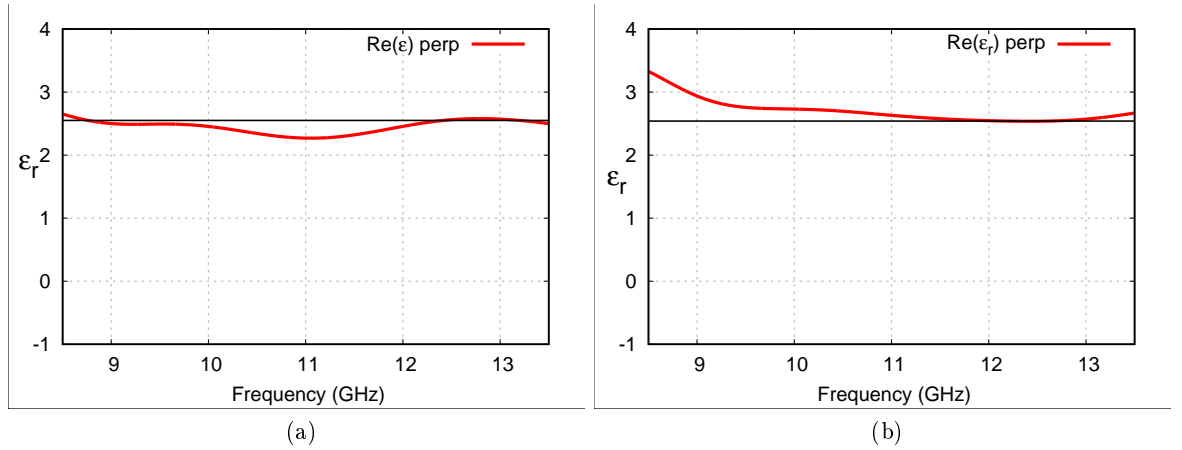


Figure 7.5.: ε_{\perp} for (a) 2.94 mm PMMA slab using low loss formula ; (b) 3 mm polystyrene slab

7.1.1. Discussion of the retrieved material parameters of simple dielectrics

Although my retrieved results agree very well with the values found in literature proving a successful calibration of the setup, many errors may influence the final result. First of all the measurements are obviously limited by the accuracy of the VNA with respect to magnitude and phase of the S parameters. Especially if $|S_{11}| < 0.2$. In this case the measured phase is so erroneous that it dominates all the other effects as can be seen in Figure 7.2. Other errors are due to the sample thickness which is a parameter in the retrieval algorithm. To reduce the measurement errors I average over several sweeps. Unfortunately this averaging is hard to quantify. The time gating also has a severe impact on the results, depending if the gate is chosen too small or too large. This also depends upon the number of frequency points and on the bandwidth used. Another effect is linked to the positioning of the sample. It should be placed at exactly the same position as the metal plate used for the REFLECT measurement. Munoz et al. [94] also showed that the error on the retrieved loss tangent varies with the real part of the permittivity for high loss materials. For $\varepsilon'_r = 25$ the error on the loss tangent is 30%, whereas for low

7.2. Experimental results for a bi-anisotropic material

permittivities $Re(\epsilon_r) = 2$ the error on the loss tangent is 6% . A low loss material has a loss tangent below 0.01, whereas as lossy material has a loss tangent above 0.1. Munoz et al. claim an uncertainty of $\pm 7\%$ for $Re(\epsilon)$ and $\pm 4\%$ for $Re(\mu)$ with respect to the waveguide method which is the most accurate method with an uncertainty of $\pm 1\%$. To clearly identify the effect of all the errors I would suggest to do several measurements without averaging the sweeps by always removing the sample completely and putting it back. From such measurements I could calculate a relative error.

7.2. Experimental results for a bi-anisotropic material

After testing my system on isotropic samples like PMMA and polystyrene I did transmission and reflection measurements on the bi-anisotropic slab. Depending on the orientation of the Omega particles with respect to the incident fields different effective material parameters are expected. This response depends on the coupling between the electric and magnetic fields with the omega structure. The details about the size of the omega inclusions and the sample are those in section 6.10. I started with the orientation presented in Figure 7.6 where a strong coupling is expected.

Orientation 1

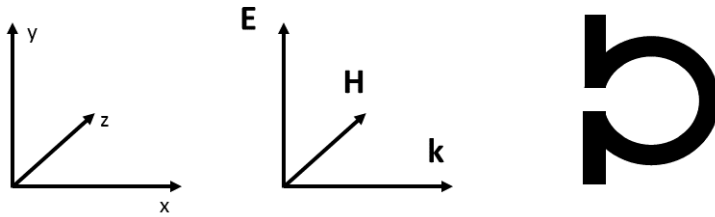


Figure 7.6.: *Electric field oriented parallel to the arms and magnetic field perpendicular to the loop. A strong coupling is expected for this configuration*

For a VNA output power of -10 dBm I only observed a very weak response. Increasing the power to 0 dBm lead to the desired results. As predicted by the theory [77, 78] the S_{11} and S_{22} (Figure 7.7) parameters differ whereas the S_{12} and S_{21} parameters are nearly identical (Figure 7.8). I observe a transmission approaching zero in the vicinity of 10.2 GHz in Figure 7.8a. The transmitted signal is so weak that the phase cannot be measured accurately anymore leading to a peak at 10.2 GHz in the phase (Figure 7.8b).

7. Experimentally Measured Material Parameters

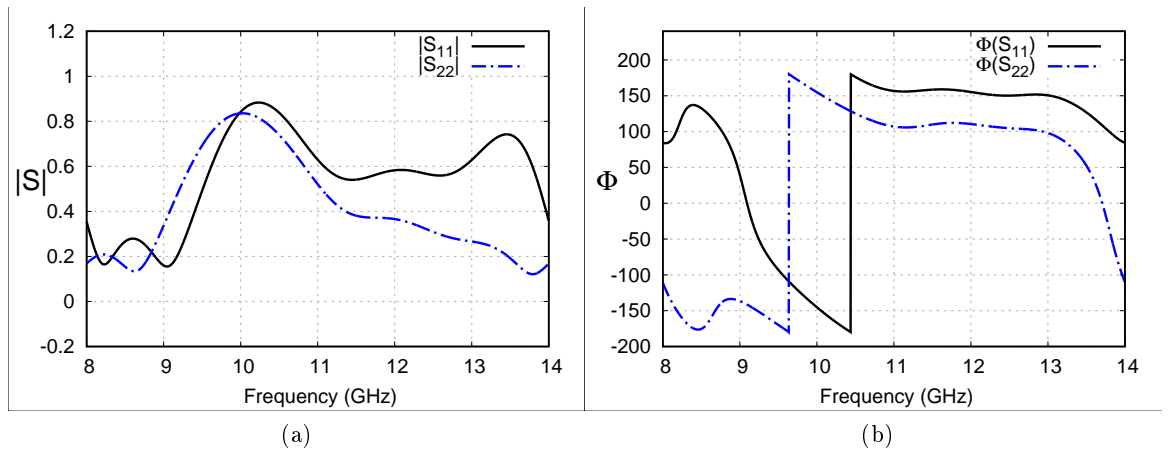


Figure 7.7.: S_{11} and S_{22} parameters of the bi-anisotropic material for 0 dBm (a) magnitude ; (b) phase

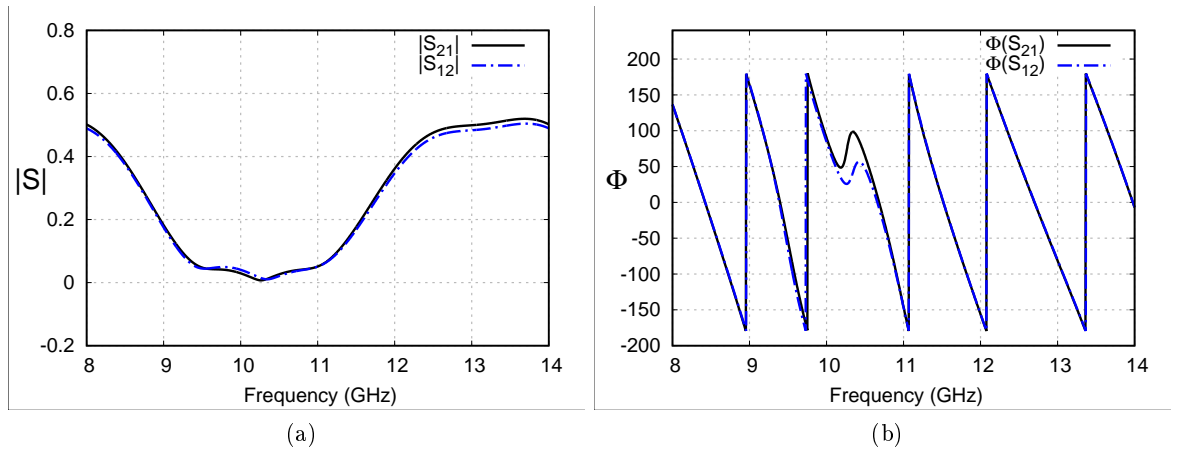


Figure 7.8.: S_{12} and S_{21} parameters of the bi-anisotropic material for 0 dBm (a) magnitude ; (b) phase

7.2. Experimental results for a bi-anisotropic material

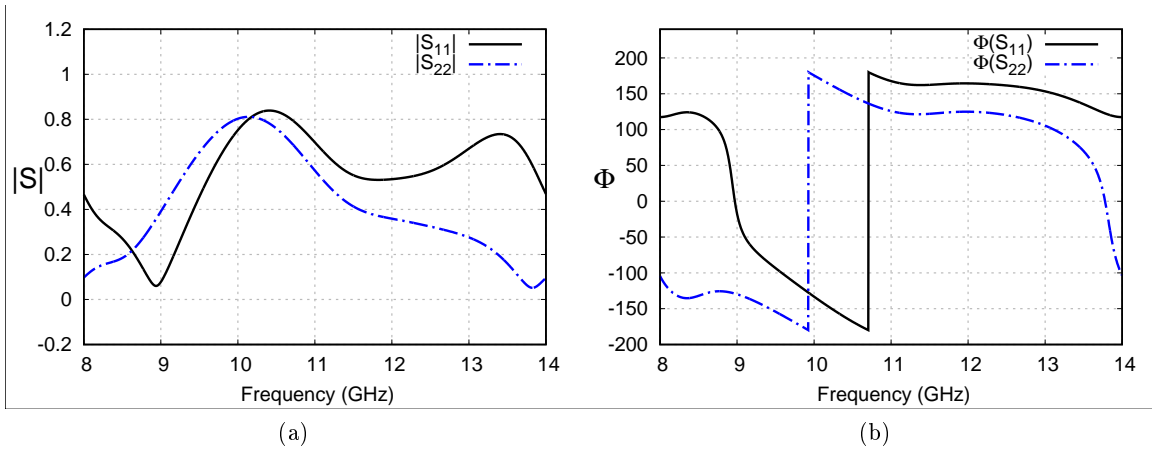


Figure 7.9.: S_{11} and S_{22} parameters of the bi-anisotropic material for 3 dBm (a) magnitude ; (b) phase

To improve the accuracy on the measurements I increased the power to 3dBm. I couldn't increase it further because the calibration standard isn't suited for higher powers. Fortunately this was enough to let some signal pass even at the resonance frequency as can be seen in Figure 7.10b. From these measurements I computed the material parameters using the algorithm from Chen [28, 26] presented in section 6.9.

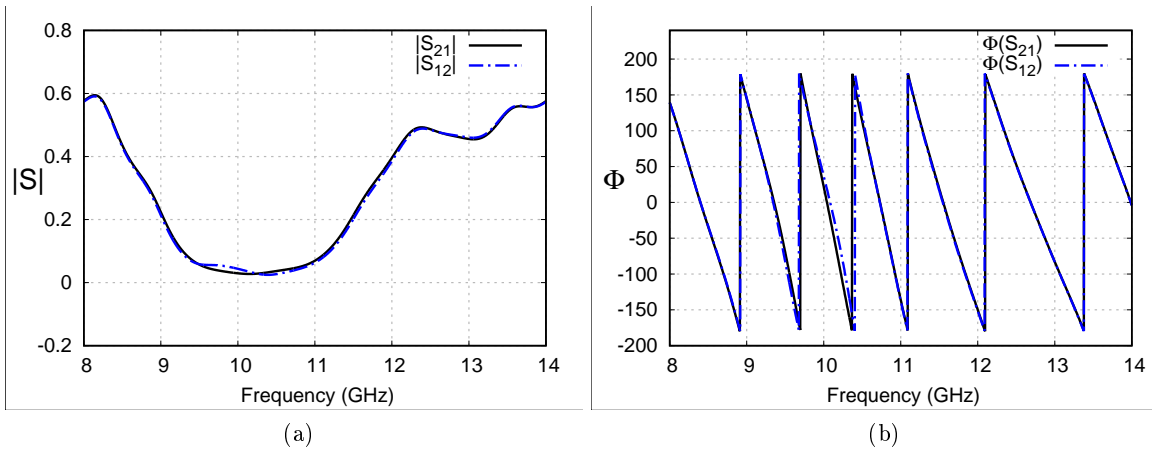


Figure 7.10.: S_{12} and S_{21} parameters of the bi-anisotropic material for 3 dBm (a) magnitude ; (b) phase

7. Experimentally Measured Material Parameters

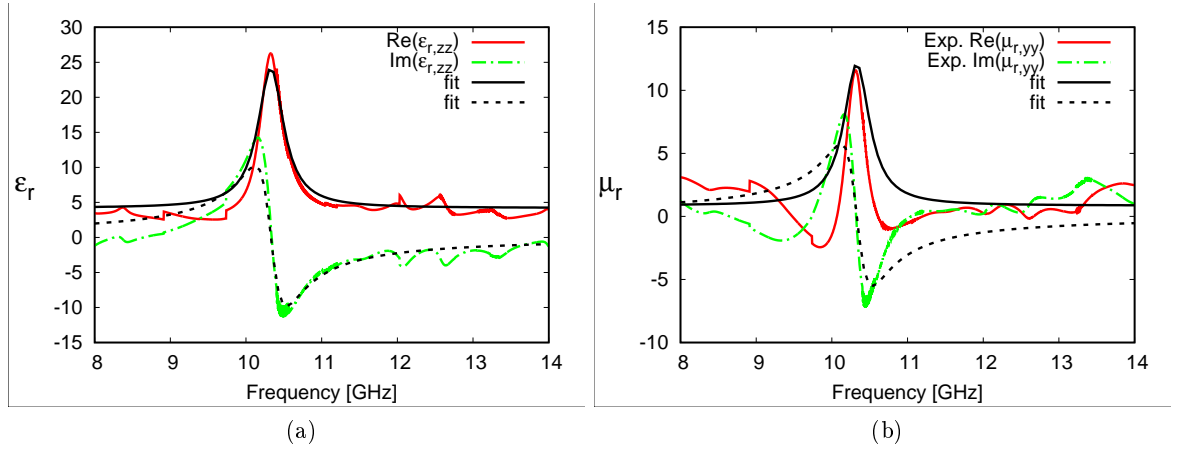


Figure 7.11.: (a) relative permittivity ; (b) relative permeability

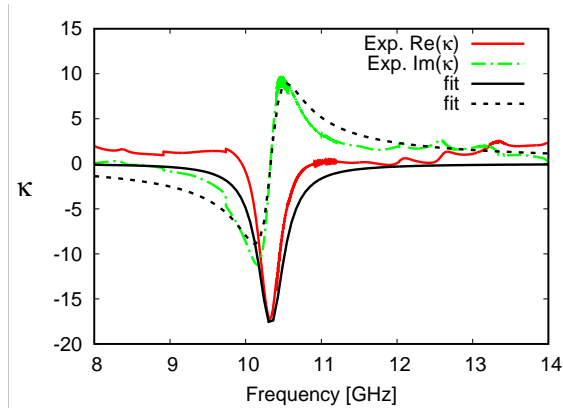


Figure 7.12.: chirality

In theory the permittivity, permeability are expected to follow the Lorentz and the chirality the Condon model, which are repeated hereafter for convenience

$$\begin{aligned}\varepsilon(\omega) &= \varepsilon_0 \left(\varepsilon_\infty + \frac{(\varepsilon_s - \varepsilon_\infty) \omega_\varepsilon^2}{\omega_\varepsilon^2 - \omega^2 + i2\omega_\varepsilon \xi_\varepsilon \omega} \right) \\ \mu(\omega) &= \mu_0 \left(\mu_\infty + \frac{(\mu_s - \mu_\infty) \omega_\mu^2}{\omega_\mu^2 - \omega^2 + i2\omega_\mu \xi_\mu \omega} \right) \\ \kappa(\omega) &= \frac{\tau_\kappa \omega_\kappa^2 \omega}{\omega_\kappa^2 - \omega^2 + i2\omega_\kappa \xi_\kappa \omega}\end{aligned}$$

Tretyakov [128] even suggests a slightly different model for the permeability where instead

7.2. Experimental results for a bi-anisotropic material

of ω_μ^2 , ω^2 appears in the numerator.

$$\mu(\omega) = \mu_0 \left(\mu_\infty + \frac{(\mu_s - \mu_\infty)\omega^2}{\omega_\mu^2 - \omega^2 + i2\omega_\mu\xi_\mu\omega} \right)$$

At the resonance both models give a very similar behavior. Slight differences only appear in the low or high frequency limit. The suggested models unfortunately do not fit the data without further modification. If I correct however $\varepsilon(\omega)$, $\mu(\omega)$ by a factor i and $\kappa(\omega)$ by -1 leading to

$$\begin{aligned} \varepsilon(\omega) &= \varepsilon_0 \left(\varepsilon_\infty + i \frac{(\varepsilon_s - \varepsilon_\infty)\omega_\varepsilon^2}{\omega_\varepsilon^2 - \omega^2 + i2\omega_\varepsilon\xi_\varepsilon\omega} \right) \\ \mu(\omega) &= \mu_0 \left(\mu_\infty + i \frac{(\mu_s - \mu_\infty)\omega_\mu^2}{\omega_\mu^2 - \omega^2 + i2\omega_\mu\xi_\mu\omega} \right) \\ \kappa(\omega) &= (-1) \frac{\tau_\kappa\omega_\kappa^2\omega}{\omega_\kappa^2 - \omega^2 + i2\omega_\kappa\xi_\kappa\omega} \end{aligned}$$

I obtain an excellent agreement between the theoretical and experimental data as can be seen in Figures 7.11 and 7.12 using the following parameters

$$\begin{aligned} \mu_{yy}(\omega) : \mu_\infty &= \mu_0 0.85, \mu_s = \mu_0 1.3, \omega_\mu = 2\pi \cdot 10.3 \text{ GHz}, \xi_\mu = 0.02 \\ \varepsilon_{zz}(\omega) : \varepsilon_\infty &= \varepsilon_0 4.2, \varepsilon_s = \varepsilon_0 5.0, \omega_\varepsilon = 2\pi \cdot 10.3 \text{ GHz}, \xi_\varepsilon = 0.02 \\ \kappa_{yz}(\omega) : \tau_\kappa &= 36.7 \text{ ps}, \omega_\kappa = 2\pi \cdot 10.3 \text{ GHz}, \xi_\kappa = 0.02 \end{aligned}$$

To understand this correction I rewrite ε , for example, using the electric susceptibility, $\varepsilon(\omega) = \varepsilon_0(\varepsilon_\infty + \chi_e(\omega))$. It seems that only the susceptibility needs to be corrected by a factor i . This is however not physical because the causality condition (subsection 2.4.5) is not fulfilled. I expect the origin of this to be in the retrieval algorithm, because i corresponds to a phase shift of $i = e^{i\pi/2}$ and similarly $-1 = e^{i\pi}$. In contrast to a simple dielectric, it seems that the metamaterials alters the phase of the S-parameters which needs to be taken into account during the retrieval process. Walien et al.[137] also expect the retrieval algorithm to be the origin of the unexpected behavior. Koschny [74] on the other hand suspects the underlying periodicity of the metamaterial to lead to this response. This explains the differences of the results retrieved from a single unit cell with a periodic arrangement. Further investigation is required to entirely understand the effect of the periodicity and the retrieval algorithm on the retrieved data.

Orientation 2

I continued with the second orientation by rotating the sample by 90 degrees, leading to a configuration depicted in Figure 7.13. For this configuration no or only a very weak coupling is expected.

7. Experimentally Measured Material Parameters

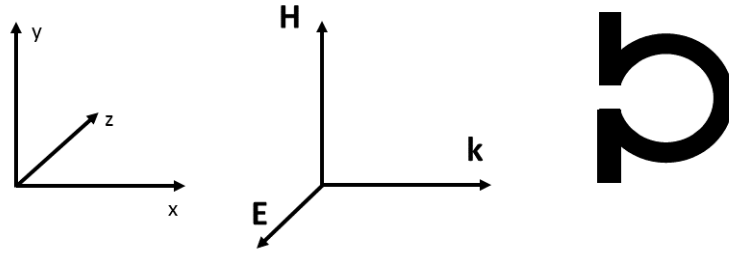


Figure 7.13.: *Magnetic field parallel to the arms and electric field perpendicular to the loop. Only a very weak coupling is expected*

The S-parameters are represented in Figures 7.14 and 7.15. Compared to the previous case where the strong coupling occurred, now the magnitude of S_{11} and S_{22} phase are identical but the phase is shifted by 180 degrees and no jump in the phase is detected (Figure 7.14).

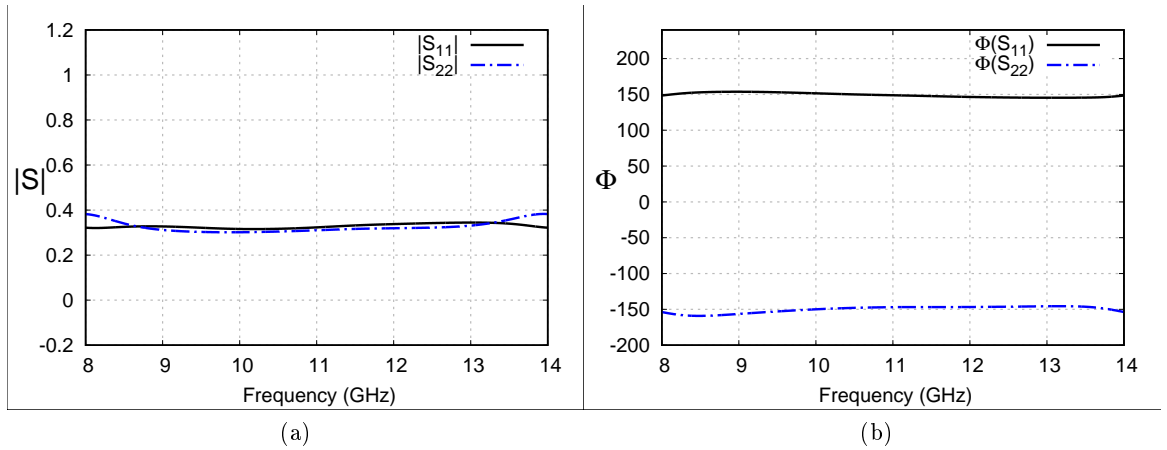


Figure 7.14.: S_{11} and S_{22} parameters of the bi-anisotropic material for 3 dBm (a) magnitude ; (b) phase

The S_{12} and S_{21} parameters show a very high transmission throughout the whole frequency range (Figure 7.15a) without any stop band (Figure 7.15b) and only three changes of the phase (Figure 7.15b) compared to the six observed in the first configuration (Figure 7.10b). The metamaterial behaves in this configuration similar to a simple dielectric.

7.2. Experimental results for a bi-anisotropic material

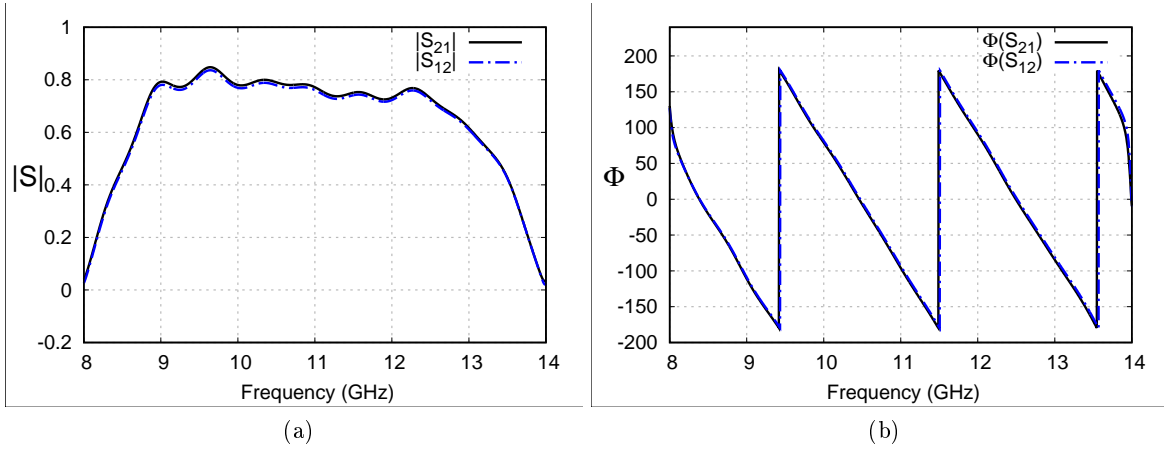


Figure 7.15.: S_{12} and S_{21} parameters of the bi-anisotropic material for 3 dBm (a) magnitude ; (b) phase

The retrieved materials parameters are shown in Figures 7.16a, 7.16b and 7.17. The periodically appearing peaks are due to the retrieval method and appear when the sample thickness is an integer multiple of one half wavelength in the sample. To demonstrate this I consider the distance between peaks which equals roughly 1 GHz. This leads to a free space wavelength of $\lambda_0 = 30\text{ cm}$. The FR4 board I use has $Re(\epsilon_r) = 4.5$, $Re(\mu_r) = 1$. The wavelength inside the dielectric $\lambda_{Diel} = \lambda_0 / \sqrt{\mu_r \epsilon_r} = 14.1\text{ cm}$. Because the peaks appear at an integer multiple of one half wavelength I obtain $d = \lambda_{Diel} / 2 \approx 7\text{ cm}$ corresponding to the thickness of my slab. This specific orientation of the metallic inclusion with respect to the electric field makes them to small capacitors which probably leads to a non negligible effect resulting in a non zero chirality.

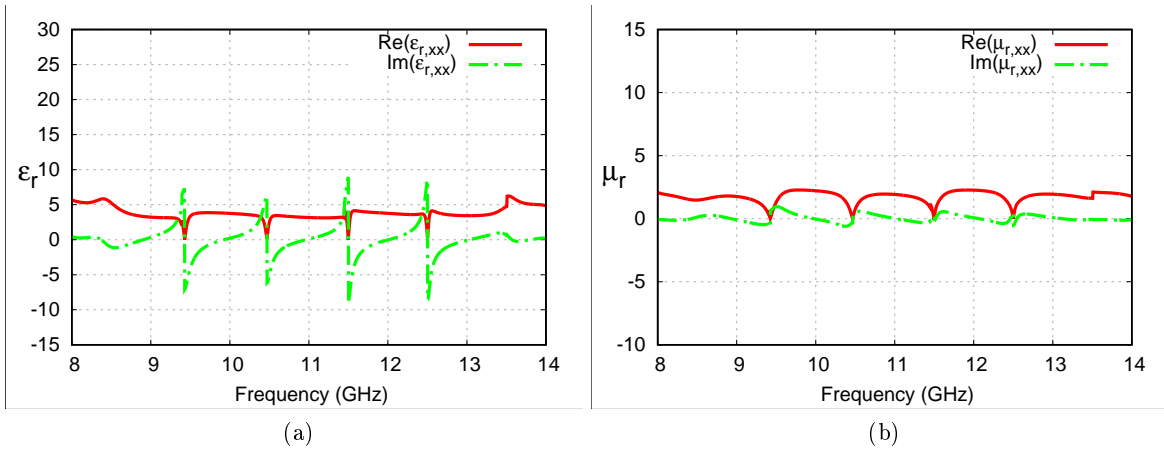


Figure 7.16.: (a) relative permittivity ; (b) relative permeability

7. Experimentally Measured Material Parameters

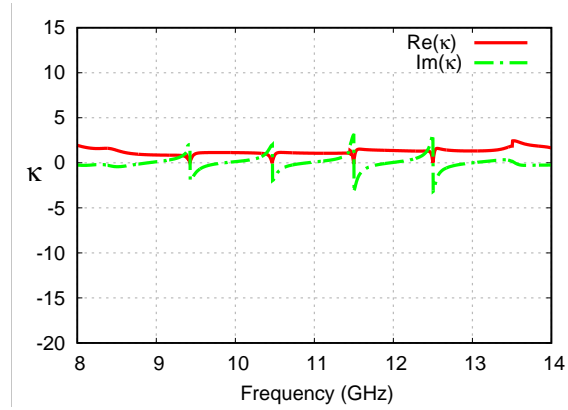


Figure 7.17.: *chirality*

Orientation 3

For the last measurement, I arranged the sample to obtain the configuration represented in Figure 7.18. In this configuration only the electric field should lead to a strong response because the field vector is parallel to the arm. The magnetic field however is parallel to the structure and cannot completely couple to it as in the first configuration (Figure 7.6)

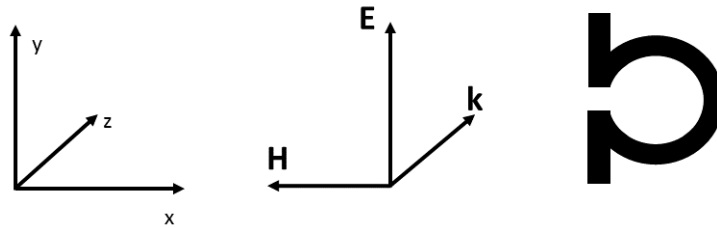


Figure 7.18.: *Magnetic field parallel to the arms and electric field perpendicular to the loop. Only a very weak coupling is expected*

The S-parameters are represented in Figures 7.19 and 7.20. The S_{12} and S_{21} parameters are very small throughout the whole frequency range. This is probably because by disassembling the sample the faces of the slabs are now perpendicular to the incident wave resulting in many metallic interfaces that leading to reflections.

7.2. Experimental results for a bi-anisotropic material

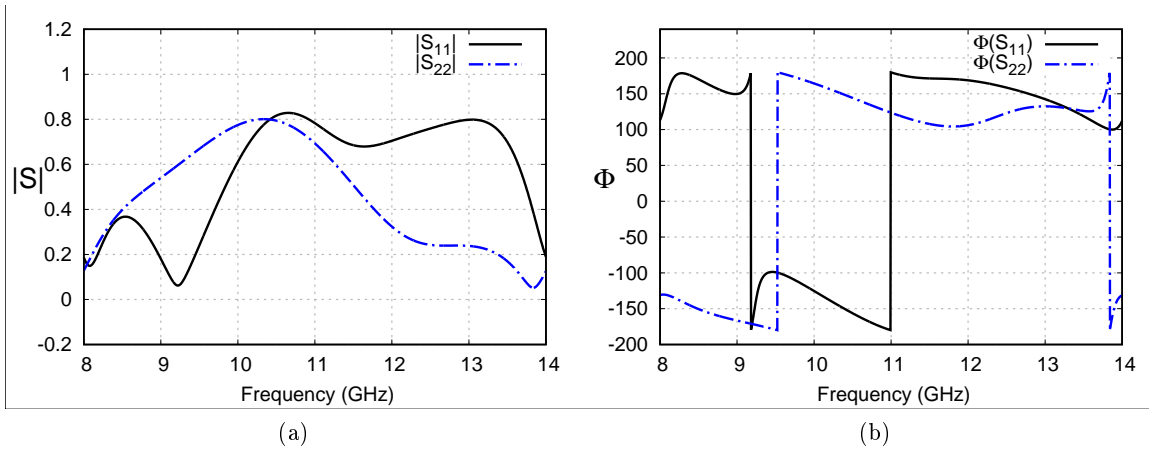


Figure 7.19.: S_{11} and S_{22} parameters of the bi-anisotropic material for 3 dBm (a) magnitude ; (b) phase

The S_{12} and S_{21} parameters show a very low transmission throughout the whole frequency range (Figure 7.20a). For this configuration

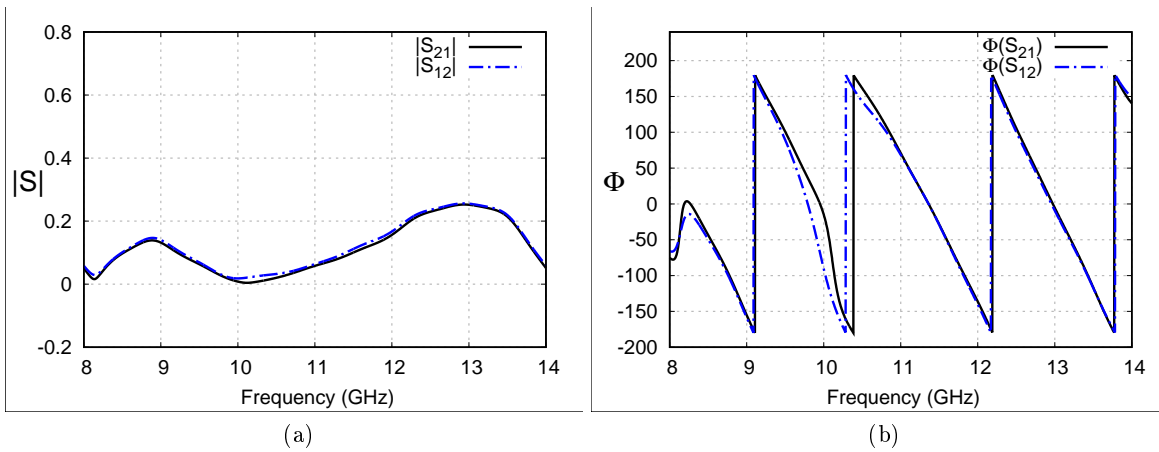


Figure 7.20.: S_{12} and S_{21} parameters of the bi-anisotropic material for 3 dBm (a) magnitude ; (b) phase

The retrieved materials parameters are shown in Figures 7.21a, 7.21b and 7.22. Again the effect of the coupling is observed. To fit the data, the same correction would be required as for the first orientation

7. Experimentally Measured Material Parameters

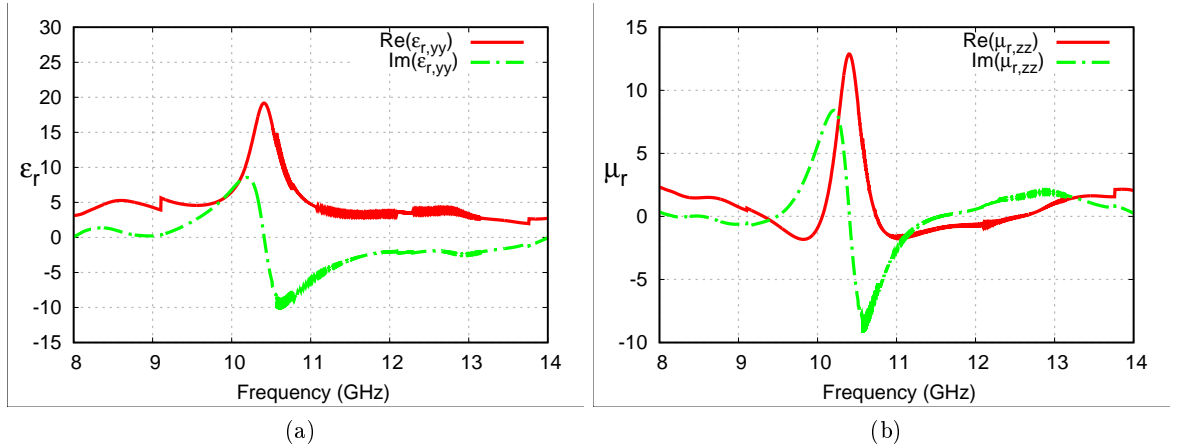


Figure 7.21.: (a) relative permittivity ; (b) relative permeability

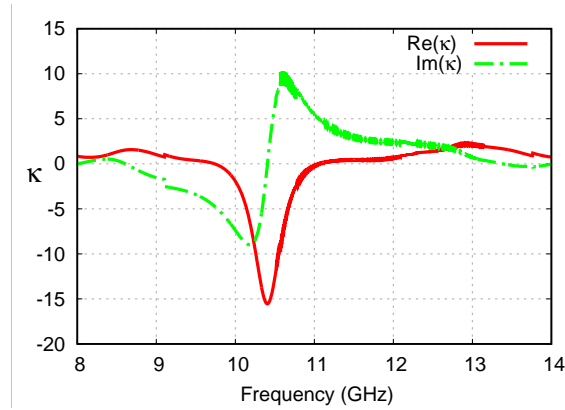


Figure 7.22.: chirality

7.2.1. Discussion of the experimental results

For the first orientation, a strong coupling between the electric and magnetic field at the resonance frequency is expected to lead to an increase or decrease in the material parameters. This response is observed for each of the material parameters between $10\text{ GHz} - 11\text{ GHz}$. Which is in a reasonable agreement with the expected resonance frequency of a single omega inclusion of 10.87 GHz as calculated analytically in section 6.10. In the second case, only a very weak coupling is expected because neither the electric nor the magnetic field can couple to the arm or the loop of the omega inclusion. Therefore the material should show characteristics close to the matrix (FR4) material, which is again confirmed by the measurement. Nevertheless, a non zero chirality is measured, but no resonance. This effect is probably due to multiple reflections of the incoming wave on the metallic omega inclusions. This effect is hidden in the strong

7.2. Experimental results for a bi-anisotropic material

response for orientation 1 and 2. For the third orientation, only the electric field can couple to the omega inclusion, therefore I expect a resonance which is less pronounced compared the first orientation. Nevertheless, the electric field still induces an magnetic field in the wire to which the magnetic field can couple. Hence the permeability and permittivity are similar for orientation 1 and 3. As already explained for orientation 1. It seems that the metamaterial adds a phase shift to the S-parameters which needs to be corrected, otherwise it leads to non physical results. Although the results confirm my expectations care has to be taken with the measured data and the retrieved material parameters due to several reasons.

1. The input power is crucial to observe the expected resonance leading to a stop band in the transmission. For the sample thickness of 7 cm and input power of 0 dBm was sufficient to observe the resonance, but the transmitted signal was too weak, at the resonance frequency, to retrieve the phase correctly. For 3 dBm the signal was fortunately strong enough to measure the phase. With the VNA I use I cannot go to higher input powers because the calibration kit doesn't allow so. Measurements at even higher power would in my opinion reduce the errors on the S parameters. Adding a second mirror between the sample and receiving antenna would also improve the signal strength by refocusing the beam in the receiving antenna.
2. Another problem linked to the metamaterial itself is the difference between the physical and electrical thickness. For a simple dielectric, the physical and electrical thicknesses are equal because the impedance does not depend on its thickness. In our case however currents will be induced on the metallic inclusions. Therefore the impedances of two slabs of different thicknesses should be computed and used to obtain the electrical thickness [28]. This will be the thickness d used in the retrieval algorithm [28]. Until now I only have a single slab and therefore I'm forced to use the physical as electrical thickness which is not correct.
3. In the retrieval algorithm a parameter m describes the phase ambiguity in the refractive index (equation (6.47)). For a given sample thickness and material parameters, the initial value for m may differ from 0. In the case of a metamaterial, samples of two different thicknesses are required to obtain the correct initial m . In my case I am more interested in the resonance phenomenon which can be observed even for a parameter m which might not be entirely correct. In the future I plan to refine the results using two samples of different thicknesses.
4. The measurement setup is very sensitive to the calibration. Currently I use the calibration technique suggested by [94]. It would however be interesting to compare this method with other calibration techniques like the GRL and TRL for a metamaterial after making the setup symmetric with a second mirror.
5. Another source of error especially for large samples is the time gating. In a metamaterial the signal converted to the time domain does not have the shape of a smooth Gaussian as for the thin dielectric samples I used as reference. This makes

7. Experimentally Measured Material Parameters

it more difficult to detect the main signal between multiple reflections. The idea is to extend our setup by a second mirror to make it symmetric. This allows us to perform a TRL or GRL calibration to fully understand the effect of time gating on the results. To further investigate the difference between the metamaterial and simple dielectric I suggest to use a slab with the same dimensions made out of the same dielectric material as the matrix of the metamaterial, but without the metallic inclusions.

8. Results of the Multiscale Approach

In this chapter I present the results from my multiscale approach and compare them with the experimentally retrieved data.

8.1. Microscale simulation of the bi-anisotropic media

8.1.1. Method 1 “Indirect retrieval method”

In this subsection I use the method described in section 5.2.1 to compute the S-parameters from a unit cell of a metamaterial. From the S-parameters I calculate the materials parameters using the retrieval algorithm presented in section 6.9. The results for the different orientations are shown below. I use the same convention as for the experimental measurements. Orientation 1 corresponds to Figure 7.6, Orientation 2 to Figure 7.13 and Orientation 3 to Figure 7.18.

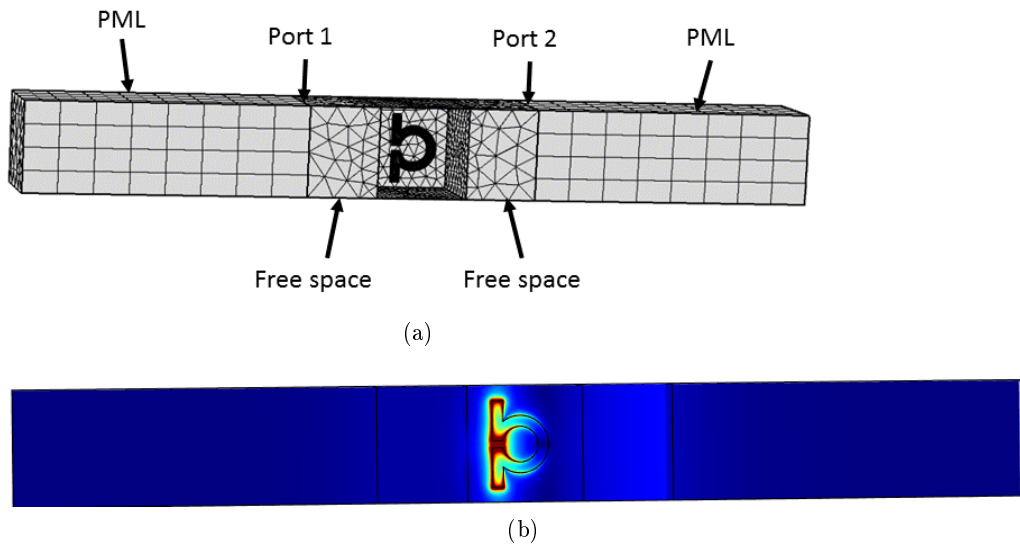


Figure 8.1.: (a) Mesh of omega including the free space region and the PML ; (b) Intensity of the electric field at (9.4 GHz)

Bare in mind that the retrieved S-parameters and material parameters correspond to a metamaterial with infinite lateral extension (extension perpendicular to the optical axis) but with a thickness of only a single unit cell. The mesh and the intensity of the electric field at a frequency are depicted in Figures 8.1a and 8.1b.

8. Results of the Multiscale Approach

Orientation 1

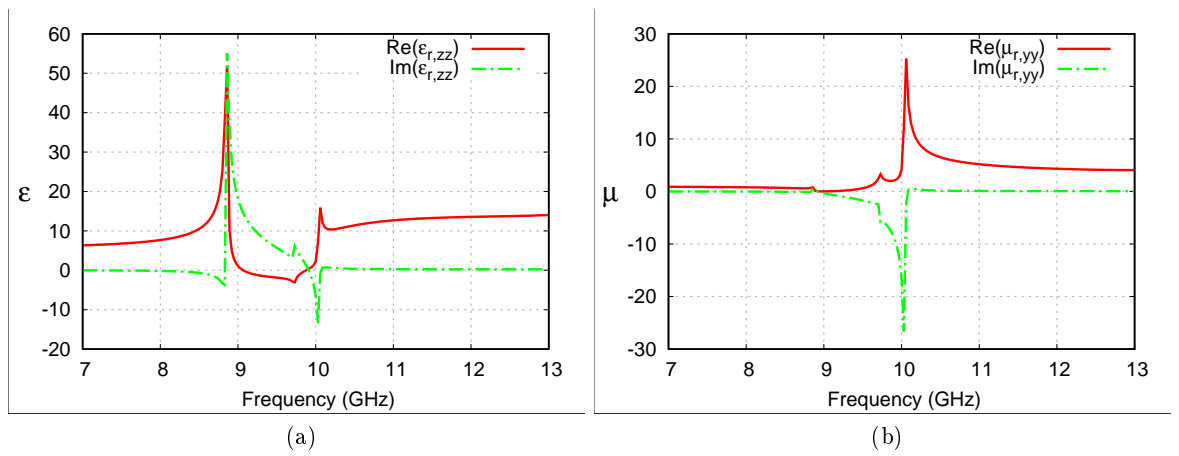


Figure 8.2.: (a) relative permittivity ; (b) relative permeability

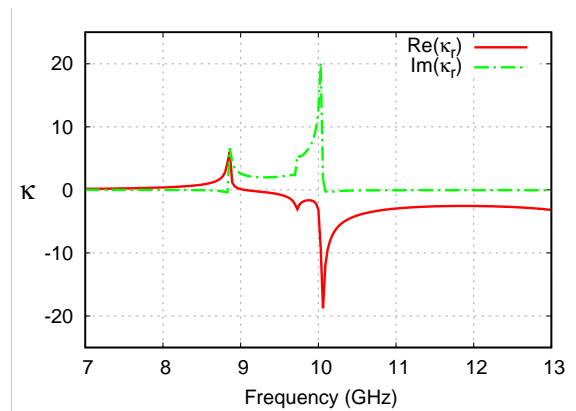


Figure 8.3.: chirality

The retrieved permeability and chirality show a narrow and very pronounced peak at a frequency of 10 GHz. Whereas in the permittivity the main peak appears 9 GHz and another smaller one at 10 GHz. The chirality on the other has a small peak at 9 GHz. In the experimentally retrieved material parameters the peaks all appear at the same resonance frequency.

Orientation 2

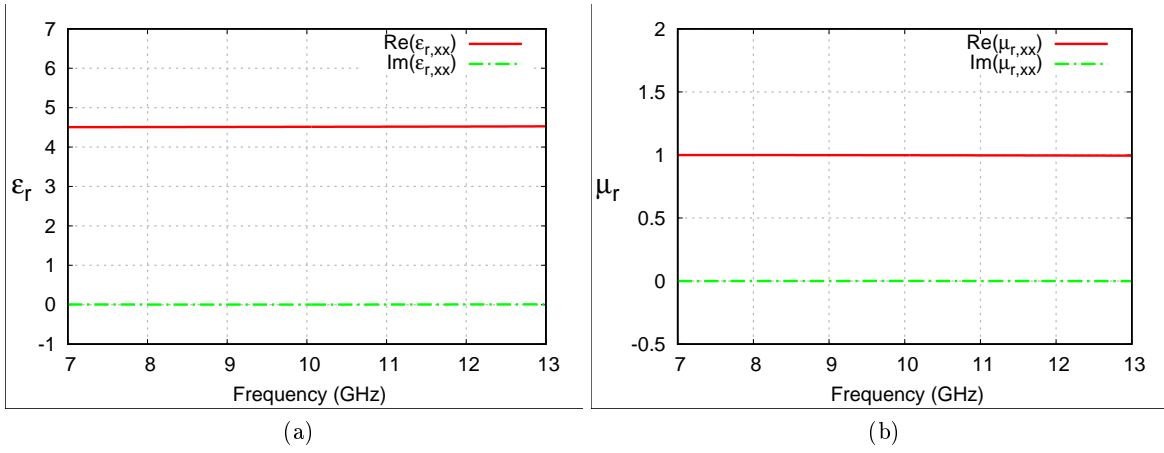


Figure 8.4.: (a) relative permittivity ; (b) relative permeability

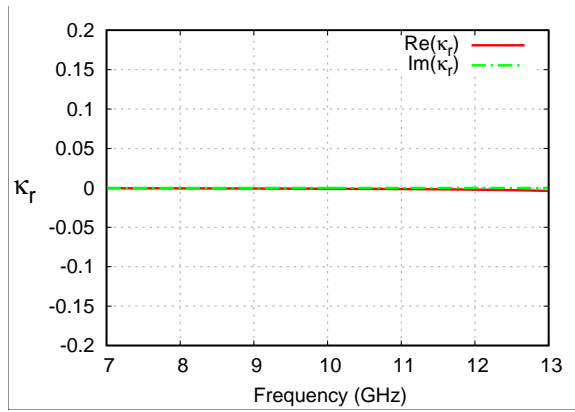


Figure 8.5.: chirality

These results agree very well with my expectations, because neither the electric nor the magnetic field couple to the omega inclusion, hence the metamaterial behaves like a simple dielectric. This results also agrees with the experimental data.

Orientation 3

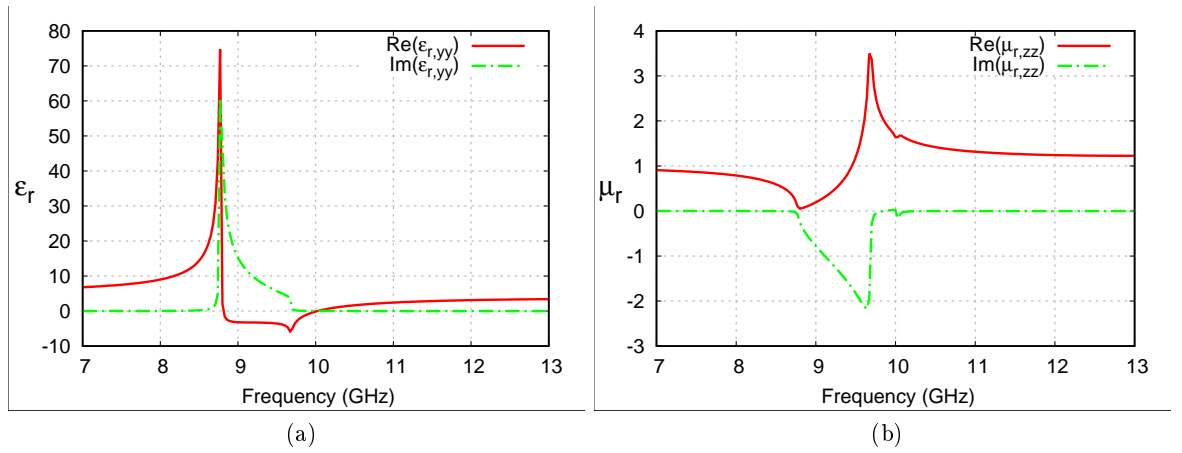


Figure 8.6.: (a) relative permittivity ; (b) relative permeability

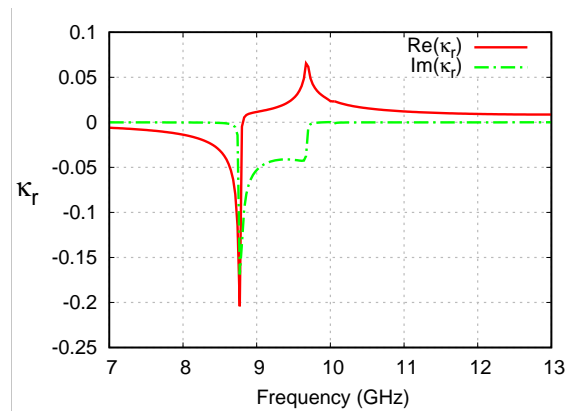


Figure 8.7.: chirality

A very narrow and pronounced peak appears for the permittivity at 10GHz . The experimental data suggest this peak to be less pronounced compared to the first orientation which is not the case. Whereas the retrieved permeability and permittivity for the experiment were very similar for orientation 1 and 3 in this simulation they are completely different with respect to shape and magnitude.

Discussion of the indirect multiscale approach results

As expected, a more or less strong resonance due the coupling of the fields for orientation 1 and 3 is observed. Surprisingly, strong responses are observed at two different frequencies, namely at 9GHz and 10GHz . This does not correspond at all to the experimental

results. However, my results look similar to those from Chen [26] where the sharp peaks/dips also appear in the retrieved data. The problem may be that the material has a thickness of a single unit cell because these peaks and dips do not appear for the experimental data where a much thicker sample is used. It may be interesting to model several unit cells instead of a single one along the optical axis to see if this has an influence on the peaks/dips. Neglecting the peaks/dips in Figure 8.2a and Figure 8.6a from $8.7\text{ GHz} - 10\text{ GHz}$ the retrieved permittivity is well below the relative permittivity $\epsilon_r = 4.5$ of the FR4 dielectric demonstrating the coupling induced by the omega inclusion. Similar results are observed for the permeability and permittivity. Orientation 2 on the other hand completely fulfills my expectations. Neither the electric field nor the magnetic field can couple to their corresponding part of the omega structure. Therefore the metamaterial behaves like a simple dielectric slab of FR4 material. The initial idea was, as explained in section 5.2.1, to fit a Lorentz/Condon model to those retrieved materials parameters. These parameters ($\epsilon_\infty, \epsilon_s, \omega_\epsilon, \xi_\epsilon \dots$) obtained from the parameter identification algorithm would have been the input for the UM-FDTD program which allows the simulation of bi-anisotropic media (section 3.8). With this program I model the experimental slab with the same dimensions $7\text{ cm} \times 15\text{ cm} \times 15\text{ cm}$ as in the experiment. The retrieved data differ however significantly from a Lorentz/Condon model and therefore the NLOPT algorithm doesn't converge.

8.1.2. Method 2 "Direct retrieval method"

In this section I present the results obtained by the direct method. In contrast to the indirect method it allows me to directly retrieve the material parameters without first calculating the S-parameters. I used a frequency domain FE solver on a unit cell with dimensions specified in section 6.10

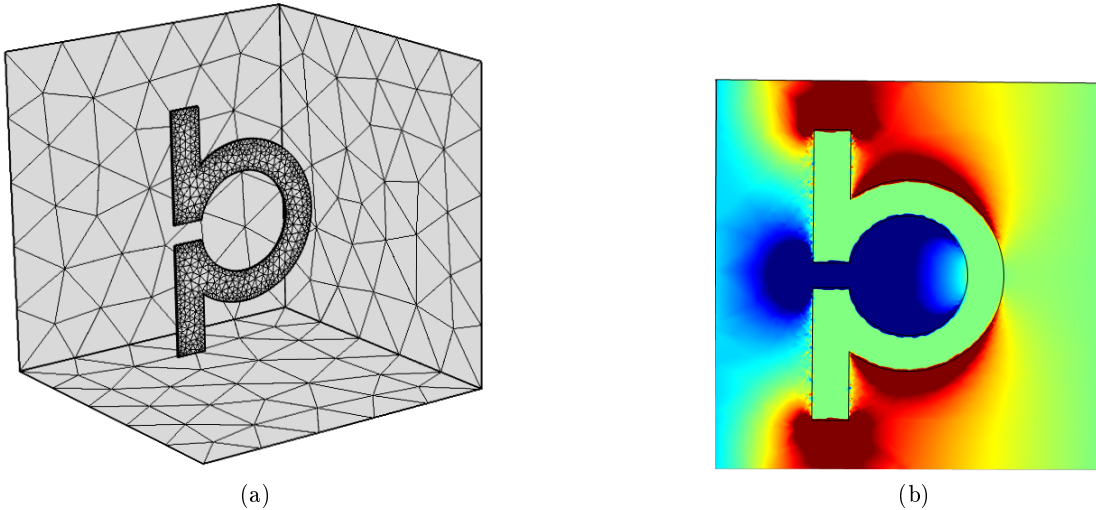


Figure 8.8.: (a) Unit cell with omega inclusion ; (b) Intensity of the electric field at the resonance frequency

8. Results of the Multiscale Approach

The omega inclusion is oriented as depicted in Figure 8.9. The optical axis is oriented along the $+x$ direction. I send a right and left hand circular polarised wave towards the unit cell.

$$\mathbf{E}(\mathbf{r}, t)_{\pm} = \begin{pmatrix} 0 \\ \pm i E_0 \\ E_0 \end{pmatrix} e^{i(\mathbf{k} \cdot \mathbf{r} - \omega t)}$$

This way the components in the material parameter matrices

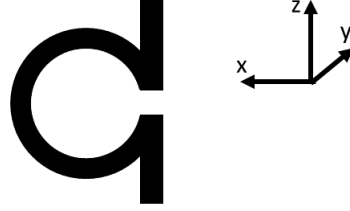


Figure 8.9.: Orientation of omega

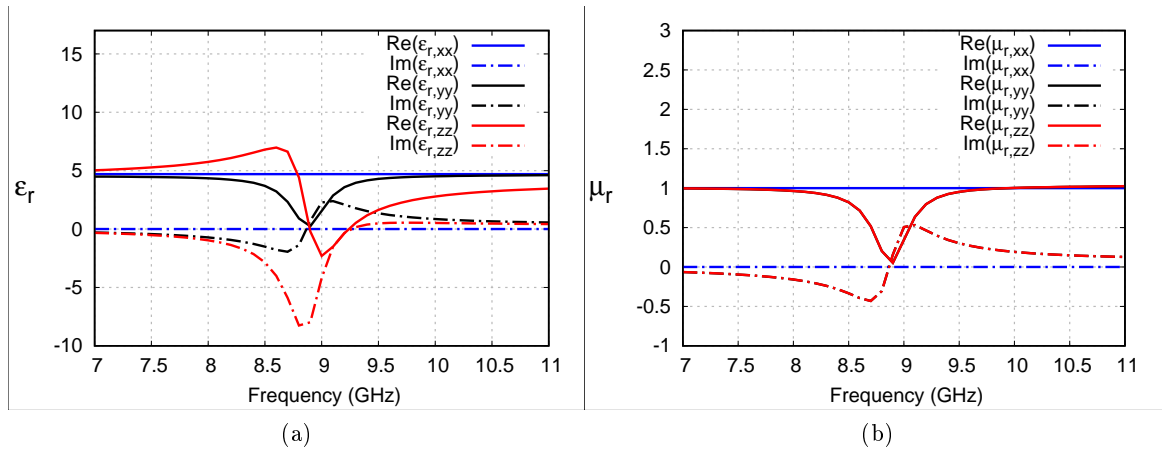


Figure 8.10.: (a) $\epsilon_{r,xx}$, $\epsilon_{r,yy}$, $\epsilon_{r,zz}$; (b) $\mu_{r,xx}$, $\mu_{r,yy}$, $\mu_{r,zz}$

The yz , zy elements are not displayed because they are 0 as expected. Currently I'm not able to retrieve a reasonable chirality, therefore no graph is displayed. For the yy , zz elements of the permittivity matrix a resonating behavior is observed both for the permittivity and permeability. Whereas $\bar{\epsilon}_{xx} \neq \bar{\epsilon}_{yy}$, $\bar{\mu}_{xx} = \bar{\mu}_{yy}$. I'm not sure if this is related to the specific shape of the omega inclusion or if there is another reason. The components μ_{xx} and ϵ_{xx} are set to the permeability and permittivity of the matrix material. They can not be computed directly because the optical axis is oriented along the x axis.

Discussion of the direct multiscale approach results

Only the ε_{zz} component follows a Lorentz model as described by equation (3.114). The other components show however a Lorentz type behavior. Maybe the circular polarised wave excitation leads to this difference between the direct multiscale results and the Lorentz model. For a circular polarised wave, one of the components perpendicular to the direction of propagation requires a phase shift of $\pi/2$ leading to a multiplication by a factor $i = e^{i\pi/2}$ for one of the electric field components. Also the experimental data required such a correction to match with the theoretical model. This needs however to be investigated in more detail. Furthermore, I wasn't able to retrieve a reasonable chirality with my method. I think however that it is possible after further and especially mathematically more rigorous investigation. To further improve the direct multiscale approach it would be interesting to test with a chiral structure like a left and right handed spring. Alternatively I will test the method suggested by [120] to see if this allows me to retrieve the chirality from a unit cell. My results also show a lower resonance frequency than the experimental data. This phenomenon is also observed in real experiments where the resonance of a single unit cell differs significantly from the response of a periodic omega media. Whereas a unit cell shows a resonance at a specific frequency, the periodic arrangement leads to a band gap over a much larger frequency range. Furthermore a shift of the bandgap to higher frequencies is observed. These effects are directly linked to the periodicity of the material [10]. Further investigation is required to see if this effect can be taken into account by modelling a single unit cell.

8.2. Macroscale Simulation

From the direct retrieval method I fitted a Lorentz model to the data obtained by the direct approach using a global optimisation algorithm from the NLOPT library. Unfortunately the code can currently just model the permittivity and permeability according to a Lorentz model described by equation (3.114). Which describes very well the permittivity. For the permeability and chirality I took the same resonance frequency and damping as for the permittivity and an electromagnetic coupling constant of $1 ps$ which is comparable to the value used by [95] because I wasn't able to retrieve a reasonable chirality with my method. Furthermore I consider only ε_{zz} , μ_{yy} , κ_{yz} as frequency dependent because I use linear polarised wave with the electric field along the z direction, the magnetic field along the y direction and the optical axis along the x direction. For the simulation with UM-FDTD I also use a higher resonance frequency as I obtained with my multiscale method because the resonance frequency changes if the unit cells are arranged periodically [10]. Resulting in the following parameters for the strong coupling

8. Results of the Multiscale Approach

(orientation 1, Figure 7.6)

$$\bar{\epsilon} = \begin{pmatrix} \epsilon_{Diel} & 0 & 0 \\ 0 & \epsilon_{Diel} & 0 \\ 0 & 0 & \epsilon_{zz}(\omega) \end{pmatrix}$$

$$\bar{\mu} = \begin{pmatrix} \mu_{Diel} & 0 & 0 \\ 0 & \mu_{yy}(\omega) & 0 \\ 0 & 0 & \mu_{Diel} \end{pmatrix}$$

$$\bar{\kappa} = \begin{pmatrix} 0 & 0 & 0 \\ 0 & 0 & \kappa_{yz}(\omega) \\ 0 & 0 & 0 \end{pmatrix}$$

$$\begin{aligned} \mu_{yy}(\omega) : \mu_{\infty} &= \mu_0 1.05, \mu_s = \mu_0 0.95, \omega_{\mu} = 2\pi \cdot 8.8 \text{ GHz}, \xi_{\mu} = 0.02 \\ \epsilon_{zz}(\omega) : \epsilon_{\infty} &= \epsilon_0 3.83, \epsilon_s = \epsilon_0 4.19, \omega_{\epsilon} = 2\pi \cdot 8.8 \text{ GHz}, \xi_{\epsilon} = 0.02 \\ \kappa_{yz}(\omega) : \tau_{\kappa} &= 1 \text{ ps}, \omega_{\kappa} = 2\pi \cdot 8.8 \text{ GHz}, \xi_{\kappa} = 0.02 \end{aligned}$$

To compute the transmission I illuminate the radome with a 10 GHz narrowband pulse with a pulse width of $1 \cdot 10^{-10} \text{ s}$. I also take the frequency shift between a unit cell and the metamaterial into account by changing the resonance frequency to 10.3 GHz instead of 8.8 GHz. The results are displayed in Figure 8.11.

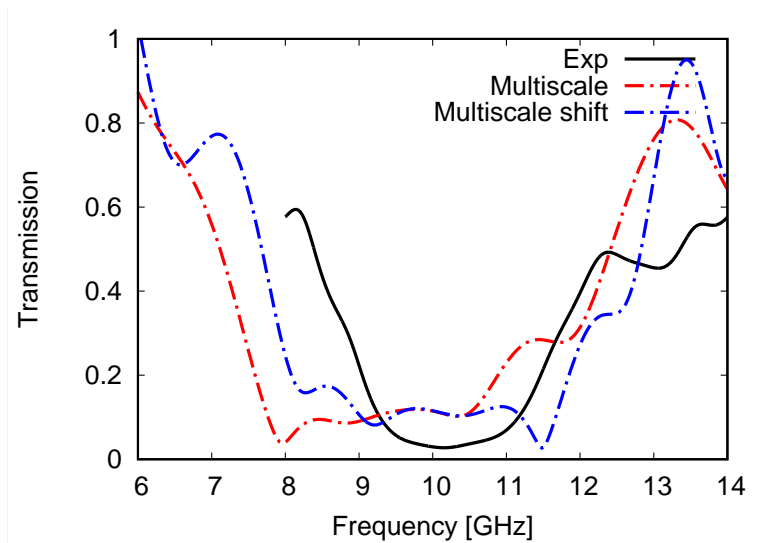


Figure 8.11.: *Experimental vs numerical transmission from direct multiscale approach*

Discussion of the macroscale simulation

Using the UM-FDTD program for bi-anisotropic materials with the material parameters from the direct retrieval method leads to a transmission which agrees reasonably well

with respect to the width of the transmission band compared the experimental data although the bandgap in my simulation is slightly larger compared to the experimental transmission. Due to the periodic arrangement and hence coupling of the resonating elements inside the sample, the position of the bandgap is shifted by a given amount with respect to our simulation of the unit cell.

9. Conclusion and Future Work

In this chapter I analyse all the different methods I developed and highlight the advantages, disadvantages and perspectives for each section

9.1. Isotropic lossy materials

A generalised version of the classical Yee scheme for implementation on hybrid meshes has been considered (UM-FDTD). The results show that it is perfectly suited for all kinds of scattering objects involving arbitrary shaped isotropic lossy dielectrics. To demonstrate this I computed the RCS of several benchmark tests, because the analytical solutions are available for these cases. Independent if a dielectric sphere with losses or a sphere coated with another dielectric is considered, the results agree very well with the theoretical results. My results demonstrate that 6 – 8 times coarser meshes can be used compared to the standard Yee algorithm. This significantly reduces the memory requirements. Furthermore, because the co-volume method is based upon field projections and not vectors only two equations need to be updated, one equation for the electric and one for the magnetic field, although I work in three dimensions. So, by moving the complexity of the algorithm into the mesh I have the simplicity of a 1D code (for isotropic cases) whereas in the classical algorithm one equation for each component of each field vector is required, making a total of six update equations. Besides I showed that my weighted averaging allows me to accurately take into account the interface between different materials. Even the modelling of PEC or multilayered objects becomes straightforward. The ability of the method to handle objects of arbitrary shape at reduced computational costs makes the approach appealing for industrial electromagnetic analysis. However, parallelising the method is required before this goal can be fully realised and the method applied to more challenging engineering applications.

9.2. Anisotropic lossy materials

I further generalised UM-FDTD to model electromagnetic wave scattering by bodies consisting of electrically and magnetically anisotropic and conducting dielectric materials, on an appropriately generated unstructured mesh. The implementation has been successfully validated by comparison with the results obtained using the discrete dipole approximation. Furthermore I compute the transmission of an EM pulse through a composite radome by taking the orientation of the fibers into account. Although good results are obtained, the simplicity of the scheme is lost compared to the isotropic case. Furthermore, the reconstruction of field vectors from field projections to do a matrix vector

9. Conclusion and Future Work

multiplication is time consuming. Therefore these operations should be reduced to a minimum. This method offers however also a big advantage, as it could act as a unstructured PML because my method is able to handle lossy materials. This could significantly reduce the memory requirements of the mesh (especially in three dimensions) because an unstructured PML could be fitted perfectly around an object.

9.3. Isotropic chiral materials

The next step towards bi-anisotropic materials was the modelling of isotropic chiral materials. This was challenging because of two reasons. First of all, the material parameters are not scalars anymore but become frequency dependent complex functions. In contrast to a frequency domain solver, our time domain solver cannot handle this directly. Therefore I used the Z-Transform and Padé approximants to deal with this. Secondly the chirality induces a coupling between the electric and magnetic fields. I validated my algorithm by comparing the numerical transmission and reflection coefficients with the theoretical solutions. Furthermore, the chirality changes the angle of the plane of polarisation and even the polarisation itself of the incident wave. This effect depends upon the chirality, frequency of the incoming wave and the thickness of the slab. The numerical and the analytical solutions agree again very well. I furthermore did a stability analysis of the algorithm because the chirality parameter leads to an instability. Increasing the damping stabilizes it again but care has to be taken because my analysis shows that a finer mesh may be required for chiral materials compared to non-chiral ones.

9.4. Bi-anisotropic materials

The modelling of bi-anisotropic materials was the most challenging task I had because it combines anisotropy, frequency dependence and coupled electric and magnetic fields. Although there exist an analytical solution as a benchmark, I am still working on the implementation of it, which is quite challenging. Meanwhile, to validate the method I model a frequency dependent anisotropic sphere (not bi-anisotropic) and compare my numerically computed RCS solution with the one obtained by DDscat, a program based upon the Discrete Dipole Approximation. My results are in a very good agreement with the results of DDscat. Furthermore, I compared the results of the bi-anisotropic code with those of the isotropic chiral code by assuming diagonal material tensors. In this special case the results of the bi-isotropic and bi-anisotropic simulation are identical as expected.

9.5. Multiscale Approach

Direct multiscale approach

This method has the advantage that no free space region or PML is required compared to the indirect method. This reduces already the computational costs. Furthermore

the effective parameters are directly retrieved from the field vectors. There is no need to first compute the S parameters and then use a retrieval algorithm to compute the material parameters. This is a big advantage because the retrieval algorithm may lead to nonphysical results at some frequencies due to instabilities as can be seen in the results of the indirect multiscale approach. Unfortunately I wasn't able to retrieve a reasonable chirality with my method. This problem needs additional investigation to make it robust. To further improve the direct multiscale approach it would be interesting to test with a chiral structure like a left and right handed spring. It may also be worth to combine four unit cells of the omega material and investigate if this allows me to retrieve the chirality. Furthermore, the resonance frequency I obtain for a unit cell is lower than the resonance frequency observed in the experimental results. This seems to be an effect of the underlying periodicity of the metamaterial at large scale. Additional research is required to take this effect into account. Generally this techniques seems to very promising, but further research has to be done.

Indirect multiscale approach

Although I observed resonance induced phenomena in the material parameters I do not think that this method is currently suitable for a multiscale approach. Mainly because pronounced peaks and dips appear at given frequencies which in my opinion are non-physical. I am not sure if they are caused by the retrieval algorithm itself or by the numerically obtained S-parameters. For the experimental S-parameters I get reasonable results without sharp peaks/dips. Maybe the problem rise because I obtain the S-parameters from a slab with a thickness of a single unit cell. It might be interesting to see what happens if several unit cells are considered.

Macroscale simulation

Using the UM-FDTD program for bi-anisotropic materials with the material parameters from the direct retrieval method I obtain a transmission which agrees reasonably well with the experimental data after correcting the resonance frequency. This demonstrates the great potential of the methods developed during this thesis for predicting the electromagnetic responses of metamaterials in real life applications.

9.6. Experimental setup

Setting up a free space measurement setup from scratch is a challenging task. The right equipment needs to be ordered which significantly depends on the frequency range. The antenna, cable holder needs to be build and the retrieval algorithms to be implemented. A VNA is required as power source, which I borrowed from the university of Luxembourg. The university of Murcia manufactured the focussing mirrors for me and the most difficult part is the calibration of the system. In the end the free space setup meets all the requirements I had and allows me to measure material parameters in the frequency range of interest between $8\text{ GHz} - 18\text{ GHz}$ for isotropic and bi-anisotropic materials. I was

9. Conclusion and Future Work

able to correctly characterise different materials like PMMA and polystyrene of different thicknesses to proof the successful calibration of the setup and working of the retrieval algorithms. I got reasonable results for both isotropic dielectrics and metamaterials. To measure the material parameters of a metamaterial is however much more challenging compared to a normal dielectric. In my opinion there are several possibilities to improve the accuracy of the measurements. First of all I ordered a second mirror which will be placed between the sample and the receiving antenna. This makes my setup symmetric and allows me to refocus the beam after its transmission through the sample and therefore increasing the intensity of the measured signal. As my results demonstrated, if the transmitted power is too low the phase cannot be measured accurately which is the main source of error in the measurement. A symmetric setup furthermore allows me to use a TRL or GRL calibration and to test if they are more accurate as the calibration I use right know. Besides, the VNA (ZVK from Rohde and Schwarz) I used is quit outdated. Therefore I was limited to 1601 measuring points. This may not be enough if I want to measure in a larger frequency band. Because after converting the frequency domain data to the time domain not enough data points may be left for a reasonable time gating. Newer VNAs allow up to 100000 measuring points and higher output powers, significantly increasing the accuracy of the measurements. Another source of error is the sample thickness of a metamaterial because it does not conform to the physical thickness as in the case of a simple dielectric, due to the coupling related effects. To correct this, two samples of different thicknesses are required. Furthermore, as explained the phase ambiguity doesn't occur if the sample thickness is below a given threshold which is furthermore related to the starting frequency, permittivity and permeability. It would be interesting to do the measurement with a slab fabricated out of the same dielectric material as our metamaterial but without the omega inclusions. For metamaterials the effect of time gating needs to be examined in more detail. For an isotropic dielectric, a single Gaussian peak, corresponding to the transmitted or reflected signal, appears in the time domain. In this case it is straightforward to the correct width of the time gate window. For a metamaterial however, several peaks appear and the choice of the width of the window for time gating is less obvious. To conclude, despite all the challenges, the free space setup is suited for the measurements of metamaterials. In my opinion the obtained S parameters are reasonable but the measurement accuracy could still be improved as explained above. The main problem however is to obtain the material parameters from the measured S parameters via the retrieval algorithm, due to its sensitivity to the phase and the numerical instabilities induced at the resonance. It may be interesting to start also for the metamaterial with a very thin sample and then increase the thickness.

Bibliography

- [1] <https://www.microwaves101.com/encyclopedias/438-s-parameters-microwave-encyclopedia-microwaves101-com>.
- [2] <http://www.airbus.com/innovation/proven-concepts/in-design/innovative-materials/>.
- [3] <http://www.premix.com/why-composites/what-composites.php>.
- [4] Measurement of dielectric material properties-application note.
- [5] George A. Baker and P.R. Graves-Morris. *Padé Approximants*. Cambridge university Press, 1996.
- [6] Pekka Alitalo and Sergei Tretyakov. Electromagnetic cloaking with metamaterials. *Materials Today*, 12(3):22–29, mar 2009.
- [7] D.F. Arago. Sur une modification remarquable qu'éprouvent les rayons lumineux dans leur passage à travers certains corps siaphanes, et sur quelques autres autres nouveaux phénomènes d'optique. *Mémoire*, 1:93–134, 1811.
- [8] S. Arslanagic, T. V. Hansen, N. A. Mortensen, A. H. Gregersen, O. Sigmund, R. W. Ziolkowski, and O. Breinbjerg. A review of the scattering-parameter extraction method with clarification of ambiguity issues in relation to metamaterial homogenization. *IEEE Antennas and Propagation Magazine*, 55(2):91–106, apr 2013.
- [9] Akbar Asadi and Ahmad Mohammadi. Fdtd formulation for the general dispersion model using the z transform method. *Mathematica Aeterna*, 4:411–424, 2014.
- [10] Koray Aydin, Zhaofeng Li, Serafettin Bilge, and Ekmel Ozbay. Experimental and numerical study of omega type bianisotropic metamaterials combined with a negative permittivity medium. *Photonics and Nanostructures - Fundamentals and Applications*, 6(1):116–121, apr 2008.
- [11] Koray Aydin, Zhaofeng Li, M Hudlicka, S A Tretyakov, and Ekmel Ozbay. Transmission characteristics of bianisotropic metamaterials based on omega shaped metallic inclusions. *New Journal of Physics*, 9, September 2007.
- [12] Constantine A. Balanis. *Advanced Engineering Electromagnetics*. John Wiley & Sons, 1989.

Bibliography

- [13] Constantine A. Balanis. *Advanced Engineering Electromagnetics*. Wiley: New York, 1989.
- [14] Constantine A. Balanis. *Advanced Engineering Electromagnetics*. Wiley, 1989.
- [15] P.G. Bartley and S.B. Begley. Improved free-space s-parameter calibration. In *2005 IEEE Instrumentation and Measurement Technology Conference Proceedings*. Institute of Electrical & Electronics Engineers (IEEE).
- [16] J. P. Berenger. A perfectly matched layer for free-space simulation in finite-difference computer codes. *Journal of Computational Physics*, 114:185–200, 1994.
- [17] David J. Bergman. Dielectric constant of a two-component granular composite: A practical scheme for calculating the pole spectrum. *Physical Review B*, 19(4):2359–2368, feb 1979.
- [18] J.B. Biot. Sur les rotations que certaines substances impriment aux axes de polarisation des rayons lumineux. *Annales de chimie et de physique*, 10:63–81, 1819.
- [19] D.V. Blackham. Free space characterization of materials. *Antenna Measurements Techniques Association Symposium*, (15):58–60, 1993.
- [20] A. Bossavit and L. Kettunen. Yee-like schemes on a tetrahedral mesh, with diagonal lumping. *International Journal of Numerical Modelling: Electronic Networks, Devices and Fields*, 1999.
- [21] D. A. G. Bruggeman. Berechnung verschiedener physikalischer konstanten von heterogenen substanzen. i. dielektrizitätskonstanten und leitfähigkeiten der mischkörper aus isotropen substanzen. *Annalen der Physik*, 416(7):636–664, 1935.
- [22] V. S. Butylkin and G. A. Kraftmakher. Passbands of bianisotropic and waveguide bianisotropic metamaterials based on planar double split rings. *Journal of Communications Technology and Electronics*, 53(1):1–14, jan 2008.
- [23] V. S. Butylkin and G. A. Kraftmakher. Nonreciprocal effects in propagation of microwaves along a waveguide structure formed from a ferrite plate and a lattice of resonant elements. *Journal of Communications Technology and Electronics*, 54(7):775–782, jul 2009.
- [24] Wenshan Cai and Vladimir Shalaev. *Optical Metamaterials: Fundamentals and Applications*, chapter 9, Transformation Optics and Electromagnetic Cloak of Invisibility, pages 159–195. Springer-Verlag New York, 2010.
- [25] Todd Hubing Changyi Su, Haixin Ke. Overview of electromagnetic modeling software. *25th Annual review of Progress in Applied Computational Electromagnetics*, 2009.

- [26] Lei Chen, Zhen-Ya Lei, Rui Yang, Xiao-Wei Shi, and Jiawei Zhang. Determining the effective electromagnetic parameters of bianisotropic metamaterials with periodic structures. *Progress In Electromagnetics Research M*, 29:79–93, 2013.
- [27] Min-Hung Chen, Bernardo Cockburn, and Fernando Reitich. High-order RKDG methods for computational electromagnetics. *Journal of Scientific Computing*, 22-23(1-3):205–226, jun 2005.
- [28] Xudong Chen, Tomasz M. Grzegorzczak, Bae-Ian Wu, Joe Pacheco, and Jin Au Kong. Robust method to retrieve the constitutive effective parameters of metamaterials. *Physical Review E*, 70(1), jul 2004.
- [29] Alexander H.-D. Cheng and Daisy T. Cheng. Heritage and early history of the boundary element method. *Engineering Analysis with Boundary Elements*, 29(3):268–302, mar 2005.
- [30] Bernardo Cockburn, Fengyan Li, and Chi-Wang Shu. Locally divergence-free discontinuous galerkin methods for the Maxwell equations. *Journal of Computational Physics*, 194(2):588–610, mar 2004.
- [31] Chris Cooke. Understanding the in-flight cell phone ban. <http://www.executivetravelmagazine.com/articles/understanding-the-in-flight-cell-phone-ban>, September 2009.
- [32] R. Courant, K. Friedrichs, and H. Lewy. über die partiellen differenzgleichungen der mathematischen physik. *Mathematische Annalen*, 100(1):32–74, dec 1928.
- [33] Steven A. Cummer, Johan Christensen, and Andrea Alù. Controlling sound with acoustic metamaterials. *Nature Reviews Materials*, 1(3):16001, feb 2016.
- [34] Carlos Henrique da Silva Santos, Marcos Sergio Goncalves, and Hugo Enrique Hernandez-Figueroa. Designing novel photonic devices by bio-inspired computing. *IEEE Photonics Technology Letters*, 22(15):1177–1179, aug 2010.
- [35] David Davidson. *Computational Electromagnetics for RF and Microwave Engineering*. Cambridge University Press, 2005.
- [36] R. W. Davies, K. Morgan, and O. Hassan. A high order hybrid finite element method applied to the solution of electromagnetic wave scattering problems in the time domain. *Computational Mechanics*, 44(3):321–331, feb 2009.
- [37] V. Demir, A.Z. Elsherbeni, and E. Arvas. FDTD formulation for dispersive chiral media using the z transform method. *IEEE Transactions on Antennas and Propagation*, 53(10):3374–3384, oct 2005.
- [38] S. Dey and R. Mittra. A locally conformal finite-difference time-domain (FDTD) algorithm for modeling three-dimensional perfectly conducting objects. *IEEE Microwave and Guided Wave Letters*, 7(9):273–275, 1997.

Bibliography

- [39] Adrian Doicu. Null-field method to electromagnetic scattering from uniaxial anisotropic particles. *Optics Communications*, 218(1-3):11–17, mar 2003.
- [40] Bruce T. Draine and Piotr J. Flatau. Discrete–dipole approximation for scattering calculations. *Journal of the Optical Society of America A*, 11:1491–1499, 1994.
- [41] T. Driscoll, D. N. Basov, W. J. Padilla, J. J. Mock, and D. R. Smith. Electro-magnetic characterization of planar metamaterials by oblique angle spectroscopic measurements. *Physical Review B*, 75(11), mar 2007.
- [42] Qiang Du, Vance Faber, and Max Gunzburger. Centroidal voronoi tessellations: Applications and algorithms. *SIAM Rev.*, 41(4):637–676, jan 1999.
- [43] Frederik Edelvik. *Hybrid Solvers for the Maxwell Equations in Time Domain*. PhD thesis, The Faculty of Science and Technology, Uppsala university, 2002.
- [44] M. El hachemi, O. Hassan, K. Morgan, D. P. Rowse, and N. P. Weatherill. A low-order unstructured mesh approach for computational electromagnetics in the time domain. *Philosophical Transactions of The Royal Society Series A*, 362:445–469, 2004.
- [45] G.V. Eleftheriades and K.G. Balmain. *Negative-Refractive Metamaterials: Fundamental Principles and Applications*. Wiley-IEEE Press, 2005.
- [46] Yuri Eremin. Method of discrete sources in electromagnetic scattering by axially symmetric structures. *Journal of Communications Technology and Electronics*, 45:269–280, 2000.
- [47] Pascal J Frey, Houman Borouchaki, and Paul-Louis George. 3D delaunay mesh generation coupled with an advancing-front approach. *Computer Methods in Applied Mechanics and Engineering*, 157(1-2):115–131, apr 1998.
- [48] A. Gansen, M. El Hachemi, S. Belouettar, O. Hassan, and K. Morgan. An effective 3D leapfrog scheme for electromagnetic modelling of arbitrary shaped dielectric objects using unstructured meshes. *Computational Mechanics*, 56(6):1023–1037, nov 2015.
- [49] A. Gansen, M. El Hachemi, S. Belouettar, O. Hassan, and K. Morgan. EM modelling of arbitrary shaped anisotropic dielectric objects using an efficient 3D leapfrog scheme on unstructured meshes. *Computational Mechanics*, may 2016.
- [50] J. C. M. Garnett. Colours in metal glasses and in metallic films. *Philosophical Transactions of the Royal Society A: Mathematical, Physical and Engineering Sciences*, 203(359-371):385–420, jan 1904.
- [51] S. Gedney, F.S. Lansing, and D.L. Rascoe. Full wave analysis of microwave monolithic circuit devices using a generalized yee-algorithm based on an unstructured grid. *IEEE Transactions on Microwave Theory and Techniques*, 44(8):1393–1400, 1996.

- [52] Jr George A. Baker and Peter Gaves-Morris. *Padé Approximants*. Cambridge University Press, 2nd edition edition, 1996.
- [53] S. Gerschgorin. Fehlerabschätzung für das differenzenverfahren zur lösung partieller differentialgleichungen. *Zeitschrift für Angewandte Mathematik und Mechanik*, 10(4):373–382, 1930.
- [54] D.K. Ghodgaonkar, V.V. Varadan, and V.K. Varadan. A free-space method for measurement of dielectric constants and loss tangents at microwave frequencies. *IEEE Transactions on Instrumentation and Measurement*, 38(3):789–793, jun 1989.
- [55] A. Gomez, A. Lakhtakia, J. Margineda, G.J. Molina-Cuberos, M.J. Nuez, J.A. Saiz Ipina, A. Vegas, and M.A. Solano. Full-wave hybrid technique for 3-D isotropic-chiral-material discontinuities in rectangular waveguides: Theory and experiment. *IEEE Transactions on Microwave Theory and Techniques*, 56(12):2815–2825, dec 2008.
- [56] Victor V Gozhenko, Anthony K Amert, and Keith W Whites. Homogenization of periodic metamaterials by field averaging over unit cell boundaries: use and limitations. *New Journal of Physics*, 15(4):043030, apr 2013.
- [57] Frank Gustrau. Elektromagnetische verträglichkeit. Lecture notes, June 2013.
- [58] K Guven, E Saenz, R Gonzalo, E Ozbay, and S Tretyakov. Electromagnetic cloaking with canonical spiral inclusions. *New Journal of Physics*, 10(11):115037, nov 2008.
- [59] M. E. Hachemi, O. Hassan, K. Morgan, D. Rowse, and N. Weatherill. A low-order unstructured-mesh approach for computational electromagnetics in the time domain. *Philosophical Transactions of the Royal Society A: Mathematical, Physical and Engineering Sciences*, 362(1816):445–469, mar 2004.
- [60] M. El Hachemi, Y. Koutsawa, H. Nasser, G. Giunta, A. Daouadji, E.M. Daya, and S. Belouettar. An intuitive computational multi-scale methodology and tool for the dynamic modelling of viscoelastic composites and structures. *Composite Structures*, 144:131–137, jun 2016.
- [61] Yang Hao and Raj Mittra. *FDTD Modelling of Metamaterials. Theory and Applications*. Artech House, 2009.
- [62] J.S Hesthaven and T Warburton. Nodal high-order methods on unstructured grids. *Journal of Computational Physics*, 181(1):186–221, sep 2002.
- [63] H.Lamb. On group-velocity. *Proceedings London Mathematical Society*, 1:473–479, 1904.
- [64] Tom Hoppin. Fieldfox handheld education series part4: Techniques for precise time domain measurements in the field. Online, january 2013.

Bibliography

- [65] Kyu-Pyung Hwang and A.C. Cangellaris. Effective permittivities for second-order accurate FDTD equations at dielectric interfaces. *IEEE Microwave and Wireless Components Letters*, 11(4):158–160, apr 2001.
- [66] IV.Lindell, A.H.Sihvola, S.A. Tretyakov, and A.J.Viitanen. *Electromagnetic Waves in Chiral and Bi-Isotropic Media*. Artech House, 1994.
- [67] D.L. Jaggard, A.R. Mickelson, and C.H. Papas. On electromagnetic waves in chiral media. *Applied Physics*, 18:211–216, 1979.
- [68] Fritz John. On integration of parabolic equations by difference methods: I. linear and quasi-linear equations for the infinite interval. *Communications on Pure and Applied Mathematics*, 5(2):155–211, may 1952.
- [69] Rose M. Joseph, Susan C. Hagness, and Allen Taflove. Direct time integration of maxwell's equations in linear dispersive media with absorption for scattering and propagation of femtosecond electromagnetic pulses. *Optics Letters*, 16(18):1412, sep 1991.
- [70] Adour V. Kabakian, Vijaya Shankar, and William F. Hall. Unstructured grid-based discontinuous galerkin method for broadband electromagnetic simulations. *Journal of Scientific Computing*, 20(3):405–431, jun 2004.
- [71] Tatsuya Kashiwa and Ichiro Fukai. A treatment by the FD-TD method of the dispersive characteristics associated with electronic polarization. *Microwave and Optical Technology Letters*, 3(6):203–205, jun 1990.
- [72] D.F. Kelley and R.J. Luebbers. Piecewise linear recursive convolution for dispersive media using FDTD. *IEEE Transactions on Antennas and Propagation*, 44(6):792–797, jun 1996.
- [73] K.F.Lindman. über eine durch ein isotropes system von spiralförmigen resonatoren erzeugt rotationspolarisation der eelektromagnetische wellen. *Annalen der Physik*, 63:621–644, 1920.
- [74] T. Koschny, M. Kafesaki, E. N. Economou, and C. M. Soukoulis. Effective medium theory of left-handed materials. *Phys. Rev. Lett.*, 93(10), sep 2004.
- [75] K. Kurokawa. Power waves and the scattering matrix. *IEEE Transactions on Microwave Theory and Techniques*, 13(2):194–202, mar 1965.
- [76] Chen L.F, Ong C.K, Neo C.P, and Varadan V.V. *Microwave Electronics Measurement and Materials Characterization*. John Wiley & Sons, 2004.
- [77] Zhaofeng Li, Koray Aydin, and Ekmel Ozbay. Determination of the effective constitutive parameters of bianisotropic metamaterials from reflection and transmission coefficients. *Physical Review E*, 79(2), feb 2009.

- [78] Zhaofeng Li, Koray Aydin, and Ekmel Ozbay. Retrieval of effective parameters for bianisotropic metamaterials with omega shaped metallic inclusions. *Photonics and Nanostructures - Fundamentals and Applications*, 10(3):329–336, jun 2012.
- [79] Erik Lier, Douglas H. Werner, Clinton P. Scarborough, Qi Wu, and Jeremy A. Bossard. An octave-bandwidth negligible-loss radiofrequency metamaterial. *Nature Materials*, 10(3):216–222, jan 2011.
- [80] Z. Lin and L. Thylen. On the accuracy and stability of several widely used FDTD approaches for modeling lorentz dielectrics. *IEEE Transactions on Antennas and Propagation*, 57(10):3378–3381, oct 2009.
- [81] K.F. Lindman. über die durch ein aktives raumgitter erzeugte rotationspolarisation der elektromagnetischen wellen. *Annalen der Physik*, 69:270–284, 1922.
- [82] D. Lixing and A. R. Sebak. 3D ftd method for arbitrary anisotropic materials. *Microwave and Optical Technology Letters*, 48:2083–2090, 2006.
- [83] L.Pasteur. Sur les relations qui peuvent exister entre la forme cristalline, la composition chimique et le sens de la polarisation rotatoire. *Annales de Chimie et de Physique*, 24:442–459, 1848.
- [84] Tiao Lu, Pingwen Zhang, and Wei Cai. Discontinuous galerkin methods for dispersive and lossy maxwell’s equations and PML boundary conditions. *Journal of Computational Physics*, 200(2):549–580, nov 2004.
- [85] R.J. Luebbers, F. Hunsberger, and K.S. Kunz. A frequency-dependent finite-difference time-domain formulation for transient propagation in plasma. *IEEE Transactions on Antennas and Propagation*, 39(1):29–34, 1991.
- [86] A C Lynch and D Simkin. Measurement of permeability and permittivity of ferrites. *Measurement Science and Technology*, 1(11):1162, 1990.
- [87] Niel K. Madsen. Divergence preserving discrete surface integral methods for maxwell’s curl equations using non-orthogonal unstructured grids. *Journal of Computational Physics*, 119(1):34–45, jun 1995.
- [88] Niel K. Madsen and Richard W. Ziolkowski. A three-dimensional modified finite volume technique for maxwell’s equations. *Electromagnetics*, 10(1-2):147–161, jan 1990.
- [89] Martin Maldovan. Sound and heat revolutions in phononics. *Nature*, 503(7475):209–217, nov 2013.
- [90] J. Margineda, G.J. Molina-Cuberos, M.J. Nunez, A.J. Garcia-Collado, and E. Marti. Electromagnetic characterization of chiral media. In *Solutions and Applications of Scattering, Propagation, Radiation and Emission of Electromagnetic Waves*. InTech, nov 2012.

Bibliography

- [91] K. Morgan, P.J. Brookes, O. Hassan, and N.P. Weatherill. Parallel processing for the simulation of problems involving scattering of electromagnetic waves. *Computer Methods in Applied Mechanics and Engineering*, 152(1-2):157–174, Jan 1998.
- [92] K. Morgan, M. El hachemi, O. Hassan, and N. P. Weatherill. 3D time domain computational electromagnetics using a H^1 finite element method and hybrid unstructured meshes. *Computational Fluid Dynamics Journal*, 13:55–66, 2004.
- [93] David M.Pozar. *Microwave Engineering (4th Edition)*. John Wiley & Sons, 2012.
- [94] J. Munoz, M. Rojo, A. Parrefio, and J. Margineda. Automatic measurement of permittivity and permeability at microwave frequencies using normal and oblique free-wave incidence with focused beam. *IEEE Transactions on Instrumentation and Measurement*, 47(4):886–892, 1998.
- [95] Vahid Nayyeri, Mohammad Soleimani, Jalil Rashed Mohassel, and Mojtaba Dehmollaian. FDTD modeling of dispersive bianisotropic media using z-transform method. *IEEE Transactions on Antennas and Propagation*, 59(6):2268–2279, jun 2011.
- [96] A. M. Nicolson and G. F. Ross. Measurement of the intrinsic properties of materials by time-domain techniques. *IEEE Transactions on Instrumentation and Measurement*, 19(4):377–382, 1970.
- [97] H.. M. Nussenzveig. *Causality and Dispersion Relations*. Academic Press, 1972.
- [98] George G. O'Brien, Morton A. Hyman, and Sidney Kaplan. A study of the numerical solution of partial differential equations. *Journal of Mathematics and Physics*, 29(1-4):223–251, apr 1950.
- [99] Alex Ortner. Metamaterialien untersucht im terahertz nah-und fernfeld. Master's thesis, Albert-Ludwigs Universität Freiburg Fakultät für Mathematik und Physik, Spetember 2010.
- [100] J. B. Pendry, A. J. Holden, W. J. Stewart, and I. Youngs. Extremely low frequency plasmons in metallic mesostructures. *Physical Review Letters*, 76(25):4773–4776, jun 1996.
- [101] J.B. Pendry, A.J. Holden, D.J. Robbins, and W.J. Stewart. Magnetism from conductors and enhanced nonlinear phenomena. *IEEE Transactions on Microwave Theory and Techniques*, 47(11):2075–2084, 1999.
- [102] J Peraire, M Vahdati, K Morgan, and O.C Zienkiewicz. Adaptive remeshing for compressible flow computations. *Journal of Computational Physics*, 72(2):449–466, oct 1987.
- [103] J. Pereda, A. Grande, O. Gonzales, and A. Vegas. FDTD modeling of chiral media by using the mobius transformation technique. *Antennas and Wireless Propagation Letters*, 5(1):327–330, dec 2006.

- [104] W.H. Pickering. Experiment performed at caltech. Private communication, 1945.
- [105] Sergey L Prosvirnin and Nikolay I Zheludev. Analysis of polarization transformations by a planar chiral array of complex-shaped particles. *Journal of Optics A: Pure and Applied Optics*, 11(7):074002, may 2009.
- [106] S. Rikte, G. Kristensson, and M. Andersson. Propagation in bianisotropic media — reflection and transmission. *IEE Proceedings - Microwaves, Antennas and Propagation*, 148(1):29, 2001.
- [107] Leno S Rocha, C Junqueira, Ediana Gambin, Alexandre N Vicente, Ali Eren Culhaoglu, and Erich Kemptner. A free space measurement approach for dielectric material characterization. 2013.
- [108] M Rojo, J Munoz, G J Molina-Cuberos, Ã J Garcia-Collado, and J Margineda. Design of an ellipsoidal mirror for freewave characterization of materials at microwave frequencies. *Measurement Science and Technology*, 27(3):035001, 2016.
- [109] G. Ropars, G. Gorre, A. Le Floch, J. Enoch, and V. Lakshminarayanan. A depolarizer as a possible precise sunstone for viking navigation by polarized skylight. *Proceedings of the Royal Society A: Mathematical, Physical and Engineering Sciences*, 468(2139):671–684, nov 2011.
- [110] Mamdouh M. I. Saadoun and Nader Engheta. A reciprocal phase shifter using novel pseudochiral or omega medium. *Microwave and Optical Technology Letters*, 5(4):184–188, 1992.
- [111] Igor Sazonov, Oubay HAssan, Ken Morgan, and Nigel P. Weatherill. Yee’s scheme for the integration of maxwell’s equation on unstructured meshes. In *European Conference in Computational Fluid Dynamics*, 2006.
- [112] Igor Sazonov, Desheng Wang, Oubay Hassan, Kenneth Morgan, and Nigel Weatherill. A stitching method for the generation of unstructured meshes for use with co-volume solution techniques. *Computer Methods in Applied Mechanics and Engineering*, 195(13-16):1826–1845, feb 2006.
- [113] Vladimir Schmidt and Thomas Wriedt. T-matrix method for biaxial anisotropic particles. *Journal of Quantitative Spectroscopy and Radiative Transfer*, 110(14-16):1392–1397, sep 2009.
- [114] Michael Selvanayagam and George V. Eleftheriades. Experimental demonstration of active electromagnetic cloaking. *Physical Review X*, 3(4), nov 2013.
- [115] Ruben Sevilla, Oubay Hassan, and Kenneth Morgan. The use of hybrid meshes to improve the efficiency of a discontinuous galerkin method for the solution of Maxwell’s equations. *Computers & Structures*, 137:2–13, jun 2014.

Bibliography

- [116] Vijaya Shankar, Alireza H. Mohammadian, and William F. Hall. A time-domain, finite-volume treatment for the Maxwell equations. *Electromagnetics*, 10(1-2):127–145, jan 1990.
- [117] R. A. Shelby, D. R. Smith, S. C. Nemat-Nasser, and S. Schultz. Microwave transmission through a two-dimensional, isotropic, left-handed metamaterial. *Applied Physics Letters*, 78(4):489, 2001.
- [118] Umran S.Inan and Robert A.Marshall. *Numerical Electromagnetics The FDTD Method*. Cambridge University Press, 2011.
- [119] D. Smith, Willie Padilla, D. Vier, S. Nemat-Nasser, and S. Schultz. Composite medium with simultaneously negative permeability and permittivity. *Physical Review Letters*, 84(18):4184–4187, May 2000.
- [120] David R. Smith and John B. Pendry. Homogenization of metamaterials by field averaging (invited paper). *Journal of the Optical Society of America B*, 23(3):391, mar 2006.
- [121] Laslo Solymar and Ekaterina Shamonina. *Waves in Metamaterials*. Oxford University Press, 2009.
- [122] Tao Su, Yongjun Liu, Wenhua Yu, and R. Mittra. A conformal mesh-generating technique for the conformal finite-difference time-domain (CFDTD) method. *IEEE Antennas and Propagation Magazine*, 46(1):37–49, feb 2004.
- [123] D.M. Sullivan. Frequency-dependent FDTD methods using z transforms. *IEEE Transactions on Antennas and Propagation*, 40(10):1223–1230, 1992.
- [124] D.M. Sullivan. Z-transform theory and the FDTD method. *IEEE Transactions on Antennas and Propagation*, 44(1):28–34, 1996.
- [125] A. Taflove, K.R. Umashankar, B. Beker, F. Harfoush, and K.S. Yee. Detailed fd-td analysis of electromagnetic fields penetrating narrow slots and lapped joints in thick conducting screens. *IEEE Transactions on Antennas and Propagation*, 36(2):247–257, 1988.
- [126] Allen Taflove. *Computational Electrodynamics: The Finite-Difference Time-Domain Method*. Artech House: Norwood, MA, 2005.
- [127] Joe F Thompson, Bharat K Soni, and Nigel P Weatherill. *Handbook of grid generation*. CRC press, 1998.
- [128] S. A. Tretyakov, C. R. Simovski, and M. Hudlička. Bianisotropic route to the realization and matching of backward-wave metamaterial slabs. *Physical Review B*, 75(15), apr 2007.

- [129] S.A. Tretyakov, A.H. Sihvola, A.A. Sochava, and C.R. Simovski. Magnetolectric interactions in bi-anisotropic media. *Journal of Electromagnetic Waves and Applications*, 12(4):481–497, jan 1998.
- [130] S.A. Tretyakov and A.A. Sochava. Proposed composite material for nonreflecting shields and antenna radomes. *Electronics Letters*, 29(12):1048, 1993.
- [131] S.A. TS.A. Tretyakov and A. A. Sihvola. Novel uniaxial bianisotropic materials: Reflection and transmission in planar structures. *Progress in Electromagnetics Research*, 9:157–179, 1994.
- [132] Christos Tsironis, Theodoros Samaras, and Loukas Vlahos. Scattered-field FDTD algorithm for hot anisotropic plasma with application to EC heating. *IEEE Transactions on Antennas and Propagation*, 56(9):2988–2994, sep 2008.
- [133] Vasundara V. Varadan and Ruyen Ro. Unique retrieval of complex permittivity and permeability of dispersive materials from reflection and transmitted fields by enforcing causality. *IEEE Transactions on Microwave Theory and Techniques*, 55(10):2224–2230, oct 2007.
- [134] Victor Veselago, Leonid Braginsky, Velery Shklover, and Christian Hafner. Negative refractive index materials. *Journal of Computational and Theoretical Nanoscience*, 3(2):1–30, 2006.
- [135] Viktor G Veselago. The electrodynamics of substances with simultaneously negative values of epsilon and mu. *Soviet Physics Uspekhi*, 10(4):509–514, Apr 1968.
- [136] Henry w. Ott. *Electromagnetic Compatibility Engineering*. John Wiley & Sons, 2009.
- [137] H. Walien, H. Kettunen, Jiaran Qi, and A. Sihvola. Anti-resonant response of resonant inclusions? In *2011 XXXth URSI General Assembly and Scientific Symposium*. Institute of Electrical and Electronics Engineers (IEEE), aug 2011.
- [138] S. Walton, O. Hassan, and K. Morgan. Reduced order mesh optimisation using proper orthogonal decomposition and a modified cuckoo search. *International Journal for Numerical Methods in Engineering*, 93(5):527–550, jul 2012.
- [139] N. P. Weatherill and O. Hassan. Efficient three-dimensional Delaunay triangulation with automatic point creation and imposed boundary constraints. *International Journal for Numerical Methods in Engineering*, 37:2005–2040, 1994.
- [140] William H. Weedon and Carey M. Rappaport. A general method for FDTD modeling of wave propagation in arbitrary frequency-dispersive media. *IEEE Transactions on An*, 45, No 3:401–410, 1997.
- [141] W.B. Weir. Automatic measurement of complex dielectric constant and permeability at microwave frequencies. *Proceedings of the IEEE*, 62(1):33–36, 1974.

Bibliography

- [142] Reed W.H. and Hill T.R. Triangular mesh methods for the neutron transport equation. *Los Alamos National Laboratory*, 1973.
- [143] Dagang Wu, Rui Qiang, J. Chen, Ce Liu, Marina Koledintseva, J. Drewniak, and Bruce Archambeault. Numerical modeling of periodic composite media for electromagnetic shielding application. In *2007 IEEE International Symposium on Electromagnetic Compatibility*. Institute of Electrical and Electronics Engineers (IEEE), jul 2007.
- [144] Z. Q. Xie, O. Hassan, and K. Morgan. Tailoring unstructured meshes for use with a 3D time domain co-volume algorithm for computational electromagnetics. *International Journal for Numerical Methods in Engineering*, 87(1-5):48–65, jul 2010.
- [145] R. Yang, Y.J. Xie, X.F. Li, and J. Jiang. Slow wave propagation in nonradiative dielectric waveguides with bianisotropic split ring resonator metamaterials. *Infrared Physics & Technology*, 51(6):555–558, oct 2008.
- [146] Kane Yee. Numerical solution of initial boundary value problems involving maxwell’s equations in isotropic media. *IEEE Transactions on Antennas and Propagation*, 14(3):302–307, may 1966.
- [147] K.S. Yee and J.S. Chen. Conformal hybrid finite difference time domain and finite volume time domain. *IEEE Transactions on Antennas and Propagation*, 42(10):1450–1455, 1994.
- [148] K.S. Yee and J.S. Chen. The finite-difference time-domain (FDTD) and the finite-volume time-domain (FVTD) methods in solving maxwell’s equations. *IEEE Transactions on Antennas and Propagation*, 45(3):354–363, mar 1997.
- [149] Wenhua Yu and R. Mittra. A conformal finite difference time domain technique for modeling curved dielectric surfaces. *IEEE Microwave and Wireless Components Letters*, 11(1):25–27, jan 2001.
- [150] Xiang Zhang and Zhaowei Liu. Superlenses to overcome the diffraction limit. *Nature Materials*, 7(6):435–441, jun 2008.
- [151] X. Zheng, H. Lee, T. H. Weisgraber, M. Shusteff, J. DeOtte, E. B. Duoss, J. D. Kuntz, M. M. Biener, Q. Ge, J. A. Jackson, S. O. Kucheyev, N. X. Fang, and C. M. Spadaccini. Ultralight, ultrastiff mechanical metamaterials. *Science*, 344(6190):1373–1377, jun 2014.
- [152] O C ZIENKIEWICZ. The stress distribution on gravity dams. *Journal of the Institution of Civil Engineers*, 27(3):244–271, jan 1947.
- [153] Richard W. Ziolkowski and Ehud Heyman. Wave propagation in media having negative permittivity and permeability. *Physical Review E*, 64(5), oct 2001.

A. The Z-Transform

In engineering or physics, a problem may be solved by transforming it from time to frequency space or vice versa. For a linear systems, the relationship between the input and output is a convolution integral in time domain but it reduces to a multiplication in the frequency domain and complicated differential equations in one domain become algebraic equations in another domain. The Laplace, Fourier and Z-transform are all linked to each other. The Z-transform is for example the discrete-time counterpart of the Laplace transform and may be therefore derived from this one. The specific problem defines which transformation is used. An analog signal is a continuous signal representing physical measurements which may be denoted by sine waves, like the human voice or analog electronic devices. In this case, due to the sine wave nature of the signal the Laplace or Fourier transform are applied. A digital signal on the other hand is the translation of information into binary format (zero or one). They represent discrete time signals. In those cases the z-transform is employed.

A.1. Derivation of the z-Transform from the Laplace transform

As mentioned before, the Z-Transform is the discrete-time counterpart of the Laplace transform. The Laplace transform $X(s)$, of a continuous-time signal $x(t)$ is defined as

$$X(s) = \int_0^{\infty} x(t)e^{-st} dt \quad (\text{A.1})$$

where $s = \sigma + j\omega$, $s \in \mathbb{C}$, $\sigma, \omega \in \mathbb{R}$, $x(t) : [0, \infty[\rightarrow \mathbb{C}$. The inverse Laplace transform is defined by

$$x(t) = \lim_{\omega \rightarrow \infty} \int_{\sigma - j\omega}^{\sigma + j\omega} X(s)e^{st} dt$$

where σ is selected so that $X(s)$ has no singularities for $s > \sigma$. Equation (A.1) is discretised by sampling the continuous-time signal $x(t)$ at time steps $t = nT_s$, denoted as $x(n)$. Assuming the sampling period $T_s = 1$, leads to

$$X(e^s) = \sum_{n=0}^{\infty} x(n)z^{-sn}$$

Substituting the variable e^s by z we obtain the one-sided z-transform equation

A. The Z-Transform

Time Domain	Frequency Domain	Z Domain
$f(t)$	$F(\omega)$	$F(z)$
$\delta(t)$	1	$1/T$
$\frac{df(t)}{dt}$	$j\omega F(\omega)$	$\frac{1-z^{-1}}{T}F(z)$
$e^{-\alpha t}u(t)$	$\frac{1}{\alpha+j\omega}$	$\frac{1}{1-e^{-\alpha T}z^{-1}}$
$e^{-\alpha t}\sin(\beta t)u(t)$	$\frac{\beta}{(\alpha^2+\beta^2)+j2\alpha\omega-\omega^2}$	$\frac{Te^{-\alpha T}\sin(\beta T)z^{-1}}{1-2e^{-\alpha T}\cos(\beta T)z^{-1}+e^{-2\alpha T}z^{-2}}$

Table A.1.: Transforming among the time, Frequency and Z Domain, ($\alpha, \beta \in \mathbb{R}$ are constants)

$$X(z) = \sum_{n=0}^{\infty} x(n)z^{-n}$$

The two sided z-transform is defined as

$$X(z) = \sum_{n=-\infty}^{\infty} x(n)z^{-n} \quad (\text{A.2})$$

A.2. Dispersive chiral FDTD Formulation using the Z Transform

I cannot immediately deal with the material parameters because the the FDTD is a time domain method but the material parameters are expressed in the frequency domain. The idea consists in transforming the constitutive equations 2.632.62 from frequency to the z domain and finally from the z to the time domain. Afterwards I can include them in the FDTD updating scheme. A multiplication of frequency-dependent terms will be represented by a convolution in the time domain. In the Z domain however the multiplication of frequency dependent materials remains a multiplication.

$$D(z) = \epsilon(z)E(z)T - \kappa(z)\sqrt{\epsilon_0\mu_0}H(z)T \quad (\text{A.3})$$

$$B(z) = \mu(z)H(z)T + \kappa(z)\sqrt{\epsilon_0\mu_0}E(z)T \quad (\text{A.4})$$

Where $T = \Delta t$ is the period of sampling in the Z domain. It corresponds to half of the time step Δt employed in time domain. $\epsilon(z), \mu(z)$ are the Z transforms of the electric permittivity and amgnetic permeability. $\kappa(z)$ is the Z transform of the time function whose Fourier transform is $j\kappa(\omega)$. Frequency domain values are obtained from the time domain using the Fourier transform defined as

$$f(t) = \frac{1}{\sqrt{2\pi}} \int_{-\infty}^{+\infty} F(\omega) e^{j\omega t} d\omega$$

$$F(\omega) = \frac{1}{\sqrt{2\pi}} \int_{-\infty}^{+\infty} f(t) e^{-j\omega t} dt$$

and Z Domain quantities are obtained using equation (A.2) where $u(t)$ is the step function

$$u(t) = 1, t \geq 0$$

$$= 0, t < 0$$

A.2.1. Definition and Properties of the Z-Transform

In the sampled time domain the function $x(t)$ becomes $x(n)$

$$x(n) = \sum_{n=-\infty}^{+\infty} x(t) \delta(t - nT)$$

where T is a uniform time interval and δ is the Dirac Delta function

$$\delta(t) = 1, t = 0$$

$$= 0 \text{ elsewhere}$$

The Z-Transform is defined by

$$Z[x(n)] = X(z) = \sum_{n=-\infty}^{+\infty} x(n) z^{-n}$$

The z variable may be interpreted as a time delay. This is the fundamental principle I use to go from the z to the time domain for obtaining an FDTD updating scheme. Without a time shift

$$x(m) \rightarrow Z \rightarrow X(z)$$

by definition. Applying a shift $x(m - k)$ I obtain

$$x(m - k) \rightarrow Z \rightarrow z^{-k} X(z) \tag{A.5}$$

Proof:

$$X(z) = \sum_{m=-\infty}^{+\infty} x(m - k) z^{-m} = \sum_{n=-\infty}^{+\infty} x(n) z^{-(n+k)} = z^{-k} \sum_{n=-\infty}^{+\infty} x(n) z^{-n} = z^{-k} X(z)$$

where I used the substitution $m = n + k$

A. The Z-Transform

A.2.2. Examples

The different transformations from one space to another will be illustrated by some examples.

1. $\frac{df(t)}{dt} \rightarrow FT \rightarrow j\omega F(\omega)$

$$\begin{aligned}
 j^n \omega^n F(\omega) &= \frac{j^n}{\sqrt{2\pi}} \int_{-\infty}^{+\infty} f(t) \omega^n e^{-j\omega t} dt \\
 &= \frac{j^n (-j)^{-n}}{\sqrt{2\pi}} \int_{-\infty}^{+\infty} f(t) \frac{d^n e^{-j\omega t}}{dt^n} dt \\
 &= \frac{(-1)^n}{\sqrt{2\pi}} (-1)^n \int_{-\infty}^{+\infty} \frac{d^n f(t)}{dt^n} e^{-j\omega t} dt \\
 &= F\left(\frac{d^n f(t)}{dt^n}\right)(\omega)
 \end{aligned}$$

where n refers to the order of the derivative. To obtain the last line I used an integration by parts. For $n = 1$ I get $F\left(\frac{df(t)}{dt}\right)(\omega) = j\omega F(\omega)$.

2. $\frac{df(t)}{dt} \rightarrow Z - Transform \rightarrow \frac{1-z^{-1}}{T} F(z)$ In the sampled time domain the function $x(t)$ becomes $x(n)$

$$x(n) = \sum_{-\infty}^{+\infty} x(t) \delta(t - nT)$$

where T is a uniform time interval and δ is the Dirac Delta function

$$\begin{aligned}
 \delta(t) &= 1, t = 0 \\
 &= 0 \text{ elsewhere}
 \end{aligned}$$

the Z-Transform is defined by

$$Z[x(n)] = X(z) = \sum_{-\infty}^{+\infty} x(n) z^{-n}$$

e.g if $x(n) = \delta(t) + 0.5\delta(t - 1T) + 0.25\delta(t - 2T)$ the Z-Transform becomes

$$\begin{aligned}
 X(z) &= \sum_{-\infty}^{+\infty} (x(n) = \delta(t) + 0.5\delta(t - 1T) + 0.25\delta(t - 2T)) z^{-n} \\
 &= 1z^{-0} + 0.5z^{-1} + 0.25z^{-2}
 \end{aligned}$$

Going from the time to the sampled time domain the derivative may be approximated by:

$$\frac{dx(t)}{dt} \cong \frac{x[nT] - x[(n-1)T]}{T}$$

A.2. Dispersive chiral FDTD Formulation using the Z Transform

Taking the Z transform of $dx(t)/dt$ and using the time shift property from equation (A.5) I obtain

$$\begin{aligned} Z\left(\frac{dx(t)}{dt}\right) &= \frac{1}{T}(z^{-0}X(z) - z^{-1}X(z)) \\ &= \frac{1 - z^{-1}}{T}X(z) \end{aligned} \quad (\text{A.6})$$

which can be found in the table.

3. $f(t) = e^{-\alpha t}u(t) \rightarrow FT \rightarrow \frac{1}{\alpha + j\omega}$, with $u(t)$ the step function and $\alpha \in \mathbb{R}$ a constant

$$\begin{aligned} F(\omega) &= \int_{-\infty}^{+\infty} f(t)e^{-j\omega t} dt \\ &= \int_{-\infty}^{+\infty} e^{-\alpha t}u(t)e^{-j\omega t} dt \\ &= \int_0^{+\infty} e^{-\alpha t}e^{-j\omega t} dt \\ &= \int_0^{+\infty} e^{-(\alpha + j\omega)t} dt \\ &= \left. \frac{e^{-(\alpha + j\omega)t}}{-(\alpha + j\omega)} \right|_0^{+\infty} \\ &= \frac{1}{\alpha + j\omega} \end{aligned}$$

4. $f(t) = e^{-\alpha t}u(t) \rightarrow Z \rightarrow \frac{1}{1 - e^{-\alpha T}z^{-1}}$, with $u(t)$ the step function and $\alpha \in \mathbb{R}$ a constant

$$\begin{aligned} Z(f(nT)) &= \sum_{n=-\infty}^{+\infty} f(nT)z^{-n} \\ &= \sum_{n=-\infty}^{+\infty} e^{-\alpha nT}u(nT)z^{-n} \\ &= \sum_{n=0}^{+\infty} e^{-\alpha nT}z^{-n} \\ &= \sum_{n=0}^{+\infty} (e^{-\alpha T}z^{-1})^n \\ &= \frac{1}{1 - e^{-\alpha T}z^{-1}} \end{aligned}$$

A. The Z-Transform

where we used

$$\sum_{n=0}^{+\infty} a^{-n} = \frac{1}{1 - a^{-1}}$$

for $a \in \mathbb{R}$ and $a \leq 1$

A.3. Z-Transform of material parameters using an analytical method

The frequency material parameters $\varepsilon(\omega)$, $\mu(\omega)$, $\kappa(\omega)$

$$\begin{aligned}\varepsilon(\omega) &= \varepsilon_\infty + \frac{(\varepsilon_s - \varepsilon_\infty)\omega_e^2}{\omega_e^2 + 2\omega_e\xi_e i\omega - \omega^2} \\ \mu(\omega) &= \mu_\infty + \frac{(\mu_s - \mu_\infty)\omega_h^2}{\omega_h^2 + 2\omega_h\xi_h i\omega - \omega^2} \\ \hat{\kappa}(\omega) &= i\kappa(\omega) = \frac{\tau_k\omega_k^2 i\omega}{\omega_k^2 + 2\omega_k\xi_k i\omega - \omega^2}\end{aligned}$$

will now be transformed from frequency to the Z domain using the relations in table (A.1). First of all I need to bring the electric permittivity and magnetic permeability into the form

$$\frac{\beta}{(\alpha^2 + \beta^2) + j2\alpha\omega - \omega^2}$$

where $\alpha, \beta \in \mathbb{R}$ are constants. Afterwards I can use Table A.1. To achieve this we define $\beta = \omega_i\sqrt{1 - \xi_i^2}$, $\alpha = \omega_i\xi_i$ with $i = \varepsilon, \mu$ depending for $\mu(\omega)$ or $\varepsilon(\omega)$ respectively, leading to

$$\frac{\omega_i^2}{\omega_i^2 + j2\omega_i\omega - \omega^2} = \frac{\omega_i}{\sqrt{1 - \xi_i^2}} \frac{\omega_i\sqrt{1 - \xi_i^2}}{(\omega_i^2\xi_i^2 + \omega_i^2(1 - \xi_i^2)) + j2\omega_i\xi_i\omega - \omega^2}$$

after rewriting

$$\begin{aligned}\varepsilon(\omega) &= \varepsilon_\infty + (\varepsilon_s - \varepsilon_\infty) \frac{\omega_\varepsilon}{\sqrt{1 - \xi_\varepsilon^2}} \frac{\omega_\varepsilon\sqrt{1 - \xi_\varepsilon^2}}{(\omega_\varepsilon^2\xi_\varepsilon^2 + \omega_\varepsilon^2(1 - \xi_\varepsilon^2)) + j2\omega_\varepsilon\xi_\varepsilon\omega - \omega^2} \\ \mu(\omega) &= \mu_\infty + (\mu_s - \mu_\infty) \frac{\omega_\mu}{\sqrt{1 - \xi_\mu^2}} \frac{\omega_\mu\sqrt{1 - \xi_\mu^2}}{(\omega_\mu^2\xi_\mu^2 + \omega_\mu^2(1 - \xi_\mu^2)) + j2\omega_\mu\xi_\mu\omega - \omega^2} \\ j\kappa(\omega) &= j\omega \frac{\tau_k\omega_k}{\sqrt{1 - \xi_k^2}} \frac{\omega_k\sqrt{1 - \xi_k^2}}{(\omega_k^2\xi_k^2 + \omega_k^2(1 - \xi_k^2)) + j2\omega_k\xi_k\omega - \omega^2}\end{aligned}$$

A.3. Z-Transform of material parameters using an analytical method

in the Z-Domain I get

$$\begin{aligned}\varepsilon(z) &= \frac{\varepsilon_\infty}{T} + \frac{(\varepsilon_s - \varepsilon_\infty)\omega_\varepsilon}{\sqrt{1 - \xi_\varepsilon^2}} \times \frac{e^{-\omega_\varepsilon \xi_\varepsilon T} \sin(\omega_\varepsilon \sqrt{1 - \xi_\varepsilon^2} T) \cdot z^{-1}}{1 - 2e^{-\omega_\varepsilon \xi_\varepsilon T} \cos(\omega_\varepsilon \sqrt{1 - \xi_\varepsilon^2} T) \cdot z^{-1} + e^{-2\omega_\varepsilon \xi_\varepsilon T} \cdot z^{-2}} \\ \mu(z) &= \frac{\mu_\infty}{T} + \frac{(\mu_s - \mu_\infty)\omega_\mu}{\sqrt{1 - \xi_\mu^2}} \times \frac{e^{-\omega_\mu \xi_\mu T} \sin(\omega_\mu \sqrt{1 - \xi_\mu^2} T) \cdot z^{-1}}{1 - 2e^{-\omega_\mu \xi_\mu T} \cos(\omega_\mu \sqrt{1 - \xi_\mu^2} T) \cdot z^{-1} + e^{-2\omega_\mu \xi_\mu T} \cdot z^{-2}} \\ \kappa(z) &= \frac{(1 - z^{-1})}{T} \frac{\tau_\kappa \omega_\kappa}{\sqrt{1 - \xi_\kappa^2}} \times \frac{e^{-\omega_\kappa \xi_\kappa T} \sin(\omega_\kappa \sqrt{1 - \xi_\kappa^2} T) \cdot z^{-1}}{1 - 2e^{-\omega_\kappa \xi_\kappa T} \cos(\omega_\kappa \sqrt{1 - \xi_\kappa^2} T) \cdot z^{-1} + e^{-2\omega_\kappa \xi_\kappa T} \cdot z^{-2}}\end{aligned}$$

$\kappa(z)$ is the Z transform of $j\kappa(\omega)$. Whereas $\varepsilon(z)$ and $\mu(z)$ are the Z transforms of $\varepsilon(\omega)$, $\mu(\omega)$. In contrast to $\varepsilon(z)$ and $\mu(z)$ in $\kappa(z)$ the factor $(1 - z^{-1})/T$ appears due to $j\omega$. Using the following definitions I can simplify equations A.3A.4

$$\begin{aligned}C_{\kappa 1} &= \frac{\tau_\kappa \omega_\kappa e^{-\omega_\kappa \xi_\kappa T} \sin(\omega_\kappa \sqrt{1 - \xi_\kappa^2} T) \sqrt{\epsilon_0 \mu_0}}{\sqrt{1 - \xi_\kappa^2}} \\ C_{\kappa 2} &= 2e^{-\omega_\kappa \xi_\kappa T} \cos(\omega_\kappa \sqrt{1 - \xi_\kappa^2} T) \\ C_{\kappa 3} &= e^{-\omega_\kappa \xi_\kappa T} \\ C_{\varepsilon 1} &= \frac{T(\varepsilon_s - \varepsilon_\infty)\omega_\varepsilon e^{-\omega_\varepsilon \xi_\varepsilon T} \sin(\omega_\varepsilon \sqrt{1 - \xi_\varepsilon^2} T)}{\sqrt{1 - \xi_\varepsilon^2}} \\ C_{\varepsilon 2} &= 2e^{-\omega_\varepsilon \xi_\varepsilon T} \cos(\omega_\varepsilon \sqrt{1 - \xi_\varepsilon^2} T) \\ C_{\varepsilon 3} &= e^{-2\omega_\varepsilon \xi_\varepsilon T} \\ C_{\mu 1} &= \frac{T(\mu_s - \mu_\infty)\omega_\mu e^{-\omega_\mu \xi_\mu T} \sin(\omega_\mu \sqrt{1 - \xi_\mu^2} T)}{\sqrt{1 - \xi_\mu^2}} \\ C_{\mu 2} &= 2e^{-\omega_\mu \xi_\mu T} \cos(\omega_\mu \sqrt{1 - \xi_\mu^2} T) \\ C_{\mu 3} &= e^{-2\omega_\mu \xi_\mu T}\end{aligned}$$

to

$$D(z) = \left(\varepsilon_\infty + \frac{C_{\varepsilon 1} z^{-1}}{1 - C_{\varepsilon 2} z^{-1} + C_{\varepsilon 3} z^{-2}} \right) E(z) - \frac{C_{\kappa 1} z^{-1} - C_{\kappa 1} z^{-2}}{1 - C_{\kappa 2} z^{-1} + C_{\kappa 3} z^{-2}} H(z) \quad (\text{A.7})$$

$$B(z) = \left(\mu_\infty + \frac{C_{\mu 1} z^{-1}}{1 - C_{\mu 2} z^{-1} + C_{\mu 3} z^{-2}} \right) H(z) + \frac{C_{\kappa 1} z^{-1} - C_{\kappa 1} z^{-2}}{1 - C_{\kappa 2} z^{-1} + C_{\kappa 3} z^{-2}} E(z) \quad (\text{A.8})$$

A. The Z-Transform

To further simplify the constitutive equations we now introduce the four new parameters $S_{\kappa e}(z)$, $S_{\kappa h}(z)$, $S_h(z)$, $S_e(z)$ and rewrite (A.7),(A.8) as

$$\begin{aligned} \mathbf{D}(z) &= \varepsilon_\infty E(z) + S_e(z)z^{-1} - S_{\kappa h}(z)z^{-1} + S_{\kappa h}(z)z^{-2} \\ \mathbf{B}(z) &= \mu_\infty H(z) + S_h(z)z^{-1} + S_{\kappa e}(z)z^{-1} - S_{\kappa e}(z)z^{-2} \end{aligned}$$

A.4. Z-Transform using padé approximants

The idea of padé approximants is to expand a function (in my case $\varepsilon(z)$, $\mu(z)$, $\kappa(z)$) as a ratio of two power series. This method is superior to a standard Taylor series expansion when the function contains poles [5].

$$\frac{\varepsilon(\mathbf{r}, z)}{\varepsilon_0} = \frac{b_0(\mathbf{r}) + b_1(\mathbf{r})z^{-1} + b_2(\mathbf{r})z^{-2} + \dots + b_{N_b-1}(\mathbf{r})z^{-(N_b-1)}}{1 + a_1(\mathbf{r})z^{-1} + a_2(\mathbf{r})z^{-2} + \dots + a_{N_a}(\mathbf{r})z^{-N_a}} \quad (\text{A.9})$$

This methods leads directly to a finite difference implementation. To illustrate this I consider a second order approximation (z^{-2}) as done in [140]. Using the consitutive relation in Z Domain $D(\mathbf{r}, z) = \varepsilon(\mathbf{r}, z)E(\mathbf{r}, z)$, equation (A.9) and omitting the spatial dependence of the field and pade coefficients I obtain

$$\begin{aligned} \varepsilon_0 D(z) &= \varepsilon(z)E(z) \\ \Leftrightarrow \frac{1}{\varepsilon_0} D(z) &= \frac{b_0 + b_1 z^{-1} + b_2 z^{-2}}{1 + a_1 z^{-1} + a_2 z^{-2}} E(z) \\ \Leftrightarrow E(z) &= \frac{1}{b_0} \left\{ \frac{1}{\varepsilon_0} [D(z) + a_1 z^{-1} D(z) + a_2 z^{-2} D(z)] - b_1 z^{-1} E(z) - b_2 z^{-2} E(z) \right\} \end{aligned}$$

To go from the Z to the time domain we use the property A.5 leading to the final update equation

$$E^{n+1} = \frac{1}{b_0} \left\{ \frac{1}{\varepsilon_0} [D^{n+1} + a_1 D^n + a_2 D^{n-1}] - b_1 E^n - b_2 E^{n-1} \right\}$$

this can be implemented more efficiently reducing the number of storage arrays from five to four using the transposed direct Form-2 structure as known from signal processing literature.

$$\begin{aligned} E^{n+1} &= \frac{1}{b_0} \left[\frac{1}{\varepsilon_0} D^{n+1} + W_1^n \right] \\ W_1^{n+1} &= \frac{a_1}{\varepsilon_0} D^{n+1} - b_1 E^{n+1} + W_2^n \\ W_2^{n+1} &= \frac{a_2}{\varepsilon_0} D^{n+1} - b_2 E^{n+1} \end{aligned}$$

The only remaining question is how to obtain the padé coefficients in Z domain from the coefficients in frequency domain.

A.4.1. Obtaining Padé coefficients

There exist several more or less accurate methods to obtain these coefficients. using approximations I can go directly from frequency to Z-domain. If the fourier transform F is defined as $F[f(t)] = F(\omega)$ then $F\left[\frac{df(t)}{dt}\right] = j\omega F(\omega)$. I can approximate a derivative as $\frac{df(t)}{dt} \simeq \frac{f(t)-f(t-\Delta t)}{\Delta t}$. Taking the Z transform leads to

$$Z\left[\frac{f(t)-f(t-\Delta t)}{\Delta t}\right] = \frac{F(z)-z^{-1}F(z)}{\Delta t} = \frac{1-z^{-1}}{\Delta t}F(z)$$

which is the same result as A.6. As an approximation we can go from the frequency to the Z domain by replacing $j\omega$ by $(1-z^{-1})/\Delta t$. This specific transformation is called Backward Difference approximation. More accurate results can be obtained by replacing $j\omega$ by $(2(1-z^{-1})) / (\Delta t(1+z^{-1}))$. This is called the bilinear transformation and is equivalent to using a trapezoidal approximation to a derivative[9]. To obtain the coefficients we consider the function we want to transform e.g $\epsilon(\omega) = \epsilon_\infty + \frac{(\epsilon_s - \epsilon_\infty)\omega_\epsilon^2}{\omega_\epsilon^2 + (j\omega)^2 + j2\omega_\epsilon\xi_\epsilon\omega}$. For simplicity I choose the Backward Difference approximation $j\omega \rightarrow (1-z^{-1})/\Delta t$ and rearrange the terms with respect to the order of z leading to

$$\begin{aligned} \epsilon(z) &= \frac{(\Delta t^2 \epsilon_s \omega_\epsilon^2 + 2\epsilon_\infty \omega_\epsilon \xi_\epsilon \Delta t + \epsilon_\infty) + (-2\epsilon_\infty \omega_\epsilon \Delta t - 2\epsilon_\infty)z^{-1} + \epsilon_\infty z^{-2}}{(\omega_\epsilon^2 \Delta t^2 + 2\omega_\epsilon \xi_\epsilon \Delta t + 1) + (-2\omega_\epsilon \xi_\epsilon \Delta t - 2)z^{-1} + z^{-2}} \\ &= \frac{(\Delta t^2 \epsilon_s \omega_\epsilon^2 + 2\epsilon_\infty \omega_\epsilon \xi_\epsilon \Delta t + \epsilon_\infty)}{(\omega_\epsilon^2 \Delta t^2 + 2\omega_\epsilon \xi_\epsilon \Delta t + 1)} + \frac{(-2\epsilon_\infty \omega_\epsilon \Delta t - 2\epsilon_\infty)}{(\omega_\epsilon^2 \Delta t^2 + 2\omega_\epsilon \xi_\epsilon \Delta t + 1)} z^{-1} + \frac{\epsilon_\infty}{(\omega_\epsilon^2 \Delta t^2 + 2\omega_\epsilon \xi_\epsilon \Delta t + 1)} z^{-2} \end{aligned} \quad (\text{A.10})$$

$$\begin{aligned} &= \frac{1 + \frac{(-2\omega_\epsilon \xi_\epsilon \Delta t - 2)}{(\omega_\epsilon^2 \Delta t^2 + 2\omega_\epsilon \xi_\epsilon \Delta t + 1)} z^{-1} + \frac{1}{(\omega_\epsilon^2 \Delta t^2 + 2\omega_\epsilon \xi_\epsilon \Delta t + 1)} z^{-2}}{1 + a_1 z^{-1} + a_2 z^{-2}} \\ &= \frac{b_0 + b_1 z^{-1} + b_2 z^{-2}}{1 + a_1 z^{-1} + a_2 z^{-2}} \end{aligned} \quad (\text{A.11})$$

Comparing the coefficients from equations (A.10) and (A.11) gives us the coefficients b_0, b_1, b_2, a_1, a_2 with respect to parameters from $\epsilon(\omega)$. In literature another method is also used, which I explain for completeness. For more details please refer to [52]. First, approximate a function f using the Taylor Series

$$\begin{aligned} T[f(x, a)] &= \sum_{n=0}^{\infty} \frac{f^{(n)}(a)}{n!} (x-a)^n \\ &= f^{(0)}(a) (x-a)^0 + f^{(1)}(a) (x-a)^1 + \frac{f^{(2)}(a)}{2!} (x-a)^2 \dots \end{aligned}$$

Where $f^{(n)} = \frac{df^n}{dx}$. Setting $a = 0$, $f^{(n)} = f_n$ and replacing x^n by z^{-n} leads to

$$T[f(z)] = f_0 + f_1 z^{-1} + f_2 z^{-2} + \dots$$

In the next step we express the function we want to approximate (e.g $\epsilon(\omega)$) as ratio of two polynomials of order L and M respectively

$$Fa(z) = \frac{b_0 + b_1 z^{-1} + b_2 z^{-2} + \dots + b_L z^{-L}}{a_0 + a_1 z^{-1} + a_2 z^{-2} + \dots + a_M z^{-M}}$$

A. The Z-Transform

where $a_0 := 1$. Solving the system

$$\begin{aligned}
 f(z) &= Fa(z) \\
 \Leftrightarrow f_0 + f_1z^{-1} + f_2z^{-2} + \dots &= \frac{b_0 + b_1z^{-1} + b_2z^{-2} + \dots + b_Lz^{-L}}{a_0 + az_1^{-1} + a_2z^{-2} + \dots + a_Mz^{-M}} \\
 \Leftrightarrow (f_0 + f_1z^{-1} + f_2z^{-2} + \dots) \cdot \\
 (a_0 + az_1^{-1} + a_2z^{-2} + \dots + a_Mz^{-M}) &= b_0 + b_1z^{-1} + b_2z^{-2} + \dots + b_Lz^{-L}
 \end{aligned}$$

Equating the coefficients from $z^{-(L+1)}, \dots, z^{-(L+M)}$ leads to the following system of equations

$$\begin{aligned}
 a_M f_{L-M+1} + a_{M-1} f_{L-M+2} + \dots + a_0 f_{L+1} &= 0 \\
 a_M f_{L-M+2} + a_{M-1} f_{L-M+3} + \dots + a_0 f_{L+2} &= 0 \\
 &\vdots \\
 a_M f_L + a_{M-1} f_{L+1} + \dots + a_0 f_{L+M} &= 0
 \end{aligned} \tag{A.12}$$

Equating the coefficients 1, z^{-L} leads to

$$\begin{aligned}
 b_0 &= f_0 \\
 b_1 &= f_1 + a_1 f_0 \\
 b_2 &= f_2 + a_1 f_1 + a_2 f_0 \\
 &\vdots \\
 b_L &= f_L + \sum_{i=1}^{\min(L,M)} a_i f_{L-i}
 \end{aligned} \tag{A.13}$$

As simple example for illustrating the method I calculate the Padé approximants for the permittivity linked to the Debye Model

$$\varepsilon(\omega) = \varepsilon_\infty + \frac{(\varepsilon_s - \varepsilon_\infty)}{1 + j\omega\tau}$$

First I apply the bilinear transformation $j\omega \rightarrow \frac{2}{\Delta t} \left(\frac{1-z^{-1}}{1+z^{-1}} \right)$ to $\varepsilon(\omega)$ to go to the Z-Domain, leading to

$$\varepsilon(z) = \frac{2\varepsilon_\infty\tau - 2\varepsilon_\infty\tau z^{-1} + \varepsilon_s\Delta t z^{-1}}{\Delta t + \Delta t z^{-1} + 2\tau - 2\tau z^{-1}}$$

Calculating the coefficients for the second order Taylor expansion

$$\begin{aligned}
 f_0 = \varepsilon(z^{-1})|_{z^{-1}=0} &= \frac{2\varepsilon_\infty\tau + \varepsilon_s\Delta t}{\Delta t + 2\tau} \\
 f_1 = \frac{\partial \varepsilon}{\partial z^{-1}}|_{z^{-1}=0} &= \frac{4\tau\Delta t(\varepsilon_s - \varepsilon_\infty)}{(\Delta t + 2\tau)^2} \\
 2f_2 = \frac{\partial^2 \varepsilon}{\partial (z^{-1})^2}|_{z^{-1}=0} &= \frac{8(\varepsilon_\infty - \varepsilon_s)(\Delta t^2\tau - 2\Delta t\tau^2)}{(\Delta t + 2\tau)^2}
 \end{aligned}$$

A.4. Z-Transform using padé approximants

I first have to solve the system of equations (A.12)

$$a_1 f_1 + a_0 f_0 = 0$$

Keep in mind that $a_0 := 1$. Leading to

$$a_1 = -\frac{f_2}{f_1} = \frac{(\Delta t - 2\tau)}{(\Delta t + 2\tau)}$$

Now I can solve the system of equations (A.13)

$$\begin{aligned} b_0 &= f_0 \\ b_1 &= f_1 + a_1 f_0 \end{aligned}$$

leading to

$$\begin{aligned} b_0 &= \frac{2\varepsilon_\infty \tau + \varepsilon_s \Delta t}{\Delta t + 2\tau} \\ b_1 &= \frac{\varepsilon_s \Delta t - 2\varepsilon_\infty \tau}{\Delta t + 2\tau} \end{aligned}$$

B. Finite Differences

The differential maxwell equations are approximated by finite difference equations. This procedure is based upon the taylor expansion. For a function $f(x) = f(x_0+h)$ the Taylor expansion is

$$f(x) = f(x_0 + h) = \sum_{n=0}^{\infty} f^{(n)}(x_0) \frac{h^n}{n!} = f(x_0) + \frac{\partial}{\partial x} f(x)|_{x=x_0} h + \frac{\partial^2}{\partial x^2} f(x)|_{x=x_0} h^2 + \dots$$

For this chapter n corresponds to the index in time (after discretization) and i for the index in space (after discretization). The Taylor series expansion in time (n) around the grid point (i,n) with $\Delta t = t^{n+1} - t^n$ is:

$$\begin{aligned} f_i^{n+1} &= f_i^n + \Delta t \frac{\partial f}{\partial t} \Big|_i^n + \frac{1}{2} (\Delta t)^2 \frac{\partial^2 f}{\partial t^2} \Big|_i^n + \dots \\ \Leftrightarrow \frac{\partial f}{\partial t} \Big|_i^n &= \frac{f_i^{n+1} - f_i^n}{\Delta t} - \frac{1}{2} \Delta t \frac{\partial^2 f}{\partial t^2} \Big|_i^n - \dots \end{aligned}$$

The second term on the right side is of first-order, because it only depends on Δt . This means that the error increases linearly with Δt . By dropping the error terms we get the First-order forward difference

$$\frac{\partial f}{\partial t} \Big|_i^n \simeq \frac{f_i^{n+1} - f_i^n}{\Delta t} \quad (\text{B.1})$$

To approximate the first derivative with second order precision we expand f_i^{n+1} and f_i^{n-1} around the grid point (i,n)

$$f_i^{n+1} = f_i^n + \Delta t \frac{\partial f}{\partial t} \Big|_i^n + \frac{1}{2} (\Delta t)^2 \frac{\partial^2 f}{\partial t^2} \Big|_i^n + \frac{1}{6} (\Delta t)^3 \frac{\partial^3 f}{\partial t^3} \Big|_i^n \quad (\text{B.2})$$

$$f_i^{n-1} = f_i^n - \Delta t \frac{\partial f}{\partial t} \Big|_i^n + \frac{1}{2} (\Delta t)^2 \frac{\partial^2 f}{\partial t^2} \Big|_i^n - \frac{1}{6} (\Delta t)^3 \frac{\partial^3 f}{\partial t^3} \Big|_i^n \quad (\text{B.3})$$

Subtracting B.3 from B.2 and dropping the error terms we find the Second-order centered difference

$$\frac{\partial f}{\partial t} \Big|_i^n \simeq \frac{f_i^{n+1} - f_i^{n-1}}{2\Delta t} \quad (\text{B.4})$$

approximating the first derivative. The problem is that in this equation we need to know the value of the function at time step $n+1$ and $n-1$. In the interleaved leapfrog algorithm it is for example necessary to define intermediate values of the derivative at

B. Finite Differences

half time/space steps. If we approximate f_i^{n+1} and f_i^n around the grid point $(i, n + \frac{1}{2})$ we get:

$$f_i^{n+1} = f_i^{n+\frac{1}{2}} + \frac{\Delta t}{2} \frac{\partial f}{\partial t} \Big|_i^{n+\frac{1}{2}} + \frac{\Delta t^2}{4} \frac{\partial^2 f}{\partial t^2} \Big|_i^{n+\frac{1}{2}} + \frac{\Delta t^3}{48} \frac{\partial^3 f}{\partial t^3} \Big|_i^{n+\frac{1}{2}} \quad (\text{B.5})$$

$$f_i^n = f_i^{n+\frac{1}{2}} - \frac{\Delta t}{2} \frac{\partial f}{\partial t} \Big|_i^{n+\frac{1}{2}} + \frac{\Delta t^2}{4} \frac{\partial^2 f}{\partial t^2} \Big|_i^{n+\frac{1}{2}} - \frac{\Delta t^3}{48} \frac{\partial^3 f}{\partial t^3} \Big|_i^{n+\frac{1}{2}} \quad (\text{B.6})$$

Subtracting B.6 from B.5 leads to a second order difference

$$\frac{\partial f}{\partial t} \Big|_i^{n+\frac{1}{2}} \simeq \frac{f_i^{n+1} - f_i^n}{\Delta t} \quad (\text{B.7})$$

We notice that even if the right hand side of B.7 is equal to the right hand side of B.1, B.7 is second order accurate for an approximation of the first order derivative at an half-time step. Until now we only considered temporal discretization. We get similar results for the spatial discretization. In this case, the temporal step n stays constant and we advance the spatial increment i . If we furthermore replace in the formulas above the temporal step width Δt by the spatial step width Δx we have the spatial finite differences.

C. Phase unwrapping

To determine m from equation 6.21, measurements of two samples with different thicknesses have to be done. This may be a problem for expensive samples. One common approach to solve this ambiguity problem is by applying a Kramer-Kronig relations to the wavenumber [133]. A Kramers-Kronig type of relation is a bidirectional relation connecting the real and imaginary parts of any complex function that is analytic in the upper half-plane \mathbb{H} . Where the upper half-plane is defined as the set of complex numbers with positive imaginary part ($\mathbb{H} = \alpha + i\beta | \beta > 0; \alpha, \beta \in \mathbb{R}$). For a causal medium, m can be chosen uniquely because for an analytic function of frequency $\rho = \alpha + i\beta$ this results in a Kramers-Kronig-type relation between α and β . Causality refers to a system where the output $y(t_0)$ only depends on the input $x(t)$ for values $t \leq t_0$ (past and current but not future inputs). The Kramers-Kronig relation which allows me to compute the real part of the complex wavenumber β from the attenuation factor α corresponds to

$$\frac{\beta_{K-K}(\omega)}{\beta_0(\omega)} = 1 + \frac{2}{\pi} P \int_0^{\infty} \frac{\omega_1 \alpha(\omega_1) / \beta_0(\omega_1)}{\omega_1^2 - \omega^2} d\omega_1 \quad (\text{C.1})$$

where $\beta_0 = 2\pi/\lambda_0$ is the free-space wavenumber. P denotes the principal value of the integral. Which is defined as

$$P \int_{-\infty}^{+\infty} f(x) dx = \lim_{R \rightarrow \infty} \int_{-R}^{+R} f(x) dx \quad (\text{C.2})$$

$$P \int_a^b f(x) dx = \lim_{r \rightarrow 0^+} \left[\int_a^{c-r} f(x) dx + \int_{c+r}^b f(x) dx \right] \quad (\text{C.3})$$

for an interval $I = [a, b], a, b \in \mathbb{R}, c \in I, c \in \mathbb{R}$. In equation (C.1) the domain extends from $[0, +\infty]$ but we only have a finite bandwidth data. This leads to truncation errors especially at the band edge [101][97]. Fortunately the results can still yield reasonable agreement with the actual data [97]. This method is employed by numerically solving equation (C.1) for example by using the trapezoidal rule with α retrieved from equation (6.22). Next β_m from equation (6.22) is computed for different m and compared with β_{K-K} from equation (C.1). Only one value of m will match with β_{K-K} . To illustrate the effect of the phase ambiguity we consider an example of an isotropic dielectric slab in free space with a given thickness $d = 0.1m$ and $\varepsilon_r = 2.0 + i0$ and $\mu_r = 1.0 + i0$ over frequency range from $[0 - 8.5] GHz$. To make the problem as realistic as possible I first

C. Phase unwrapping

create a “touchstone” file. Where the S-parameters are computed according to Arslanagic [8].

$$S_{11} = \frac{(1 - Z^2)(\eta^2 - \eta_0^2)}{(\eta + \eta_0)^2 - (\eta - \eta_0)^2 Z^2} \quad (\text{C.4})$$

$$S_{21} = \frac{4\eta\eta_0 Z}{(\eta + \eta_0)^2 - (\eta - \eta_0)^2 Z^2} \quad (\text{C.5})$$

with $\eta = \sqrt{\mu/\varepsilon}$ the impedance inside the dielectric, η_0 , the impedance of free space and $Z = e^{-ikd}$, with d the thickness of the slab and $k = \omega^2\varepsilon\mu$ the wavevector. For an isotropic material we assume $S_{11} = S_{22}$ and $S_{21} = S_{12}$. These parameters are complex in general. Next we use the NRW procedure to extract the material parameters. At a frequency of 8.5GHz the wavelength in the dielectric equals $\lambda_{Diel}(8.5\text{GHz}) = \lambda_0/\sqrt{\varepsilon\mu} = 0.0375/1.41 \approx 0.0265\text{m}$. This is about four times smaller than the sample and therefore the condition that m of equation (6.21) equals 0 over the whole frequency range is not fulfilled. What happens if we nevertheless keep $m = 0$ for a frequency varying from $[0 - 8.5]\text{GHz}$ is illustrated in Figure C.1a. The permittivity differs significantly from what we expect. The origin of this problem becomes clear by considering the phase of the transmission coefficient T , which can be computed as $\phi = \text{atan}(T''/T')$ represented in Figure C.1b.

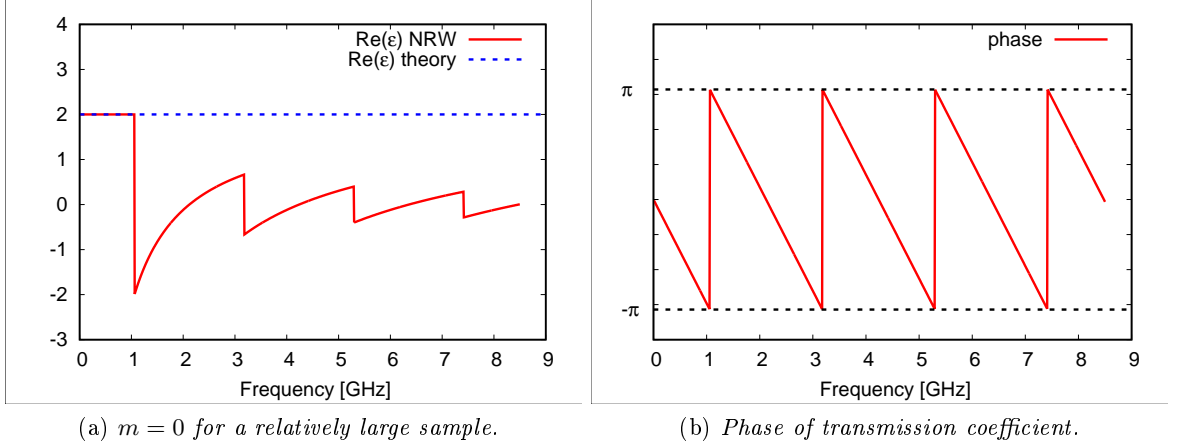


Figure C.1.

The jumps in the retrieved permittivity occur at the same frequencies as the jumps in the phase of the transmission, oscillating between $\pm\pi$. The phase is referred to as wrapped. Unwrapping the phase allows us to solve the ambiguity issue [76]. This procedure is called phase unwrapping and is an easy to implement alternative to the Kramers-Kronig relation method, which still may be used to validate the initial value of m . Therefore we increment m by 1, $m \rightarrow m + 1$ over the bandwidth everytime we detect a jump in the

phase. We then use this new value of m for further calculation of the permittivity and permeability. The difference between the wrapped and unwrapped phase is illustrated in Figure C.2b. The effect of the unwrapping on the permittivity is shown in Figure C.2a. Now we observe the expected agreement between the theoretical and retrieved permittivity.

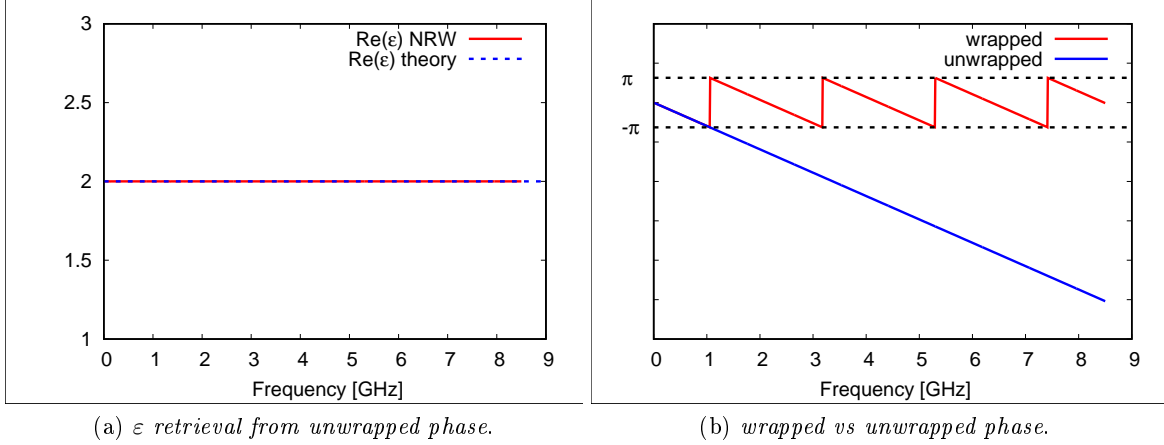


Figure C.2.: *Effect of wrapped vs unwrapped phase on the permittivity retrieval.*

The ambiguity problem for m doesn't occur if the starting frequency of the measurement is below a given minimum frequency f_{min} (equation (C.6))[76] because in this case we start at $m = 0$.

$$\epsilon_r \mu_r \leq \left(\frac{c}{2df_{min}} \right)^2 \quad (\text{C.6})$$

where d is the thickness and c the speed of light. What happens if f_{min} is not small enough? To illustrate this we keep all the parameters the same as before in the example, we only increase f_{min} from $0 \rightarrow 1.059GHz$. The result from equation (C.6) is $\epsilon_r \mu_r = 2.0035$ if we now slightly increase f_{min} to $1.060GHz$ and equation (C.6) is $\epsilon_r \mu_r = 1.9997$. This means for $f_{min} = 1.060GHz$ the algorithm should not be working properly anymore. The reason for this becomes obvious in Figure C.3a and Figure C.3b. The first jump in the phase is skipped in Figure C.3b. Therefore our assumption $m = 0$ is not valid anymore. In this case we would have to start at $m = 1$ instead to get the expected result. The effect on the permittivity is significant if the initial guess for m is wrong, as can be seen in Figure C.4a and Figure C.4b. Fortunately the difference from the obtained value with respect to the expected result is so important that obviously something went wrong.

C. Phase unwrapping

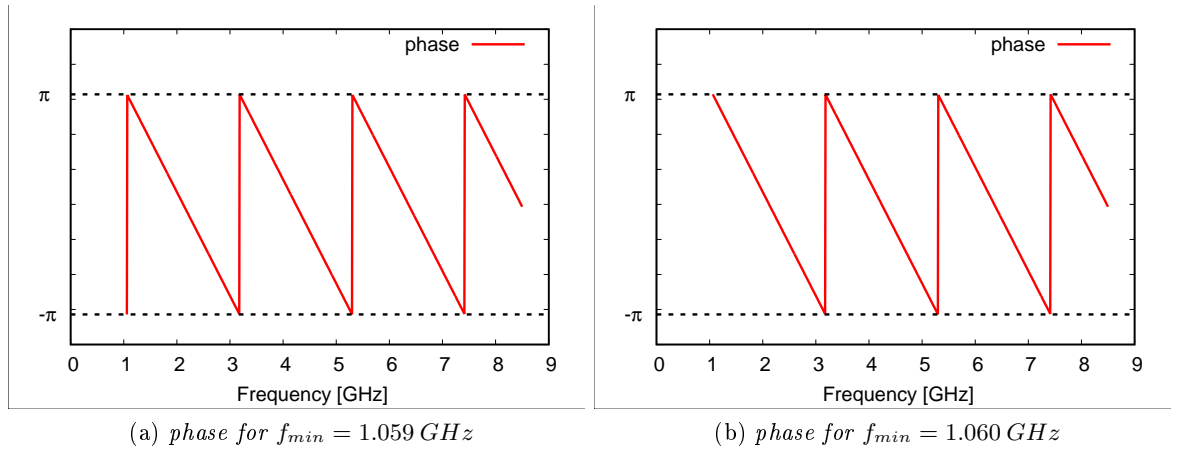


Figure C.3.: Effect of different starting frequencies on the phase

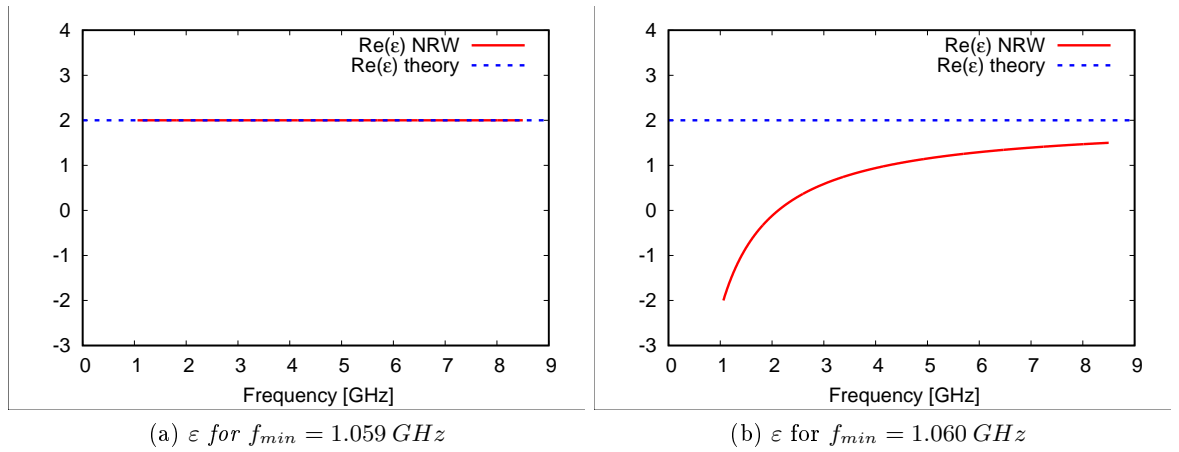


Figure C.4.: Effect of different starting frequencies on the permittivity